Quantum Criticality and Superconductivity in Systems Without Quasiparticles

A DISSERTATION PRESENTED
BY
CHENYUAN LI
TO
THE DEPARTMENT OF PHYSICS

IN PARTIAL FULFILLMENT OF THE REQUIREMENTS
FOR THE DEGREE OF
DOCTOR OF PHILOSOPHY
IN THE SUBJECT OF
PHYSICS

HARVARD UNIVERSITY
CAMBRIDGE, MASSACHUSETTS
MAY 2024

Dissertation Advisor: Professor Subir Sachdev Chenyuan Li

Quantum Criticality and Superconductivity in Systems Without Quasiparticles

Abstract

The discovery of high-temperature superconductors has raises questions that extend beyond the scope of quasiparticles, a foundational concept in condensed matter theory. This dissertation explores new theoretical approaches to quantum matter without quasiparticle excitations, with a particular focus on quantum criticality and the associated superconductivity in correlated electron compounds.

The soluble Sachdev-Ye-Kitaev (SYK) model has recently emerged as a fascinating platform to address the unusual metallic states with T-linear resistivity. We first consider different variants of random Hubbard models, which share many similarities to key aspects of the original SYK model. Using a large M analysis and a renormalization group method, we propose the existence of quantum critical points with fractionalized excitations separating two distinct phases, which provides insights into the quantum phase transitions and non-Fermi liquid behaviors observed in cuprate superconductors.

In the second part of this dissertation, we examine the interplay between non-Fermi liquids and superconductivity with two different pairing mechanisms. Under the framework of random Hubbard model, we demonstrate that superconductivity emerging from non-Fermi liquids strongly deviates from the BCS theory by tuning the relative strength of hopping and exchange interactions. Furthermore, we investigate a two-dimensional Yukawa-SYK model with spatially randomn interactions coupling a Fermi surface to a scalar field associated with a quantum phase transition. Our theory agrees well with transport properties analysed in cuprates, such as a T-linear resistivity and Planckian dissipation.

Contents

List of figures

To my parents.

Acknowledgments

Firstly, I would like to express my deepest gratitude to my thesis advisor, Prof. Subir Sachdev, for his invaluable mentorship and unwavering support. His broad vision and keen insights on physics have been truly inspiring: I have always enjoyed attending his lectures, working with him, and seeing his unique perspectives and approach. Throughout the challenging moments of my PhD journey, I am grateful to have his guidance and encouragement.

I would also like to thank my other dissertation committee members, Prof. Ashvin Vishwanath, and Prof. Philip Kim, for all the comments and advice they have given me over the years. I would like to thank Ashvin for his quantum matter course, which demystifies quantum field theory for me. I am also grateful for Philip's advice on teaching and presentations. Their feedback were invaluable throughout this process.

My sincere appreciation also goes to Professors David Nelson, Arthur Jaffe and Greg Kestin, for their guidance and encouragement during my time as a teaching fellow. I am also grateful for the inspiring discussions and feedback with Professors Eun-Ah Kim and Michael Lawler throughout their visit at Harvard.

I am grateful to be a part of Subir's group, with the opportunity to interact and collaborate closely with an outstanding group of individuals. Among them, I would particularly like to express my gratitude to Darshan G Joshi, from whom I have learned many aspects of condensed matter theory. I am also grateful to Ilya Esterlis, for generously sharing his numerical techniques and providing his guidance to my research. Moreover, I owe a great deal of thanks to Haoyu Guo for the invaluable discussions and patience to answer my questions. I would also like to thank my collaborators, Antoine Georges, Grigory Tarnopolsky, Davide Valentinis, Joerg Schmalian, Aavishkar Patel, Alex Kruchkov, Stephen Carr, Ziyan Zhu, Efthimios Kaxiras, for their support, insights and outstanding feedback in our joint projects. In addition, I want to thank Debanjan Chowdhury, Aavishkar Patel, Julia Steinberg, Rhine Samajdar, Henry Shackleton, Yanting Teng, Maria Tikhanovskaya, Maine Christos, Alexander Nikolaenko, Serhii Kryhin, Yunchao Zhang, who have been part of Subir's group during my time at Harvard. I truly appreciate their support and friendship.

It is also a great pleasure to have many physics friends. I would like to thank Xueyang Song, Shang liu, Ruihua Fan, Hengyun Zhou, Grace Zhang, Pavel Dolgirev, Luyi Qiu, for guiding me through my PhD journey. A special thanks to my fellow housemates, Haoyu Guo, Deng Pan, Zeyu Hao and Ruolan Xue, for their unlimited support throught the past six years.

My gratitude extends to the staff in the department of physics at Harvard, especially to Lisa Cacciabaudo, Elizabeth Alcock, Silke Exner, Jacob Barandes, who provided an enriching academic environment and necessary administrative support.

Finally, I'd like to thank my parents, Yan and Qing, for encouraging me to pursue a PhD in a different country and for all the love and support. This thesis is dedicated to them.

* * *

This thesis was typeset using LaTeX, originally developed by Leslie Lamport and based on Donald Knuth's TeX. A template that can be used to format a PhD dissertation with this look & feel has been released under the permissive AGPL license, and can be found online at github.com/suchow/Dissertate or from its lead author, Jordan Suchow, at suchow@post.harvard.edu.

1

Introduction

1.1 Landau Fermi Liquids and Beyond

How to understand an interacting many-body system lies at the heart of quantum condensed matter physics. In principle, the physical properties of such system can be deduced from the corresponding Schrödinger equation. However, it is almost impossible to solve a complex system of 10^{23} interacting particles under the current computing power. Landau's Fermi liquid theory [5, 6], initially aimed to explain the properties of liquid ^{3}He, turns out to offer a phenomenological way of predicting how electron-electron interactions influence the electronic properties of metals. This theory also provides a highly successful description of non-metallic states, such as semiconductors, magnets, superconductors, and superfluids, establishing it as one of the corner-stones of traditional many-body physics [7].

One of the key elements in Landau's Fermi liquid theory is the concept of "quasiparticles"

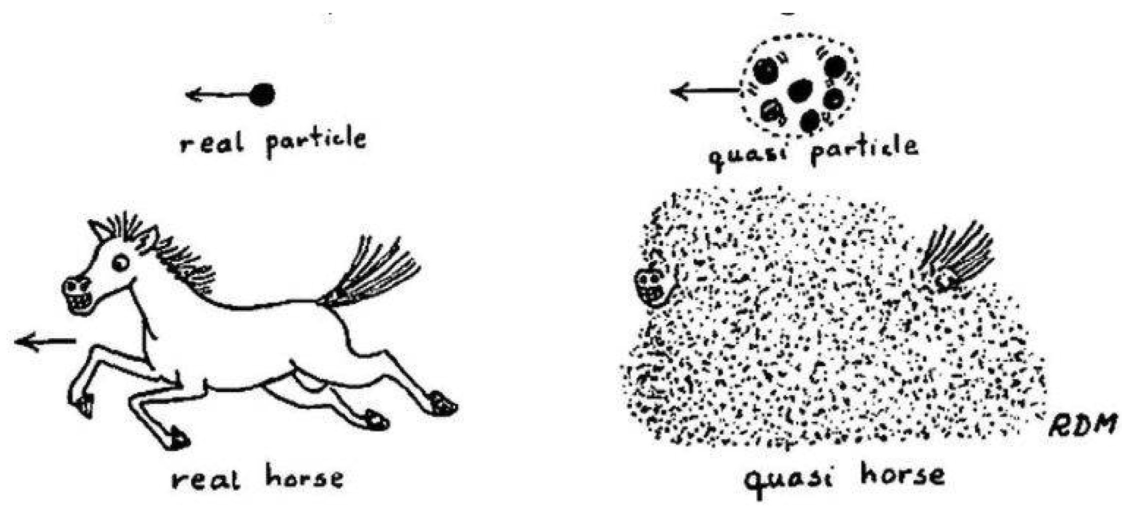

Figure 1.1: The real particle plus its cloud is the quasi particle. From R. D. Mattuck, *A Guide to Feynman Diagrams in the Many- body Problem*, Dover (1992).

[8] (Figure 1.1), on which much of modern condensed matter physics is built. However, in the last forty years, numerous experiments including the discovery of high temperature superconductors in 1986, presented challenges to the dominant position of Landau Fermi liquid theory. The unusual metallic state of these materials suggests a collapse of well-defined quasiparticles, prompting the need for new quantum theories to address entangled states of matter. In the following sections, we will encounter quantum matter that do not host quasiparticle excitations.

1.1.1 Fermi liquid theory of metals

The basic assumption of Landau's theory is that the low-energy eigenstates are labeled by occupation numbers which cannot change during the adiabatic turning on of the interaction. In this process, free electrons adiabatically turn into slowly-decaying Landau quasiparticles with the same quantum numbers. In light of this one-to-one correspondence, the language of the free fermion systems can be employed to describe the dressed quasiparticles in the Landau Fermi liquid: the energy of such low-lying excitations can therefore be written as a function of quasiparticle occupation numbers [9]

$$E = E_0 + \sum_{\alpha} \epsilon_\alpha \delta n_\alpha + \sum_{\alpha,\beta} F_{\alpha,\beta} \delta n_\alpha \delta n_\beta + \mathcal{O}\left((\delta n)^3\right) . \tag{1.1}$$

Here E_0 is the ground state energy, α labels the single-fermion eigenstate, ϵ_α denotes the energy of the single-quasiparticle states, $F_{\alpha,\beta}$ represents the interaction between quasiparticles, and δn_α is the change of quasiparticle occupation with respect to the ground state. The quasiparticle near the Fermi surface behaves like a real particle surrounded by its cloud (Figure 1.1), though it may have an effective mass different from the real mass and a lifetime due to the Landau interactions.

Whether the quasiparticle excitations are long-lived is essential to the stability of the Fermi liquid. While quasiparticles are not exact eigenstates and do decay over time, the decay rate diminishes much more rapidly than the quasiparticle energy in spatial dimensions $d > 1$. In a Fermi liquid, it is the quasiparticle-quasiparticle scattering that primarily contribute to this decay, and these can be estimated by the Fermi golden rule. Employing this method, the inverse lifetime is given by the sum of the probabilities of all the allowed decay processes [10]:

$$\frac{1}{\tau_{\boldsymbol{k}}} \sim \sum_{\boldsymbol{k}'\boldsymbol{q}} \frac{|W(\boldsymbol{q})|^2}{L^d} n_{\boldsymbol{k}'}(1 - n_{\boldsymbol{k}'+\boldsymbol{q}})(1 - n_{\boldsymbol{k}-\boldsymbol{q}})\delta(\varepsilon_{\boldsymbol{k}-\boldsymbol{q}} + \varepsilon_{\boldsymbol{k}'+\boldsymbol{q}} - \varepsilon_{\boldsymbol{k}} - \varepsilon_{\boldsymbol{k}'}) , \tag{1.2}$$

where $\frac{|W(\boldsymbol{q})|^2}{L^d}$ is the matrix element of an effective interaction between quasiparticles, with the initial states $\boldsymbol{k}$ and $\boldsymbol{k}'$ being occupied, whereas the final states $\boldsymbol{k} - \boldsymbol{q}$ and $\boldsymbol{k}' + \boldsymbol{q}$ being unoccupied. At low temperatures $T \to 0$, the inverse lifetime of a quasiparticle in the vicinity of the Fermi level vanishes as T^2, which is much smaller than the quasiparticle energy. This affirms that the quasiparticles are indeed long-lived and well-defined.

This quasiparticle picture is central to the study of transport phenomena. For instance, it predicts the low-temperature resistivity of metal increases quadratically with temperature, represented by

$$\rho(T) = \rho_0 + AT^2 \,, \text{ as } T \to 0 \tag{1.3}$$

where ρ_0 denotes the residual resistivity stemming from impurity scattering. It also leads to the linear in T temperature dependence of the electron specific heat, and a magnetic susceptibility χ independent of temperature.

1.1.2 BCS theory: Fermi-Liquid Superconductivity

The Landau Fermi liquid theory extends beyond describing the normal state of metals; it also lays the groundwork for our understanding of various non-metallic states, which are realized as certain instabilities of a Fermi liquid [7]. One notable example is the BCS pairing theory of superconductivity, introduced by Bardeen, Cooper and Schrieffer in 1957[11]. With an attractive interaction between the quasiparticles near the Fermi surface, the total energy of the system can be reduced through the formation of Cooper pairs. Thus, the superconducting transition is interpreted as an instability of the normal state at some finite temperature.

In a mean field approximation, we can simplify the HCS Hamiltonian as in Ref. [12]

$$H_{\mathrm{BCS}} = \sum_{\boldsymbol{k}\sigma}(\varepsilon_{\boldsymbol{k}} - \mu)c^\dagger_{\boldsymbol{k}\sigma}c_{\boldsymbol{k}\sigma} - \sum_{\boldsymbol{k}}\left[\Delta_{\boldsymbol{k}}c^\dagger_{\boldsymbol{k}\uparrow}c^\dagger_{-\boldsymbol{k}\downarrow} + \Delta^*_{\boldsymbol{k}}c_{-\boldsymbol{k}\downarrow}c_{\boldsymbol{k}\uparrow}\right], \tag{1.4}$$

where

$$\Delta = \frac{U_0}{V}\sum_{\boldsymbol{k}}\langle c_{-\boldsymbol{k}\downarrow}c_{\boldsymbol{k}\uparrow}\rangle_{H_{\mathrm{BCS}}} \tag{1.5}$$

will be self-consistently determined. After employing a Bogoliubov transformation, the eigenvalues give the spectrum

$$E_{\boldsymbol{k}} = \pm\sqrt{(\varepsilon_{\boldsymbol{k}} - \mu)^2 + |\Delta|^2}\,. \tag{1.6}$$

Here Δ plays the role of the BCS energy gap: a minimum energy Δ is required to create a Bogoliubov quasiparticle excitation. Below a critical temperature T_c, there is a $\Delta \neq 0$ solution that has lower energy than the non-superconducting normal state. Temperature dependence of the gap energy from tunnel experiments is shown in Figure 1.2, along with values predicted by the BCS theory [13]. The ratio of zero temperature energy gap Δ_0 and

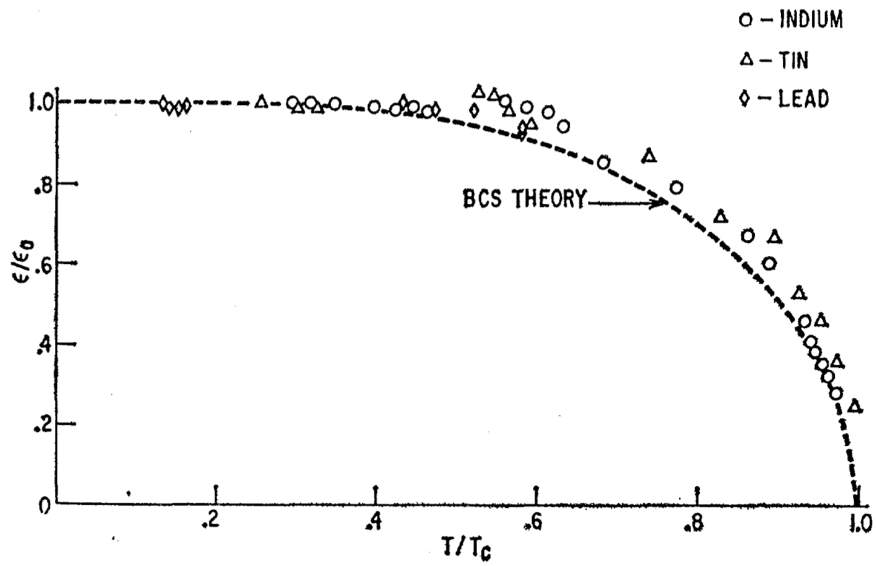

Figure 1.2: Temperature dependence of the gap energy for In, Sn and Pb, compared with the BCS theory (dashed). Figure taken from [13].

T_c turns out to be a universal dimensionless number

$$\frac{2\Delta_0}{T_c} = 2\pi e^{-\gamma} \approx 3.53 \tag{1.7}$$

which was verified in lower T_c superconductors [14].

1.1.3 Non-Fermi liquids

A large number of strongly correlated systems, such as materials with incompletely filled d- or f-electron shells, exhibit anomalous metallic properties strikingly deviated from the conventional Fermi liquid behavior [15]. Prominent among these are the high-temperature cuprate superconductors [16, 17], iron-based superconductors [18–20], heavy-fermion materials [21], and moiré systems [22]. Some of these materials retain their non-Fermi liquid behavior as temperature decreases, whereas others transit to Fermi liquids below a specific low-energy threshold [23]. It is challenging to describe the physcial properties in a universal way for such a rich family of non-Fermi liquid systems.

One of the most notable features is the linear-in-T resistivity observed in the family of cuprate superconductors. This strange metallicity can possibly be explained by the marginal Fermi liquids, where the lifetime of marginally coherent quasiparticles obeys $1/\tau(\epsilon) \sim |\epsilon|$ [24] . However, the marginal Fermi liquid self-energy, defined by single-particle properties, does not necessarily contribute to transport properties like dc conductivity: a marginal fermi liquid can be a conventional metal instead of a strange metal [25]. We will discuss the cuprate phenomenology in more details in Section 1.3.

1.2 Quantum Criticality

Much of recent work in strongly correlated materials has focused on quantum critical point (QCP), which separates two distinct quantum states of matter at zero temperature. Such continuous quantum phase transitions are driven by a nonthermal parameter like pressure, doping or a magnetic field. The presence of a QCP could provide insights into the non-Fermi liquid behaviors observed in unconventional superconductors, potentially unraveling the fundamental mechanism of superconductivity itself [20].

A representative phase diagram near a quantum critical point is shown in Figure 1.3. Here we consider a second-order phase transition at T_0 that can be suppressed by tuning g: T_0 decreases to 0 as $g \to g_c$. There are two diverging characteristic length scales as g approaches g_c: the order parameter correlation length

$$\xi \propto |g - g_c|^{-\nu}\,, \tag{1.8}$$

and correlation time

$$\xi_\tau \propto \xi^z\,, \tag{1.9}$$

where ν is the correlation length exponent, z is the dynamical critical exponent [20, 26]. At

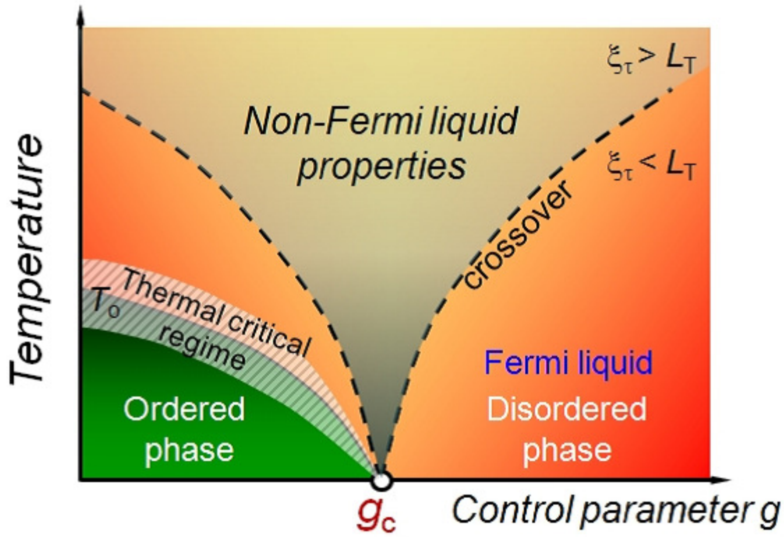

Figure 1.3: Schematic phase diagram near a quantum critical point, g_c. The second-order phase transition to an ordered phase at T_0 can be suppressed by the control parameter g. A non-Fermi liquid fan appears above the crossover line where the correlation time ξ_τ and the thermal length L_T become comparable. Figure taken from [20].

finite temperatures, the thermal fluctuations can be characterized by a timescale

$$L_\tau = \frac{\hbar}{k_B T}. \tag{1.10}$$

Consequently, we distinguish two regimes within the disordered phase by comparing the values of ξ_τ and L_τ. In the regime where $\xi_\tau \ll L_\tau$, quasiparticles remain well-defined, and the system displays Fermi-liquid like transport properties, which result from thermal average of independent quasiparticles. However, in the regime where $\xi_\tau \gg L_\tau$, the quasiparticle description breaks down due to the influence of the QCP at $g = g_c$, rendering the system unable to be described by the ground state wave function. In this quantum critical regime, the physical properties of the system significantly deviate from the standard Fermi liquid theory. For example, in the 2D case, the resistivity becomes linear-in-T and the specific heat behaves as $C_{\mathrm{el}}(T)/T \sim \log(T)$[27]. The influence of QCP can extend to finite temperatures, creating a quantum critical fan as a rich environment for exploring non-Fermi liquid physics

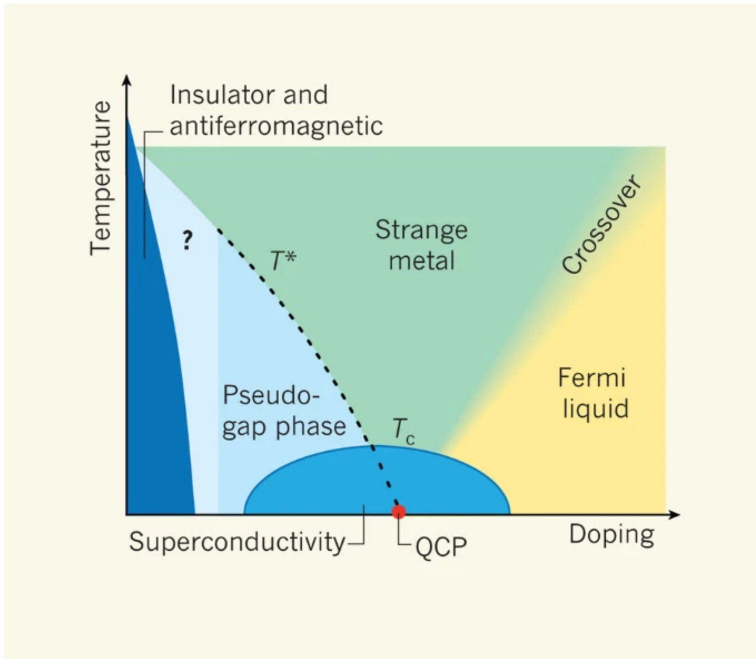

Figure 1.4: Phase diagram of hole-doped cuprates. Numerous phases are shown, including insulating antiferromagnet, pseudogap, strange metal, Fermi liquid and superconductor. The pseudogap phase below T^* ends at a $T = 0$ quantum critical point (red dot). Figure reproduced from [29].

[20, 28].

1.3 Cuprate phenomenology

Since the discovery of cuprate superconductors in 1986 [30], significant efforts have been devoted to revealing the mysterious mechanism of high-temperature superconductivity and other related novel phenomena. It is commonly understood that superconductivity arises through the electron or hole doping of an antiferromagnetic parent Mott insulator. Notably, hold-doped cuprates exhibit various underlying ground states, including a strange metal and a pseudogap metal at intermediate doping levels, both of which strongly deviate from the conventional Fermi liquid behavior (Figure 1.4). The emergence of these strongly correlated states and their transition to superconductivity challenge the celebrated BCS theory, propelling continued research in this dynamic field.

1.3.1 Pseudogap critical point

The pseudogap phase, a remarkable phenomena in cuprates, occurs below a temperature T^* that diminishes with increased doping, and concludes at a critical point inside the T_c dome as superconductivity is removed by a large magnetic field (Figure 1.4). This is different from the paradigm of an antiferromagnetic quantum critical point found in other systems, such as electron-doped cuprates [31], iron-based superconductors [20] and heavy-fermion metals [21]. The striking properties of the pseudogap critical point at $T = 0$ can be summarized as the following [32]:

1. Anti-nodal spectral gap opens and density of states decreases below p^*.
2. Carrier density drastically reduced from $n \simeq 1 + p$ at $p > p^*$ to $n \simeq p$ at $p < p^*$
3. Signatures of quantum criticality at p^*, with $\rho \sim T$ and $C_{\mathrm{el}} \sim T \log T$ as $T \to 0$

Whether the QCP in hole-doped cuprates is linked to antiferromagnetic correlations, as in the electron-doped scenario, remains an unresolved question. The absence of long-range order just below p^* suggests the potential existence of a novel state that does not break translational symmetry [32]. In this dissertation, we will present a simple rationale for the existence of a quantum critical point in hole-coped cuprates.

1.3.2 Strange metal

The strange metal right above p^* (Figure 1.4) represents an unusual metallic state that deviates significantly from the conventional Fermi liquid behavior [32–35]. Recent experimental observations highlighting the novel properties of strange metals are summarized below [15, 36, 37]:

1. The DC resistivity is T-linear at low temperatures, a deviation from the predictions of Fermi liquid theory. A distinguishing feature of strange metals, as opposed to bad

metals, is that their resistivity stays below the Mott-Ioffe-Regel limit [36], yielding $\rho(T) < h/e^2$ in $d = 2$ spatial dimensions. This resistivity can also be modeled by the Drude formula

$$\frac{1}{\rho(T)} = \frac{ne^2\tau_{\text{trans}}}{m^*}, \tag{1.11}$$

where n represents the carrier density determined from doping, and m^* is an effective mass obtained from specific heat measurements. The scattering rate $1/\tau_{\text{trans}}$ thus exhibits a Planckian behavior with $1/\tau_{\text{trans}} \sim k_B T/\hbar$, as observed in various strange metal experiments [34, 35, 37, 38].

2. The optical conductivity follows the form of a generalized Drude formula

$$\sigma(\omega) = \frac{K}{\dfrac{1}{\tau_{\text{trans}}(\omega)} - i\omega \dfrac{m^*_{\text{trans}}(\omega)}{m}} \quad ; \quad \frac{1}{\tau_{\text{trans}}(\omega)} \sim |\omega| \Phi_\sigma \left(\frac{\hbar\omega}{k_B T} \right), \tag{1.12}$$

where the constant K can be determined by (1.11), and the effective mass m^*_{trans} is estimated using Kramers-Kronig relations [39]. The frequency-dependent transport scattering rate $1/\tau_{\text{trans}}(\omega)$ obeys an ω/T scaling, paralleled by the inelastic scattering rate (1.13) observed in photoemission experiments [37, 40].

3. The inelastic electron self-energy in the vicinity of optimal doping shows a scaling behavior expressed as

$$\frac{1}{\tau_{\text{in}}(\omega)} = 2\,\text{Im}\Sigma(\omega) \sim |\omega| \Phi_\Sigma \left(\frac{\hbar\omega}{k_B T} \right), \tag{1.13}$$

indicating a marginal Fermi liquid [24, 37, 40].

4. The specific heat exhibits a scaling of $C_{\text{el}} \sim T \ln(1/T)$ as $T \to 0$ [37, 41].

Given the limitations of the quasiparticle-based theory, it remains a significant challenge to develop models that accurately reflect the universal properties of strange metals and elu-

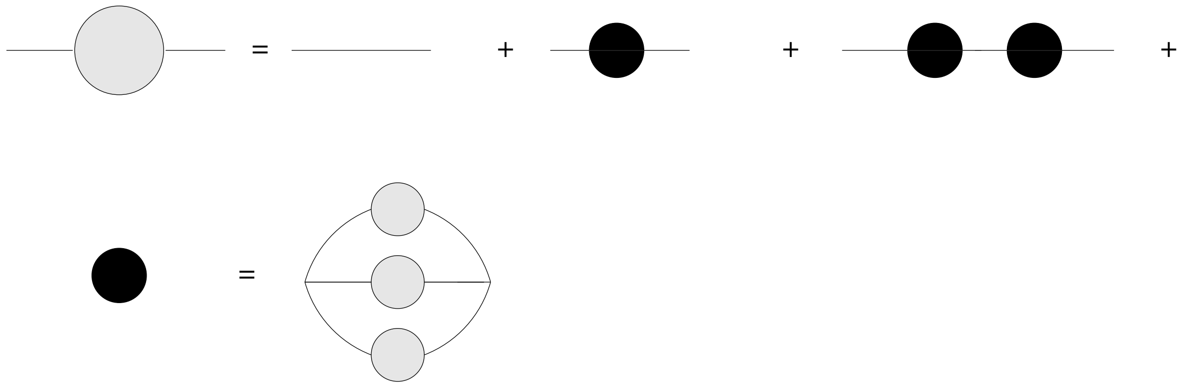

Figure 1.5: Graphical representation of the Dyson equations. Here the solid circle denotes the self energy Σ and the dotted circle denotes the dressed Green's function G. Figure taken from [43].

cidate their relationship with unconventional superconductivity. In this dissertation, we will explore various generations of Sachdev-Ye-Kitaev (SYK) models, which successfully characterize quantum phases of matter in the absence of quasiparticle excitations.

1.4 The Sachdev-Ye-Kitaev model

Originally introduced by Sachdev and Ye [1] and further refined by Kitaev [42], the SYK model provides an intriguing framework for probing non-Fermi liquid physics [15] and enhancing our understanding of quantum theory of black holes [37]. A prevalent variant of the SYK model consists of N fermions with a chemical potential μ and a random four-body interaction $U_{ij;k\ell}$:

$$H_4 = \frac{1}{(2N)^{3/2}} \sum_{ijk\ell=1}^{N} U_{ij;k\ell}\, c_i^\dagger c_j^\dagger c_k c_\ell - \mu \sum_i c_i^\dagger c_i \,, \tag{1.14}$$

where $U_{ij;k\ell}$ are independent Gaussian random variables with zero mean, variance U^2, and $U_{ij;k\ell} = -U_{ji;k\ell} = -U_{ij;\ell k} = U^*_{k\ell;ij}$. In the large N limit, this model is exactly solvable and can be performed graphically. The two-point Green's function in imaginary time is defined as

$$G(\tau) = -\frac{1}{N}\sum_{i=1}^{N}\left\langle \mathcal{T}_\tau c_i(\tau) c_i^\dagger(0)\right\rangle , \tag{1.15}$$

where $\mathcal{T}_\tau$ is time-ordering. As $N \to \infty$, only the 'melon' graph for the Dyson self energy survives (Figure 1.5), leading to the exact Schwinger-Dyson equations

$$G(i\omega_n) = \frac{1}{i\omega_n + \mu - \Sigma(i\omega_n)} \quad , \quad \Sigma(\tau) = -U^2 G^2(\tau) G(-\tau) \, . \tag{1.16}$$

These two equations typically require numerical methods for solutions due to their non-linear nature. However, at the low energy limit $\tau \gg 1/U$, a conformal solution can be analytically deduced [1, 37]:

$$G(i\omega) \sim -i\mathrm{sgn}(\omega)|\omega|^{-1/2} \quad , \quad \Sigma(i\omega) - \Sigma(0) \sim -i\mathrm{sgn}(\omega)|\omega|^{1/2} \, . \tag{1.17}$$

The spectral function $A(\omega) \sim 1/\sqrt{\omega}$ diverges and exhbits no δ-function peaks, indicating an absence of well-defined quasiparticles. The non-Fermi liquid nature of the model is further underscored by the $\hbar\omega/k_BT$ scaling of self energy and the exponentially small energy-level spacing near the ground state [37].

Nevertheless, as a $0+1$ dimensional theory lacking spatial structure, the SYK model must be generalized to non-zero spatial dimensions to effectively study the anomalous transport properties of strange metals. Earliest examples of incoherent metal built from SYK models usually consist of a lattice of SYK clusters connected by particle hopping [44]. These models demonstrate a crossover from heavy Fermi liquid to a incoherent metal regime where quasi-particle description fails. Moreover, explicitly adding pairing terms into a lattice SYK model allows for the study of the transition from incoherent metal to superconductivity [45]. But such non-Fermi liquid characteristics, like T-linear resistivity, cannot survive down to the lowest energies in models with quadratic terms, leading to a bad metal instead of a strange metal. This limitation has prompted our investigation into random exchange models that reintroduce 'Mottness', which refers to the extent to which electrons are inclined to localize due to repulsive interactions near a Mott transition [15].

The Hamiltonian of the original SY model [1] with N spins is given by

$$H_J = \frac{1}{\sqrt{N}} \sum_{1\leq i<j\leq N} J_{ij} \boldsymbol{S}_i \cdot \boldsymbol{S}_j, \tag{1.18}$$

where J_{ij} are independent Gaussian random variables with zero mean and variance J^2. Although this model is not exactly solvable in the large N limit, analytical solutions can be derived in two ways [15]. One approach is to generate the spin symmetry to SU(M) and considering the large M limit, thereby producing the same Schwinger-Dyson equations as those of the SYK Model (1.14). Another approach uses renormalization group methods to obtain analytical results near certain fixed points. Both methods will be explored in the forthcoming chapters.

1.5 Organization of this thesis

A large portion of this dissertation focuses on quantum phase transitions in random Hubbard models and their relationship to cuprate phenomenology.

In chapter 2, to captures the physics of hole-doped cuprates, we consider a random version of t-J model:

$$H_{tJ} = \frac{1}{\sqrt{N}} \sum_{i,j=1}^{N} \sum_{\alpha} t_{ij} \, \mathcal{P} c_{i\alpha}^\dagger c_{j\alpha} \mathcal{P} + \frac{1}{\sqrt{N}} \sum_{1\leq i<j\leq N} J_{ij} \, \boldsymbol{S}_i \cdot \boldsymbol{S}_j - \mu \sum_{i\alpha} c_{i\alpha}^\dagger c_{i\alpha} \, . \tag{1.19}$$

Here $\mathcal{P}$ denotes the projection to non-doubly occupied states, $\boldsymbol{S}_i = (1/2) c_{i\alpha}^\dagger \sigma_{\alpha\beta} c_{i\beta}$ is electron spin. Using a dynamical mean field theory, we map the model to a quantum impurity problem. The existence of a QCP is confirmed at critical doping by renormalization group (RG) analysis, where the spin susceptibility decays exactly as $1/\tau$, in contrast to the $1/\tau^2$ behavior expected in a Fermi liquid. Such a peculiar scaling property can be understood by fractionalizing the electrons into spinons and holons. Within our critical theory, two representations are used with either bosonic holons and fermionic spinons, or fermionic holons and bosonic spinons, so the strongly coupled QCP intuitively exhibits a boson-fermion duality. Away from the critical point, a runaway RG flow indicates the lower energy state is a boson that should be condensed. This yields two confining phases flanking the deconfined QCP: a disordered Fermi liquid (FL) with carrier density $1+p$ for $p>p_c$, and a metallic spin glass with carrier density p for $p<p_c$. Our theory provides an attractive description of QCP in the phase diagram of hole-doped cuprates, where the carrier density changes across the critical point. The SYK-like structure of the QCP exists all the way down to $T=0$, and naturally connects with a class of theories that have the strange T-linear resistivity.

In chapter 3, we move to the half-filled case to study another type of quantum phase transition, the continuous metal-insulator transition (MIT). With a finite Hubbard repulsion U and double occupancy allowed, the Hamiltonian has the form

$$H=\frac{1}{\sqrt{N}}\sum_{i,j=1}^{N}\sum_{\alpha}t_{ij}\,c_{i\alpha}^{\dagger}c_{j\alpha}+\frac{1}{\sqrt{N}}\sum_{1\leq i<j\leq N}J_{ij}\,\boldsymbol{S}_i\cdot\boldsymbol{S}_j+\sum_{i=1}^{N}\left(-\mu(n_{i\uparrow}+n_{i\downarrow})+Un_{i\uparrow}n_{i\downarrow}\right) \tag{1.20}$$

leading to a MIT in tuning U at half-filling. In the large M theory with SU(M) spin symmetry, the electron can be fractionalized into fermionic spinons and bosonic rotors, which gives rise to a deconfined critical point separating a disordered Fermi liquid from an insulating spin glass. The obtained exponents for the electron and spin correlators agree with a numerical study of $M=2$ random Hubbard model by Cha *et al.* [46]. For $M=2$, RG is performed on a quantum impurity model, yielding a finite coupling fixed point as a candidate to describe the transition. However, unlike our previous work on the random 't-J' model, we are unable to rule out the presence of a metallic spin glass phase at small U.

These SYK-inspired random exchange models also provides a framework to understand disordered two-dimensional systems proximate to superconductivity. Numerous experiments have observed an 'anomalous' metals state, also regarded as a 'failed superconductor', with low temperature conductivity significantly higher than that of a usual Fermi liquid. However, no available model of fluctuating superconductivity in a metallic background can consistently explain the existing observations. In chapter 4, we propose a dynamical mean-field model by introducing an additional random Cooper-pair hopping term to the random t-U-J theory, where the Hubbard U can take values of both signs. Electrons in this model can be fractionalized into partons such as spinons, holons and doublons, indicating critical points or phases between a superconducting phase and a disordered Fermi liquid in this model. The low temperature conductivity in these intermediate critical phases is derived by considering a large dimensionality limit, yielding temperature-independent values moderately enhanced from those in the disordered metal. This study proposes a candidate theory for the anomalous metal, and intrigues further research on superconducting states within these models of random couplings.

The second part of this dissertation explores the interplay between non-Fermi liquids and superconductivity. In chapter 5, we present a large M study of the transition from normal state to superconductor within the random t-U-J framework. Here, superconductivity is driven by an attractive on-site interaction U between electrons, with the normal state being either a Fermi liquid or a non-Fermi liquid depending on the relative strength of hopping and exchange interaction. These simple yet tractable models effectively capture the competition between the different energy scales in a quantitative manner, and show how strong interactions can modify the nature of superconductivity from the celebrated BCS paradigm.

However, the interaction that leads to pairing in the random exchange model above is different from the origin of non-Fermi liquids. This motivates the study of an electron-phonon variant of the SYK model in chapter 6, where the mechanism that leads to the failure of the quasiparticle picture is equally responsible for pairing. Following the previous theoretical work of a large N theory of critical Fermi surfaces [25, 47, 48], we consider a two-dimensional Yukawa-Sachdev-Ye-Kitaev model that describes spatially random Yukawa interactions between a Fermi surface and a scalar field associated with a quantum phase transition. The Yukawa-SYK model, as an extension beyond the original 0+1d version, proves to be an effective foundational framework for investigating theories of transport in non-zero spatial dimensions. We argue that a self-consistent disorder averaged analysis of this model describes a wide class of disordered quantum critical metals over a significant intermediate temperature range. Full numerical solutions of this limit will be presented, such as superconducting transition temperatures, electronic spectral functions, frequency-dependent conductivity, and superfluid stiffness. Our findings align closely with the transport analysis in the cuprates Michon *et al.* [39], and demonstrate a linear relationship between the superconducting critical temperature and the slope of the linear-T resistivity.

2

Deconfined critical point in a doped random quantum Heisenberg magnet

2.1 Introduction

Much evidence has now accumulated for a fundamental transformation in the ground state of the cuprate superconductors near optimal hole doping $p = p_c$ [49–61]. The transformation is primarily associated with a change in the mobile carrier density from to p to $1 + p$ as p increases across p_c. There are indications of various broken symmetries for $p < p_c$, including charge and bond density waves [51, 52], spin glass order [59–61], orbital currents [57] and nematic order [52]. However, it appears that the restoration of the broken symmetry cannot be the driving mechanism for a quantum phase transition at $p = p_c$: the broken symmetries are weak and differ among the cuprates, and the transport [53], thermodynamic [54–56], electronic [50–52, 58], and spin dynamics [59–61] signatures are strong.

This paper will study a model with all-to-all randomness (see (2.1) below) which exhibits a deconfined quantum critical point [62] with many similarities to the mysterious cuprate phenomenology. Our model has a quantum critical point at $p = p_c$ with fractionalized excitations, separating metallic states with carriers densities of p and $1 + p$ (see Figure 2.1). The overdoped state is a conventional disordered Fermi liquid, the underdoped 'pseudogap' phase with carrier density p has spin glass order, but the quantum critical point is described by fractionalized excitations. Our critical theory is distinct from a Landau-Hertz-Millis-type theory [63, 64] of the quantum fluctuations of the spin glass order in a metal; the latter theory has no fractionalization at criticality and does not exhibit a change in carrier density across the transition. Moreover, our $p = p_c$ critical theory is expected to maximally chaotic [43], similar to the Sachdev-Ye-Kitaev (SYK) [1, 42] models, and unlike the Landau theories [65].

Our results provide a simple rationale for the existence of a quantum phase transition in correlated metals with 'Mottness'. Broken symmetries are not essential, and only play a secondary role. At low doping, we have fermionic 'holons' of density p, moving in a background of condensed bosonic 'spinons' (see Figure 2.1). At higher doping, we have condensed bosonic holons, so that the fermionic spinons behave like a Fermi liquid of hole-like carrier density $1 + p$. This statistical transmutation, and corresponding transformation in the many-body state, is accomplished by a strongly coupled deconfined critical point which exhibits a boson-fermion duality. Note that, because of the presence of the Higgs-like condensates on both sides of the critical point, there is no true fractionalization for either $p > p_c$ or $p < p_c$.

There have been discussions [66] of deconfined critical points between a magnetic metal with 'small' Fermi surfaces, and a non-magnetic heavy Fermi liquid with a 'large' Fermi surface (a review of related ideas is in Ref. [67]). However, to date, no tractable realization of this scenario has been found in non-random systems. Our results show that a similar scenario is naturally realized in models with random couplings. We also note the study of Ref [68], which found an evolution between small and large Fermi surface across optimal doping in a plaquette dynamical mean field theory.

Our model is in the class of SYK models [1, 42] with random all-to-all couplings, which have been extensively exploited recently for descriptions of strange metals and the quantum information theory of black holes. Specifically, we generalize the insulating random Heisenberg magnet originally studied in Ref. [1] to metallic states of a $t - J_{ij}$ model at non-zero doping, along the lines of Ref. [69]. We consider electrons, annihilated by $c_{i\alpha}$, spin $\alpha =\uparrow,\downarrow$ on sites $i = 1 \ldots N$ with double occupancy prohibited $\sum_\alpha c^\dagger_{i\alpha} c_{i\alpha} \leq 1$. The Hamiltonian is the familiar t-J model with

$$H_{tJ} = \frac{1}{\sqrt{N}} \sum_{i \neq j=1}^{N} t_{ij} P\, c^\dagger_{i\alpha} c_{j\alpha} P + \frac{1}{\sqrt{N}} \sum_{i<j=1}^{N} J_{ij} \boldsymbol{S}_i \cdot \boldsymbol{S}_j - \mu \sum_i c^\dagger_{i\alpha} c_{i\alpha} \tag{2.1}$$

where P is the projection on non-doubly occupied sites, μ is the chemical potential and $\boldsymbol{S}_i = (1/2) c^\dagger_{i\alpha} \boldsymbol{\sigma}_{\alpha\beta} c_{i\beta}$ is the spin operator on site i, with $\boldsymbol{\sigma}$ the Pauli matrices. The complex hoppings $t_{ij} = t^*_{ji}$ and the real exchange interactions J_{ij} are independent random numbers with zero mean and mean-square values $\overline{|t_{ij}|^2} = t^2$ and $\overline{J^2_{ij}} = J^2$. We will work at a variable hole density p, defined by

$$\frac{1}{N} \sum_i \left\langle c^\dagger_{i\alpha} c_{i\alpha} \right\rangle = 1 - p\,. \tag{2.2}$$

The insulating $p = 0$ case of H_{tJ} was studied in Ref. [1], and in Ref. [69] for non-zero p, after generalizing the SU(2) spin symmetry to SU(M) and taking the large M limit (see Appendix A.3). A gapless critical ground state was found [1] at large M for $p = 0$. However, subsequent numerical studies [3, 4] of the insulating SU($M = 2$) case found a spin glass ground state, and such insulating spin glass states had also been examined in the large M limit [70, 71]. At non-zero p, the particular large M limit in Ref. [69] predicted a Fermi liquid ground state for all $p > 0$. We argue here that for the physical SU(2) case, the Fermi liquid only appears above a critical doping $p > p_c$, and that there is a metallic critical state very similar to the critical state of Ref. [1] at $p = p_c$. Our study was motivated by the observation of such critical spin correlations in metals in numerical studies of multi-orbital

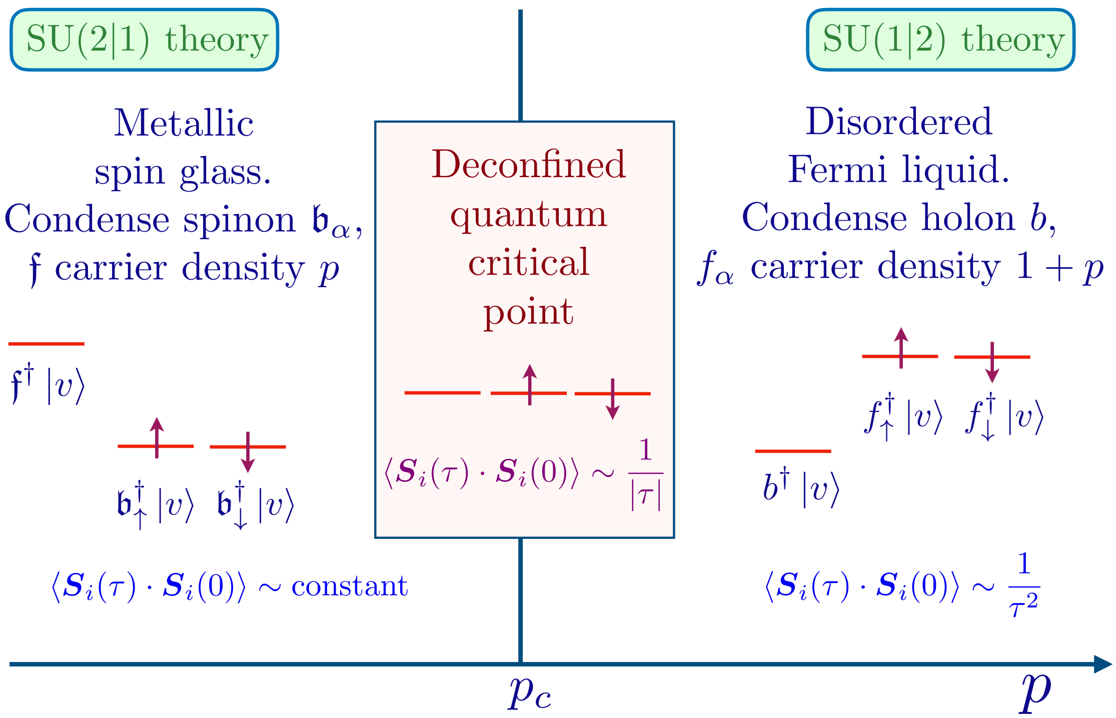

Figure 2.1: Proposed phase diagram of H_{tJ} in (2.1) as function of hole doping p. The three states on each site are realized either by fermionic spinons (f_α) and bosonic holons (b) with operators as in (2.3), or by bosonic spinons ($\mathfrak{b}_\alpha$) and fermionic holons ($\mathfrak{f}$) with operators as in (2.5); $\left|v\right>$ is the holon and spinon vacuum. The three states are nearly degenerate at $p = p_c$, which implies $p_c = 1/3$ at zeroth order. The critical theory can be described by both operator representations and exhibits an exact fermion-boson duality. Away from the critical point, the lower energy state is chosen to be bosonic, and that boson is condensed: so the spinons $\mathfrak{b}_\alpha$ condense for $p < p_c$, and the holons b condense for $p > p_c$. The spin correlations of SY [1], decaying as $1/|\tau|$, are realized at $p = p_c$. In the impurity model H_{imp} in (2.16), increasing p corresponds to increasing s_0.

Hubbard models [72, 73], and at the metal-insulator transition of a disordered Hubbard model at half-filling ($p = 0$) [46].

It is convenient to describe the 3 states on each site of the t-J model by spinon and holon operators. We can choose the spinons to be either fermions or bosons, and the holon to have the opposite statistics: the final results should be the same for all physical observables. With fermionic spinons f_α and bosonic holons b, the 3 physical states are $f_\alpha^\dagger |v\rangle$ and $b^\dagger |v\rangle$ (where $|v\rangle$ is the spinon and holon vacuum, and we drop site indices), see Fig. 2.1. Then the operators

$$c_\alpha = b^\dagger f_\alpha \quad , \quad \boldsymbol{S} = \frac{1}{2} f_\alpha^\dagger \boldsymbol{\sigma}_{\alpha\beta} f_\beta \quad , \quad V = b^\dagger b + \frac{1}{2} f_\alpha^\dagger f_\alpha \tag{2.3}$$

are all physical observables which realize the superalgebra SU(1|2) [74] (see Appendix A.1). We are interested in the 3-dimensional representation of physical states obeying

$$f_\alpha^\dagger f_\alpha + b^\dagger b = 1\,; \tag{2.4}$$

Hence, the physical states are invariant under the U(1) gauge transformation $f_\alpha \to f_\alpha e^{i\phi}$, $b \to b e^{i\phi}$, while individual spinon and holon excitations carry U(1) gauge charges.

Alternatively we can use a representation with bosonic spinons $\mathfrak{b}_\alpha$ and fermionic holons $\mathfrak{f}$. Now the gauge-invariant operators are

$$c_\alpha = \mathfrak{f}^\dagger \mathfrak{b}_\alpha \quad , \quad \boldsymbol{S} = \frac{1}{2} \mathfrak{b}_\alpha^\dagger \boldsymbol{\sigma}_{\alpha\beta} \mathfrak{b}_\beta \quad , \quad V = \mathfrak{f}^\dagger \mathfrak{f} + \frac{1}{2} \mathfrak{b}_\alpha^\dagger \mathfrak{b}_\alpha \,. \tag{2.5}$$

This realizes the same superalgebra SU(2|1) $\equiv$ SU(1|2) as (2.3), and the same 3-dimensional representation is obtained by the constraint

$$\mathfrak{b}_\alpha^\dagger \mathfrak{b}_\alpha + \mathfrak{f}^\dagger \mathfrak{f} = 1\,. \tag{2.6}$$

Note that while we find it convenient to refer to the superalgebra, there will be no supersymmetry in our results: H_{tJ} does not commute with all SU(1|2) generators.

We can now describe the structure of our main results illustrated in Fig. 2.1. We find a deconfined critical point $p = p_c$ at which the 3 spinon and holon states are nearly degenerate. Assuming all three states are equally probable at criticality, we obtain a critical density $p_c = 1/3$. Indeed, $p_c = 1/3$ is the zeroth order result of our renormalization group (RG) analysis, as we show in Appendix A.4.2; however, there are non-universal higher order corrections to the value of p_c. We can formulate this critical theory using *either* of the representations in (2.3) and (2.5). This exact fermion-boson duality is an elementary analog of the fermion-boson duality of 2+1 dimensional field theories describing the deconfined critical point of the square lattice antiferromagnet [75, 76]; as in the 2+1 dimensional theories, we will find that a Wess-Zumino-Witten [74, 77–80] term ($\mathcal{S}_B$ in (2.10) and (2.12) below) plays a central role in the criticality.

Away from the critical point, there is a runaway RG flow to states in which either the spinon or holon states are lower in energy. As illustrated in Fig. 2.1, we argue that this RG flow implies that we should now *choose* between the representations in (2.3) and (2.5) so that the lower energy state is a boson, and we should condense that boson. For $p > p_c$, the holon states are lower in energy; so we should choose (2.3) and condense b—this breaks the U(1) gauge symmetry, and we obtain a disordered Fermi liquid in which the f_α behave like electrons of density $1 - p$ (which is the same as holes of density $1 + p$ for the underlying Hubbard model). Conversely, for $p < p_c$, the spinon states are lower in energy; so we should choose (2.5) and condense $\mathfrak{b}_\alpha$—this again breaks the U(1) gauge symmetry, and we obtain a metallic spin glass in which the $\mathfrak{f}$ behave like holes of density p. Note that as $p \to 0$, this metallic spin glass becomes the insulating spin glass found in earlier studies [3, 4, 70, 71]. The large-M limit considered in Ref. [69] captures the disordered Fermi liquid, but does not capture the metallic spin-glass phase and the deconfined critical point at a non-zero $p = p_c$.

We will describe the nature of the infinite volume ($N \to \infty$) limit of H_{tJ} in Section 2.2, and map possible critical states of the large N limit to quantum impurity models in Section 2.2.1. The RG analysis of the impurity model appears in Section 2.3, where we obtain critical exponents of the deconfined critical point to two-loop order; the anomlaous dimensions of the electron and spin operators are obtained to all-loop order. We turn to the phases flanking the critical point in Section 2.4, and summarize our results in Section 2.5. The appendices contain various technical details; in particular, the RG equations for a generalized model with SU(M) spin symmetry appear in Appendix A.2, and the large M analysis appears in Appendix A.3.

2.2 Large volume limit

The limit of large volume ($N \to \infty$) of H_{tJ} is obtained by the methods described in Refs. [1, 70, 71] for the insulating model at $p = 0$. We introduce field replicas in the path integral, and average over t_{ij} and J_{ij}. At the $N = \infty$ saddle point, the problem reduces to a single site problem, with the fields carrying replica indices. The replica structure is important in the spin glass phase [70, 71], which we will explore in subsequent work. In the interests of simplicity, we drop the replica indices here as they play no significant role in the critical theory and the RG equations. Within the imaginary time path integral formalism (with $\tau \in [0, 1/T]$, with T the temperature), the solution of the model involves a local single-site effective action which reads:

$$\begin{aligned}
\mathcal{Z} &= \int \mathcal{D}c_\alpha(\tau) e^{-\mathcal{S}-\mathcal{S}_\infty} \\
\mathcal{S} &= \int d\tau \left[c_\alpha^\dagger(\tau) \left(\frac{\partial}{\partial \tau} - \mu \right) c_\alpha(\tau) \right] + t^2 \int d\tau d\tau' R(\tau - \tau') c_\alpha^\dagger(\tau) c_\alpha(\tau') \\
&\quad - \frac{J^2}{2} \int d\tau d\tau' Q(\tau - \tau') \boldsymbol{S}(\tau) \cdot \boldsymbol{S}(\tau') \,,
\end{aligned} \tag{2.7}$$

In this expression, μ is the chemical potential determined to satisfy (2.2) and $\mathcal{S}_\infty$ is the action associated with the constraint of no double occupancy ($U = \infty$). Decoupling the path integral introduces fields analogous to R and Q which are initially off-diagonal in the spin SU(2) indices. We have assumed above that the large-volume limit is dominated by the saddle point in which spin rotation symmetry is preserved on the average, and so R and Q

were taken to diagonal in spin indices. The path integral $\mathcal{Z}$ is a functional of the fields $R(\tau)$ and $Q(\tau)$, and we define its correlators

$$\begin{aligned} \overline{R}(\tau-\tau') &= -\left\langle c_\alpha(\tau)c^\dagger_\alpha(\tau')\right\rangle_{\mathcal{Z}} \\ \overline{Q}(\tau-\tau') &= \frac{1}{3}\left\langle \boldsymbol{S}(\tau)\cdot\boldsymbol{S}(\tau')\right\rangle_{\mathcal{Z}} \end{aligned} \tag{2.8}$$

In the thermodynamic ($N\to\infty$) limit, the solution of the model is obtained by imposing the two self-consistency conditions:

$$R(\tau)=\overline{R}(\tau) \quad , \quad Q(\tau)=\overline{Q}(\tau). \tag{2.9}$$

These equations and the mapping to a local effective action are part of the extended dynamical mean-field theory framework (EDMFT), which becomes exact for random models on fully connected lattices [64]. They can also be viewed as an EDMFT approximation to the non-random t-J model [68, 81–83]. To make contact with notations often used in the (E)DMFT literature, we note that $t^2R(\tau-\tau')$ is the self-consistent 'hybridization function' (dynamical mean-field) $\Delta(\tau-\tau')$.

This path-integral representation can be formulated in the SU(1|2) representation (2.3) as:

$$\begin{aligned} \mathcal{Z} &= \int \mathcal{D}f_\alpha(\tau)\mathcal{D}b(\tau)\mathcal{D}\lambda(\tau)e^{-\mathcal{S}_B-\mathcal{S}_{tJ}} \\ \mathcal{S}_B &= \int d\tau\left[f^\dagger_\alpha(\tau)\frac{\partial}{\partial\tau}f_\alpha(\tau)+b^\dagger(\tau)\frac{\partial}{\partial\tau}b(\tau)+i\lambda(\tau)\left(f^\dagger_\alpha(\tau)f_\alpha(\tau)+b^\dagger(\tau)b(\tau)-1\right)\right] \\ \mathcal{S}_{tJ} &= \int d\tau\, s_0\, f^\dagger_\alpha(\tau)f_\alpha(\tau)+t^2\int d\tau d\tau' R(\tau-\tau')f^\dagger_\alpha(\tau)b(\tau)b^\dagger(\tau')f_\alpha(\tau') \\ &\quad -\frac{J^2}{2}\int d\tau d\tau' Q(\tau-\tau')\boldsymbol{S}(\tau)\cdot\boldsymbol{S}(\tau')\,, \end{aligned} \tag{2.10}$$

where $\boldsymbol{S}(\tau)$ is to be represented by (2.3). Here $\mathcal{S}_B$ is the kinematic Berry phase (*i.e.* the Wess-Zumino-Witten term [77]) of the SU(1|2) superspin at each site [74], $\mathcal{S}_{tJ}$ is the action containing the terms arising from H_{tJ}, λ is the Lagrange multiplier imposing Eq. (2.4) and the chemical potential s_0 is determined to satisfy (2.2), which now becomes

$$\left\langle b^\dagger b \right\rangle_{\mathcal{Z}} = p \,. \tag{2.11}$$

Note that $\mathcal{Z}$ is a U(1) gauge theory, and under the U(1) gauge transformation $\lambda \to \lambda - \partial_\tau \phi$.

Let us also present the exactly equivalent formulation of the large N saddle point in terms of the SU(2|1) superspin. Now the Berry phase $\mathcal{S}_B$ in (2.10) is replaced by

$$\mathcal{S}_B = \int d\tau \left[\mathfrak{b}^\dagger_\alpha(\tau) \frac{\partial}{\partial\tau} \mathfrak{b}_\alpha(\tau) + \mathfrak{f}^\dagger(\tau) \frac{\partial}{\partial\tau} \mathfrak{f}(\tau) + i\lambda(\tau) \left(\mathfrak{b}^\dagger_\alpha(\tau)\mathfrak{b}_\alpha(\tau) + \mathfrak{f}^\dagger(\tau)\mathfrak{f}(\tau) - 1 \right) \right] \,, \tag{2.12}$$

while $\mathcal{S}_{tJ}$ has the same form, apart from representing $c_\alpha(\tau)$ and $\boldsymbol{S}(\tau)$ by (2.5), and replacing the s_0 term by $s_0 \mathfrak{b}^\dagger_\alpha(\tau)\mathfrak{b}_\alpha(\tau)$. The density constraint determining s_0 in (2.11) is replaced by

$$\left\langle \mathfrak{f}^\dagger \mathfrak{f} \right\rangle_{\mathcal{Z}} = p \,. \tag{2.13}$$

Appendix A.3 analyzes the path integral (2.10) using a large M expansion in an approach which generalizes the SU(2) spin symmetry to SU(M); a similar large M method has been used previously for a Hubbard model [84–86] and other phases of a disordered t-J model [87].

The body of the paper will focus on an RG analysis of $\mathcal{Z}$. This is performed by expressing it in terms of an auxiliary quantum impurity problem, which we will now set up.

2.2.1 Mapping to a quantum impurity problem

In our RG analysis, we find it useful to consider the path integral as a functional of the fields $R(\tau)$ and $Q(\tau)$ with an arbitrary time dependence, and to defer imposition of the self-consistency conditions in (2.9). As we are looking for critical states, we assume that these fields have a power-law decay in time with

$$Q(\tau) \sim \frac{1}{|\tau|^{d-1}} \quad , \quad R(\tau) \sim \frac{\mathrm{sgn}(\tau)}{|\tau|^{r+1}} \,. \tag{2.14}$$

where, for now, d and r are arbitrary numbers determining exponents, which will only be determined after imposing (2.9). Our analysis exploits the freedom to choose d and r: we will show that a systematic RG analysis of the path integral $\mathcal{Z}$ is possible to all orders in ϵ and $\bar{r}$, where

$$\epsilon = 3 - d \quad , \quad \bar{r} = \frac{1-r}{2} \;\; ; \;\; Q(\tau) \sim \frac{1}{|\tau|^{2-\epsilon}} \quad , \quad R(\tau) \sim \frac{\mathrm{sgn}(\tau)}{|\tau|^{2-2\bar{r}}} \,. \tag{2.15}$$

The analysis assumes ϵ and $\bar{r}$ are of the same order, and expands order-by-order in homogeneous polynomials in ϵ and $\bar{r}$. Such RG analyses were carried out in Refs. [88–90] for an insulating spin model in which $t = 0$, and by Fritz and Vojta [91–93] for a pseudogap Anderson impurity model in which $J = 0$ (see also Refs. [94, 95]); we note that the $\bar{r}$ expansion of Refs. [91–93] was in good agreement with numerical studies [96]. We will combine these analyses here, and our notations here for ϵ and $\bar{r}$ follow these earlier works.

We proceed by decoupling the last two terms in $\mathcal{S}$ by introducing fermionic (ψ_α) and bosonic (ϕ_a, $a = x, y, z$) fields respectively, and then the path integral $\mathcal{Z}$ reduces to a quantum impurity problem. The 'impurity' is a SU(1|2) superspin realizing the 3 states on each site of the t-J model, and this is coupled to a 'superbath' of the ψ_α and ϕ_a excitations. The quantum impurity problem is specified by the Hamiltonian

$$\begin{aligned} H_{\mathrm{imp}} \quad &= (s_0 + \lambda) f_\alpha^\dagger f_\alpha + \lambda\, b^\dagger b + g_0 \left(f_\alpha^\dagger b\, \psi_\alpha(0) + \mathrm{H.c.} \right) + \gamma_0 f_\alpha^\dagger \frac{\sigma^a_{\alpha\beta}}{2} f_\beta\, \phi_a(0) \\ &\quad + \int |k|^r dk\, k\, \psi_{k\alpha}^\dagger \psi_{k\alpha} + \frac{1}{2} \int d^d x \left[\pi_a^2 + (\partial_x \phi_a)^2 \right] \,. \end{aligned} \tag{2.16}$$

For completeness let us also explicitly present the Hamiltonian using a SU(2|1) impurity of bosonic spinons and fermionic holons

$$\begin{aligned} H_{\mathrm{imp}} \quad &= (s_0 + \lambda) \mathfrak{b}_\alpha^\dagger \mathfrak{b}_\alpha + \lambda\, \mathfrak{f}^\dagger \mathfrak{f} + g_0 \left(\mathfrak{b}_\alpha^\dagger \mathfrak{f}\, \psi_\alpha(0) + \mathrm{H.c.} \right) + \gamma_0 \mathfrak{b}_\alpha^\dagger \frac{\sigma^a_{\alpha\beta}}{2} \mathfrak{b}_\beta\, \phi_a(0) \\ &\quad + \int |k|^r dk\, k\, \psi_{k\alpha}^\dagger \psi_{k\alpha} + \frac{1}{2} \int d^d x \left[\pi_a^2 + (\partial_x \phi_a)^2 \right] \,. \end{aligned} \tag{2.17}$$

We note several features of $H_{\rm imp}$, which apply equally to (2.16) and (2.17):

- The bosonic bath is realized by a free massless scalar field in d spatial dimensions, as in Refs. [88–90]. The field π_a is canonically conjugate to the field ϕ_a. The impurity spin $\boldsymbol{S}$ couples to the value of ϕ_a at the spatial origin, $\phi_a(0) \equiv \phi_a(x = 0, \tau)$. It is easy to verify that upon integrating out ϕ_a from $H_{\rm imp}$, we obtain the J term in $\mathcal{S}_{tJ}$, with $Q(\tau)$ obeying (2.14).

- The fermionic bath is realized by free fermions $\psi_{k\alpha}$ with energy k and a 'pseudogap' density of states $\sim |k|^r$. The impurity electron operator c_α is coupled to $\psi_\alpha(0) \equiv \int |k|^r dk\, \psi_{k\alpha}$. Integrating out $\psi_{k\alpha}$ from $H_{\rm imp}$ yields the t term in $\mathcal{S}_{tJ}$, with $R(\tau)$ obeying (2.14).

- We have replaced the path integral over the Lagrange multiplier $i\lambda$ in $\mathcal{S}_B$ by a constant real λ. The constraint (2.4) can be conveniently and exactly imposed by the Abrikosov method of sending $\lambda \to \infty$ [90–93], as we will see in Section 2.3. So the consequences of $\mathcal{S}_B$ will be accounted for exactly, and that is also the case for the alternative analysis in Appendix A.2, where $\mathcal{S}_B$ is accounted for by the exact implementation of the superalgebras.

- The two formulations of $H_{\rm imp}$ in (2.16) and (2.17) are equivalent, and lead to identical RG equations. This is because, ultimately, the quantum dynamics depends only upon the superspin algebra and the representation of the superspin on each site, and these are the same for SU(2|1) formulation by (2.3,2.4) and SU(1|2) formulation by (2.5,2.6). An explicit derivation of the one-loop RG equations using only the superspin algebra and representation appears in Appendix A.2.

- The model is now characterized by 3 couplings constants, s_0, γ_0, and g_0, we will derive the RG equations for these couplings in Section 2.3. The coupling of the superspin to the fermionic bath is g_0, and to the bosonic bath is γ_0: we will see that the RG flow of these couplings is marginal for small ϵ and $\bar{r}$, and they are attracted to a deconfined critical point.

- The coupling s_0 acts like a 'Zeeman field' on the superspin, which breaks the degeneracy between the spinon and holon states. The flow of s_0 is strongly relevant at the deconfined critical point, and this drives the system into one of the two phases in Fig. 2.1.

We note that impurity models with both fermionic and bosonic baths have been considered earlier by Sengupta [97], and by Si and collaborators [98–100], but not for the 'superspin' case with significant particle-hole asymmetric charge fluctuations on the impurity site. Specifically, we fully project out doubly occupied states, while keeping holon states low energy, and these features are crucial to the structure of our critical theory, as in Refs. [91–93]. Also, the effect of a Zeeman field in an impurity spin model with a bosonic environment was studied in Refs. [101–103] in the context of the superfluid-insulator transition.

2.3 RG analysis

This section will present the RG analysis of the impurity model defined by (2.16). The RG analysis will initially not account for the self-consistency conditions (2.9). We will apply them later in Section 2.3.5.

We will employ the SU(1|2) superspin formulation, although essentially the same analysis can be applied to the SU(2|1) superspin, with exactly the same results. A key feature of the computation is that we impose the local constraint (2.4) exactly. This implemented by the Abrikosov method of taking the $\lambda \to \infty$ limit, as described in earlier analyses [90–93].

An alternative approach to obtain the RG equations generalizes the method of Refs. [88, 89] for SU(2) spins to superspins in either SU(2|1) or SU(1|2). This method utilizes only gauge-invariant information contained in the superspin algebra and its representation, and is presented in Appendix A.2. The RG equations are identical to those obtained in this section.

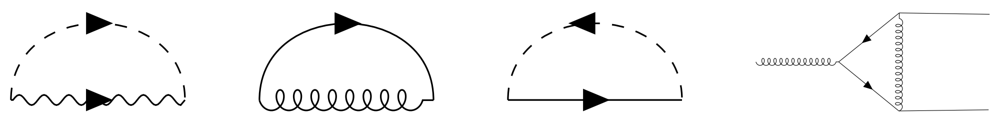

Figure 2.2: One-loop diagrams for self energy and vertex corrections. Fermion self-energy diagrams are shown in (a) and (b), boson self energy is shown in (c), and γ_0 vertex correction is shown in (d). In these diagrams, solid line is for f propagator, dashed line is for ψ propagator, wavy is for b propagator, and spiral is for ϕ propagator.

At the tree-level, we can identify the scaling dimensions from (2.16):

$$\begin{aligned} &\dim[f] = \dim[b] = 0\,, \quad \dim[\psi_{k\alpha}] = -\frac{1+r}{2} = -\dim[\psi_\alpha(0)]\,, \\ &\dim[g_0] = \frac{1-r}{2} \equiv \bar{r}\,, \quad \dim[\gamma_0] = \frac{3-d}{2} \equiv \frac{\epsilon}{2}\,, \quad \dim[\phi_a] = \frac{d-1}{2}\,. \end{aligned} \tag{2.18}$$

This establishes $r = 1$ and $d = 3$ as upper critical dimensions.

We define the following renormalized fields and couplings,

$$f_\alpha = \sqrt{Z_f} f_{R\alpha}\,, \quad b = \sqrt{Z_b} b_R\,, \quad g_0 = \frac{\mu^{\bar{r}} Z_g}{\sqrt{Z_f Z_b}} g\,, \quad \gamma_0 = \frac{\mu^{\epsilon/2} Z_\gamma}{Z_f \sqrt{Z_\phi \widetilde{S}_{d+1}}} \gamma\,, \quad \phi_a = \sqrt{Z_\phi} \phi_{Ra}\,, \tag{2.19}$$

where $\widetilde{S}_d = \Gamma(d/2-1)/(4\pi^{d/2})$. The renormalization factors are to be obtained from self-energy and vertex corrections, as we will show below. We will work with $s_0 = 0$ and subsequently derive the flow away from it. Also, we work at zero temperature, i.e., $\beta \to \infty$.

2.3.1 Fermion and boson self energy

Interaction terms in our action lead to self-energy corrections to the fermion and boson propagator. The corresponding Feynman diagrams at one-loop level are shown in Fig. 2.2 (a)-(c). Here we show explicit result for one-loop diagrams.

We first calculate the fermionic self energy at one-loop level. At this level there are no diagrams which mixes the vertices corresponding to the bosonic bath coupling and the fermionic bath coupling. Here we have two relevant diagrams and we quote the self-energy below:

$$\begin{aligned}
\Sigma^f_{2.2(a)} &= -g_0^2 \frac{1}{\beta}\sum_{i\omega_n}\int_{-\infty}^{\infty} dk \frac{|k|^r}{i\omega_n - k}\frac{1}{i\nu - i\omega_n - \lambda} = g_0^2\int_{-\infty}^{\infty} dk \frac{|k|^r\theta(k)}{i\nu-\lambda-k} \qquad (\text{Recall } \lambda\to\infty) \\
&= g_0^2 \pi \csc(\pi r)(\lambda - i\nu)^r = A_\mu (i\nu-\lambda) g^2\left[-\frac{1}{2\bar{r}} + i\pi\right] \qquad , \qquad (2.20) \\
\Sigma^f_{2.2(b)} &= \gamma_0^2 \frac{3}{4}\frac{1}{\beta}\sum_{i\omega_n}\int \frac{d^dk}{(2\pi)^d}\frac{1}{\omega_n^2+k^2}\frac{1}{i\nu+i\omega_n-\lambda} = \gamma_0^2\frac{3}{4}\frac{S_d}{2}\int_0^\infty dk \frac{k^{d-2}}{i\nu-\lambda-k} \\
&= \gamma_0^2\frac{3}{4}\frac{S_d}{2}\pi\csc(\pi(d-2))(\lambda-i\nu)^{-2+d} = B_\mu \frac{3}{4}\gamma^2(i\nu-\lambda)\left[-\frac{1}{\epsilon}+\frac{1}{2}(\aleph + 2i\pi)\right], \qquad (2.21)
\end{aligned}$$

where we wrote $\int d^dk/(2\pi)^d = S_d \int dk k^{d-1}$, $S_d = 2/(\Gamma(d/2)(4\pi)^{d/2})$,

$$A_\mu = \mu^{2\bar{r}}(i\nu-\lambda)^{-2\bar{r}}\frac{Z_g^2}{Z_f Z_b}, \tag{2.22}$$

$$B_\mu = \mu^{\epsilon}(i\nu-\lambda)^{-\epsilon}\frac{Z_\gamma^2}{Z_f^2 Z_\phi}, \tag{2.23}$$

$$\aleph = 2(\gamma_E - 1) = -0.845569\ldots, \tag{2.24}$$

with γ_E being the Euler's constant.

For the bosonic self energy there is only one diagram (Fig. 2.2(c)) at the one-loop level. The self energy is evaluated as follows:

$$\begin{aligned}
\Sigma^b_{2.2(c)} &= 2g_0^2\frac{1}{\beta}\sum_{i\omega_n}\int_{-\infty}^{\infty} dk\frac{|k|^r}{i\omega_n-k}\frac{1}{i\nu+i\omega_n-\lambda} = g_0^2\int_{-\infty}^{\infty} dk\frac{|k|^r\theta(k)}{i\nu-\lambda-k} \qquad (\text{Recall } \lambda\to\infty) \\
&= 2g_0^2\pi\csc(\pi r)(\lambda-i\nu)^r = A_\mu(i\nu-\lambda)2g^2\left[-\frac{1}{2\bar{r}}+i\pi\right] \qquad .
\end{aligned} \tag{2.25}$$

A factor of 2 is due to the spin index of internal f and ψ-line.

The expressions for $\Sigma^f_{2.2(a)}$ and $\Sigma^f_{2.2(c)}$ agree with those in Refs. [91–93], while that for $\Sigma^f_{2.2(b)}$ agrees with that in Ref. [90]. Similarly, the self-energy diagrams at two-loop level are evaluated in a straightforward manner, as shown in Appendix A.4.

2.3.2 Vertex correction

There is no one-loop vertex correction to the fermionic bath coupling g_0. However, it does acquire corrections at two-loop level. The bosonic bath coupling γ_0 has vertex corrections both at the one-loop and two-loop level. The one-loop diagram is shown in Fig. 2.2(d). Here we explicitly evaluated the one-loop vertex correction to γ_0,

$$\begin{aligned}\Gamma^{\gamma}_{2.2(d)} &= (-\frac{1}{4})\gamma_0^3 \frac{1}{\beta}\sum_{i\omega_{1n}}\int \frac{d^d k_1}{(2\pi)^d}\frac{1}{\omega_{1n}^2+k_1^2}\frac{1}{i\Omega_{1n}+i\omega_{1n}-\lambda}\frac{1}{i\Omega_{2n}+i\omega_{1n}-\lambda}\\ &= (-\frac{1}{4})\gamma_0^3\int\frac{d^d k_1}{(2\pi)^d}\frac{1}{2k_1}\frac{1}{i\Omega_{1n}-k_1-\lambda}\frac{1}{i\Omega_{2n}-k_1-\lambda}\\ &= -\gamma_0 B_\mu \gamma^2 \frac{1}{4}\left[\frac{1}{\epsilon}-1+\frac{1}{2}\left(-\aleph-2i\pi\right)\right].\end{aligned} \tag{2.26}$$

This expression agrees with that in Ref. [90]. We can similarly evaluate the two-loop level corrections and these are quoted in the Appendix A.4.

2.3.3 Beta functions and fixed points

We now demand the cancellation of poles in the expression for the renormalized vertex and the f/b Green's functions at the external frequency, $i\nu-\lambda=\mu$. This leads to the following expressions of the renormalization factors. Note that $Z_\phi = 1$ exactly, owing to the absence of bulk interaction terms such as ϕ^4. For the rest we have,

$$Z_f = 1-\frac{g^2}{2\bar{r}}-\frac{3\gamma^2}{4\epsilon}-\frac{15\gamma^4}{32\epsilon^2}+\frac{3\gamma^4}{8\epsilon}-\frac{g^4}{4\bar{r}^2}+\frac{g^4}{2\bar{r}}-\frac{3g^2\gamma^2}{8\epsilon\bar{r}}+\frac{3g^2\gamma^2}{8\bar{r}(\epsilon+2\bar{r})}+\frac{3g^2\gamma^2(2+\aleph)}{8(\epsilon+2\bar{r})}, \tag{2.27}$$

$$Z_b = 1-\frac{g^2}{\bar{r}}-\frac{g^4}{4\bar{r}^2}+\frac{g^4}{2\bar{r}}-\frac{3g^2\gamma^2}{4\epsilon\bar{r}}+\frac{3g^2\gamma^2}{2\epsilon(\epsilon+2\bar{r})}+\frac{3(2-\aleph)g^2\gamma^2}{4(\epsilon+2\bar{r})}, \tag{2.28}$$

$$Z_g = 1+\frac{g^4}{4\bar{r}}, \tag{2.29}$$

$$Z_\gamma = 1+\frac{\gamma^2}{4\epsilon}+\frac{9\gamma^4}{32\epsilon^2}-\frac{\gamma^4}{8\epsilon}+\frac{g^2\gamma^2}{4\epsilon\bar{r}}-\frac{g^2\gamma^2}{4\bar{r}(\epsilon+2\bar{r})}-\frac{g^2\gamma^2\aleph}{4(\epsilon+2\bar{r})}. \tag{2.30}$$

Using Eqns. (A.74) and (A.75), we obtain the beta functions as follows:

$$\beta(g) = -\bar{r}g + \frac{3}{2}g^3 + \frac{3}{8}g\gamma^2 - g^5 + \frac{3}{16}g^3\gamma^2\aleph - \frac{9}{8}g^3\gamma^2 - \frac{3}{8}g\gamma^4 \tag{2.31}$$

$$\beta(\gamma) = -\frac{\epsilon}{2}\gamma + \gamma^3 + g^2\gamma - \gamma^5 - \frac{5}{8}g^2\gamma^3\aleph - \frac{3}{4}g^2\gamma^3 - 2g^4\gamma \tag{2.32}$$

We can find the fixed points to two-loop order by setting the beta functions to zero. This gives us four fixed points $(g*^2, \gamma*^2)$:

$$FP_1 = (0,0)\,, \tag{2.33}$$

$$FP_2 = \left(0, \frac{\epsilon}{2} + \frac{\epsilon^2}{4}\right)\,, \tag{2.34}$$

$$FP_3 = \left(\frac{2\bar{r}}{3} + \frac{8}{27}\bar{r}^2, 0\right)\,, \tag{2.35}$$

$$\begin{aligned} FP_4 = \Bigg(&-\frac{\epsilon}{6} + \frac{8\bar{r}}{9} + \epsilon^2\left[-\frac{25}{324} + \frac{\aleph}{24}\right] + \bar{r}^2\left[-\frac{304}{729} + \frac{8\aleph}{27}\right] + \epsilon\bar{r}\left[\frac{119}{243} - \frac{5\aleph}{18}\right], \\ &\frac{2\epsilon}{3} - \frac{8\bar{r}}{9} + \epsilon^2\left[\frac{40}{81} - \frac{\aleph}{9}\right] + \bar{r}^2\left[\frac{1600}{729} - \frac{64\aleph}{81}\right] + \epsilon\bar{r}\left[-\frac{416}{243} + \frac{20\aleph}{27}\right]\Bigg)\,. \end{aligned} \tag{2.36}$$

The stability of the fixed points can be analyzed by looking at the eigenvalues of the stability matrix. We find that the Gaussian fixed point is always unstable. Importantly, we find that the non-trivial fixed point, FP_4, with $g* \neq 0$ and $\gamma* \neq 0$ is stable for a range of values in the parameter space of ϵ and $\bar{r}$. In Fig. 2.3 we plot the RG flow in the $g - \gamma$ plane at one-loop level and show the different fixed points.

These fixed points corresponds to the underlying t-J model at a non-zero doping density p. However, the precise value of p depends upon high energy details, and cannot be deduced from the fixed point couplings, as we discuss in Appendix A.4.2.

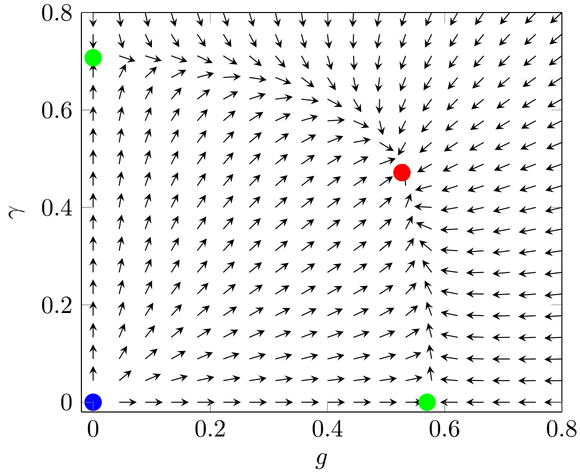

Figure 2.3: One loop RG flow in the $g-\gamma$ plane plotted for $\epsilon = 1$ and $\bar{r} = 0.5$. The red point is the stable fixed point (FP_4), green points are the saddle (FP_2 and FP_3) and blue point is the unstable Gaussian fixed point (FP_1). Note that the flow in the s direction is always relevant (not shown).

2.3.4 Anomalous dimensions of f_α and b

With the beta function at hand, it is straight forward to calculate the anomalous dimension of the fermion and boson propagators, defined as follows:

$$\eta_f = \mu \frac{d \ln Z_f}{d\mu}\bigg|_{FP}, \qquad \eta_b = \mu \frac{d \ln Z_b}{d\mu}\bigg|_{FP}. \tag{2.37}$$

Note that these anomalous dimensions are gauge-dependent, and not physically observable. We have defined them in the gauge $\lambda =$ constant. In terms of the coupling constants,

$$\eta_f = g^2 + \frac{3}{4}\gamma^2 - 2g^4 - \frac{3}{4}\gamma^4 - \frac{3}{4}g^2\gamma^2\left(1 + \frac{\aleph}{2}\right), \tag{2.38}$$

$$\eta_b = 2g^2 - 2g^4 - \frac{3}{4}g^2\gamma^2(2 - \aleph). \tag{2.39}$$

At the fixed points, we obtain the following expressions for the anomalous dimension,

$$FP_1 : \eta_f = 0\,, \quad \eta_b = 0\,, \tag{2.40}$$

$$FP_2 : \eta_f = \frac{3}{8}\epsilon\,, \quad \eta_b = 0 \quad \eta_f \text{ does not recieve correction at two loop }, \tag{2.41}$$

$$FP_3 : \eta_f = \frac{2}{3}\bar{r} - \frac{16}{27}\bar{r}^2\,, \quad \eta_b = \frac{4}{3}\bar{r} - \frac{8}{27}\bar{r}^2\,, \tag{2.42}$$

$$FP_4 : \eta_f = \frac{1}{3}\epsilon + \frac{2}{9}\bar{r} - \frac{\epsilon^2}{81} - \frac{256}{729}\bar{r}^2 + \frac{32}{243}\epsilon\bar{r}\,, \quad \eta_b = -\frac{1}{3}\epsilon + \frac{16}{9}\bar{r} - \frac{7}{162}\epsilon^2 - \frac{896}{729}\bar{r}^2 + \frac{112}{243}\epsilon\bar{r}\,. \tag{2.43}$$

2.3.5 Anomalous dimensions of the electron and spin operators

We now calculate the anomalous dimensions η_c and η_S of the physical and gauge-invariant composite operators, the electron c_α and the spin $\boldsymbol{S}$ specified in (2.3), defined such that

$$\overline{R}(\tau) \sim \frac{\mathrm{sgn}(\tau)}{|\tau|^{\eta_c}} \quad , \quad \overline{Q}(\tau) \sim \frac{1}{|\tau|^{\eta_S}}\,, \tag{2.44}$$

at large τ. We will show that it is possible to determine these anomalous dimensions to *all orders* in the ϵ and $\bar{r}$ expansions, as was also the case in previous analyses [88–93].

To compute these scaling dimensions, we add source terms to the action

$$\mathcal{S}_c = \frac{1}{\beta}\sum_{i\omega_n}\left(\Lambda_S f^\dagger_\alpha \frac{\sigma^a_{\alpha\beta}}{2} f_\beta + \Lambda_c[f^\dagger_\alpha b + H.c.]\right)\,. \tag{2.45}$$

Within the field-theoretic RG scheme, we have

$$\Lambda_S = \frac{Z_{ff}\Lambda_{S,R}}{Z_f}\,, \qquad \Lambda_c = \frac{Z_{fb}\Lambda_{c,R}}{\sqrt{Z_f Z_b}}\,. \tag{2.46}$$

The composite operators $\hat{S} = f^\dagger_\alpha(\sigma^a_{\alpha\beta}/2)f_\beta$ and $c^\dagger_\alpha = f^\dagger_\alpha b$ are renormalized as follows:

$$\hat{S} = \sqrt{Z_S}\hat{S}_R\,, \qquad c = \sqrt{Z_c}c_R\,. \tag{2.47}$$

It turns out that the diagrams contributing to the vertex corrections to Λ_S and Λ_c are exactly those we encountered while evaluating Z_γ and Z_g respectively. Thus we have,

$$Z_S = \left(\frac{Z_f}{Z_\gamma}\right)^2 , \qquad Z_c = \frac{Z_f Z_b}{Z_g^2} . \tag{2.48}$$

It is these identities which enable use to compute the anomalous dimensions exactly. We evaluate the required anomalous dimensions as,

$$\eta_S = \frac{d \ln Z_S}{d \ln \mu} , \qquad \eta_c = \frac{d \ln Z_c}{d \ln \mu} . \tag{2.49}$$

We can now make an exact statement for η_S for fixed points with $\gamma \neq 0$. From Eqns. (2.49) and (2.48) we obtain,

$$\eta_S = \frac{2}{Z_f Z_\gamma} \left[\left(Z_\gamma \frac{\partial Z_f}{\partial g} - Z_f \frac{\partial Z_\gamma}{\partial g} \right) \beta(g) + \left(Z_\gamma \frac{\partial Z_f}{\partial \gamma} - Z_f \frac{\partial Z_\gamma}{\partial \gamma} \right) \beta(\gamma) \right] . \tag{2.50}$$

Substituting the above equation in Eqn. (A.75), we obtain,

$$\frac{\epsilon}{2} \gamma Z_\gamma Z_f - \gamma \eta_S \frac{Z_f Z_\gamma}{2} + \beta(\gamma) Z_f Z_\gamma = 0 , \tag{2.51}$$

which leads to

$$\gamma \eta_S = \gamma \epsilon + 2\beta(\gamma) . \tag{2.52}$$

The first term on the r.h.s. of (2.52) arises from the tree-level scaling dimension, while the second term contains potential corrections higher order in ϵ. However, at the fixed point where $\gamma = \gamma^* \neq 0$, we have $\beta(\gamma^*) = 0$ and therefore,

$$\eta_S = \epsilon , \quad \text{to all orders in } \epsilon \text{ and } \bar{r}. \tag{2.53}$$

The same value of η_S is also obtained in the large M expansion in (A.64) and (A.67).

Similarly, using Eqns. (2.49) and (2.48) in combination with Eqn. (A.74) we obtain the following relation:

$$g\eta_c = 2\bar{r}g + 2\beta(g)\,. \tag{2.54}$$

Thus at the fixed point, $\beta(g^*) = 0$, such that $g^* \neq 0$, we obtain

$$\eta_c = 2\bar{r}\,, \quad \text{to all orders in } \epsilon \text{ and } \bar{r}. \tag{2.55}$$

The same value of η_c is also obtained in the large M expansion in (A.54) and (A.56).

We can now state the main result of this subsection: at the non-trivial fixed point FP_4 $(g^* \neq 0, \gamma^* \neq 0)$ we have $\eta_S = \epsilon$ and $\eta_c = 2\bar{r}$ to all orders in ϵ and $\bar{r}$.

Finally, we can impose the self-consistency condition, Eq. (2.9). This implies equating the exponents in Eq. (2.14) to the anomalous dimensions found above, *i.e.*, $\eta_S = d - 1$ and $\eta_c = r + 1$. Solving these equations requires using values of ϵ and $\bar{r}$ which are of order unity, but because Eqs. (2.53) and (2.55) are valid to all orders, we can use such values with confidence. Solving these self-consistency conditions we obtain our exact results for η_c and η_S

$$\eta_S = 1 \quad , \quad \eta_c = 1\,, \tag{2.56}$$

at the self-consistent values $\epsilon = 1$ and $\bar{r} = 1/2$. These anomalous dimensions imply the critical correlators at FP_4

$$\langle \boldsymbol{S}(\tau) \cdot \boldsymbol{S}(0) \rangle \sim \frac{1}{|\tau|} \quad , \quad \left\langle c_\alpha(\tau) c_\alpha^\dagger(0) \right\rangle \sim \frac{\mathrm{sgn}(\tau)}{|\tau|}\,, \tag{2.57}$$

as indicated in Fig. 2.1. We note that the fixed point FP_4 in (2.36) is stable when evaluated at $\epsilon = 1$ and $\bar{r} = 1/2$, although formally we cannot trust our expansion for the stability exponent at such large values of ϵ and $\bar{r}$.

2.4 Moving away from the critical point

The RG flow equations presented in Section 2.3.3 have a fixed point FP_4 which realizes the deconfined critical point of Fig. 2.1. This fixed point has one relevant direction, corresponding to the on-site energy s which distinguishes the local energy of the spinon and holon states. As s flows to $+\infty$, the holon state is lower in energy, corresponding to the $p > p_c$ region of the phase diagram in Fig. 2.1. Conversely, as s flows to $-\infty$, the spinon states are lower in energy, corresponding to the $p < p_c$ region of the phase diagram.

We can now exploit the choice of superspin representations between SU(1|2) and SU(2|1) to understand the fate of the RG flow. The energy of the ground state is minimized if we maximize the occupation of the lower energy state, and this is achieved if we choose the representation in which this lower energy state is bosonic. This implies that we should choose SU(1|2) for $p > p_c$ and SU(2|1) for $p < p_c$, as indicated in Fig. 2.1. We now describe the structure of these theories in turn

2.4.1 Overdoped region

In the SU(1|2) theory for $p > p_c$, we condense the boson b. With $\langle b \rangle \neq 0$, we have from (2.3), $c_\alpha \sim f_\alpha$, and the hopping term t_{ij} in H_{tJ} in (2.1) reduces to a renormalized hopping term for the f_α spinons. Indeed, the resulting theory for the f_α fermions is similar to that studied by Parcollet and Georges [69], and more recently in SYK-like extensions [44, 104–107].

A description of this phase, far from the $p = p_c$ critical point, can be obtained from H_{tJ} in (2.1) by taking the large M limit of Ref. [69]: we consider spinons f_α with $\alpha = 1 \dots M$, the bosons b do not acquire any additional index (so we are considering a SU($1|M$) superspin), and we rescale $t^2 \to t^2/M^2$ and $J^2 \to J^2/M$. (Note that this large M limit is distinct from that described in our Appendix A.3, where the bosons do acquire an additional index, and we rescale $t^2 \to t^2/M$ and $J^2 \to J^2/M$.)

In the large M limit of Ref. [69], the b bosons can be replaced by their condensate $\langle b \rangle =$

$b_0\sqrt{M}$. The f_α fermions have an effective hopping of strength $t\, b_0^2$. As shown in Ref. [69], the theory behaves a like a disordered Fermi liquid below a coherence scale

$$E_c = \frac{(tb_0^2)^2}{J}. \tag{2.58}$$

Note that this disordered Fermi liquid has a hole carrier density of $1+p$. This follows from $c_\alpha \sim f_\alpha$, and the density of f_α fermions obtained from (2.4) and (2.11).

As we approach the critical point, with $p \searrow p_c$, we expect E_c and $\langle b \rangle$ to both vanish algebraically. However, we do not expect the large M theory of Ref. [69] to properly describe the approach to the critical point: in this large M theory, we obtain an insulating state as $\langle b \rangle$ vanishes, whereas our $p = p_c$ critical point is metallic. Indeed, as b is gauge-charged field, the value of $\langle b \rangle$ is not a gauge-invariant quantity which can be directly compared between different approaches. However, the crossover scale E_c is better defined, and we can deduce the behavior of E_c near $p = p_c$ by the RG analysis of Section 2.3. We expect

$$E_c \sim |p - p_c|^{1/\lambda_s} \tag{2.59}$$

where λ_s is the relevant RG eigenvalue with which s flows away from the FP_4 fixed point, specified in (A.84).

2.4.2 Pseudogap region

For $p < p_c$, we use the SU(2|1) theory, and condense the $\mathfrak{b}_\alpha$ spinons to obtain spin glass order, as described in Refs. [70, 71]. The presence of the mobile $\mathfrak{f}$ fermions will make this a metallic spin glass with carrier density p, as determined by (2.13).

We need to extend the insulating spin glass theory of Refs. [70, 71] to the metallic spin glass, and this will be studied in greater detail in future work. Here we note that a systematic description appears possible in the large M limit of a SU($M|M'$) formulation noted in Appendix A.1.1, where the $\mathfrak{f}$ fermions acquire an additional 'orbital' label $\ell = 1 \dots M'$, and we

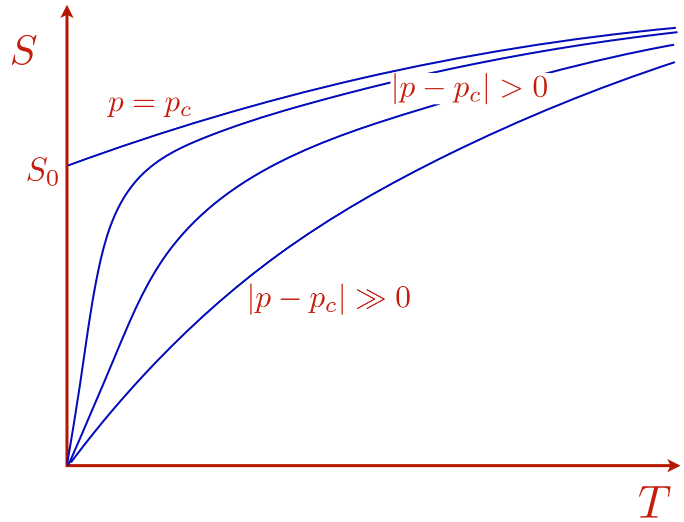

Figure 2.4: Schematic plot of the temperature dependence of the entropy S of H_{tJ}. At $p = p_c$, there is a non-vanishing extensive entropy at zero temperature S_0. The linear-in-T coefficient of the specific heat $\gamma = \lim_{T\to 0} C/T = \lim_{T\to 0} dS/dT$ diverges as we approach p_c.

keep $k = M'/M$ fixed in the large M limit. This should be contrasted from the SU($M'|M$) theory described in Appendix A.3, in which the b_ℓ bosons are assumed to not condense.

2.4.3 Specific heat

This section discusses qualitative features of the specific across the phase transition at $p = p_c$.

Right at $p = p_c$, the critical theory is expected [71] to have a non-vanishing extensive entropy S_0 as $T \to 0$. This follows from the similarity of the random insulating magnet [1], and many other models in the SYK class.

Away from $p = p_c$, we expect that the entropy follows the behavior of the critical point at temperatures above the coherence scale E_c, before vanishing lineary with T at temperatures below E_c, as shown in Fig. 2.4. We can therefore estimate that the linear-in-T coefficient of the specific heat C is

$$\gamma = \lim_{T\to 0} \frac{C}{T} = \lim_{T\to 0} \frac{dS}{dT} \sim \frac{S_0}{E_c} \tag{2.60}$$

So we expect γ to diverge as $|p - p_c|^{-1/\lambda_s}$ in the infinite range model H_{tJ}. It is notable that this behavior resembles experimental observations [56].

2.5 Conclusions

We have presented a RG analysis (in Section 2.3) of the phase diagram of the t-J model in (2.1) with random and all-to-all hopping and spin exchange. The predictions of this analysis are presented in Fig. 2.1: a deconfined critical point which separates two phases without fractionalization: a 'pseudogap' metallic spin glass phase with carrier density p, from a disordered Fermi liquid with carrier density $1 + p$. The change in the carrier density across the critical point, and the behavior of the specific heat across the critical point implied by the entropy in Fig. 2.4 are in good qualitative accord with experimental observations [53–56]. The SYK-like structure of the deconfined critical point connects naturally with a class of theories with linear-in-T resistivity in the strange metal [44, 69, 104–107]; a linear-in-T resistivity was also found in numerical studies [82, 83] of lattice models without disorder described by equations closely related to those of the large M limit of Appendix A.3. And we note that there is a recent report of spin glass correlations in the pseudogap phase [61], extending earlier impurity-induced observations [59, 60].

It is useful to compare the structure of H_{tJ} in (2.1) with that of SYK lattice models [44, 104–106]. The SYK models have a random 4-fermion interaction term, and a random 2-fermion hopping term of strength t, but no on-site fermion constraint. At the lowest energies, the 2-fermion term is always relevant and drives the system away from SYK criticality to a Fermi liquid state. In the present t-J model analysis, the presence of the local constraint (2.4) or (2.6) is crucial; in terms of the fractionalized particles in (2.3) or (2.5), *both* the t and J terms are 4-particle terms. Consequently, they can balance each other, and allow for a critical SYK-like state to exist at a critical $p = p_c$ all the way down to $T = 0$. At $p = p_c$, the 3 states of the t-J model obeying the constraint (2.4) or (2.6) are nearly degenerate in our perturbative renormalization group analysis. Consequently, we find $p_c = 1/3$ at zeroth order (see Fig. 2.1).

Appendix A.3 presents a low energy analysis of the large M saddle point of H_{tJ} obtained by generalizing the SU(2) symmetry to SU(M). The main difference from the RG analysis is that a critical *phase* appears in the low energy and large M theory, rather than a critical point. However, the exponents of the gauge-invariant spin and electron operators in the appropriate large M phase are the *same* as those obtained by the renormalization group analysis of the deconfined critical point to all orders in ϵ and $\bar{r}$: compare (A.64,A.67) and (A.54,A.56) with (2.53) and (2.55). We also note that the similarity between Appendix A.3 and the SYK equations indicates that our critical theory obeys maximal chaos [43].

A useful perspective on our renormalization group analysis provided by viewing the 3 states on each site as different orientations of a SU(1|2) or SU(2|1) superspin [74]. In the large N limit of a N-site t-J model with random and all-to-all interactions, we obtain an impurity model in which the superspin is coupled to both fermionic and bosonic baths self-consistently. In addition, there is a 'Zeeman field' acting on the superspin which breaks the degeneracy between the spinon and holon states; this field is a strongly relevant perturbation at the deconfined critical point, and drives the system into the two phases flanking the critical point. (See Refs. [101–103] for analogous RG studies of a relevant "Zeeman field" at an impurity site (represented by a SU(2) spin) in a Bose-Hubbard model at the superfluid-insulator transition, which are in good agreement with numerics.) In the overdoped phase, the holon state has a lower energy (see Fig. 2.1): so we use the SU(1|2) superspin in which the holon is a boson, and condense it to obtain a disordered Fermi liquid, analogously to Ref. [69]. Conversely, in the underdoped phase, the spinon states have a lower energy, so we use the SU(2|1) superspin in which the spinons are bosons, and condense them to obtain a metallic spin glass.

Despite our use of the superspin terminology, the model studied and the renormalization group equations are not supersymmetric: the fermionic c_α generators in (2.3) and (2.5) do not commute with the Hamiltonian. We can extend H_{tJ} by including off-site interations with the generator V in (2.3) and (2.5), and this will include density-density interactions. With this extension, we have the possibility of charge glass order in the pseudogap, and critical density fluctuations (likely similar to those observed in Refs. [108, 109]) at possibly supersymmetric fixed points. (Supersymmetric t-J models have been studied in one dimension without disorder [110–114].)

Finally, we comment on the extent to which a model with all-to-all randomness can be mapped to the cuprates. Randomness is present in the experimental systems, and also serves important simplifying purposes in our theoretical analysis. Moreover, certain approximations to models without randomness lead to closely related saddle point equations [68, 81–83]. Several of the broken symmetries do not exist in the random model, and subtle questions [115] about the structure of the Fermi surface in momentum space can be avoided. However, the central issues of carrier density, fractionalization, emergent gauge charges, and associated quantum phase transitions remain well defined even in the presence of randomness. Given the recent spin glass observations [61], and as we noted in Section 2.4.2, it will be useful to study the metallic pseudogap state, and the interplay between the spin glass order and charge transport. A possible approach is the extend the large M theory of Refs. [70, 71] to include fermionic holons, as well as numerical studies for $M = 2$.

3

Metal-insulator transition in a random Hubbard model

3.1 Introduction

The Mott metal-insulator transition is central to an understanding of correlated electrons [116]. In many three-dimensional correlated electron compounds, and in dynamic mean-field theories, this transition is first order. However, there are cases when the transition can be continuous, with interesting possibilities for non-Fermi liquid and 'strange metal' behavior at non-zero temperature in the vicinity of the critical point. One case which has been much studied theoretically [117–120] is when the Mott insulator is a spin liquid with a spinon Fermi surface, and the continuous transition involves condensation of an electrically charged boson which also carries charges under an emergent gauge field.

In the present paper, we will focus on the continuous (or nearly continuous) Mott transition observed recently in a numerical study of a Hubbard model supplemented by random exchange interactions by Cha *et al.* [46]. Such a model was previously studied by Florens *et al.* [86] using a large M approach which generalized the SU(2) spin symmetry to SU(M). In the large M limit, the saddle point equations obtained by Florens *et al.* [86] turn out to be essentially identical to the saddle point equations of a different model studied recently by Fu *et al.* [87]. Fu *et al.* [87] obtained analytic results on the low energy structure of gapless states in their model, and so we can transfer their results to the random Hubbard model of Florens *et al.* [86] and Cha *et al.* [46]. We will find that the large M exponents obtained by Fu *et al.* [87] for the critical state in Section 3.3.2.1 agree with the corresponding exponents for the electron and spin correlators at the continuous Mott transition obtained numerically Cha *et al.* [46] for the case with SU(2) spin symmetry. In the large M theory, the Mott criticality is realized by a deconfined critical point [62], described by the fractionalization of the electron into fermionic spinons and charged scalars both carrying an emergent U(1) gauge charge. We argue that this deconfined critical point separates a disordered Fermi liquid from an insulating spin glass (see Fig. 3.1).

In Section 3.4, we will present a renormalization group (RG) study of the random Hubbard model for the case with SU(2) spin symmetry (and also for general SU(M)). As in a recent study of the random t-J model [2], the RG is performed on a quantum impurity model, with the impurity site coupled to fermionic and bosonic baths, and supplemented by self-consistency conditions. The RG analysis follows methods developed in Refs. [89, 92]. For the particle-hole symmetric case relevant to half-filling, the RG requires a perturbative treatment of the on-site repulsion (the Hubbard U) between the electrons in the context of an ϵ expansion (defined in (3.34)). The solution of the self-consistency conditions requires an extrapolation to $\epsilon = 1$; unlike the previous work [2], we are unable to perform this extrapolation with any reliability as we do not have access to the needed exponents to all orders in ϵ.

The RG analysis in the small U,ϵ expansion yields a finite coupling fixed point with one relevant direction. This fixed point is a candidate to describe the metal-insulator transition

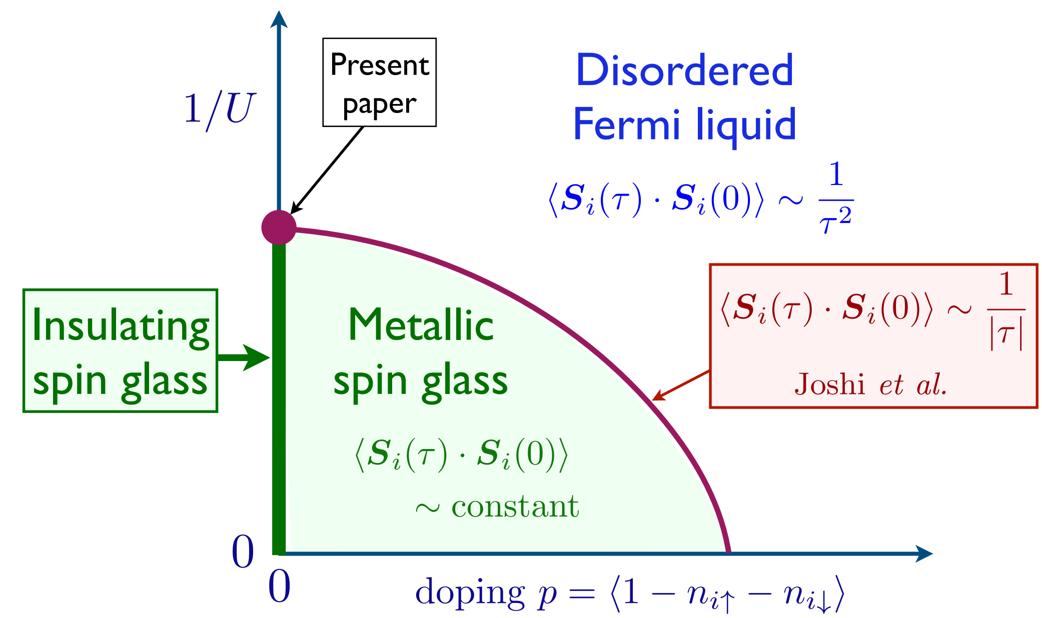

Figure 3.1: Proposed phase diagram of the random Hubbard model in (3.1) with SU(2) spin symmetry. The present paper describes the metal insulator transition at $p = 0$ between the insulating spin glass and the disordered Fermi liquid as a deconfined critical point in Section 3.3. The non-zero p transition between two metallic states at large U was described by Joshi *et al.* [2] as deconfined critical point in a random t-J model.

at $p = 0$ in Fig. 3.1, with the larger U direction away from the fixed point flowing to the insulating spin glass state. However, we don't really have control over the computation far from the fixed point, and it is possible that the fixed point actually describes the onset of metallic spin glass order from the disordered Fermi liquid, as indicated in the phase diagram in Fig. 3.4. We also note that there is a previous Landau-type theory [63, 64] for such a metal-metal transition, and this will be reviewed in the present small U context in Appendix B.2.

We turn to a description of the model of interest in this paper, for the case with SU(2) spin symmetry. We consider electrons, annihilated by $c_{i\alpha}$, spin $\alpha =\uparrow, \downarrow$ on N sites $i = 1 \ldots N$ with the Hamiltonian

$$H = \sum_{i=1}^{N} \left(-\mu(n_{i\uparrow} + n_{i\downarrow}) + U n_{i\uparrow} n_{i\downarrow}\right) + \frac{1}{\sqrt{N}} \sum_{i\neq j=1}^{N} t_{ij} c_{i\alpha}^{\dagger} c_{j\alpha} + \frac{1}{\sqrt{N}} \sum_{i<j=1}^{N} J_{ij} \boldsymbol{S}_i \cdot \boldsymbol{S}_j \tag{3.1}$$

where μ is the chemical potential,

$$n_{i\alpha} = c_{i\alpha}^\dagger c_{i\alpha} \quad , \quad \boldsymbol{S}_i = \frac{1}{2} c_{i\alpha}^\dagger \boldsymbol{\sigma}_{\alpha\beta} c_{i\beta} \tag{3.2}$$

are the number and spin operators with $\boldsymbol{\sigma}$ the Pauli matrices. The density of the electrons is specified by the filling p

$$p = \langle 1 - n_{i\uparrow} - n_{i\downarrow} \rangle \ . \tag{3.3}$$

We can take the t_{ij} to be all equal between the sites of a Bethe lattice with large co-ordination number, or use a fully connected cluster in which all $t_{ij} = t_{ji}^*$ are independent random variables with zero mean and $\overline{|t_{ij}|^2} = t^2$. We will focus on the random case because it is a bit simpler, but equivalent results apply to the Bethe lattice. The real exchange interactions J_{ij} are independent random numbers with zero mean and mean-square value $\overline{J_{ij}^2} = J^2$.

Let us take a broader perspective, and consider the phase diagram of H as a function of U and hole density away from half-filling, $p = 0$; see Fig. 3.1. At large U and $p = 0$, we have an insulating spin glass state: at $p = 0$ we need only consider the spin-only model with the J_{ij} interactions, and a spin glass state was found in numerical studies [3, 4], in contrast to the critical spin liquid appearing in the large M limit [1]. We will be interested here in the approach to the spin glass insulator at $p = 0$ from the small U side, across a metal-to-insulator transition from a disordered Fermi liquid at small U and $p = 0$. Upon doping the spin glass, we expect a metallic spin glass state for a range of non-zero p, before there is a distinct quantum phase transition to a disordered Fermi liquid state at a nonzero p: this large U transition is also expected to be described by a deconfined critical point, and is discussed in a separate paper [2].

The outline of the paper is as follows. Section 3.2 will described the limit of a large number of sites, N, where H is mapped onto a non-local in time effective action for a single site with self-consistency conditions on its correlators. Section 3.3 will describe the solution of the single site problem for the case where the SU(2) spin symmetry is generalized to SU(M)

with M large: we will describe the correspondence between the large M solutions, and the numerical results of Cha *et al.* [46] for $M = 2$. Section 3.4 presents the RG analysis of the single site model with SU(2) symmetry obtained in Section 3.2. Appendix B.2 reviews the theory of Ref. [63] for the onset of metallic spin glass order in a disordered Fermi liquid in a conventional Landau-type transition (and not via a large U deconfined critical point [2]) which can be present at small U, as indicated in Fig. 3.4.

3.2 Large volume limit

The limit of large volume ($N \to \infty$) of H is obtained by the methods described in Refs. [1, 2, 46, 70, 71]. We introduce field replicas in the path integral, and average over t_{ij} and J_{ij}. At the $N = \infty$ saddle point, the problem reduces to a single site problem, with the fields carrying replica indices. The replica structure is important in the spin glass phase [70, 71]. In the interests of simplicity, we drop the replica indices here as they play no significant role in the critical theory and the RG equations. Within the imaginary time path integral formalism (with $\tau \in [0, 1/T]$, with T the temperature), the solution of the model involves a local single-site effective action which reads:

$$\begin{aligned}
\mathcal{Z} &= \int \mathcal{D}c_\alpha(\tau) e^{-\mathcal{S}} \\
\mathcal{S} &= \int d\tau \left[c_\alpha^\dagger(\tau) \left(\frac{\partial}{\partial \tau} - \mu \right) c_\alpha(\tau) + \frac{U}{2} c_\alpha^\dagger(\tau) c_\beta^\dagger(\tau) c_\beta(\tau) c_\alpha(\tau) \right] \\
&\quad - t^2 \int d\tau d\tau' R(\tau - \tau') c_\alpha^\dagger(\tau) c_\alpha(\tau') - \frac{J^2}{2} \int d\tau d\tau' Q(\tau - \tau') \boldsymbol{S}(\tau) \cdot \boldsymbol{S}(\tau') \,, \quad (3.4)
\end{aligned}$$

In this expression, μ is the chemical potential chosen to ensure $p = 0$. Decoupling the path integral introduces fields analogous to R and Q which are initially off-diagonal in the spin SU(2) indices. We have assumed above that the large-volume limit is dominated by the saddle point in which spin rotation symmetry is preserved on the average, and so R and Q were taken to diagonal in spin indices. The path integral $\mathcal{Z}$ is a functional of the fields $R(\tau)$

and $Q(\tau)$, and we define its correlators

$$\begin{aligned}\overline{R}(\tau-\tau') &= -\left\langle c_\alpha(\tau)c_\alpha^\dagger(\tau')\right\rangle_{\mathcal{Z}} \\ \overline{Q}(\tau-\tau') &= \frac{1}{3}\left\langle \boldsymbol{S}(\tau)\cdot\boldsymbol{S}(\tau')\right\rangle_{\mathcal{Z}}\end{aligned} \tag{3.5}$$

In the thermodynamic ($N\to\infty$) limit, the solution of the model is obtained by imposing the two self-consistency conditions:

$$R(\tau)=\overline{R}(\tau) \quad , \quad Q(\tau)=\overline{Q}(\tau). \tag{3.6}$$

These equations and the mapping to a local effective action are part of the extended dynamical mean-field theory framework (EDMFT), which becomes exact for random models on fully connected lattices [64]. They can also be viewed as an EDMFT approximation to non-random models [68, 81–83].

3.3 Large M theory

We consider here a large M generalization of the N-site Hubbard model, following Refs. [84–87], and examine the structure of the large M limit at $N=\infty$. We consider an electron $c_{p,\alpha}$ with a spin index $\alpha=1\ldots M$, and an 'orbital' index $p=1\ldots M'$ (the index p should not be confused with the doping p). We will take the limit of large number of sites, N, followed by the limit of large M and M' at fixed

$$k\equiv\frac{M'}{M}\,. \tag{3.7}$$

We are interested in the case with SU(2) spin symmetry which has the values $M=2$, $M'=1$, $k=1/2$. The large M,M' limit requires us to fractionalize the electron as

$$c_{ip\alpha}^\dagger=X_{ip}f_{i\alpha}^\dagger\,, \tag{3.8}$$

where X_{ip} is a complex 'slave rotor' [84, 85], with $p = 1 \ldots M'$, obeying the constraint

$$\sum_{p=1}^{M'} |X_{ip}|^2 = M' \,. \tag{3.9}$$

This representation has a U(1) gauge invariance

$$X_{ip} \to X_{ip} e^{i\phi_i(\tau)} \quad , \quad f_{i\alpha} \to f_{i\alpha} e^{i\phi_i(\tau)} \tag{3.10}$$

We shall be interested in the sector in which the U(1) gauge charge is fixed on each site by [84]

$$\sum_{\alpha=1}^{M} f_{i\alpha}^\dagger f_{i\alpha} + \hat{L}_i = \frac{M}{2} \tag{3.11}$$

where $\hat{L}_i$ is the U(1) angular momentum operator for the rotors.

The Hamiltonian generalizing (3.1) we shall study in this section is a combination of those in Refs. [1, 84, 86]:

$$\begin{aligned} H &= \frac{U}{2M'} \sum_i \left(\sum_{\alpha=1}^{M} f_{i\alpha}^\dagger f_{i\alpha} - \frac{M}{2} \right)^2 + \epsilon_0 \sum_{ip\alpha} f_{i\alpha}^\dagger f_{i\alpha} \\ &\quad + \frac{1}{\sqrt{NM}} \sum_{i,j,p,\alpha} t_{ij} c_{ip\alpha}^\dagger c_{jp\alpha} + \frac{1}{\sqrt{NM}} \sum_{i>j,\alpha\beta} J_{ij} f_{i\alpha}^\dagger f_{i\beta} f_{j\beta}^\dagger f_{j\alpha} \,. \end{aligned} \tag{3.12}$$

The value of ϵ_0 is adjusted to fix the average electron density at each site, $\sum_{\alpha=1}^{M} f_{i\alpha}^\dagger f_{i\alpha}$ to equal $M/2$ for the half-filled case.

We now take the large volume limit of Section 3.2. For (3.12), the $N \to \infty$ limit reduces to the following single-site path integral (replacing (2.10))

$$
\begin{aligned}
\mathcal{Z} &= \int \mathcal{D}f_\alpha \mathcal{D}X_p \mathcal{D}\lambda \mathcal{D}h e^{-\mathcal{S}} \\
\mathcal{S} &= \int_0^{1/T} d\tau \left[\frac{1}{2U} \sum_p \left| \left(\frac{\partial}{\partial\tau} + ih \right) X_p \right|^2 + i\lambda \left(\sum_p |X_p|^2 - M' \right) + \sum_\alpha f_\alpha^\dagger \left(\frac{\partial}{\partial\tau} + \epsilon_0 + ih \right) f_\alpha - ih\frac{M}{2} \right] \\
&\quad - \frac{t^2}{M} \sum_{p,\alpha} \int_0^{1/T} d\tau d\tau' R^*(\tau-\tau') X_p(\tau) X_p^*(\tau') f_\alpha^\dagger(\tau) f_\alpha(\tau') \\
&\quad - \frac{J^2}{2M} \sum_{\alpha,\beta} \int_0^{1/T} d\tau d\tau' Q(\tau-\tau') f_\alpha^\dagger(\tau) f_\beta(\tau) f_\beta^\dagger(\tau') f_\alpha(\tau') \,. \qquad (3.13)
\end{aligned}
$$

Here T is the temperature, λ is the Lagrange multiplier imposing Eq. (3.9) and h is the Lagrange multiplier imposing Eq. (3.11). The U(1) gauge invariance (3.10) applies also to (3.13) after we transform

$$h \to h - \partial_\tau \phi \,. \qquad (3.14)$$

The self-consistency equations (3.6) now become

$$
\begin{aligned}
R(\tau-\tau') &= -\frac{1}{MM'} \sum_{p,\alpha} \left\langle X_p(\tau) X_p^*(\tau') f_\alpha^\dagger(\tau) f_\alpha(\tau') \right\rangle_{\mathcal{Z}} \\
Q(\tau-\tau') &= \frac{1}{M^2} \sum_{\alpha,\beta} \left\langle f_\alpha^\dagger(\tau) f_\beta(\tau) f_\beta^\dagger(\tau') f_\alpha(\tau') \right\rangle_{\mathcal{Z}} \,. \qquad (3.15)
\end{aligned}
$$

Having taken the large N limit, we can now take the large M, M' limit at fixed $k = M'/M$. We have set things up so we can decouple the quartic terms in $\mathcal{S}$ by Hubbard-Stratonovich fields, perform the path integrals over f_α and X_p, and then perform a $1/M$ expansion about the saddle point. The large M saddle point equations are essentially those obtained in Ref. [87], and we adapt the relevant analysis here. We limit ourselves to the particle-hole symmetric case with doping $p = 0$, in which case we can set $\epsilon_0 = 0$ and $h = 0$. We obtain for the f fermion Green's function, G_f, and the X correlator χ

$$G_f(i\omega_n) = \frac{1}{i\omega_n - \Sigma_f(i\omega_n)} \quad , \quad \Sigma_f(\tau) = -J^2 G_f^2(\tau) G_f(-\tau) + k\, t^2 G_f(\tau)\chi^2(\tau) \tag{3.16}$$

$$\chi(i\omega_n) = \frac{1}{\omega_n^2/U + \chi_0^{-1} - P(i\omega_n) + P(i\omega_n = 0)} \quad , \quad P(\tau) = -t^2 G_f(\tau) G_f(-\tau)\chi(\tau) \tag{3.17}$$

where

$$i\lambda = \chi_0^{-1} + P(i\omega_n = 0) \tag{3.18}$$

is the saddle point value of $i\lambda$. Note that we have introduced notation so that

$$\chi(i\omega_n = 0) \equiv \chi_0\,, \tag{3.19}$$

is the static X susceptibility. Formally, the value of χ_0 is to be determined by solving the constraint equation Eq. (3.9):

$$T \sum_{\omega_n} \chi(i\omega_n) = 1\,. \tag{3.20}$$

The saddle-point equations (3.16), (3.17), and (3.20) were examined numerically and analytically in Ref. [87] in the context of a different model. Here we transfer their analysis to our model. We recall the analytic low energy structure of the solutions, starting with large U, and then with decreasing U. At very large U, we expect the X boson correlators to decay rapidly in time, and to become progressively longer ranged as U is decreased. A sketch of our proposed large M phase diagram is shown in Fig. 3.2.

3.3.1 Gapped boson

At very large U, we expect an energy gap in the boson correlator $\chi(\omega)$, corresponding to exponential decay of X correlators, and the Mott gap in an insulator. In this case, we can simply drop the boson Green's function in (3.16) at low energy, and (3.16) reduces to the equations of the spin-only model examined originally in Ref. [1]. As argued there, the fermion

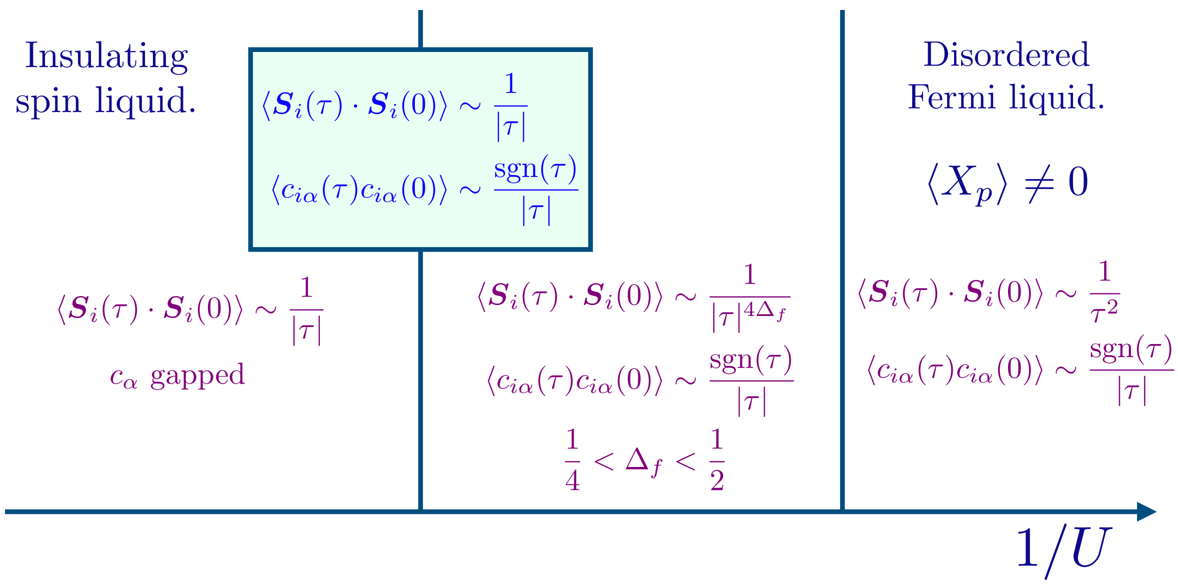

Figure 3.2: Schematic phase diagram in the large M limit. This section does not describe the disordered Fermi liquid where the X_p condense; for $M' > 1$, this phase also has orbital glass order, associated with the orbital index $p = 1 \ldots M'$. For the physical case $M = 2$, $M' = 1$, the insulating spin liquid is expected to be replaced by an insulating spin glass [3, 4], and we argue that the intermediate critical phase with $1/4 < \Delta_f < 1/2$ may not exist.

Green's function is gapless with the large imaginary time ($\tau \to \infty$) form at $T = 0$

$$G_f(\tau) = -\mathrm{sgn}(\tau)\frac{F}{|\tau|^{2\Delta_f}}\,. \tag{3.21}$$

The exponent $\Delta_f = 1/4$ [1]. Although the f fermion is gapless, the X boson is gapped, and so the electron c is also gapped, and this solution describes an insulator. The spin correlations in this insulator are however gapless: the spin operator is $S^a = c^\dagger_{p\alpha}T^a_{\alpha\beta}c_{p\beta}$, where T^a, with $a = 1\ldots M^2-1$, is a generator of SU(M), and it has the long-time correlator

$$\langle S^a(\tau)S^a(0)\rangle \sim \frac{1}{|\tau|^{4\Delta_f}}\,. \tag{3.22}$$

With $\Delta_f = 1/4$, we conclude that the spin correlator decays as $1/|\tau|$. From numerical studies of the insulating quantum magnet [3, 4], we now know that the present insulating, gapless 'spin-fluid' solution is present only at large M. For the case $M = 2$ of interest to us, the insulator has spin-glass order. So we expect that the large M gapped X solution discussed will be mapped at $M = 2$ to the insulating spin glass state found by Cha *et al.* [46] at large U.

The nature of the gapped boson correlator was also examined in Ref. [87], and it was found that

$$\chi(\tau) \sim \frac{e^{-m|\tau|}}{\sqrt{|\tau|}} \tag{3.23}$$

at large $|\tau|$, where m is the Mott gap.

3.3.2 Gapless boson

With decreasing U, we expect solutions in which the boson X is critical or condensed, as shown in Fig. 3.2. We consider the critical case. Along with the low frequency form for the fermion in (3.21), we assume a power-law form for the boson correlator at long times τ:

$$\chi(\tau) = \frac{C}{|\tau|^{2\Delta_b}}\,. \tag{3.24}$$

We will find below that consistency requires that $\Delta_b \leq 1/4$, and so from (3.19) $\chi_0 = \infty$ due to a IR divergence. In the large M limit, the ansatzes (3.21) and (3.24) imply that the gauge-invariant electron Green's function decays as

$$G_c(\tau) = -\left\langle c_{p\alpha}(\tau) c^\dagger_{p\alpha}(0) \right\rangle \sim -\frac{\mathrm{sgn}(\tau)}{|\tau|^{2(\Delta_f+\Delta_b)}} \,. \tag{3.25}$$

Following Ref. [87], we will now see by explicit computation that the ansatzes (3.21) and (3.24) are indeed valid solutions of the saddle point equations (3.16) and (3.17) at long times. First, we need the Fourier transforms at $T = 0$ which are at small ω

$$\begin{aligned} G_f(i\omega) &= -2i\,\mathrm{sgn}(\omega)\frac{F}{|\omega|^{1-2\Delta_f}}\cos(\pi\Delta_f)\Gamma(1-2\Delta_f) \\ \chi(i\omega) &= 2\frac{C}{|\omega|^{1-2\Delta_b}}\sin(\pi\Delta_b)\Gamma(1-2\Delta_b)\,. \end{aligned} \tag{3.26}$$

From Eq. (3.16) and (3.17), the self energies are

$$\begin{aligned} \Sigma_f(\tau) &= -\mathrm{sgn}(\tau)\left(\frac{J^2F^3}{|\tau|^{6\Delta_f}} + \frac{k\,t^2FC^2}{|\tau|^{2\Delta_f+4\Delta_b}}\right) \\ P(\tau) &= \frac{t^2F^2C}{|\tau|^{4\Delta_f+2\Delta_b}}\,, \end{aligned} \tag{3.27}$$

and their Fourier transforms are

$$\begin{aligned} \Sigma_f(i\omega) &= -2i\,\mathrm{sgn}(\omega)\left(\frac{J^2F^3}{|\omega|^{1-6\Delta_f}}\cos(3\pi\Delta_f)\Gamma(1-6\Delta_f)\right. \\ &\qquad \left. + \frac{kt^2FC^2}{|\omega|^{1-2\Delta_f-4\Delta_b}}\cos(\pi(\Delta_f+2\Delta_b))\Gamma(1-2\Delta_f-4\Delta_b)\right) \\ P(i\omega) - P(i\omega=0) &= 2\frac{t^2F^2C}{|\omega|^{1-4\Delta_f-2\Delta_b}}\sin(\pi(2\Delta_f+\Delta_b))\Gamma(1-4\Delta_f-2\Delta_b)\,. \end{aligned} \tag{3.28}$$

From Eqns (3.26) and (3.28), and using $G_f(i\omega)\Sigma_f(i\omega) = -1$ and $\chi(i\omega)(P(i\omega) - P(i\omega=0)) = -1$ in the limit of low ω, we see that solutions are only possible when

$$\Delta_f + \Delta_b = 1/2\,. \tag{3.29}$$

From (3.25) we now see that the electron Green's function $G_c(\tau)$ always has the decay $\sim 1/\tau$, which is the same as that in a Fermi liquid. This is in agreement with the electron correlator obtained by Cha *et al.* [46] at the metal-insulator critical point, and in the Fermi liquid phase.

Further examination of the saddle point equations shows that two classes of solutions are possible, depending upon whether $\Delta_f > 1/4$ or $\Delta_f = 1/4$. We will examine these solutions in the following subsections.

3.3.2.1 $\Delta_f = \Delta_b = 1/4$

In this case, both terms in Σ in Eq. (3.28) have the same low frequency power-law, and so both contribute to the low ω limit. The Schwinger-Dyson equations have solutions which reduce to

$$\begin{aligned} J^2 F^4 + kt^2 C^2 F^2 &= \frac{1}{4\pi} \\ t^2 C^2 F^2 &= \frac{1}{4\pi}. \end{aligned} \tag{3.30}$$

These can be solved uniquely for both $F > 0$ and $C > 0$ provided again $k < 1$. The existence of a unique low ω solution with these exponents indicates that Eq. (3.20) will be satisfied at only a particular value of the couplings *i.e.* this solution corresponds to a critical point as U is decreased to smaller values from the gapped boson phase: numerical evidence for this structure was obtained by Fu *et.al.* [87].

Consequently, we identify the present $\Delta_f = \Delta_b = 1/4$ solution with the metal-insulator critical point found by Cha *et al.* [46]. Indeed, via (3.22) the spin correlator decays as $1/|\tau|$, and via (3.25), the electron correlator decays as $1/\tau$, and these correspond to the leading exponents found numerically by Cha *et al.* [46].

Although the $1/\tau$ decay of the electron correlator is the same as that of a Fermi liquid, the spin correlator is distinct from the $1/\tau^2$ decay in a Fermi liquid. Indeed, the presence of a $1/\tau$ electron correlator *and* a $1/|\tau|$ spin correlator is evidence for fractionalization at this critical point: both correlators are simply understood from a fractionalization of c into X and f in (3.8), and from the scaling dimensions $\Delta_f = \Delta_b = 1/4$.

3.3.2.2 $\Delta_f > 1/4$

With a further decrease in U, Ref. [87] found that we should consider the case with a faster decrease in spin correlations. With $\Delta_f > 1/4$, the first term in $\Sigma_f(i\omega)$ in Eq. (3.28) is subdominant and can be ignored. Then the Schwinger-Dyson equations can be solved, and they simplify to the relations

$$\begin{aligned} k t^2 F^2 C^2 \frac{4\pi \cot(\pi \Delta_f)}{2 - 4\Delta_f} &= 1 \\ t^2 F^2 C^2 \frac{\pi \cot(\pi \Delta_f)}{\Delta_f} &= 1 \,. \end{aligned} \tag{3.31}$$

Note that these equations are independent of J, and so the asymptotic low energy structure does not depend upon the strength of the exchange interactions. They are consistent only if we choose the scaling dimensions

$$\Delta_f = \frac{1}{2k+2} \quad , \quad \Delta_b = \frac{k}{2k+2} \,. \tag{3.32}$$

Note that $\Delta_f > 1/4$ requires $k < 1$. So the exponents are limited to the ranges

$$\frac{1}{4} < \Delta_f < \frac{1}{2} \quad , \quad 0 < \Delta_b < \frac{1}{4} \,. \tag{3.33}$$

This analysis of the low ω limit of the saddle point equations does not determine the values of F and C separately, only the value of their product CF. So we expect that the $\Delta_f > 1/4$ solution defines a critical phase which extends over a range of value of the couplings.

Ref. [87] labeled this critical phase as 'quasi-Higgs'. The numerical results of Cha *et al.* [46] do not indicate such an extended critical phase for the SU(2) case. It is possible that such a phase only appears for larger M, and is absent, or very small in extent, for $M = 2$.

We now argue that with a further decrease in U, the quasi-Higgs phase will be replaced by an actual Higgs phase, as sketched in Fig. 3.2. Note from (3.28) and (3.29) that $P(i\omega) - P(0) \sim |\omega|^{2\Delta_f}$, and so with $\Delta_f < 1/2$ (see (3.33)), the frequency integral in (3.20) has no infra-red divergence (recall $\chi_0^{-1} = 0$). Consequently [70, 71], at small enough U we will not be able to satisfy (3.20) with a critical boson solution, and we expect the quasi-Higgs phase to be replaced by a Higgs phase in which the X boson condenses *i.e.* $\Delta_b = 0$. With X condensed, a low frequency analysis of the saddle point equations shows that $\Delta_f = 1/2$. Consequently, such a Higgs phase realizes the disordered Fermi liquid, with electron correlations decaying as $1/\tau$, and spin correlations decaying as $1/\tau^2$.

3.4 Renormalization group analysis

This section returns to the problem as defined in Section 3.2 for $M = 2$. We will view the path integral in (2.10) as a quantum impurity problem in the presence of a bosonic bath $Q(\tau)$ and a fermionic bath $R(\tau)$; we defer imposition of the self-consistency conditions in (3.6). We will then follow the RG approach of Refs. [92, 93] who studied a symmetric Anderson impurity coupled to a fermionic bath. The symmetric case is of relevance to us because we are considering the particle-hole symmetric case at half-filling, $p = 0$. Our problem also has a bosonic bath, not present in the earlier work [92, 93], and we will include this bath using the methods of Ref. [89].

As we are looking for critical states, we assume that the fields $Q(\tau)$ and $R(\tau)$ have a power-law decay in time with

$$Q(\tau) \sim \frac{1}{|\tau|^{d-1}} \quad , \quad R(\tau) \sim \frac{\mathrm{sgn}(\tau)}{|\tau|^{r+1}} \,. \tag{3.34}$$

where, for now, d and r are arbitrary numbers determining exponents. Ultimately, once we have found a RG fixed point, the values of d and r can be fixed by using the self-consistency condition in (3.6). For now, our analysis exploits the freedom to choose d and r: we will show that a systematic RG analysis of the path integral $\mathcal{Z}$ in (2.10) is possible in an expansion in ϵ and ϵ', where

$$\epsilon = 1 - 2r \quad , \quad \epsilon' = 2 - d \ ; \ Q(\tau) \sim \frac{1}{|\tau|^{1-\epsilon'}} \quad , \quad R(\tau) \sim \frac{\text{sgn}(\tau)}{|\tau|^{(3-\epsilon)/2}} \,. \tag{3.35}$$

The analysis assumes ϵ and ϵ' are of the same order, and expands order-by-order in homogeneous polynomials in ϵ and ϵ'.

We note that the perturbation expansion in power of ϵ is closely related to a weak-coupling small U expansion of the symmetric Anderson model [92]. Consequently, the analysis is carried out directly in terms of the physical electron operator c_α, and we will not fractionalize the electron into rotors and spinons, as we did in (3.8) for the large M expansion in Section 3.3. It therefore possible that a critical point found in this approach is not 'deconfined'.

We proceed by decoupling the last two terms in the action $\mathcal{S}$ in (2.10) by introducing fermionic (ψ_α) and bosonic (ϕ_a, $a = x, y, z$) fields respectively, and then the path integral reduces to a quantum impurity problem. The 'impurity' is a single site of a particle-hole symmetric Hubbard model with 4 possible states, and this is coupled to the 'bulk' ψ_α and ϕ_a excitations. The quantum impurity problem is specified by the Hamiltonian

$$\begin{aligned} H_{\text{imp}} \quad &= -\mu(n_\uparrow + n_\downarrow) + U n_\uparrow n_\downarrow + g_0 \left(c_\alpha^\dagger \, \psi_\alpha(0) + \text{H.c.} \right) + \gamma_0 c_\alpha^\dagger \frac{\sigma^a_{\alpha\beta}}{2} c_\beta \, \phi_a(0) \\ &\quad + \int |k|^r dk \, k \, \psi^\dagger_{k\alpha} \psi_{k\alpha} + \frac{1}{2} \int d^d x \left[\pi_a^2 + (\partial_x \phi_a)^2 \right] \,. \end{aligned} \tag{3.36}$$

We now note features of the baths coupled to the impurity site.

The bosonic bath is realized by a free massless scalar field in d spatial dimensions, as in Refs. [88–90]. The field π_a is canonically conjugate to the field ϕ_a. The impurity spin $\boldsymbol{S}$ couples to the value of ϕ_a at the spatial origin, $\phi_a(0) \equiv \phi_a(x = 0, \tau)$. It is easy to verify that upon integrating out ϕ_a from H_{imp}, we obtain the J term in $\mathcal{S}$, with $Q(\tau)$ obeying (3.34).

The fermionic bath is realized by free fermions $\psi_{k\alpha}$ with energy k and a 'pseudogap' density of states $\sim |k|^r$. The impurity electron operator c_α is coupled to $\psi_\alpha(0) \equiv \int |k|^r dk \, \psi_{k\alpha}$.

Integrating out $\psi_{k\alpha}$ from H_{imp} yields the t term in $\mathcal{S}$, with $R(\tau)$ obeying (3.34).

It turns out that the structure of the RG shows that there is additional 'boundary' renormalization of ϕ_a^2 that must be accounted for in the ϵ, ϵ' expansion, and this introduces a new coupling ζ. This is an important distinction from the previous analysis of the t-J model at non-zero p [2], where there were no additional boundary renormalizations; this boundary renormalization prevents us from making an all-orders extrapolation of certain exponents that was possible earlier [2]. Our RG analysis will be carried out for the following action which includes the ζ coupling

$$
\begin{aligned}
\mathcal{S}_c =& \int \frac{d\omega}{2\pi} c_\alpha^\dagger(\omega)(iA_0 \text{sgn}(\omega)|\omega|^r)c_\alpha(\omega) + \frac{1}{2}\int d^d x d\tau [(\partial_\tau \phi_a)^2 + (\partial_x \phi)^2] \\
&+ \frac{U_0}{2}\int d\tau c_\alpha^\dagger c_\beta^\dagger c_\beta c_\alpha + \gamma_0 \int d\tau c_\alpha^\dagger \frac{\sigma^a_{\alpha\beta}}{2} c_\beta \phi_a(0) + \frac{\zeta_0}{2}\int d\tau \phi_a(0)^2 \,, \qquad (3.37)
\end{aligned}
$$

Note that we have already integrated out the fermionic bath $\psi_{k\alpha}$ (as was also done in Refs. [92, 93]), to obtain a non-local propagator for the electron c_α; A_0 is an unimportant normalization constant which has absorbed the value of g_0. The action $\mathcal{S}_c$ contains three coupling constants, U_0, γ_0, and ζ_0, and we will present their renormalization group flow below.

3.4.1 RG equations and fixed points

The RG equations of the action (3.37) are derived for the SU($M = 2$) case and $M' = 1$. To the leading order, the flow equations are (notice that in this case we define $\beta_U = (\beta_U + \beta_V)|_{U+V\to U}$)

$$
\begin{aligned}
\beta_\gamma &= \frac{1}{2}(\epsilon - \epsilon')\gamma - \frac{\gamma U}{\pi A_0^2} + \frac{\zeta\gamma}{2\pi} \,, \\
\beta_U &= \epsilon U - \frac{3\gamma^2}{8\pi} \,, \\
\beta_\zeta &= -\epsilon'\zeta + \frac{\zeta^2}{2\pi} + \frac{\gamma^2}{2\pi A_0^2} \,, \qquad (3.38)
\end{aligned}
$$

where $\epsilon = 1 - 2r$ and $\epsilon' = 2 - d$. Using the beta functions (3.38) we find the following four fixed points $(\gamma^{*2}, U^*, \zeta^*)$:

$$FP_1 = (0, 0, 0) \tag{3.39}$$

$$FP_2 = (0, 0, 2\pi\epsilon') \tag{3.40}$$

$$FP_3 = \big(\frac{4\pi^2 A_0^2}{9}\epsilon(\epsilon + \xi), \frac{\pi A_0^2}{6}(\epsilon + \xi), \frac{\pi}{3}(3\epsilon' - 2\epsilon + \xi)\big) \tag{3.41}$$

$$FP_4 = \big(\frac{4\pi^2 A_0^2}{9}\epsilon(\epsilon - \xi), \frac{\pi A_0^2}{6}(\epsilon - \xi), \frac{\pi}{3}(3\epsilon' - 2\epsilon - \xi)\big) \tag{3.42}$$

where $\xi = \sqrt{9\epsilon'^2 - 8\epsilon^2}$. In order for the fixed points (3.41) and (3.42) to be real ξ has to be real, which gives the condition $\epsilon'^2 > 8\epsilon^2/9$. Additionally, for the fixed point (3.42) to be real we should also have $\epsilon > \xi$, which gives $\epsilon'^2 < \epsilon^2$.

We now analyze the stability of the fixed points by looking at the eigenvalues of the stability matrix (see Appendix B.1 for details) and thus the RG flow. We will be interested in the situation when the non-trivial fixed points (3.41) and (3.42) are real, i.e., $8/9 < (\epsilon'/\epsilon)^2 < 1$. We will have $\epsilon > 0$, and discuss the situations when ϵ' is positive or negative.

(i) $\epsilon' > 0$: In this case, the trivial fixed point (3.40) is the only stable fixed point. The Gaussian fixed point (3.39) and the non-trivial fixed point (3.41) have one relevant direction and two irrelevant directions, while the other non-trivial fixed point (3.42) has one irrelevant direction and two relevant directions in the RG flow phase-space of (γ^2, U, ζ). This is shown in Fig. 3.3 (a), with a 2d projection on the $U - \gamma$ plane shown in Fig. 3.3 (b). Therefore, the non-trivial fixed point (3.41) separates the RG flow between large γ or U and small γ or U, and thus corresponds to a quantum critical point. We discuss the anomalous dimensions of the spin and electron correlators at this fixed point in Sec. 3.4.2.

(i) $\epsilon' < 0$: In this case, the Gaussian fixed point now becomes the stable fixed point, while the other trivial fixed point (3.40) now has one relevant and two irrelevant directions. The discussion of the non-trivial fixed points is the same as in case (i). The corresponding RG flow projected in the $U - \gamma$ plane is shown in Fig. 3.3 (c). Here again the fixed point (3.41)

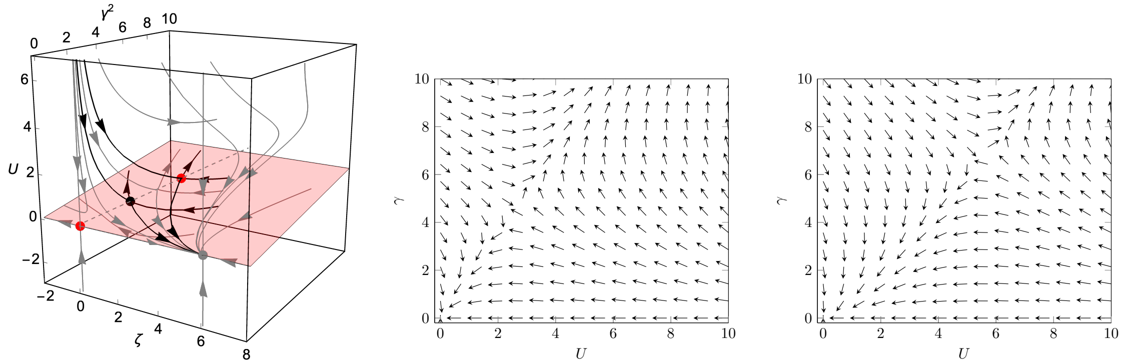

(a) **(b)** **(c)**

Figure 3.3: (a) Schematic one-loop RG flow diagram in the $\zeta - \gamma^2 - U$ space for $\epsilon' > 0$. The gray point is the stable fixed point (FP_2), red points are the fixed points (FP_1, FP_3) with one relevant direction, and the black point is the non-trivial fixed point (FP_4) with two relevant directions. All four fixed points are on the same plane $\frac{3\gamma^2}{8\pi\epsilon} - U = 0$ coloured in light red. The black lines are the separatrices for the non-trivial fixed points. (b) One-loop RG flow projected on to the $U - \gamma$ plane for $\epsilon' > 0$. (c) Same as (b) for $\epsilon' < 0$. In both (b) and (c) the nature of the flow is similar and controlled by the non-trivial fixed point FP_3 (3.41), which corresponds to a quantum critical point.

separates the flow at large γ or U and small γ or U, and therefore corresponds to a quantum critical point.

3.4.2 Scaling dimensions

A significant feature of the action (3.37) is that the quadratic term in the c_α does not get renormalized because of its non-analytic dependence on frequency. Consequently, the electron correlator has the same long-time decay as in the Gaussian theory

$$G_c(\tau) \sim \frac{\mathrm{sgn}(\tau)}{|\tau|^{1-r}} \tag{3.43}$$

and the scaling dimension of the electron operator is given exactly by

$$\dim[c_\alpha] = (1-r)/2 = (1+\epsilon)/4\,. \tag{3.44}$$

This result is the same as that in the t-J model analysis by Joshi *et al.* [2]. Comparing with (3.34) and the self-consistency condition in (3.6), we observe that the only possible self-consistent value is $r = 0$ or $\epsilon = 1$. Clearly, the ϵ-expansion cannot be trusted at this large value in determining other features of the RG. Note that the electron scaling dimension in (3.44) at $r = 0$ agrees with the gapless boson solutions of the large M analysis, where the scaling dimension of c_α is specified by (3.25) and (3.29).

Turning to the spin operator $\boldsymbol{S}$, we now find important differences from the t-J model analysis [2]. The scaling dimension of $\boldsymbol{S}$ is not a RG invariant because of the boundary renormalization associated with the coupling ζ. The spin operator $\boldsymbol{S}$ mixes with the boundary value of the bosonic bath field $\phi_a(0)$. This mixing is described by the matrix of anomalous dimensions is

$$\gamma_{ij} = \begin{pmatrix} -\dfrac{U}{\pi A_0^2} & \dfrac{\gamma}{2\pi A_0^2} \\ \dfrac{\gamma}{2\pi} & \dfrac{\zeta}{2\pi} \end{pmatrix} . \tag{3.45}$$

The full scaling dimensions are obtained by adding $\text{diag}(1 - r, \frac{d-1}{2})$ to γ_{ij} and diagonalizing the full matrix. At the fixed points we find,

$$FP_1 : \Delta_+ = \frac{1-\epsilon'}{2}, \quad \Delta_- = \frac{1+\epsilon}{2}, \tag{3.46}$$

$$FP_2 : \Delta_+ = \frac{1+\epsilon'}{2}, \quad \Delta_- = \frac{1+\epsilon}{2}, \tag{3.47}$$

$$FP_3 : \Delta_+ = \frac{1+\epsilon'}{2}, \quad \Delta_- = \frac{1-\epsilon'}{2}, \tag{3.48}$$

$$FP_4 : \Delta_+ = \frac{1+\epsilon'}{2}, \quad \Delta_- = \frac{1-\epsilon'}{2}. \tag{3.49}$$

Note that these expressions are valid for both positive and negative values of ϵ', as long as the conditions mentioned above are met.

Let us use these scaling dimensions to impose the second of self-consistency conditions in (3.6). We consider the case of primary interest, the fixed point FP_3, with non-zero coupling. We have to match the exponent in (3.35) with the smaller of the two exponents at FP_3; this leads us to conclude that self-consistency is achieved for any $\epsilon' \geq 0$. Presumably a specific value of ϵ' will be chosen at higher orders.

Finally, let us combine the consequences of the two self-consistency conditions in (3.6). From the first condition we found above that $\epsilon = 1$. Using $\epsilon' \geq 0$, we also have the restriction on the existence of FP_3 at real couplings, $\epsilon' > \sqrt{8/9}\epsilon$, and so the values of ϵ' are restricted to $\epsilon' > \sqrt{8/9} = 0.943$. We expect spin correlations to decay with time, and so (3.35) also restricts $\epsilon' < 1$. But let us note that all these results are obtained as leading terms an expansion in ϵ and ϵ', so these large values cannot be trusted.

3.4.3 Physical interpretation

The physical interpretation of the quantum criticality described by the fixed point FP_3 remains an interesting open question. It is possible that it describes the deconfined disordered Fermi liquid-spin glass insulator transition at $p = 0$ in Fig. 3.1. However, another reasonable possibility is that the larger U side of the $p = 0$ transition in Fig. 3.1 is not an insulator, but a metallic spin glass. We sketch a possible phase diagram in Fig. 3.4, which shows that increasing U or J from a disordered Fermi liquid can lead either to a metallic spin glass or an insulating spin glass. One indication we are approaching a metallic spin glass phase is that the critical spin correlations at FP_3 decay extremely slowly. By (3.35), the spin correlations decay with the exponent $(1 - \epsilon')$, and we estimated above that $0 < (1 - \epsilon') < 0.057$ by (the unreliable) extrapolation from the one-loop results.

In Appendix B.2, we will review an alternative Landau-type theory [63, 64] of the transition to metallic spin glass order from a metallic phase. It is unlikely that the fixed point obtained in this section is the same as that of Appendix B.2: whereas the present RG analysis, when combined with the self-consistency conditions, requires $\epsilon' > 0$ on quite general grounds, we will see that the critical exponents in Appendix B.2 require $\epsilon' < 0$.

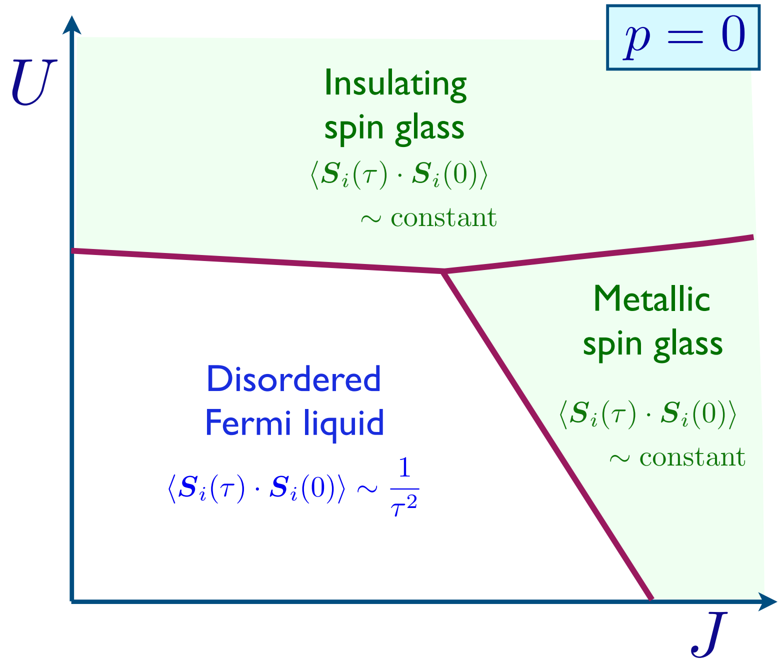

Figure 3.4: Schematic phase diagram at half-filling, $p = 0$, as a function of the Hubbard repulsion, U, and the mean-square exchange interaction J.

3.5 Conclusions

Our paper has presented two approaches to analyzing the metal-insulator transition of the random Hubbard model (3.1) at half-filling ($p = 0$); see Fig. 3.1.

The large M analysis in Section 3.3 leads to the fractionalization of the electron c_α into a boson X (with scaling dimension Δ_b) and a fermion f (with scaling dimension Δ_f). We argued that the deconfined critical point with $\Delta_f = \Delta_b = 1/4$ realized the metal-insulator transition observed numerically by Cha *et al.* [46]. These exponents imply the electron correlator in (3.25) and the spin correlator in (3.22), both consistent with the results of Cha *et al.* [46]. Given the similarity of the structure of this deconfined critical point to that of the Sachdev-Ye-Kitaev model, we expect it to share its unusual properties, including the non-vanishing low temperature entropy [71], and the maximal quantum Lyapunov exponent [42, 121–123].

We presented a renormalization group analysis of the random Hubbard model in Section 3.4. This turns out to be effectively a small U analysis, and to leading order in an ϵ expansion we found a fixed point (FP_3) possibly describing a metal-insulator transition. The renormalization group results have to be supplemented by the imposition of a self-consistency relation on the exponents, and we found that this required extrapolation to values of ϵ of order unity where our expansion breaks down. Consequently, we are not able to obtain the exponents accurately in this approach. We also discussed the possibility that FP_3 described the onset of a metallic spin glass phase from a disordered Fermi liquid, and that FP_3 was an alternative to the Landau theory of such a transition [63, 64] (the latter is reviewed in Appendix B.2).

4

Critical anomalous metals near superconductivity in models with random interactions

4.1 Introduction

The quantum phase transition out of the superconductor in disordered two-dimensional systems has been the focus of intense theoretical and experimental study in the past few decades [124–134]. Depending upon experimental conditions, the non-superconducting phase can either be an insulator or an 'anomalous' metal [124]. In an early proposal [134], it was argued that the breakdown of screening with increasing disorder could lead to a metallic phase with weak interactions and disorder. However, as argued by Kapitulnik *et al.* [124], observations show that the metallic phase is anomalous, with a much larger conductivity than in the 'normal' metal state at higher temperatures. They dubbed it a 'failed superconductor': they surveyed the large body of experimental data, and concluded that no available model of fluctuating superconductivity in a metallic background can consistently explain the existing observations.

Given this impasse, further advances would be greatly aided by a dynamical mean-field model which displays a quantum phase of matter analogous to an anomalous metal (a 'dynamical mean-field' is a theory which is mean-field in space, but includes fluctuations in time). In this paper, we propose such a model with a critical metallic state which shares some characteristics with those in the Sachdev-Ye-Kitaev (SYK) models [1, 42, 135, 136]. We consider a model of electrons with random pair-hopping and spin exchange terms, and find evidence that a critical anomalous metal phase appears either as a critical point or a critical phase between a disordered Fermi liquid and a superconductor. But unlike earlier studies of the superconductor-metal transition [134], the interactions do not scale to weak-coupling at the critical point, and there are large anomalous exponents.

The infinite-range interactions (or large spatial dimensionality) in our models imply that it cannot capture aspects of the physics that are associated with low dimensionality. These include weak localization and interaction corrections associated with diffusive electrons which were key ingredients in the theory of Finkel'stein [134]. However, these effects require coherent quasiparticle excitations, which will turn out to be absent in our SYK-like model. Indeed, from our dynamical mean-field model, our proposal is that the anomalous metal is controlled by non-quasiparticle dynamics, and so it is a useful starting point to ignore such effects which have so far been at the forefront in the theory of disordered interacting electrons. Quantum Griffiths effects associated with rare regions will also be absent in our model, but there is little experimental indication that rare regions control the observed anomalous metal.

The critical exponents of our anomalous metal turn out to have a natural interpretation in a dynamical mean-field theory of fractionalization of the electron into spinons, holons, and doublons. Galitski *et al.* [132] introduced the idea of fractionalizing electrons and

Cooper pairs in a theory of the anomalous metal, and examined a dual theory of fermionic vortices carrying flux $h/(2e)$. It is difficult to make contact with microscopic physics in such a dual formulation, and their theory relies on a conjecture on the vanishing of an average dual field acting on the fermionized vortices. In Section 4.4, we will implement fractionalization directly on the electrons, and show that it applies in the large M limit of a model with USp(M) spin rotation symmetry. Furthermore, in Section 4.3 we will employ a renormalization group analysis to obtain very similar critical states without explicit reference to fractionalized degrees of freedom.

We will carry out our analysis on a very general class of electronic Hamiltoinans with both disorder and interations. Consider a model of electrons (c) with on-site interaction U and chemical potential μ, and hopping and interaction terms between the sites:

$$
\begin{aligned}
H \;=\; & -\mu \sum_{i=1}^{N} c_{i\alpha}^{\dagger} c_{i\alpha} + U \sum_{i=1}^{N} \left(c_{i\uparrow}^{\dagger} c_{i\uparrow} - \frac{1}{2} \right) \left(c_{i\downarrow}^{\dagger} c_{i\downarrow} - \frac{1}{2} \right) + \frac{1}{\sqrt{N}} \sum_{i \neq j=1}^{N} t_{ij} c_{i\alpha}^{\dagger} c_{j\alpha} \\
& + \frac{1}{\sqrt{N}} \sum_{i<j=1}^{N} \left[J_{ij} \boldsymbol{S}_i \cdot \boldsymbol{S}_j + K_{ij} n_i n_j \right] + \frac{1}{\sqrt{N}} \sum_{i \neq j=1}^{N} L_{ij} \, c_{i\uparrow}^{\dagger} c_{i\downarrow}^{\dagger} c_{j\downarrow} c_{j\uparrow} \, . \qquad (4.1)
\end{aligned}
$$

(The $1/\sqrt{N}$ normalizations are for future convenience.) The hopping between the sites is t_{ij}, and there are three classes of interaction terms between the sites: a spin-exchange interaction J_{ij} with $\boldsymbol{S} = c_{\alpha}^{\dagger}(\boldsymbol{\sigma}_{\alpha\beta}/2)c_{\beta}$ ($\boldsymbol{\sigma}$ are the Pauli matrices), a Cooper-pair hopping term L_{ij}, and a density-density interaction K_{ij} with $n = c_{\alpha}^{\dagger} c_{\alpha}$; however, we note that we will only consider the $K_{ij} = 0$ case here—see comments below on changes expected for non-zero K_{ij}. Such a class of Hamiltonian has been much studied in the context of the 'universal Hamiltonian' for quantum dots [137–139], which take a random set of t_{ij} to obtain the random, extended, single-particle eigenstates of a Fermi liquid description of the quantum dot. Kurland *et al.* [137] argued that in such a Fermi liquid phase, the effects of interactions for a sufficiently large and chaotic (in the single particle sense) quantum dot can be accounted for by taking $J_{ij} = J/\sqrt{N}$, $K_{ij} = K/\sqrt{N}$, $L_{ij} = L/\sqrt{N}$ for some constants J, K, L for all i and j. Then the interaction terms can be written as complete squares, dependent only upon the total spin, number and pairing operator of the quantum dot.

As in previous work [2, 46, 140–142], our central thesis is that Hamiltonians like (4.1) can also exhibit non-Fermi liquid phases or critical points in which the interaction terms cannot be accounted for so simply. To access these non-Fermi liquid states without quasiparticle excitations, we will consider the model in which the J_{ij}, K_{ij}, and L_{ij} are independent real random numbers for each pair of sites i, and j, instead of the constant values assumed in theories of quantum dots [137, 139]. So the randomness in the interaction terms is treated at an equal footing with the randomness in t_{ij} (which is also an independent real random number), and we can choose

$$\begin{aligned} &\overline{t_{ij}} = 0 \quad , \quad \overline{J_{ij}} = 0 \quad , \quad \overline{K_{ij}} = 0 \quad , \quad \overline{L_{ij}} = 0 \\ &\overline{t_{ij}^2} = t^2 \quad , \quad \overline{J_{ij}^2} = J^2 \quad , \quad \overline{K_{ij}^2} = K^2 \quad , \quad \overline{L_{ij}^2} = L^2 \,, \end{aligned} \tag{4.2}$$

and independent of N with the normalizations in (4.1). In previous works, Joshi *et al.* [2, 141] considered cases with the on-site, non-random interaction term $U \to \infty$. Then, double occupancy on each site is prohibited, and the L_{ij} term has no effect. In this manner, they obtained a critical metal state with SYK character, and proposed it as a candidate for optimal doping criticality in the hole-doped cuprates. This critical metal appeared between a metallic spin glass phase and a Fermi liquid phase. Numerical evidence for SYK criticality between a metallic spin glass and Fermi liquid has appeared in recent work on a SU(2) model [142]. We also note earlier numerical evidence for SYK criticality in a SU(2) model at the metal-insulator transition at half-filling [46].

In the present paper, we will consider the case where U is small and can take values of both signs. Then, both the L_{ij} term, and a $U < 0$ can favor a superconducting ground state. We find evidence for critical metallic states with SYK character between a superconducting phase and a Fermi liquid phase, and propose it as a candidate theory for the anomalous metal discussed by Kapitulnik *et al.* [124]. We will provide both a renormalization group and a large M analysis of this anomalous metal. For simplicity, we will consider the case where the density-density interaction is neglected, $K = 0$. We have considered the effects of non-zero K for a related model in another paper [141], and found that it did not change the basic structure of the critical phase, and mainly modified certain critical exponents. We expect a similar consequence of a non-zero K here. Given the significant complexity of our analysis below, we choose to defer a full analysis of the effects of K to later work.

The model which is the focus of this paper will be introduced in Section 4.2. As in earlier work [142–144], we can also consider models in the limit of large spatial dimension with nearest-neighbor non-random hopping and nearest-neighbor random exchange; this leads to the same saddle-point dynamical mean-field equations, and also allows definition of the conductivity and other transport observables.

In Section 4.3 we present a renormalization group (RG) analysis of the model of Section 4.2 for the case at half-filling ($\mu = 0$). This analysis does not require a large M limit, and we retain the SU(2) spin symmetry. We use the mapping of the model of Section 4.2 to an impurity model with a self-consistent bath. We assume that the bath correlators have a power-law decay and, following Ref. [2], show that for suitable exponents a RG analysis is possible, analogous to the field-theoretic ϵ expansion. This RG analysis ignores the self-consistency condition on the bath; but the self-consistency is imposed *a posteriori* on the exponents of the correlators, although not the amplitudes. Our ϵ expansion is carried out at $U = 0$, and finds fixed points at which U is a strongly relevant perturbation about $U = 0$. We can therefore identify the fixed points with critical points between a superconductor and a disordered Fermi liquid. We note that the RG analysis in Section 4.3 is carried out entirely with the electron operator and its composites, and there is no explicit reference to fractionalized degrees of freedom. Precisely the same RG results are obtained using fractionalization of the electron into spinons, holons, and doublons, and imposing the same local constraint on the fractionalized fields. This acts as a strong check on our RG computations, and shows explicitly that the use of fractionalized variables is optional when the gauge constraint is imposed exactly.

Section 4.4 turns to a solvable large M limit of the model at general μ, obtained by generalizing the spin symmetry from SU(2) to USp(M). For our large M limit, we will have to explicitly fractionalize the electron into spinons, holons an doublons. In the body of the paper we present the formulation where we make the spinons fermionic, and the holons and doublons bosonic; Appendix C.3 considers the alternative formulation where the spinons and bosonic, and the holons and doublons are fermionic, and obtains similar results. The large M limit admits intermediate critical points or phases at variable density between the metal and the superconductor whose structure we will describe in some detail. In particular, we will show that the conductivities of these intermediate critical phases can be larger than that of the disordered Fermi liquid. The large M solutions can be viewed as relatives of the critical points found in the RG analysis of Section 4.3. This conclusion is supported by the agreement between the exponents of the electron, spin, and Cooper pair operators between the large M computations of Section 4.4, and the RG computations of Section 4.3, as we will review in Section 4.5.

4.2 Model

We will consider the model with all-to-all and random electron hopping, spin exchange, and Cooper-pair hopping: this is the Hamiltonian in (4.1), with $K_{ij} = 0$. Our analysis can be extended to non-zero K_{ij} without significant difficulty [141], but we choose not to do so here in the interests of simplicity; we do not expect significant changes to be induced by the K_{ij}. The random parameters in the Hamiltonian obey (4.2). We can also consider a model without time-reversal symmetry with t_{ij} and L_{ij} complex, but the results in the non-superconducting state will remain unchanged in the all-to-all interaction limit.

Let us first discuss the possible phases of the model. For small $U > 0$ the electrons can freely hop around to form a metal. Depending on the exchange interaction we may have a disordered Fermi liquid or a metallic spin glass [140, 142]. For large $U > 0$, doubly-occupancy is energetically costly thus restricting the electron movement to form a Mott insulator. This is likely to be a spin glass, although in the large M limit (where M corresponds to SU(M) generalization of SU(2)) one obtains the SY state [1]. This metal-insulator quantum phase transition at finite $U > 0$ in this model has been recently studied both analytically [140] and numerically [46], with an evidence for a SYK-like criticality. On the other hand, for large $U < 0$, one expects to obtain a superconductor. Thus near $U = 0$ we expect a metal-superconductor quantum phase transition. This phase transition and its vicinity will be discussed in detail here.

We note that we could equally consider a model on large-dimensional lattice with non-random hopping, and nearest-neighbor random exchange. Such a model leads to the same large volume limit, with the same on-site dynamical mean-field equations [142–144]. Such a limit allows definition of transport quantities, and we will need it here to define the appropriate correlator needed to define the conductivity.

The Hilbert space of (4.1) on each site has four states: empty ($|0\rangle$), singly occupied ($|\uparrow\rangle$ or $|\downarrow\rangle$) and doubly occupied ($|\uparrow\downarrow\rangle$). As we are working at small U, there is no constraint we need to impose and we can perform computations directly using the electron operator c_α. This will be our strategy in the Section 4.3. We will introduce a fractionalized representation later in Section 4.4 when we study a large M limit.

4.2.1 Large-volume limit

Models with random interactions often offer the possibility of simplification in the large-volume limit, i.e., $N \to \infty$. We formally introduce replica indices for the fields in the path integrals and perform a disorder average over t_{ij}, J_{ij}, and L_{ij}. Consequently we arrive at an effective single-site action. Since we are interested in the critical point the replica indices do not play a significant role. These are important when studying a spin-glass phase. The entire procedure follows the methodology developed in Refs. [1, 70, 71]. In the end when $N \to \infty$ and dropping the replica indices for simplicity, we arrive at the effective single-site action below. (As we noted above, the same single-site action can also be obtained in the limit of large dimensionality.)

$$\mathcal{Z} = \int \mathcal{D}c_\alpha(\tau) e^{-\mathcal{S}_0 - \mathcal{S}_1}\,, \tag{4.3}$$

$$\mathcal{S}_0 = \int d\tau \left[c^\dagger_\alpha(\tau) \frac{\partial}{\partial\tau} c_\alpha(\tau) - \mu c^\dagger_\alpha(\tau) c_\alpha(\tau) + U c^\dagger_\uparrow(\tau) c^\dagger_\downarrow(\tau) c_\downarrow(\tau) c_\uparrow(\tau) \right], \tag{4.4}$$

$$\begin{aligned} \mathcal{S}_1 = \int d\tau d\tau' \Big[& t^2 R(\tau-\tau') c^\dagger_\alpha(\tau) c_\alpha(\tau') - \frac{J^2}{2} Q(\tau-\tau') \boldsymbol{S}(\tau)\cdot\boldsymbol{S}(\tau') \\ & - L^2 P(\tau-\tau')\, c^\dagger_\uparrow(\tau) c^\dagger_\downarrow(\tau) c_\downarrow(\tau') c_\uparrow(\tau') \Big]. \end{aligned} \tag{4.5}$$

The fields R, Q, and P have to be determined self-consistently. With respect to the above path integral we have the correlators,

$$\begin{aligned} \bar{R}(\tau-\tau') &= -\left\langle c_\alpha(\tau) c^\dagger_\alpha(\tau') \right\rangle_{\mathcal{Z}} \\ \bar{Q}(\tau-\tau') &= \frac{1}{3} \left\langle \boldsymbol{S}(\tau)\cdot\boldsymbol{S}(\tau') \right\rangle_{\mathcal{Z}} \\ \bar{P}(\tau-\tau') &= \left\langle c_\downarrow(\tau) c_\uparrow(\tau) c^\dagger_\uparrow(\tau') c^\dagger_\downarrow(\tau') \right\rangle_{\mathcal{Z}}\,. \end{aligned} \tag{4.6}$$

To find the solution of the problem defined by (4.1) we have to impose the following self-consistency conditions:

$$\begin{aligned} R(\tau-\tau') &= \bar{R}(\tau-\tau') \\ Q(\tau-\tau') &= \bar{Q}(\tau-\tau') \\ P(\tau-\tau') &= \bar{P}(\tau-\tau')\,. \end{aligned} \tag{4.7}$$

This is the difficult part in obtaining the solution. Note that since t_{ij} and L_{ij} are real random variables, in principle, upon disorder averaging we also obtain the anomalous (pairing) fields in (4.5). However, our analyses below will be restricted to non-superconducting states where the anomalous correlators vanish, and so we have omitted them in our presentation for simplicity. If we consider t_{ij} and L_{ij} to be complex then the anomalous fields do not arise. So as long as we are not in the superconducting phase the analyses with real or complex t_{ij}

and L_{ij} are same.

4.3 Renormalization group analysis

In this section we present a renormalization-group study of the model in (4.3) - (4.5). To make progress and set-up our RG let us for the moment ignore the self-consistency conditions, (4.7). We shall come back to it later in our analysis. Furthermore, since we are interested in criticality let us assume a power-law time dependence for R, Q and P fields,

$$R(\tau) \sim \frac{\mathrm{sgn}(\tau)}{|\tau|^{r+1}}\,, \quad Q(\tau) \sim \frac{1}{|\tau|^{d-1}}\,, \quad P(\tau) \sim \frac{1}{|\tau|^{d'-1}}\,, \tag{4.8}$$

where r, d and d' are arbitrary numbers. The idea is similar to that introduced in Ref. [2]. This allows us to decouple the quartic terms in the action, (4.5), by introducing a fermionic and two bosonic bath fields. Consequently, the path integral reduces to a quantum impurity problem with the following impurity Hamiltonian:

$$\begin{aligned} H_{\mathrm{imp}} = & -\mu\, c^\dagger_\alpha c_\alpha + U\left(c^\dagger_\uparrow c_\uparrow - \frac{1}{2}\right)\left(c^\dagger_\downarrow c_\downarrow - \frac{1}{2}\right) \\ & + g_0\left[c^\dagger_\alpha\, \psi_\alpha(0) + \mathrm{H.c.}\right] + \gamma_0 c^\dagger_\alpha \frac{\sigma^a_{\alpha\beta}}{2} c_\beta\, \phi_a(0) + v_0\left[c_\downarrow c_\uparrow\, \zeta(0) + \mathrm{H.c.}\right] \\ & + \int |k|^r dk\, k\, \psi^\dagger_{k\alpha}\psi_{k\alpha} + \frac{1}{2}\int d^d x\left[\pi_a^2 + (\partial_x\phi_a)^2\right] + \frac{1}{2}\int d^{d'} x\left[\tilde{\pi}^*\tilde{\pi} + (\partial_x\zeta)(\partial_x\zeta^*)\right]\,, \end{aligned} \tag{4.9}$$

where $a = (x, y, z)$, σ^a are the Pauli matrices, π_a is canonically conjugate to the bosonic-bath field ϕ_a, $\tilde{\pi}$ is canonically conjugate to the bosonic-bath field ζ, and $\psi_{k\alpha}$ is a fermionic-bath field. Additionally, $\phi_a(0) \equiv \phi_a(x = 0)$, $\zeta(0) \equiv \zeta(x = 0)$ and $\psi_\alpha(0) \equiv \int |k|^r dk\, \psi_{k\alpha}$. As discussed in Sec. 4.2, we will perform the RG about half-filling and small U, and so we will set $\mu = 0$ and expand perturbatively in U in the following RG calculations.

Let us start by writing the tree-level scaling dimensions of the fields and couplings,

$$
\begin{aligned}
&\dim[c_\alpha] = 0\,, \quad \dim[\psi_{k\alpha}] = -\frac{1+r}{2} = -\dim[\psi_\alpha(0)]\,, \quad \dim[\phi_a] = \frac{d-1}{2}\,, \quad \dim[\zeta] = \frac{d'-1}{2} \\
&\dim[g_0] = \frac{1-r}{2} \equiv \bar{r}\,, \quad \dim[\gamma_0] = \frac{3-d}{2} \equiv \frac{\epsilon}{2}\,, \quad \dim[v_0] = \frac{3-d'}{2} \equiv \frac{\epsilon'}{2}\,. \qquad (4.10)
\end{aligned}
$$

Thus we will be using $\bar{r}$, ϵ, and ϵ' as our expansion parameters in perturbative RG calculation. To set-up our field-theoretic RG, we introduce the following renormalization factors for the electron operator and coupling constants,

$$
c_\alpha = \sqrt{Z_c}c_{\alpha,R}\,, \quad g_0 = \frac{\mu^{\bar{r}}Z'_g g}{\sqrt{Z_c}}\,, \quad \gamma_0 = \frac{\mu^{\epsilon/2}Z'_\gamma\gamma}{Z_c}\,, \quad v_0 = \frac{\mu^{\epsilon'/2}Z'_v v}{Z_c}\,. \qquad (4.11)
$$

Note that the action in (4.9) does not contain any interaction terms for the bath fields. As a result, the bath fields do not get renormalized. In the below subsections we shall calculate the electron self energy and vertex corrections at one-loop order to obtain the renormalization factors defined above.

We note that a perturbative RG was performed for H_{imp} without the ζ bath field in Ref. [140] by a different method which chose field definitions so that the tree level scaling dimension of γ was $\epsilon = 2-d$ rather than $\epsilon = 3-d$ in (4.10). That approach led to an additional boundary renormalization of the operator ϕ^2, and a different scaling structure. Here we choose the method above because it leads to results compatible with the large M analysis in Section 4.4.

4.3.1 Self-energy of electron

We begin with the evaluation of the electron self energy. There are three contributions to the electron self energy, one each from the g_0, γ_0, and v_0 vertices. These are shown in Fig.

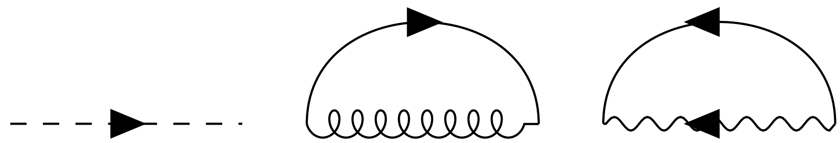

Figure 4.1: Feynman diagrams for the self energy of electrons. Here the solid line is electron propagator, dashed line is ψ propagator, curly curve is ϕ propagator and wavy curve is ζ propagator.

4.1 and evaluate as follows:

$$\Sigma_{4.1(a)}(i\nu) = g_0^2 \int dk \frac{|k|^r}{i\nu - k} = -\frac{g_0^2}{\bar{r}}(i\nu)^{1-2\bar{r}} = -\frac{g^2}{\bar{r}} i\nu A'_\mu \,, \tag{4.12}$$

$$\Sigma_{4.1(b)}(i\nu) = \gamma_0^2 \frac{3}{4} \int \frac{d^d k}{(2\pi)^d} \frac{1}{\beta} \sum_{i\omega} \frac{1}{\omega^2 + k^2} \frac{1}{i\nu + i\omega} = -\gamma_0^2 \frac{3}{4\epsilon}(i\nu)^{1-\epsilon} = -\frac{3\gamma^2}{4\epsilon} i\nu B'_\mu \,, \tag{4.13}$$

$$\Sigma_{4.1(c)}(i\nu) = -v_0^2 \int \frac{d^d k}{(2\pi)^d} \frac{1}{\beta} \sum_{i\omega} \frac{1}{\omega^2 + k^2} \frac{1}{-i\nu - i\omega} = -v_0^2 \frac{1}{\epsilon'}(i\nu)^{1-\epsilon'} = -\frac{v^2}{\epsilon'} i\nu C'_\mu \,, \tag{4.14}$$

where $A'_\mu = \mu^{2\bar{r}}(i\nu)^{-2\bar{r}} Z_g'^2/Z_c$, $B'_\mu = \mu^{\epsilon}(i\nu)^{-\epsilon} Z_\gamma'^2/Z_c^2$, and $C'_\mu = \mu^{\epsilon'}(i\nu)^{-\epsilon'} Z_v'^2/Z_c^2$. Demanding the cancellation of poles at the external frequency $i\nu = \mu$, we immediately get,

$$Z_c = 1 - \frac{g^2}{\bar{r}} - \frac{3\gamma^2}{4\epsilon} - \frac{v^2}{\epsilon'} \,. \tag{4.15}$$

4.3.2 Vertex corrections

Next we evaluate the vertex corrections. The g_0 vertex has no corrections and so $Z'_g = 1$. Let us first calculate the correction to γ_0 vertex. There are two one-loop diagrams shown in Fig. 4.2 (a) and (b), which evaluate as

$$\Gamma_{4.2(a)} = \gamma_0^3 \left(-\frac{1}{4}\right) \int \frac{d^d k}{(2\pi)^d} \frac{1}{\beta} \sum_{i\omega} \frac{1}{\omega^2 + k^2} \frac{1}{i\omega + i\Omega_1} \frac{1}{i\omega + i\Omega_2} = -\gamma_0 \frac{\gamma^2}{4\epsilon} B'_\mu \,, \tag{4.16}$$

$$\Gamma_{4.2(b)} = \gamma_0 v_0^2 \int \frac{d^d k}{(2\pi)^d} \frac{1}{\beta} \sum_{i\omega} \frac{1}{\omega^2 + k^2} \frac{1}{i\omega + i\Omega_1} \frac{1}{i\omega + i\Omega_2} = \gamma_0 \frac{v^2}{\epsilon'} C'_\mu \,. \tag{4.17}$$

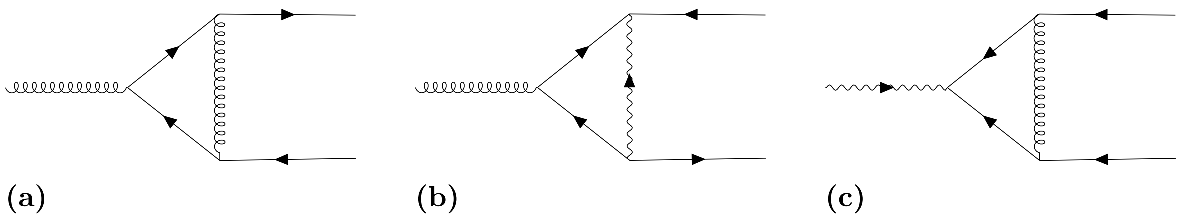

Figure 4.2: Feynman diagrams for the vertex corrections. Diagrams in (a) and (b) contribute to γ_0 vertex correction, while that in (c) contribute to v_0 vertex correction. Conventions are the same as in Fig. 4.1.

In (4.16), $i\Omega_1 = i\Omega_2$ are external electron frequencies. Similarly, in (4.17) $i\Omega_1 = -i\Omega_2$ are external electron frequencies. We can compute the v_0 vertex correction, which has only one contribution at one-loop level (Fig. 4.2 (c)),

$$\Gamma_{4.2(c)} = v_0\gamma_0^2\frac{3}{4}\int\frac{d^dk}{(2\pi)^d}\frac{1}{\beta}\sum_{i\omega}\frac{1}{\omega^2+k^2}\frac{1}{i\omega+i\Omega_1}\frac{1}{i\omega+i\Omega_2} = v_0\frac{3\gamma^2}{4\epsilon'}B'_\mu\,. \tag{4.18}$$

Here $i\Omega_1 = -i\Omega_2$ are external electron frequencies. The above vertex corrections then lead to following renormalization factors:

$$Z'_\gamma = 1+\frac{\gamma^2}{4\epsilon}-\frac{v^2}{\epsilon'}\,, \tag{4.19}$$

$$Z'_v = 1-\frac{3\gamma^2}{4\epsilon}\,. \tag{4.20}$$

4.3.3 Beta functions and fixed points

Having obtained the renormalization factors we can now derive the RG flow equations. Using Eqs. (4.11), (4.15), (4.19), and (4.20) we get the following beta functions,

$$\beta(g) = -\bar{r}g+g^3+\frac{3}{8}g\gamma^2+\frac{gv^2}{2}\,, \tag{4.21}$$

$$\beta(\gamma) = -\frac{\epsilon}{2}\gamma+\gamma^3+2\gamma g^2\,, \tag{4.22}$$

$$\beta(v) = -\frac{\epsilon'}{2}v+v^3+2vg^2\,. \tag{4.23}$$

The RG flow described by the beta functions found above has seven fixed points and a fixed line in the $\gamma = 0$ plane, which are located using the condition $\beta(g) = \beta(\gamma) = \beta(v) = 0$. These fixed points/line $(g*^2, \gamma*^2, v*^2)$ are as follows:

$$FP_1 : (0, 0, 0) \ , \tag{4.24}$$

$$FP_2 : (\bar{r}, 0, 0) \ , \tag{4.25}$$

$$FP_3 : \left(0, \frac{\epsilon}{2}, 0\right) \ , \tag{4.26}$$

$$FP_4 : \left(4\bar{r} - \frac{3\epsilon}{4}, 2\epsilon - 8\bar{r}, 0\right) \ , \tag{4.27}$$

$$FP_5 : \left(0, 0, \frac{\epsilon'}{2}\right) \ , \tag{4.28}$$

$$FP_6 : \left(0, \frac{\epsilon}{2}, \frac{\epsilon'}{2}\right) \ , \tag{4.29}$$

$$FP_7 : \left(\bar{g}^2, 0, \bar{v}^2\right) \ , \quad \text{such that } 2\bar{g}^2 + \bar{v}^2 = 2\bar{r} \text{ with } \epsilon' = 4\bar{r}. \tag{4.30}$$

$$FP_8 : \left(-\frac{4\bar{r}}{3} + \frac{\epsilon}{4} + \frac{\epsilon'}{3}, \frac{8\bar{r}}{3} - \frac{2\epsilon'}{3}, \frac{8\bar{r}}{3} - \frac{\epsilon}{2} - \frac{\epsilon'}{6}\right) \ . \tag{4.31}$$

Note that FP_7 is not a fixed point but a fixed line; an ellipse in the $\gamma = 0$ plane described by the condition $2\bar{g}^2 + \bar{v}^2 = 2\bar{r}$ with $\epsilon' = 4\bar{r}$. Thus FP_7 occurs only at a fine-tuned value and is generically not present. Also note that FP_2 and FP_5 lie on the same curve that describes the ellipse of FP_7. However, FP_2 and FP_5 do not require any fine tuning and are generically present. It so happens that if $\epsilon' = 4\bar{r}$ then the fixed line FP_7 exists and it passes through both FP_2 and FP_5.

Let us now discuss the conditions when the fixed points are real. The fixed point FP_2 is real for any $\bar{r} > 0$, FP_3 is real for any $\epsilon > 0$, FP_5 is real for any $\epsilon' > 0$, and FP_6 is real for any $\epsilon, \epsilon' > 0$. The fixed point FP_4 is real if $16\bar{r}/3 > \epsilon > 4\bar{r}$. While the fixed point FP_8 is real if $(16\bar{r} - \epsilon')/3 > \epsilon > (16\bar{r} - 4\epsilon')/3$. We emphasize again that FP_7 exists only if $\epsilon' = 4\bar{r}$. If $\epsilon' = 4\bar{r}$ then FP_8 also lies in the $\gamma = 0$ plane, and in fact it lies on the ellipse describing FP_7.

We discuss in detail the stability of the fixed points in Appendix C.1. In particular, the non-trivial fixed point FP_6, (4.29), is stable at the self-consistent values of ϵ, ϵ', and $\bar{r}$, which will be determined in the next subsection. It is interesting to note that this fixed point has $g = 0$, and so charge transport occurs only via Cooper pair hopping, and not via single-particle hopping. So we may consider this as describing a critical Bose metal.

4.3.4 Anomalous dimensions of spin, electron and SC order-parameter operators

We now calculate the anomalous dimensions of the electron, spin, and SC order-parameter operators. These exponents are physical observables in scattering and spectroscopic experiments. Our aim is to evaluate the exponents corresponding to the spin correlator $\langle \boldsymbol{S}(\tau)\cdot\boldsymbol{S}(0)\rangle$, the electron correlator $\langle c_\alpha(\tau)c^\dagger_\alpha(0)\rangle$, and the SC order-parameter correlator $\langle \Delta(\tau)\Delta^\dagger(0)\rangle$. For this purpose, we define the following renormalization factors: $\hat{S} = \sqrt{Z_S}\hat{S}_R$ and $\Delta = \sqrt{Z_\Delta}\Delta_R$. To evaluate these we use the strategy of introducing source terms in the action. From this analysis it is straightforward to see that

$$Z_S = \left(\frac{Z_c}{Z'_\gamma}\right)^2 = 1 - \frac{2\gamma^2}{\epsilon} - \frac{2g^2}{\bar{r}}\,, \tag{4.32}$$

$$Z_\Delta = \left(\frac{Z_c}{Z'_v}\right)^2 = 1 - \frac{2g^2}{\bar{r}} - \frac{2v^2}{\epsilon'}\,. \tag{4.33}$$

We have already evaluated Z_c in (4.15).

It is now straightforward to express the required anomalous dimensions in terms of the coupling constants,

$$\eta_S = \frac{d\ln Z_S}{d\ln\mu} = 4g^2 + 2\gamma^2\,, \tag{4.34}$$

$$\eta_c = \frac{d\ln Z_c}{d\ln\mu} = 2g^2 + \frac{3}{4}\gamma^2 + v^2\,, \tag{4.35}$$

$$\eta_\Delta = \frac{d\ln Z_\Delta}{d\ln\mu} = 4g^2 + 2v^2\,. \tag{4.36}$$

These can be evaluated at the respective fixed points,

$$FP_1 : \eta_S = 0\,, \qquad \eta_c = 0\,, \qquad \eta_\Delta = 0 \tag{4.37}$$

$$FP_2 : \eta_S = 4\bar{r}\,, \qquad \eta_c = 2\bar{r}\,, \qquad \eta_\Delta = 4\bar{r}\,, \tag{4.38}$$

$$FP_3 : \eta_S = \epsilon\,, \qquad \eta_c = \frac{3\epsilon}{8}\,, \qquad \eta_\Delta = 0\,, \tag{4.39}$$

$$FP_4 : \eta_S = \epsilon\,, \qquad \eta_c = 2\bar{r}\,, \qquad \eta_\Delta = 16\bar{r} - 3\epsilon\,, \tag{4.40}$$

$$FP_5 : \eta_S = 0\,, \qquad \eta_c = \frac{\epsilon'}{2}\,, \qquad \eta_\Delta = \epsilon'\,, \tag{4.41}$$

$$FP_6 : \eta_S = \epsilon\,, \qquad \eta_c = \frac{3\epsilon}{8} + \frac{\epsilon'}{2}\,, \qquad \eta_\Delta = \epsilon'\,, \tag{4.42}$$

$$FP_7 : \eta_S = 4\bar{g}^2\,, \qquad \eta_c = 2\bar{r}\,, \qquad \eta_\Delta = \epsilon'\,, \tag{4.43}$$

$$FP_8 : \eta_S = \epsilon\,, \qquad \eta_c = 2\bar{r}\,, \qquad \eta_\Delta = \epsilon'\,. \tag{4.44}$$

Similar to Ref. [2], we can obtain an exact result here for the spin, electron, and SC order-parameter anomalous dimensions. Using Eqs. (4.11), and (4.34) to (4.36) we obtain the exact result that if $g^* \neq 0$ then $\eta_c = 2\bar{r}$, if $\gamma^* \neq 0$ then $\eta_S = \epsilon$, and if $v^* \neq 0$ then $\eta_\Delta = \epsilon'$ at all orders in ϵ, ϵ' and $\bar{r}$. In particular this means that at the non-trivial fixed FP_8 we have $\eta_c = 2\bar{r}$, $\eta_S = \epsilon$, and $\eta_\Delta = \epsilon'$ at all orders in the perturbation theory. Note that for $K_{ij} \neq 0$ in (4.1) the exponent of density operator is similarly determined exactly at the fixed points with non-zero density coupling.

Now we are in a position to impose the self-consistency condition, (4.7), that we had neglected so far. We shall impose the self-consistency condition at the fixed point FP_6, (4.29). This simply means equating the exponents of $Q(\tau)$ and $P(\tau)$ in (4.8) to the anomalous dimensions calculated for the spin and SC order-parameter operators, i.e., $2 - \epsilon = \epsilon$ and $2 - \epsilon' = \epsilon'$. Solving these equations yields the self-consistent values of $\epsilon = \epsilon' = 1$ at the fixed point FP_6. This means that the spin and SC order-parameter correlators decay as $1/\tau$. And we again emphasize that this result is true at all orders in ϵ, ϵ' and $\bar{r}$. Note that since $g^* = 0$ at FP_6 there is no self-consistency condition for $R(\tau)$ and hence the value of $\bar{r}$ is not fixed. Remarkably, at the self-consistent values of $\epsilon = \epsilon' = 1$ the fixed point FP_6 is stable at one-loop order for $\bar{r} < 7/16$; although we can not formally trust this result at such large values of ϵ and ϵ'. We also note that had we decided to consider fixed point FP_8, we need to impose the self-consistency condition of all P, Q, and R, which fixes the values of $\epsilon = \epsilon' = 2\bar{r} = 1$. This means that spin, electron, and SC order-parameter correlators decay as $1/\tau$ at FP_8. However, at one-loop order FP_8 is always unstable for real values. But one can not rule out the possibility that at large values of our expansion parameters and at strong coupling the non-trivial fixed point FP_8 is stable and controls the RG flow.

4.4 Fractionalization and Large-M analysis

In this section, we discuss another approach to solve the model introduced in (4.1). Here we shall fractionalize the electron operator into spinons, holon and doublon. Also we will generalize the SU(2) spin symmetry to USp(M). As we shall see this allows us to solve a set of saddle-point equations and find a conformal solution of the electron Green's function. In particular, we shall calculate the residual conductivity. We discuss this approach in detail in the following.

With the electron operator c_α, we represent the 4 states on each site using fermionic spinons f_α, a bosonic holon b, and a bosonic doublon d as follows:

$$|0\rangle \quad \Rightarrow \quad b^\dagger|v\rangle\,, \quad c^\dagger_\alpha|0\rangle \Rightarrow f^\dagger_\alpha|v\rangle\,, \quad c^\dagger_\uparrow c^\dagger_\downarrow|0\rangle \Rightarrow d^\dagger|v\rangle\,, \tag{4.45}$$

where $|v\rangle$ is the vaccumm state. We therefore fractionalize the electron into spinons, holon, and doublon in the following manner:

$$
\begin{aligned}
c_\alpha &= f_\alpha b^\dagger + \varepsilon_{\alpha\beta} f_\beta^\dagger d\,, && (4.46)\\
c_\alpha^\dagger c_\alpha &= n = 1 + d^\dagger d - b^\dagger b\,, && (4.47)\\
\boldsymbol{S} &= \frac{1}{2} c_\alpha^\dagger \boldsymbol{\sigma}_{\alpha\beta} c_\beta = \frac{1}{2} f_\alpha^\dagger \boldsymbol{\sigma}_{\alpha\beta} f_\beta\,, && (4.48)\\
\left(c_\uparrow^\dagger c_\uparrow - \frac{1}{2}\right)\left(c_\downarrow^\dagger c_\downarrow - \frac{1}{2}\right) &= \frac{1}{2}\left(d^\dagger d + b^\dagger b - \frac{1}{2}\right)\,, && (4.49)\\
c_\downarrow c_\uparrow &= b^\dagger d\,, && (4.50)
\end{aligned}
$$

with the constraint, $f_\alpha^\dagger f_\alpha + b^\dagger b + d^\dagger d = 1$. Such a fractionlization was studied early on by Kotliar and Ruckenstein [145], and applied to the Mott transition at large positive U. Here, we shall study the behavior at small and negative U, and allow for critical, gapless, SYK-like states in which the bosons don't condense.

Using Eqs. (4.46) - (4.50), we can write the Hamiltonian in (4.1) in terms of the fractionalized particles, f, b, and d, as

$$
\begin{aligned}
H &= \sum_{i=1}^{N}\left(-\mu(d_i^\dagger d_i - b_i^\dagger b_i) + \frac{U}{2}(d_i^\dagger d_i + b_i^\dagger b_i)\right)\\
&\quad + \frac{1}{\sqrt{N}}\sum_{i\neq j=1}^{N} t_{ij} c_{i\alpha}^\dagger c_{j\alpha} + \frac{1}{\sqrt{N}}\sum_{i<j=1}^{N} J_{ij}\boldsymbol{S}_i\cdot\boldsymbol{S}_j + \frac{1}{\sqrt{N}}\sum_{i\neq j=1}^{N} L_{ij}\, b_i^\dagger d_i d_j^\dagger b_j\,. \qquad (4.51)
\end{aligned}
$$

Most of our analysis will be on the particle-hole symmetric case $\mu = 0$; the form of the particle-hole symmetry is briefly discussed in Sec. 4.4.2.

Next, we generalize the model in (4.51) to a model with M spin indices and M' orbital indices. We then study the model in the large-M limit at a fixed $k \equiv M'/M$. As it will become clear later, this allows us to find an analytic solution for our model in the low-energy limit. The original model has $M = 2$, $M' = 1$, $k = 1/2$. In this generalization, the electron operator is

$$
c_{\ell\alpha} = f_\alpha b_\ell^\dagger + \mathcal{J}_{\alpha\beta} f_\beta^\dagger d_\ell\,, \qquad (4.52)
$$

where $\mathcal{J}$ is the USp(M) invariant tensor [146], while $\alpha = 1 \dots M$ (M even), and $\ell = 1 \dots M'$. This representation has a U(1) gauge invariance,

$$f_{i\alpha} \to f_{i\alpha} e^{i\phi_i(\tau)}, \quad b_{i\ell} \to b_{i\ell} e^{i\phi_i(\tau)}, \quad d_{i\ell} \to d_{i\ell} e^{i\phi_i(\tau)} . \tag{4.53}$$

We also have the constraint fixing the U(1) gauge charge on each site,

$$\sum_{\alpha=1}^{M} f_{i\alpha}^\dagger f_{i\alpha} + \sum_{\ell=1}^{M'} \left(b_{i\ell}^\dagger b_{i\ell} + d_{i\ell}^\dagger d_{i\ell} \right) = \frac{M}{2} . \tag{4.54}$$

Then the large M, M' Hamiltonian is

$$\begin{aligned} H &= \sum_{i,\ell} \left(-\mu \left(d_{i\ell}^\dagger d_{i\ell} - b_{i\ell}^\dagger b_{i\ell} \right) + \frac{U}{2} \left(b_{i\ell}^\dagger b_{i\ell} + d_{i\ell}^\dagger d_{i\ell} \right) \right) + \frac{1}{\sqrt{NM}} \sum_{i,j,\ell,\alpha} t_{ij} c_{i\ell\alpha}^\dagger c_{j\ell\alpha} \\ &\quad + \frac{1}{\sqrt{NM}} \sum_{i>j,\alpha\beta} J_{ij} f_{i\alpha}^\dagger f_{i\beta} f_{j\beta}^\dagger f_{j\alpha} + \frac{1}{\sqrt{NM}} \sum_{i \neq j, \ell\ell'} L_{ij} b_{i\ell}^\dagger d_{i\ell'} d_{j\ell'}^\dagger b_{j\ell} . \end{aligned} \tag{4.55}$$

The large M analysis will proceed as Refs. [87] and [2]. We first take the $N \to \infty$ limit and perform disorder average, as discussed in Sec. 4.2.1 to obtain the single-site action in the large-M limit,

$$\begin{aligned} \mathcal{Z} &= \int \mathcal{D} f_\alpha \mathcal{D} b_\ell \mathcal{D} d_\ell \mathcal{D} \lambda e^{-\mathcal{S}} \\ \mathcal{S} &= \int_0^{1/T} d\tau \left[\sum_\ell b_\ell^\dagger \left(\frac{\partial}{\partial \tau} + \mu + \frac{U}{2} + i\lambda \right) b_\ell + \sum_\ell d_\ell^\dagger \left(\frac{\partial}{\partial \tau} - \mu + \frac{U}{2} + i\lambda \right) d_\ell \right. \\ &\qquad \left. + \sum_\alpha f_\alpha^\dagger \left(\frac{\partial}{\partial \tau} + i\lambda \right) f_\alpha - i\lambda \frac{M}{2} \right] + \frac{t^2}{M} \sum_{\ell\alpha} \int_0^{1/T} d\tau d\tau' R(\tau - \tau') c_{\ell\alpha}^\dagger(\tau) c_{\ell\alpha}(\tau') \\ &- \frac{J^2}{2M} \sum_{\alpha\beta} \int_0^{1/T} d\tau d\tau' Q(\tau - \tau') f_\alpha^\dagger(\tau) f_\beta(\tau) f_\beta^\dagger(\tau') f_\alpha(\tau') \\ &- \frac{L^2}{M} \sum_{\ell\ell'} \int_0^{1/T} d\tau d\tau' P(\tau - \tau') b_\ell^\dagger(\tau) d_{\ell'}(\tau) d_{\ell'}^\dagger(\tau') b_\ell(\tau') , \end{aligned} \tag{4.56}$$

where T is the temperature. Here $\lambda(\tau)$ is the Lagrange multiplier imposing the constraint in

(4.54) and the self-consistency conditions read as follows:

$$\begin{aligned} R(\tau-\tau') &= -\frac{1}{MM'}\sum_{\ell\alpha}\left\langle c_{\ell\alpha}(\tau)c^\dagger_{\ell\alpha}(\tau')\right\rangle_{\mathcal{Z}} , \\ Q(\tau-\tau') &= \frac{1}{M^2}\sum_{\alpha\beta}\left\langle f^\dagger_\alpha(\tau)f_\beta(\tau)f^\dagger_\beta(\tau')f_\alpha(\tau')\right\rangle_{\mathcal{Z}} , \\ P(\tau-\tau') &= \frac{1}{M'^2}\sum_{\ell\ell'}\left\langle b_\ell(\tau)d^\dagger_{\ell'}(\tau)d_{\ell'}(\tau')b^\dagger_\ell(\tau')\right\rangle_{\mathcal{Z}} . \end{aligned} \tag{4.57}$$

Alternatively, we can also use a representation with bosonic spinons $\mathfrak{b}_\alpha$, fermionic holons $\mathfrak{f}_\ell$ and fermionic doublons $\mathfrak{d}_\ell$. This is discussed in detail in Appendix C.3.

4.4.1 Saddle-point equations

We will now write down the saddle-point equations obtained from the action in (4.56). Using the condensed matter notations, we first introduce the following Green's functions

$$G_f(\tau,\tau') = -\frac{1}{M}\sum_\alpha\left\langle T_\tau(f_\alpha(\tau)f^\dagger_\alpha(\tau'))\right\rangle_{\mathcal{Z}} , \tag{4.58}$$

$$G_b(\tau,\tau') = -\frac{1}{M'}\sum_\ell\left\langle T_\tau(b_\ell(\tau)b^\dagger_\ell(\tau'))\right\rangle_{\mathcal{Z}} , \tag{4.59}$$

$$G_d(\tau,\tau') = -\frac{1}{M'}\sum_\ell\left\langle T_\tau(d_\ell(\tau)d^\dagger_\ell(\tau'))\right\rangle_{\mathcal{Z}} , \tag{4.60}$$

corresponding to the spinon, f, holon, b, and the doublon, d. Note that one can also construct anomalous Green's functions as well as a mixed Green's function involving b and d. However, we take these to vanish as they break the U(1) gauge symmetry, (4.53), down to $\mathcal{Z}_2$.

From the action in (4.56), it is straightforward to obtain the saddle point equations for the fractionalized particles:

$$\Sigma_f(\tau) = kt^2 R(-\tau) G_d(\tau) - kt^2 R(\tau) G_b(\tau) + J^2 Q(\tau) G_f(\tau)\,, \tag{4.61}$$

$$\Sigma_b(\tau) = t^2 G_f(\tau) R(-\tau) + k^2 L^2 G_d(\tau) P(\tau)\,, \tag{4.62}$$

$$\Sigma_d(\tau) = -t^2 R(\tau) G_f(\tau) + k^2 L^2 G_b(\tau) P(-\tau)\,, \tag{4.63}$$

$$G_a^{-1}(i\omega) = i\omega - \mu_a - \Sigma_a(i\omega)\,, \quad a = f, b, d\,. \tag{4.64}$$

Here μ_a are chemical potentials, determined by U and the saddle point value of λ to satisfy

$$\left\langle f^\dagger f \right\rangle = \delta_f\,, \tag{4.65}$$

$$\left\langle b^\dagger b \right\rangle = \delta_b\,, \tag{4.66}$$

$$\left\langle d^\dagger d \right\rangle = \delta_d\,, \tag{4.67}$$

$$\frac{2}{MM'} \sum_{\ell,\alpha} \left\langle c^\dagger_{\ell\alpha} c_{\ell\alpha} \right\rangle = n = 1 - \delta = 1 + \delta_d - \delta_b\,, \tag{4.68}$$

with the gauge-charge constraint (4.54) implying

$$\delta_f + k(\delta_b + \delta_d) = \frac{1}{2}\,. \tag{4.69}$$

In terms of the Green's functions, the self-consistency equations are expressed as follows:

$$\begin{aligned} R(\tau) &= -G_f(\tau) G_b(-\tau) + G_f(-\tau) G_d(\tau)\,, \\ Q(\tau) &= -G_f(\tau) G_f(-\tau)\,, \\ P(\tau) &= G_b(\tau) G_d(-\tau)\,. \end{aligned} \tag{4.70}$$

Now our aim is to look for the solution of these saddle-point equations, which we discuss in the following subsections and refer to technical details in Appendix C.2.

4.4.2 Particle-hole symmetry

Before we discuss the solutions of our saddle-point equations, we briefly comment on the particle-hole symmetry here. The form of the electron Green's function in terms of the fractionalized particles is

$$G_c(\tau) = -G_f(\tau)G_b(-\tau) + G_f(-\tau)G_d(\tau)\,. \tag{4.71}$$

The model considered here has particle-hole symmetry at $\mu = 0$, which exchanges the holon and doublon. The particle-hole transformation can be written as follows:

$$b \to -d\,, \quad d \to b\,, \quad f_\alpha \to f_\alpha\,, \tag{4.72}$$

Under this transformation we have $G_b(\tau) = G_d(\tau)$ and thus $\sigma_b(\Omega) = \sigma_d(\Omega)$. Importantly, $c_\alpha \to \epsilon_{\alpha\beta}c_\beta^\dagger$, which means that $n \to 2 - n$. Therefore, the electron Green's function is an odd function due to particle-hole symmetry, i.e., $G_c(\tau) = -G_c(-\tau)$. Also note that the spin operator is invariant under this transformation.

4.4.3 Critical solution of saddle-point equations

We will now work towards finding solutions to the saddle-point equations, Eqs. (4.61) - (4.64) assuming that the spinons, holons, and doublons are all gapless. The basic strategy is to find the constraints on the parameters of our low-frequency ansatz by the saddle-point equations. In terms of the imaginary time, τ, such that $|\tau| \gg 1/J$ we write at $T = 0$,

$$G_a(\tau) = -\mathrm{sgn}(\tau)\frac{C_a\Gamma(2\Delta_a)\sin(\pi\Delta_a + \mathrm{sgn}(\tau)\theta_a)}{\pi|\tau|^{2\Delta_a}}\,, \tag{4.73}$$

where parameters C_a, Δ_a and θ_a are real, with more details explained in Appendix C.2. The spectral densities (C.18) in comparison with (C.20) immediately yields the following relations of the exponents for nonzero t, J, and L,

$$\Delta_b + \Delta_d = \frac{1}{2}\,, \tag{4.74}$$

and a restriction on asymmetry angles

$$\frac{\sin(\pi\Delta_b + \theta_b)\sin(\pi\Delta_d + \theta_d)}{\sin^2(\pi\Delta_f + \theta_f)} = \frac{\sin(\pi\Delta_b - \theta_b)\sin(\pi\Delta_d - \theta_d)}{\sin^2(\pi\Delta_f - \theta_f)}\,. \tag{4.75}$$

We can now evaluate the anomalous dimensions of the electron, spin, and SC order-parameter operators in the present large M limit. Specifically, as the electron Green's function is given by Eqs. (4.71), spin correlator by $\langle \mathbf{S}(\tau)\cdot\mathbf{S}(0)\rangle \sim -G_f(\tau)G_f(-\tau)$, and SC order-parameter correlator by $\langle \Delta(\tau)\Delta^\dagger(0)\rangle \sim G_b(\tau)G_d(-\tau)$, it is straightforward to see the anomalous dimension of the corresponding operators are

$$\eta_c = \mathrm{Min}\{2(\Delta_f + \Delta_b),\, 2(\Delta_f + \Delta_d)\}\,, \tag{4.76}$$

$$\eta_S = 4\Delta_f\,, \tag{4.77}$$

$$\eta_\Delta = 2(\Delta_b + \Delta_d) = 1\,. \tag{4.78}$$

Examining the saddle-point equations leads to several possible solutions. Since we are interested in the general $t-J-L$ model, we will focus on the case with nonzero t, J, L first and then discuss other special scenarios.

4.4.3.1 $\Delta_f = \Delta_b = \Delta_d = 1/4$

In this case, the exponents in t^2, J^2 and L^2 terms in $\Sigma_{f,b,d}$ (see (C.18)) are equal, and so all terms are important in our low-frequency analysis. Comparison of (C.18) with (C.20) yields

$$t^2C_f^2C_b^2\cos(2\theta_f) - k^2L^2C_b^2C_d^2\cos(2\theta_d) - 2t^2C_f^2C_bC_d\tfrac{\sin(\pi/4-\theta_d)\sin^2(\pi/4+\theta_f)}{\sin(\pi/4+\theta_b)} = \pi\,, \quad (4.79)$$

$$t^2C_f^2C_d^2\cos(2\theta_f) - k^2L^2C_b^2C_d^2\cos(2\theta_b) - 2t^2C_f^2C_bC_d\tfrac{\sin(\pi/4-\theta_b)\sin^2(\pi/4+\theta_f)}{\sin(\pi/4+\theta_d)} = \pi\,, \quad (4.80)$$

$$\begin{aligned} J^2C_f^4\cos(2\theta_f) - kt^2C_f^2\Big[&C_b^2\cos(2\theta_b) + C_d^2\cos(2\theta_d) \\ &- 4C_bC_d\tfrac{\sin\left(\pi/4-\theta_f\right)\sin(\pi/4+\theta_b)\sin(\pi/4+\theta_d)}{\sin\left(\pi/4+\theta_f\right)}\Big] = \pi \end{aligned} \quad (4.81)$$

as well as the restriction on asymmetry angles (4.75). Notice the bounds $|\theta_f| < \pi/4$, $\pi/4 < \theta_b < \pi/2$ and $\pi/4 < \theta_d < \pi/2$, which leads to all the coefficients on the left-hand sides of Eqs. (4.79) - (4.81) being positive. Since C_f, C_b, C_d are defined to be real positive numbers, we find another constraint for θ_f, θ_b and θ_d:

$$-\cos(2\theta_f) \leq -k\big[\cos(2\theta_b) - \cos(2\theta_d)\big] \leq \cos(2\theta_f)\,, \quad (4.82)$$

Therefore the parameters of the solution (θ_d, C_f, C_b and C_d) are fully determined by the two asymmetry angles θ_f and θ_b. Recall that the values of θ_f and θ_b are related to the particle densities δ_b, δ_d via the Luttinger constraints derived by techniques in Ref. [136]:

$$\frac{\theta_f}{\pi} + \left(\frac{1}{2} - \Delta_f\right)\frac{\sin(2\theta_f)}{\sin(2\pi\Delta_f)} = \frac{1}{2} - \delta_f\,, \quad (4.83)$$

$$\frac{\theta_b}{\pi} + \left(\frac{1}{2} - \Delta_b\right)\frac{\sin(2\theta_b)}{\sin(2\pi\Delta_b)} = \frac{1}{2} + \delta_b\,, \quad (4.84)$$

$$\frac{\theta_d}{\pi} + \left(\frac{1}{2} - \Delta_d\right)\frac{\sin(2\theta_d)}{\sin(2\pi\Delta_d)} = \frac{1}{2} + \delta_d\,. \quad (4.85)$$

And from (4.68), we see that at half-filling with particle-hole symmetry, we have $n = 1$ and $\delta_b = \delta_d$.

It is useful to recall now all the parameters and constraint equations for the low energy behavior of the large M ansatz. The low energy ansatz in (4.73) with $\Delta_f = \Delta_b = \Delta_d = 1/4$ is determined by the 6 parameters C_f, θ_f, C_b, θ_b, C_d, θ_d. Let us also regard the densities of the fractionalized particles δ_f, δ_b, and δ_d as unknown quantities to be determined by the electronic doping density δ. So at fixed δ we have 9 parameters specifying the low energy solution. These parameters are fully determined by δ by 9 equations: the Luttinger relations (4.83), (4.84), (4.85), the density constraints (4.68), (4.69), and the saddle point equations (4.75), (4.79), (4.80), (4.81). Now let us consider the solution of the saddle-point equations at all energies (this has to be done numerically, and we will not carry out the numerical analysis here; such a numerical analysis has been carried out for the t-J model in Refs. [147, 148]). The saddle point equations (4.61), (4.62), (4.63) will lead to definite values of the self energies $\Sigma_f(i\omega = 0)$, $\Sigma_d(i\omega = 0)$, $\Sigma_d(i\omega = 0)$. But the gapless nature of the ansatz in (4.73) requires that $G_f^{-1}(i\omega = 0) = G_b^{-1}(i\omega = 0) = G_d^{-1}(i\omega = 0) = 0$, which requires cancellation of the zero frequency self energy by the chemical potential [1]. The chemical potentials of the 3 fractionalized particles in (4.56) are determined by the 3 parameters μ, λ, and U. As U is not a free parameter, we conclude that the single parameter U must be tuned to realize the critical solution (4.73). So this large-M solution describes a critical point at a fixed density δ, but is present for variable δ.

From Eqs. (4.74), (4.76), (4.77), and (4.78) we immediately see that in this critical point $\eta_c = \eta_S = \eta_\Delta = 1$, i.e., the electron, spin, and SC order parameter correlators all decay as $1/\tau$. In particular, the $1/\tau$ decay of the spin correlator is in stark contrast to its $1/\tau^2$ decay in Fermi liquid phase. Such a critical behavior of spin correlator is similar to the SYK-like criticality [1, 42]. The present scenario can be understood as a direct consequence of the fractionalization of electron into spinons, holon, and doublon, wherein the correlator of each of these particles decay as $1/\sqrt{\tau}$. As we shall show in the next subsection the conductivity of this critical phase is larger than that of a Fermi liquid metal. Therefore, this solution is a candidate anomalous metal. In Sec. 4.3 we presented a weak-coupling RG analysis for the case of $M = 2, M' = 1$, and we found a SYK-like critical point, FP_8 in (4.31). The critical point therein is related to the critical point studied here. Our one-loop weak-coupling RG analysis found FP_8 to be unstable. However, as mentioned earlier we expect this fixed point to be stable at strong coupling such that it corresponds to the present large-M solution.

4.4.3.2 $\Delta_f > 1/4$

For $\Delta_f > 1/4$, we neglect the subdominant terms in our low-frequency analysis. The saddle point equations Eqs. (4.79)-(4.81) are now modified as

$$1/2 = \Delta_f + \Delta_b \,, \tag{4.86}$$

$$1/2 = \Delta_d + \Delta_b \,, \tag{4.87}$$

$$1 = -\frac{k^2 L^2 C_b^2 C_d^2 \sin(\pi\Delta_b + \theta_b)\sin(\pi\Delta_b - \theta_b)}{2\pi\Delta_b \sin(2\pi\Delta_b)} \,, \tag{4.88}$$

$$1 = -\frac{k t^2 C_f^2 C_b^2 \sin(\pi\Delta_b + \theta_b)\sin(\pi\Delta_b - \theta_b)}{2\pi\Delta_b \sin(2\pi\Delta_b)} \,, \tag{4.89}$$

$$-k = \frac{\sin(\pi\Delta_f + \theta_f)\sin(\pi\Delta_f - \theta_f)/\Delta_f}{\sin(\pi\Delta_b + \theta_b)\sin(\pi\Delta_b - \theta_b)/\Delta_b - \sin(\pi\Delta_d + \theta_d)\sin(\pi\Delta_d - \theta_d)/\Delta_d} \,, \tag{4.90}$$

or the other set of equations by making a replacement $\Delta_b \leftrightarrow \Delta_d$, $\theta_b \leftrightarrow \theta_d$, $C_b \leftrightarrow C_d$. Since the Luttinger relations (4.83), (4.84), (4.85), the density constraints (4.68) remain the same here, so this solution corresponds to a critical phase. Here the anomalous dimensions of the spin operator, $\eta_S > 1$, while that of the SC order parameter, $\eta_\Delta = 1$. The saddle-point of the J term vanishes in this solution, and the solution only depends upon the values of t and L. So this solution is the analog of the fixed point FP_7 had only the g and v couplings non-zero.

4.4.3.3 Solutions at $t = 0$

In this case, the combination of (C.18) and (C.20) yields $\Delta_f = 1/4$ and still satisfies the constraints (4.74). We can assume $\Delta_b = \Delta > 0$, $\Delta_d = 1/2 - \Delta > 0$ and therefore Eqs.

(4.79)-(4.81) are modified to

$$J^2 C_f^4 \cos(2\theta_f) = \pi\,, \tag{4.91}$$
$$-k^2 L^2 C_b^2 C_d^2 \frac{\cos(2\theta_d) + \cos(2\pi\Delta)}{(1-2\Delta)\sin(2\pi\Delta)} = 2\pi\,, \tag{4.92}$$
$$-k^2 L^2 C_b^2 C_d^2 \frac{\cos(2\theta_b) - \cos(2\pi\Delta)}{2\Delta\sin(2\pi\Delta)} = 2\pi\,, \tag{4.93}$$

Therefore the parameters of the solution (θ_b, C_f and the product $C_b C_d$) are fully determined by the asymmetry angles θ_f, θ_d and exponent Δ. Since C_f, C_b, C_d are defined to be real positive numbers, we find a constraint in analogy with (4.82) for θ_d and Δ at $t = 0$:

$$\cos(2\theta_d) + \cos(2\pi\Delta) \leq 0\,. \tag{4.94}$$

This solution corresponds to a critical phase with $\eta_S = \eta_\Delta = 1$ and $\eta_c \leq 1$. Our weak-coupling RG in Sec. 4.3 yielded a stable 'Bose metal' fixed point, FP_6 in (4.29), with these properties.

4.4.3.4 Solutions at $L = 0$

For $\Delta_f = \Delta_b = \Delta_d = 1/4$, the saddle point equations have the same form as Eqs. (4.79)-(4.81) without L terms, but the condition to keep all C_f, C_b, C_d real and positive is different from (4.82):

$$-\cos(2\theta_f) \leq -k\big[\cos(2\theta_b) + \cos(2\theta_d)\big] \leq \cos(2\theta_f)\,. \tag{4.95}$$

This solution actually is a special case in Sec. 4.4.3.1.

For $\Delta_f > 1/4$ the J^2 term in (C.18) is subdominant compared to the t^2 term, and so we neglect it in our low-frequency analysis. The combination of (C.18) and (C.20) yields

$$1/2 = \Delta_f + \Delta_b\,, \tag{4.96}$$

$$1/2 = \Delta_f + \Delta_d\,, \tag{4.97}$$

$$1 = t^2 C_f^2 C_b^2 \frac{\sin(\pi\Delta_f + \theta_f)\sin(\pi\Delta_f - \theta_f)}{2\pi\Delta_f \sin(2\pi\Delta_f)} - t^2 C_f^2 C_b C_d \frac{\sin(\pi\Delta_d - \theta_d)\sin^2(\pi\Delta_f + \theta_f)}{2\pi\Delta_f \sin(2\pi\Delta_f)\sin(\pi\Delta_b + \theta_b)}\,, \tag{4.98}$$

$$1 = t^2 C_f^2 C_d^2 \frac{\sin(\pi\Delta_f + \theta_f)\sin(\pi\Delta_f - \theta_f)}{2\pi\Delta_f \sin(2\pi\Delta_f)} - t^2 C_f^2 C_b C_d \frac{\sin(\pi\Delta_b - \theta_b)\sin^2(\pi\Delta_f + \theta_f)}{2\pi\Delta_f \sin(2\pi\Delta_f)\sin(\pi\Delta_d + \theta_d)}\,, \tag{4.99}$$

$$-k = \frac{\sin(\pi\Delta_f + \theta_f)\sin(\pi\Delta_f - \theta_f)/\Delta_f}{\sin(\pi\Delta_b + \theta_b)\sin(\pi\Delta_b - \theta_b)/\Delta_b + \sin(\pi\Delta_d + \theta_d)\sin(\pi\Delta_d - \theta_d)/\Delta_d}\,, \tag{4.100}$$

along with the restriction on the asymmetry angles (4.75). Therefore the parameters of the solution (Δ_b, Δ_d, θ_b, θ_d, and the product $C_f C_b$, $C_f C_d$) are fully determined by the asymmetry angle θ_f and exponent Δ_f. This solution corresponds to a critical phase with $\eta_S > 1$, $\eta_\Delta < 1$ and $\eta_c = 1$.

4.4.4 Non-critical phases

As in Ref. [87], we obtain non-critical phases by gapping or condensing the bosons. A solution with both b and d gapped is possibly only at half-filling, and this describes a gapless spin liquid of the f spinons. Such a solution is only reasonable at large U. If we condense only one of b and d, then we Higgs the U(1) gauge symmetry, but leave the global U(1) symmetry unbroken–such a solution is therefore a disordered Fermi liquid, as in Ref. [2]. Finally, if we condense both b and d, we break both the gauge and global U(1) symmetries, and the solution is a superconductor.

4.4.5 Conductivity

We shall now compare the zero temperature residual conductivity between the normal state, and the critical point corresponding to the solution $\Delta_f = \Delta_b = \Delta_d = 1/4$ found above. Let us denote the residual conductivities in the normal and the critical phases by σ_0^N and σ_0^A respectively. We shall show below that for a wide-range of asymmetry parameters the ratio $\mathcal{R} \equiv \sigma_0^A/\sigma_0^N > 1$. This suggests that the critical phase is in fact an anomalous metal phase, similar to that reported in experiments in the vicinity of a metal-SC phase transition. In this section, we will need to revert to the large dimensionality limit to properly define the expressions for the conductivity [143, 144].

The calculation in the critical (anomalous metal) phase uses techniques from Ref. [143], which applies a more general formalism using time-reparameterization symmetry in SYK-like models. Following the steps in Ref. [143], we first generalize the Greens function to finite temperature,

$$G_a(\theta) = -\frac{C_a\Gamma(2\Delta_a)}{\pi}\frac{\sin(\theta_a + \pi\Delta_a)}{|2\sin\frac{\theta}{2}|^{2\Delta_a}}e^{-\mathcal{E}_a\theta}, \quad \theta \in (0, 2\pi)\,, \tag{4.101}$$

where we choose $\theta = 2\pi\tau/\beta$. $\mathcal{E}_a$ is determined by

$$e^{2\pi\mathcal{E}_a} = \frac{\sin(\theta_a + \pi\Delta_a)}{\sin(\theta_a - \pi\Delta_a)}\zeta_a\,, \tag{4.102}$$

where $\zeta_b = \zeta_d = 1$, $\zeta_f = -1$ indicate the periodicity of $G_a(\theta)$. Here the subscript $a = f, b, d$ is used for spinon, holon and doublon respectively.

The Kubo formula for conductivity on the Bethe lattice from electron hopping is derived in Ref. [143]

$$\mathrm{Re}\,\sigma(\nu) = \frac{M'e^2t^2a^{2-d}}{2\pi z}\int d\omega A_c(\omega)A_c(\omega+\nu)\frac{n_F(\omega) - n_F(\omega+\nu)}{\nu}\,, \tag{4.103}$$

where a is lattice constant, z is coordination number, d is spatial dimension and $A_c(\omega) = -2\,\mathrm{Im}\,G_c(\omega + i\eta)$ is electron spectral density. We can introduce the bosonic Cooper pair

Green's function $G_\Delta(\theta) \equiv G_b(\theta)G_d(-\theta)$, whose contribution to conductivity is an analogy with the electron contribution after making the replacement $e \to 2e$, $A_c \to A_\Delta$, $n_F \to n_B$ and $t^2 \to kL^2$. The residual conductivity now yields

$$\sigma_0^A = \frac{M'e^2t^2a^{2-d}}{2\pi z}\int d\omega A_c(\omega)^2\beta n_F(\omega)n_F(-\omega)+\frac{M'(2e)^2kL^2a^{2-d}}{2\pi z}\int d\omega A_\Delta(\omega)^2\beta n_B(\omega)n_B(-\omega)\,, \tag{4.104}$$

where $A_\Delta(\omega) = -2\,\mathrm{Im}\,G_\Delta(\omega+i\eta)$ is Cooper pair spectral density,

$$A_c(\omega) = 2\pi C e^{-\pi\mathcal{E}}\frac{\cosh(\beta\omega/2)}{\cosh(\beta\omega/2-\pi\mathcal{E})} + 2\pi C' e^{-\pi\mathcal{E}'}\frac{\cosh(\beta\omega/2)}{\cosh(\beta\omega/2-\pi\mathcal{E}')}\,, \tag{4.105}$$

$$A_\Delta(\omega) = -2\pi C_\Delta e^{-\pi\mathcal{E}_\Delta}\frac{\sinh(\beta\omega/2)}{\cosh(\beta\omega/2-\pi\mathcal{E}_\Delta)}\,. \tag{4.106}$$

Here the parameters are defined as $\mathcal{E} = \mathcal{E}_f - \mathcal{E}_b$, $\mathcal{E}' = \mathcal{E}_d - \mathcal{E}_f$, $\mathcal{E}_\Delta = \mathcal{E}_b - \mathcal{E}_d$,

$$C = C_f C_b \sin(\theta_f + \pi/4)\sin(\theta_b - \pi/4)/\pi, \tag{4.107}$$

$$C' = -C_f C_d \sin(\theta_f - \pi/4)\sin(\theta_d + \pi/4)/\pi, \tag{4.108}$$

$$C_\Delta = C_b C_d \sin(\theta_b + \pi/4)\sin(\theta_d - \pi/4)/\pi. \tag{4.109}$$

We now have all the ingredients to calculate the residual conductivity using (4.104). Inserting Eqs. (4.105)-(4.106) into (4.104) we obtain,

$$\sigma_0^A = 2\pi\frac{M'e^2a^{2-d}}{z}\left[t^2\left(C^2e^{-2\pi\mathcal{E}}+C'^2e^{-2\pi\mathcal{E}'}-2CC'e^{-\pi(\mathcal{E}+\mathcal{E}')}\frac{\pi(\mathcal{E}-\mathcal{E}')}{\sinh[\pi(\mathcal{E}-\mathcal{E}')]}\right)+4kL^2C_\Delta^2e^{-2\pi\mathcal{E}_\Delta}\right]. \tag{4.110}$$

In the normal state with semi-circle density $A_c(\omega) = \sqrt{4t^2-(\omega+\mu)^2}/t^2$, only electron contributes to the residual conductivity. Therefore, at zero temperature and $\mu = 0$ the normal state residual conductivity is

$$\sigma_0^N = \frac{M'e^2t^2a^{2-d}}{2\pi z}\int d\omega A_c(\omega)^2\beta n_F(\omega)n_F(-\omega) = \frac{2M'e^2a^{2-d}}{\pi z}\,. \tag{4.111}$$

Now we have the ratio of these two residual conductivities,

$$\mathcal{R} = \frac{\sigma_0^A}{\sigma_0^N} = \pi^2 \left[t^2 \left(C^2 e^{-2\pi\mathcal{E}} + C'^2 e^{-2\pi\mathcal{E}'} + 2CC' e^{-\pi(\mathcal{E}+\mathcal{E}')} \frac{\pi(\mathcal{E}-\mathcal{E}')}{\sinh\left[\pi(\mathcal{E}-\mathcal{E}')\right]} \right) + 4kL^2 C_\Delta^2 e^{-2\pi\mathcal{E}_\Delta} \right]. \tag{4.112}$$

As we can see from Sec. 4.4.3, the above ratio has only two parameters, namely, θ_f and θ_b. In Fig. 4.3 we make a density plot of $\mathcal{R}$ with contours as a function of these parameters. The ratios are calculated at a given set of parameters $k = 1/2$, $t = 1/2$, $J = 1$, $L = 0$ and 5 in two schemes: the fermionic spinon scheme in Sec. 4.4 and the bosonic spinon scheme discussed in Appendix C.3. In the particle-hole symmetric case, the only solution is $\theta_f = 0$, $\theta_b = \pi/2$ with $\mathcal{R} \approx 5$ at $L = 5$ and $\mathcal{R} = \pi/2$ at $L = 0$ for both schemes. We further explore the particle-hole symmetric solution at $k = 1/2$ but arbitrary positive t, J, L parameters, and obtain the ratio in the range of

$$\frac{\pi}{2} \leq \mathcal{R}\big|_{\theta_f=0,\,\theta_b=\pi/2} = 2\pi \frac{JL + t^2}{JL + 4t^2} \leq 2\pi\,. \tag{4.113}$$

More generally, for arbitrary k, t, J, L parameters,

$$\mathcal{R}\big|_{\theta_f=0,\,\theta_b=\pi/2} = \pi \frac{kJ^2L^2 + (1-2k)t^4 + \sqrt{k^2J^2L^2t^4 + (1-2k)^2t^8}}{k^2J^2L^2 + 2(1-2k)t^4 + 2\sqrt{k^2J^2L^2t^4 + (1-2k)^2t^8}} = \begin{cases} \pi/k, & \text{if } JL \gg t^2 \\ \pi/2, & \text{if } JL \ll t^2\,. \end{cases} \tag{4.114}$$

The limit $JL \gg t^2$ likely describes a Bose metal, where incoherent pairs of electrons carry the charge current instead of bare electrons.

We now briefly discuss the conductivity of the phases corresponding to the RG fixed point FP_7 and FP_6, which are associated with the large M saddle points in Sections 4.4.3.2 and 4.4.3.3 respectively. For FP_7, we assume $\Delta_f = \Delta_d = \Delta > 1/4$, so $\Delta_b = 1/2 - \Delta < 1/4$ and the ratio of these two residual conductivities yields

$$\mathcal{R} = \frac{\pi(1-2\Delta)\sin\pi(1-2\Delta)}{k}\left[\frac{3}{2}\cos(2\pi\Delta) - 2\cos(2\theta_d) + \frac{1}{2}\cos(2\theta_f)\right] < \frac{5\pi}{4k}\,. \tag{4.115}$$

For FP_6, we consider the case with $t = 0$, $\Delta_f = 1/4$, $\Delta_b = \Delta$, $\Delta_d = 1/2 - \Delta$. The ratio becomes

$$\mathcal{R} = -\frac{4\pi\Delta\sin 2\pi\Delta}{k}\left[\cos(2\pi\Delta) + \cos(2\theta_d)\right]. \tag{4.116}$$

The maximum of $\mathcal{R} = 11.4$ reaches at $\Delta = 0.365$, $\theta_d = \pi/2$.

As a reminder, we also quote here the value of zero temperature residual conductivity in the critical phase found in a related model, namely the random t-J model without double occupancy. The result obtained in Ref. [143] is

$$\mathcal{R}^{tJ} = \frac{\sigma_0^{tJ}}{\sigma_0^N} = 2\pi C^2 e^{-2\pi\mathcal{E}}\frac{M' e^2 t^2 a^{2-d}}{z}\Big/\sigma_0^N = -\frac{\pi}{4}\cos(2\theta_b) \leq \frac{\pi}{4}\,. \tag{4.117}$$

4.5 Conclusions

We have examined a model of interacting electrons with random and all-to-all hopping and interactions in (4.1): this yields a theory which is mean-field in space but includes fluctuations in time. The interactions are in one-to-one correspondence with the interactions in the universal Hamiltonian for disordered metallic grains [137–139]. The universal Hamiltonian has the same interaction strength acting between any pair of sites, but we instead take each interaction term to be an independent random number. An important characteristic of our analysis is that the random hopping and interaction terms are treated at an equal footing. We then employed RG and large M computations to argue, as in Ref. [2], that such models lead to critical metallic solutions similar to those in the SYK models. For the class of models examined here, with the on-site Hubbard interaction parameter small, we have argued that

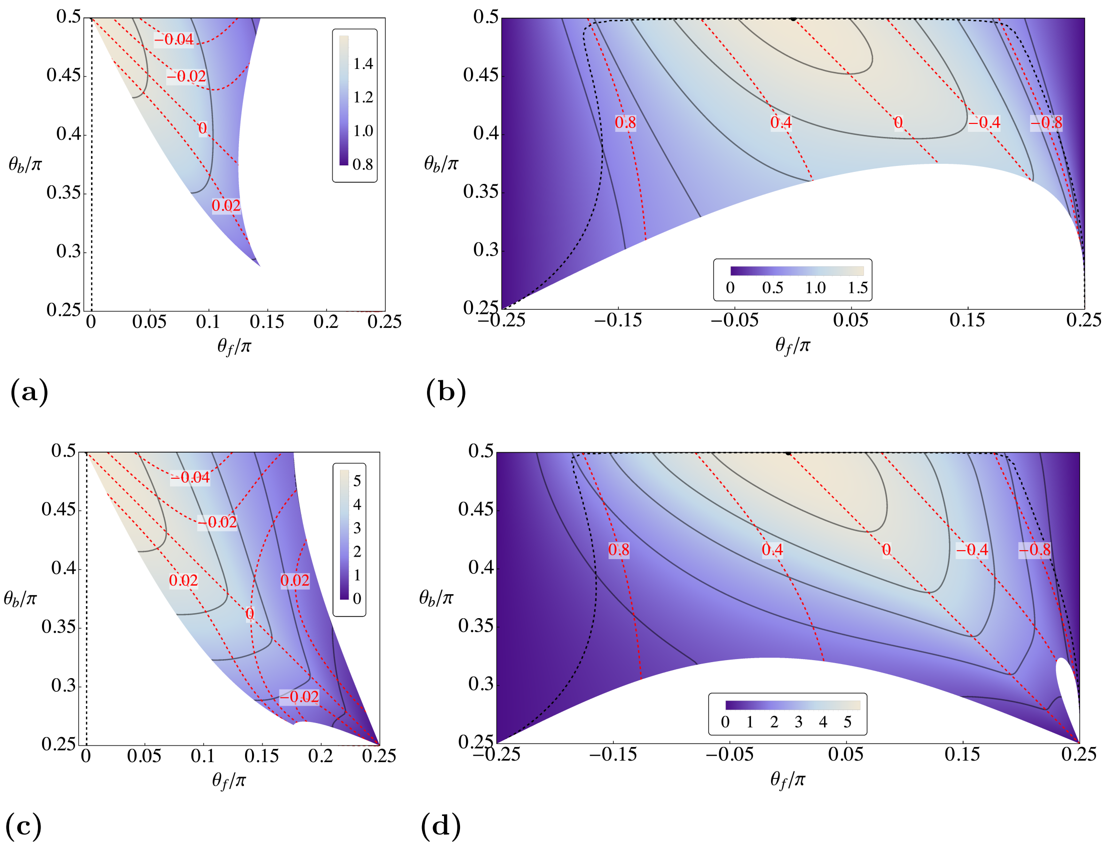

Figure 4.3: The ratio of large M background conductivity to normal state solution, $\mathcal{R} = \sigma_0^A/\sigma_0^N$, in a density plot for possible asymmetry parameters θ_f and θ_b in different representations; the full black lines are contours of equal $\mathcal{R}$. The ratio is calculated at $k = 1/2$, $t = 1/2$, $J = 1$ and different L. (a) Bosonic holon scheme with $L = 0$. (b) Fermionic holon scheme with $L = 0$. (c) Bosonic holon scheme with $L = 5$. (d) Fermionic holon scheme with $L = 5$. The red dashed lines are contours of constant doping density δ obtained by solving (4.68,4.84,4.85), and the black dashed lines shows the solution of (4.75,4.83,4.84,4.85). Spectral positivity and the conditions for real C_f, C_b, C_d parameters restrict the range of solutions: (a) is bounded by (4.75,4.95,C.13), (b) is bounded by (C.40,C.44,C.46), (c) is bounded by (4.75,4.82,C.13), and (d) is bounded by (C.40,C.44,C.45),. We could identify the ratio $\mathcal{R}$ in the two schemes (a) and (b) or (c) and (d) by $\theta_f \leftrightarrow \pi/2 - \theta_b$.

such critical metals can realize a critical point or phase between a disordered Fermi liquid and a superconductor, and so are candidate dynamical mean-field descriptions of the anomalous metallic 'failed superconductor' [124].

The experimental observations are largely in two-dimensional systems, while our model has either infinite-range interactions or large spatial dimensionality, a characteristic of dynamical mean-field theories. So our model does not capture effects that have been viewed as crucial to the physics of disordered interacting electrons: weak localization and interaction corrections from diffusive electrons. However, such effects require long-lived quasiparticles, and the absence of quasiparticles in our theory is reason to hope that our dynamical mean-field theory is useful starting point for a theory in two dimensions which can be applied real materials.

Another perspective on our anomalous metal is provided by an analogy with the large U work of Joshi *et al.* [2]. That work examined the transition between a metallic spin glass and a disordered Fermi liquid, and proposed a description in terms of a deconfined spin liquid with doped charge carriers. Our present work is carried out at small $|U|$, and has fluctuations in the Nambu pseudospin space along with spin fluctuations. So we may consider the anomalous metal as a 'deconfined pseudospin liquid' found at the transition between a supercondutor and a disordered Fermi liquid.

Our RG computations in Section 4.3, and our large M computation in Section 4.4 yielded a number of candidate solutions for the critical anomalous metal. There are interesting connections between these two classes of solutions, and we list below 3 solutions from each method that have similar physical properties and exponents. Notice, however, that the stability of the phases differs between the two methods, and so we are not able to reliably determine the optimal candidate.

The exponents η_c, η_S, η_Δ determine the decay of the electron, spin, and Cooper-pair correlators in imaginary time $\sim 1/\tau^\eta$. The Bose metal transports charge primarily via Cooper pair hopping, and single electron hopping is subdominant.

The conductivities of the anomalous critical metal phases were computed in Section 4.4.5 in the large M theory. Here, we followed the large-M formulation of the conductivity in a

RG	Large M
Fixed point FP_8 $\eta_c = \eta_S = \eta_\Delta = 1$ Unstable critical point	Solution in Sec. 4.4.3.1 $\eta_c = \eta_S = \eta_\Delta = 1$ Stable critical point
Fixed point FP_7 $\eta_c = \eta_\Delta = 1$ Present only for $\epsilon' = 4\bar{r}$ Line of stable critical points	Solution in Sec. 4.4.3.2 $\eta_c = \eta_\Delta = 1$, $\eta_S > 1$ Stable critical phase
Fixed point FP_6 $\eta_S = \eta_\Delta = 1$ Stable critical point Critical Bose metal	Solution in Sec. 4.4.3.3 $\eta_S = \eta_\Delta = 1$, $\eta_c \leq 1$ Critical phase unstable to $t \neq 0$ Critical Bose metal

Table 4.1: Comparison between the properties of fixed points obtained by RG and large M analysis.

large dimension lattice, which was discussed in Ref. [143]. It should be noted that this large M approach yields residual resistivities which are significantly higher than those obtained numerically in the SU(2) solution of the same model [46]. So we computed the ratios of the conductivity of large M solution of the critical anomalous metal to that of the disordered Fermi liquid, as an estimate of any enhancement of the conductivity in the anomalous metal in the large M limit. As presented in Section 4.4.5 there is a moderate, but not large, enhancement in this ratio in our computations. It would be of interest to perform numerical studies for the SU(2) case, similar to that in Ref. [46], for models like (4.1) with Cooper pair hopping, and compute their conductivities between the Fermi liquid and superconducting phases.

5

Superconductivity of non-Fermi liquids described by Sachdev-Ye-Kitaev models

5.1 Introduction

The classic BCS theory provides a highly successful description of the onset of superconductivity (SC) from a Fermi liquid (FL). However, in modern correlated electron materials, the normal state at the onset of higher temperature superconductivity is usually not a Fermi liquid. Below the critical temperature, basic aspects of the BCS superconducting state (such as the breaking of U(1) gauge symmetry by an electron pair condensate) continue to hold, but numerous quantitative details on the critical temperature, superconducting gap amplitude, and electron spectral function are not described by BCS theory.

A popular class of theories for the onset of superconductivity from a non-Fermi liquid

(NFL) focus on a normal state which has a Fermi surface coupled to a critical boson [149–154]. The boson could represent a symmetry breaking order parameter at a quantum critical point, or an emergent excitation associated with spin liquid physics. This critical boson plays a dual role—it leads to the breakdown of quasiparticles in the normal state, and it also leads to superconductivity at low temperature (T) by inducing pairing between the underlying electrons. The precise manner in which the non-Fermi liquid gives way to superconductivity at low T is not well understood, and remains a topic of great interest.

In this paper, we will address the interplay between the non-Fermi liquid and superconductivity using a different class of simpler and more tractable models. These models do not have much spatial structure because of the presence of all-to-all hopping and interactions. However, they have the virtue of being exactly solvable, and so can describe the competition between the different energy scales in a quantitative manner. We consider the Sachdev-Ye-Kitaev (SYK) type of models [1, 42], which are a rare class of solvable models leading to non-Fermi liquid phases [15]. Models in this class have been recently studied in different contexts of strongly correlated systems. In this work we consider a model of electrons with an attractive on-site interaction. In the spirit of SYK models, we consider random and all-to-all hopping, exchange interaction, and Cooper-pair hopping. This model was previously considered by us and for weak interaction an anomalous metal phase (or a Bose metal) was shown to exist [155] in the proximity of superconducting phase. In this work our focus is on the superconducting phase, and the associated thermal phase transition. Depending on the relative strength of the hopping amplitude and exchange interaction, the normal state at higher temperatures is either a FL or a NFL. Thus our model allows us to systematically investigate the emergence of superconductivity by continuously tuning between FL and NFL normal states. Moreover, we show that SC emerging from a NFL has certain unique features in the spectral function that are absent in the case of a FL-SC transition.

There have been previous studies of superconductivity in SYK models [156–164]. However, our model is distinct from the previously considered models. In our model in (5.18), we start with a SU(2) spin symmetry (see H_J in (5.20)), just as in the original Sachdev-Ye (SY) model

[1]. In previous models the random and all-to-all SYK term is in general not SU(2) symmetric: in Refs. [156, 157] a general Hamiltonian of two coupled SYK models is considered, which has a SU(2) symmetry only at a special point ($\alpha = 1/4$ in the notation used in Ref. [156]), and it corresponds to the zero hopping limit with $U = t = L = 0$ in our model. However, it is shown in Refs. [156, 157] that at this SU(2) symmetric point there is no superconductivity, which is consistent with our results. Ref. [159] also examined models without any hopping, but did examine finite N corrections. The models of Refs. [161, 162] are related to the one examined here, but with lattice rather than random matrix hopping: the lattice dispersions and all-to-all random hopping for electrons lead to equations with similar solutions [15]. Because of the simpler form of our equations, we are able to present spectral functions within the superconducting phase across the full range of the crossover between the FL and NFL cases.

The plan of the paper is as follows. In Sec. 5.2 we first study SC in a simple model of attractive Hubbard model with random and all-to-all hopping. Then we introduce our model in Sec. 5.3 and discuss the saddle-point equations. These equations are solved to obtain the normal state and SC solutions in Sec. 5.4. Therein we discuss several observables. Finally we conclude in Sec. 5.5. Technical details are provided in Appendices.

5.2 Random matrix Bogoliubov-de Gennes theory

Before we dive into the actual model and its detailed analysis, let us first consider a simpler case. In this section we present a BCS theory of superconductivity for a Hubbard model with attractive on-site interaction U along with a random and all-to-all hopping. Our main purpose here is to introduce the formalism in a more familiar setting. Curiously, the spectral functions in the superconducting state in this simple model do not appear to have been obtained earlier, although there have been results for other quantities for finite N [165, 166].

We consider a model of electrons $c_{i\alpha}$, with $i = 1 \dots N$ a site index, and $\alpha = 1 \dots M$ a USp(M) index. We have thus enlarged the usual SU(2) spin symmetry. The USp(M) group,

M even, is defined by the set of $M \times M$ unitary matrices $\mathcal{U}$ such that

$$\mathcal{U}^T \mathcal{J} \mathcal{U} = \mathcal{J} \,, \tag{5.1}$$

where

$$\mathcal{J}_{\alpha\beta} = \mathcal{J}^{\alpha\beta} = \begin{pmatrix} & 1 & & & & \\ -1 & & & & & \\ & & & 1 & & \\ & & -1 & & & \\ & & & & \ddots & \\ & & & & & \ddots \end{pmatrix} \tag{5.2}$$

is the generalization of the ε tensor to $M > 2$. It is clear that $\mathrm{USp}(M) \subset \mathrm{SU}(M)$ for $M > 2$, while $\mathrm{USp}(2) \cong \mathrm{SU}(2)$. We will consider SYK-like models on N sites with $\mathrm{USp}(M)$ symmetry, and take the $N \to \infty$ limit followed by the $M \to \infty$ limit. We don't expect the large M limit to significantly modify the results, as discussed in Ref. [15]; the large N limit is more significant, and there can additional phases at finite N, as discussed in Refs. [159, 163].

We shall calculate the electron spectral density using a set of saddle-point equations, which we derive below. We consider an attractive Hubbard model on a random hopping matrix with the Hamiltonian,

$$H_{tU} = -\frac{1}{\sqrt{N}} \sum_{i<j} t_{ij} \left(c^\dagger_{i\alpha} c^\alpha_j + c^\dagger_{j\alpha} c^\alpha_i \right) + \sum_i \left[-\mu c^\dagger_{i\alpha} c^\alpha_i + \frac{U}{2M} \left| \mathcal{J}^{\alpha\beta} c^\dagger_{i\alpha} c^\dagger_{i\beta} \right|^2 \right] \,, \tag{5.3}$$

where t_{ij} is a *real* random number with zero mean and root-mean-square value t, N is the number of sites, μ is the chemical potential and $U < 0$ is the attractive on-site interaction. In terms of the electron annihilation (creation) operator, $c_\alpha (c^\dagger_\alpha)$, the number operator $n_\alpha = c^\dagger_\alpha c_\alpha$.

We perform a disorder average to obtain the following action:

$$
\begin{aligned}
\overline{\mathcal{S}} \;=\; & \sum_i \int d\tau \left[c^{\dagger}_{i\alpha}(\tau) \left(\frac{\partial}{\partial \tau} - \mu \right) c^{\alpha}_{i}(\tau) + \frac{U}{2M} \left| \mathcal{J}^{\alpha\beta} c^{\dagger}_{i\alpha}(\tau) c^{\dagger}_{i\beta}(\tau) \right|^2 \right] \\
& + \frac{t^2}{2N} \int d\tau d\tau' \left[\left| \sum_i c^{\dagger}_{i\alpha}(\tau) c^{\beta}_{i}(\tau') \right|^2 - \left| \sum_i c^{\dagger}_{i\alpha}(\tau) c^{\dagger}_{i\beta}(\tau') \right|^2 \right] \,, \qquad (5.4)
\end{aligned}
$$

where τ is the imaginary time. Note that we have ignored here the replica indices as they are not significant for the present discussion. Next, we proceed by the G-Σ method used for SYK models. We introduce the normal and anomalous Green's functions G and F respectively, as well as the normal and anomalous self energies Σ and Φ respectively. We can then write the path integral as

$$
\mathcal{Z}_{tU} = \int \mathcal{D}G\mathcal{D}F\mathcal{D}\Sigma\mathcal{D}\Phi\mathcal{D}c \, \exp(-\mathcal{S}_0 - \mathcal{S}_1) \,, \qquad (5.5)
$$

where, initially, the role of the self energies is to impose delta functions which define the Green's functions as two-point fermion correlators. Let us now look at the two contributions in the action. First we have,

$$
\begin{aligned}
\mathcal{S}_0 \;=\; & \int d\tau \sum_i c^{\dagger}_{i\alpha}(\tau) \left(\frac{\partial}{\partial \tau} - \mu \right) c^{\alpha}_{i}(\tau) + \int d\tau d\tau' \Sigma(\tau, \tau') \left[\sum_i c^{\dagger}_{i\alpha}(\tau) c^{\alpha}_{i}(\tau') - NMG(\tau', \tau) \right] \\
& + \int d\tau d\tau' \frac{\Phi(\tau, \tau')}{2} \left[\mathcal{J}^{\alpha\beta} \sum_i c^{\dagger}_{i\alpha}(\tau) c^{\dagger}_{i\beta}(\tau') + NMF^*(\tau, \tau') \right] \\
& - \int d\tau d\tau' \frac{\Phi^*(\tau, \tau')}{2} \left[\mathcal{J}_{\alpha\beta} \sum_i c^{i\alpha}(\tau) c^{\beta}_{i}(\tau') - NMF(\tau, \tau') \right] . \qquad (5.6)
\end{aligned}
$$

For the interaction terms in (5.4), we need to introduce additional Hubbard-Stratonovich terms which decouple the quartic fermion interactions, and then use the large M limit to replace these fields by their saddle-point values. This procedure has been carried out explicitly for a related model in Ref. [167], and we do not display the intermediate steps here. Assuming the saddle-point has USp(M) symmetry, we can obtain the final answer more directly simply by the following identifications in the interaction terms:

$$
\begin{aligned}
c^{\dagger}_{\alpha}(\tau) c^{\beta}(\tau') &\Rightarrow \delta^{\beta}_{\alpha} G(\tau', \tau)\,, \\
c^{\alpha}(\tau) c^{\beta}(\tau') &\Rightarrow -\mathcal{J}^{\alpha\beta} F(\tau, \tau')
\end{aligned}
\tag{5.7}
$$

In this manner we obtain the second contribution in the action,

$$
\frac{\mathcal{S}_1}{NM} = \frac{U}{2} \int d\tau \, |F(\tau,\tau)|^2 + \frac{t^2}{2} \int d\tau d\tau' \left[G(\tau,\tau') G(\tau',\tau) - F(\tau,\tau') F^*(\tau',\tau) \right] . \tag{5.8}
$$

Now we take the variational derivative of the action with respect to G and F^*, and obtain the saddle-point equations,

$$
\begin{aligned}
\Sigma(\tau,\tau') &= t^2 G(\tau,\tau')\,, \\
\Phi(\tau,\tau') &= -U F(\tau,\tau) \delta(\tau - \tau') + t^2 F(\tau,\tau')\,.
\end{aligned}
\tag{5.9}
$$

These equations have to be supplemented by the Dyson equations obtained from the single-site action for the fermions, which follows from the first 2 spin components of the action $\mathcal{S}_0$,

$$
\mathcal{S}_c = T \sum_{\omega} \left(c^{\dagger}_{\uparrow}(i\omega), c_{\downarrow}(-i\omega) \right) \begin{pmatrix} -i\omega - \mu + \Sigma(i\omega) & \Phi(i\omega) \\ \Phi^*(i\omega) & -i\omega + \mu - \Sigma(-i\omega) \end{pmatrix} \begin{pmatrix} c_{\uparrow}(i\omega) \\ c^{\dagger}_{\downarrow}(-i\omega) \end{pmatrix} , \tag{5.10}
$$

where T is the temperature. We can now write down the combined saddle point equations,

$$
\begin{aligned}
G_\Sigma(i\omega) &\equiv \frac{1}{i\omega + \mu - \Sigma(i\omega)}\,, \\
\Sigma(i\omega) &= t^2 G(i\omega) = t^2 \frac{[G_\Sigma(-i\omega)]^{-1}}{|\Phi(i\omega)|^2 + [G_\Sigma(i\omega)G_\Sigma(-i\omega)]^{-1}}\,, \\
\Delta &= -UT\sum_\omega \frac{\Phi(i\omega)}{|\Phi(i\omega)|^2 + [G_\Sigma(i\omega)G_\Sigma(-i\omega)]^{-1}}\,, \\
F(i\omega) &= \frac{\Phi(i\omega)}{|\Phi(i\omega)|^2 + [G_\Sigma(i\omega)G_\Sigma(-i\omega)]^{-1}}\,, \\
\Phi(i\omega) &= \Delta + t^2 F(i\omega)\,.
\end{aligned}
\tag{5.11}
$$

The normal and anomalous Green's function in the superconducting state are $G(i\omega)$ and $F(i\omega)$ along the Matsubara frequency axis, while $G_\Sigma(i\omega)$ is an intermediate quantity defined for notational convenience; $G(i\omega) = G_\Sigma(i\omega)$ only in the normal state where $\Delta = F(i\omega) = 0$.

It is useful to first solve these equations in the normal state solution by setting $\Delta = F(i\omega) = 0$, which yields for $\mu < 2t$

$$
G(i\omega) \equiv G_0(i\omega) = \frac{i\omega + \mu}{2t^2} - i\frac{\mathrm{sgn}(\omega)}{2t^2}\sqrt{4t^2 + (\omega - i\mu)^2}\,, \tag{5.12}
$$

where the sign in front of the square-root is discontinuous across the real frequency axis, and is chosen so that $G_0(z) \sim 1/z$ as $|z| \to \infty$. This yields the expected semi-circle density of states.

Next, we can linearize the equations (5.11) in Δ at $T > 0$, and so obtain the superconducting critical temperature T_c. We find the condition

$$
1 = -UT\sum_{\omega_n} \frac{G_0(i\omega_n)G_0(-i\omega_n)}{1 - t^2 G_0(i\omega_n)G_0(-i\omega_n)}\,, \tag{5.13}
$$

with ω_n a Matsubara frequency. At small $|\omega_n|$ we obtain from (5.12) that

$$
t^2 G_0(i\omega_n)G_0(-i\omega_n) = 1 - \frac{2|\omega_n|}{\sqrt{4t^2 - \mu^2}} + \mathcal{O}(\omega_n^2)\,. \tag{5.14}
$$

We can now observe that the denominator in (5.13) has a singularity at $\omega_n = 0$, which yields the BCS log divergence. This implies that there is superconductivity at $T = 0$ for infinitesimal negative U.

We can analytically solve Eqs. (5.11) at $T = 0$ to linear order in Δ for general μ. Such a solution will be valid for $|\omega|, \sqrt{4t^2 - \mu^2} \gg \Delta$. We find,

$$
\begin{aligned}
F(i\omega) &= \Delta \frac{\left(\sqrt{4t^2 + (\omega - i\mu)^2} + \sqrt{4t^2 + (\omega + i\mu)^2} - 2|\omega|\right)}{4|\omega|} + \mathcal{O}(\Delta^3)\,, \\
G(i\omega) &= G_0(i\omega) + \mathcal{O}(\Delta^2)\,.
\end{aligned}
\tag{5.15}
$$

Note that $F(i\omega)$ is a real and even function of ω along the imaginary frequency axis. However, neither F nor G are analytic at $\omega = 0$. Similarly, we can see that $G(-i\omega) = G^*(i\omega)$, and for $\mu = 0$ $G(i\omega)$ is purely imaginary, with $G(-i\omega) = -G(i\omega)$.

At $\mu = 0$, the exact solution of the saddle-point equations in (5.11) is

$$
\begin{aligned}
G(i\omega) &= -\frac{i\omega}{2t^2}\left(\frac{\sqrt{\omega^2 + 4t^2 + \Delta^2}}{\sqrt{\omega^2 + \Delta^2}} - 1\right)\,, \\
F(i\omega) &= \frac{\Delta}{2t^2}\left(\frac{\sqrt{\omega^2 + 4t^2 + \Delta^2}}{\sqrt{\omega^2 + \Delta^2}} - 1\right)\,.
\end{aligned}
\tag{5.16}
$$

Analytic continuation gives the spectral function, $A(\omega) \equiv -\frac{1}{\pi}\,\mathrm{Im}\,G(\omega + i\delta)$,

$$
A(\omega) = \frac{|\omega|}{2\pi t^2}\frac{\sqrt{4t^2 + \Delta^2 - \omega^2}}{\sqrt{\omega^2 - \Delta^2}}\,, \quad \Delta < |\omega| < \sqrt{\Delta^2 + 4t^2}\,. \tag{5.17}
$$

The spectral function is plotted in Figure 5.1a, along with the numerical results obtained by exact diagonalization of random realizations of the Hamiltonian in (5.3). As expected, the gap is centered at $\omega = 0$, between Δ and $-\Delta$. It is also straightforward to obtain the imaginary part of the retarded anomalous Green's function, which is shown in Figure 5.1c. For $\mu \neq 0$ an analytic solution is no longer possible, and we show numerical results in Figs. 5.1b,d.

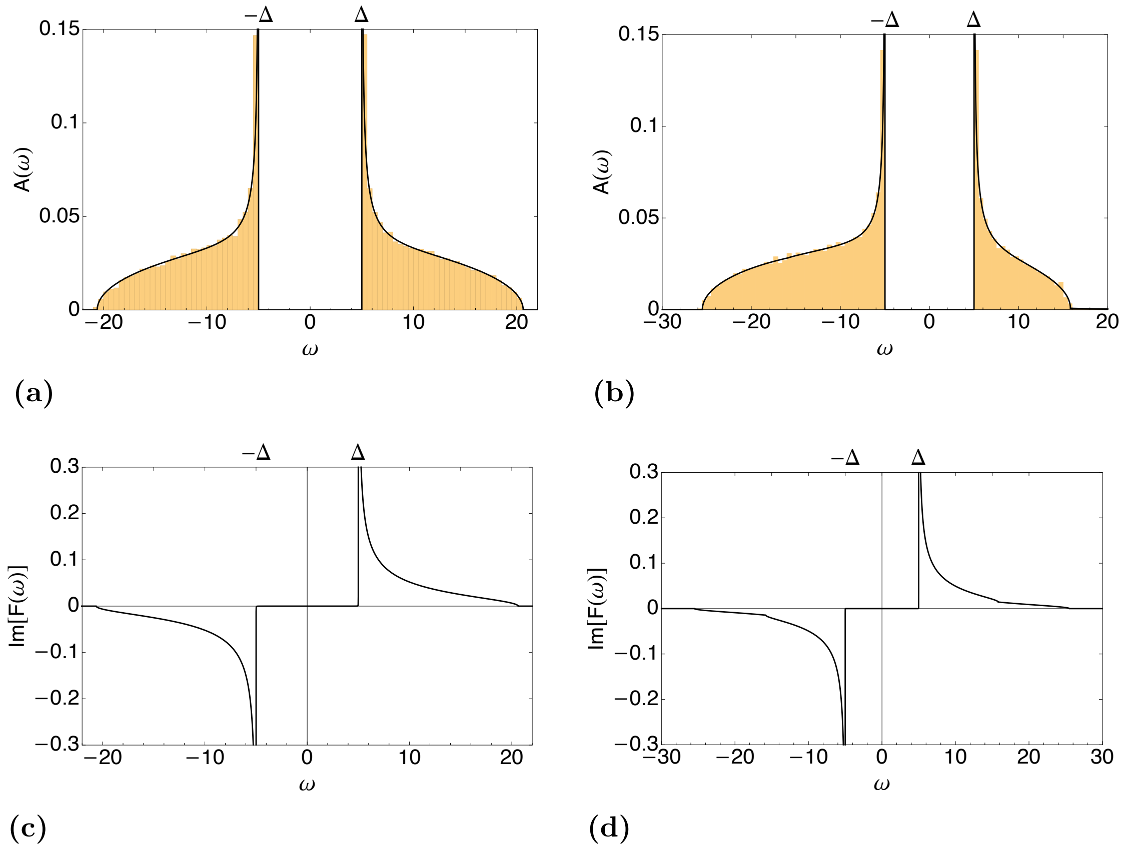

Figure 5.1: (a) The spectral function, $A(\omega)$, of the normal Green's function in the SC phase at a fixed Δ for the particle-hole symmetric case ($\mu = 0$). The solid line is exact solution to the saddle point equations Eqs. (5.11), and the yellow bars are obtained by averaging exact diagonalizations of random instances of (5.3). (b) Same as (a) but $\mu = 5$. (c) Imaginary part of the anomalous Green's function $F(\omega)$ in the SC phase at a fixed Δ and $\mu = 0$. (d) Same as (c) with $\mu = 5$. In all the plots, $t = 10$ and $\Delta = 5$.

5.3 Model

Having discussed the basic set-up we are now ready to discuss our model. To the random Hubbard model considered in the previous section, we will now add random and all-to-all spin exchange and Cooper-pair hopping terms. So the full Hamiltonian is

$$H = H_{tU} + H_J + H_L\,, \tag{5.18}$$

$$H_{tU} = -\frac{1}{\sqrt{N}}\sum_{i<j} t_{ij}\left(c^{\dagger}_{i\alpha}c^{\alpha}_{j} + c^{\dagger}_{j\alpha}c^{\alpha}_{i}\right) + \sum_{i}\left[-\mu c^{\dagger}_{i\alpha}c^{\alpha}_{i} + \frac{U}{2M}\left|\mathcal{J}^{\alpha\beta}c^{\dagger}_{i\alpha}c^{\dagger}_{i\beta}\right|^2\right], \tag{5.19}$$

$$H_J = \frac{1}{\sqrt{NM}}\sum_{i<j} J_{ij}\, c^{\dagger}_{i\alpha}c^{\beta}_{i}c^{\dagger}_{j\beta}c^{\alpha}_{j}\,, \tag{5.20}$$

$$H_L = -\frac{1}{2\sqrt{NM}}\sum_{i<j} L_{ij}\mathcal{J}^{\alpha\beta}\mathcal{J}_{\gamma\delta}\left[c^{\dagger}_{i\alpha}c^{\dagger}_{i\beta}c^{\gamma}_{j}c^{\delta}_{j} + c^{\dagger}_{j\alpha}c^{\dagger}_{j\beta}c^{\gamma}_{i}c^{\delta}_{i}\right]. \tag{5.21}$$

Recall that we have solved H_{tU} in Sec. 5.2. H_J describes the exchange interaction of the original SY model [1], while H_L describes the random Cooper-pair hopping. In the above Hamiltonian, J_{ij} are real random numbers with zero mean value and root-mean-square value of J. Similarly, L_{ij} can be either real or complex random numbers with zero mean value and root-mean-square value of L.

For clarity, let us consider the contribution of individual terms in the Hamiltonian in (5.18). The first term, H_{tU}, in (5.19) was already dealt with in Sec. 5.2. Next, let us consider the contribution of H_J in (5.20) to the action of the full Hamiltonian. After averaging over Gaussian random variable J_{ij} the resulting action is

$$\overline{\mathcal{S}}_J = -\frac{J^2}{4NM}\int d\tau d\tau'\left|\sum_i c^{\dagger}_{i\alpha}(\tau)c^{\beta}_{i}(\tau)c^{\dagger}_{i\gamma}(\tau')c^{\delta}_{i}(\tau')\right|^2. \tag{5.22}$$

In the large M limit, we can use an identity analogous to (5.7),

$$c^{\dagger}_{\alpha}(\tau)c^{\beta}(\tau)c^{\dagger}_{\gamma}(\tau')c^{\delta}(\tau') \Rightarrow \delta^{\delta}_{\alpha}\delta^{\beta}_{\gamma}G(\tau,\tau')G(\tau',\tau) + \mathcal{J}^{\beta\delta}\mathcal{J}_{\alpha\gamma}F^{*}(\tau,\tau')F(\tau,\tau')\,. \tag{5.23}$$

Here we have dropped factorizations associated with equal-time Green's functions. Then the contribution to the action from the H_J term is $\mathcal{S}_J$ with,

$$\frac{\mathcal{S}_J}{NM} = -\frac{J^2}{4}\int d\tau d\tau'\left(\left[G(\tau,\tau')G(\tau',\tau)\right]^2 + \left|F(\tau,\tau')F(\tau',\tau)\right|^2\right). \tag{5.24}$$

Finally, let us consider the contribution from the random Cooper-pair hopping term, H_L, in (5.21). Averaging over real Gaussian random variable L_{ij} yields the action,

$$
\begin{aligned}
\overline{\mathcal{S}}_L \;=\; & -\frac{L^2}{8NM}\int d\tau d\tau' \mathcal{J}^{\alpha\beta}\mathcal{J}^{\mu\nu}\mathcal{J}_{\gamma\delta}\mathcal{J}_{\rho\sigma}\Bigg[\\
& \left(\sum_i c^\dagger_{i\alpha}(\tau)c^\dagger_{i\beta}(\tau)c^\rho_i(\tau')c^\sigma_i(\tau')\right)\left(\sum_j c^\dagger_{j\mu}(\tau')c^\dagger_{j\nu}(\tau')c^\gamma_j(\tau)c^\delta_j(\tau)\right) \\
& +\left(\sum_i c^\dagger_{i\alpha}(\tau)c^\dagger_{i\beta}(\tau)c^\dagger_{i\mu}(\tau')c^\dagger_{i\nu}(\tau')\right)\left(\sum_j c^\gamma_j(\tau)c^\delta_j(\tau)c^\rho_j(\tau')c^\sigma_j(\tau')\right)\Bigg] \quad (5.25)
\end{aligned}
$$

Note that the last term would be absent for complex L_{ij}. Now, we use large M identities similar to Eqs. (5.7) and (5.23), again dropping equal-time factorizations,

$$
\begin{aligned}
c^\dagger_\alpha(\tau)c^\dagger_\beta(\tau)c^\rho(\tau')c^\sigma(\tau') \;&\Rightarrow\; \left(\delta^\sigma_\alpha\delta^\rho_\beta-\delta^\rho_\alpha\delta^\sigma_\beta\right)\left[G(\tau,\tau')\right]^2 , \\
c^\dagger_\alpha(\tau)c^\dagger_\beta(\tau)c^\dagger_\mu(\tau')c^\dagger_\nu(\tau') \;&\Rightarrow\; \left(\mathcal{J}_{\alpha\nu}\mathcal{J}_{\beta\mu}-\mathcal{J}_{\alpha\mu}\mathcal{J}_{\beta\nu}\right)\left[F^*(\tau,\tau')\right]^2 . \qquad (5.26)
\end{aligned}
$$

The contribution of the H_L term to the action is $\mathcal{S}_L$ with,

$$
\frac{\mathcal{S}_L}{NM} = -\frac{L^2}{4}\int d\tau d\tau' \left(\left[G(\tau,\tau')G(\tau',\tau)\right]^2 + \left|F(\tau,\tau')F(\tau',\tau)\right|^2\right) , \qquad (5.27)
$$

having the same form as $\mathcal{S}_J$ in (5.24).

So finally, the action corresponding to the full Hamiltonian in (5.18) is

$$
\mathcal{S} = \mathcal{S}_0 + \mathcal{S}_1 + \mathcal{S}_J + \mathcal{S}_L \, , \qquad (5.28)
$$

with the terms $\mathcal{S}_0$ and $\mathcal{S}_1$ quoted in Eqs. (5.6) and (5.8) respectively, while the terms $\mathcal{S}_J$ and $\mathcal{S}_L$ are shown in Eqs. (5.24) and (5.27) respectively.

Putting everything together, the final saddle-point equations for the normal and anomalous equations are

$$G_\Sigma(i\omega) \equiv \frac{1}{i\omega + \mu - \Sigma(i\omega)}\,, \tag{5.29}$$

$$\Sigma(\tau,\tau') = t^2 G(\tau,\tau') - (J^2+L^2) G^2(\tau,\tau') G(\tau',\tau)\,, \tag{5.30}$$

$$G(i\omega) = \frac{[G_\Sigma(-i\omega)]^{-1}}{|\Phi(i\omega)|^2 + [G_\Sigma(i\omega)G_\Sigma(-i\omega)]^{-1}}\,, \tag{5.31}$$

$$\Delta = -UT\sum_\omega \frac{\Phi(i\omega)}{|\Phi(i\omega)|^2 + [G_\Sigma(i\omega)G_\Sigma(-i\omega)]^{-1}}\,, \tag{5.32}$$

$$F(i\omega) = \frac{\Phi(i\omega)}{|\Phi(i\omega)|^2 + [G_\Sigma(i\omega)G_\Sigma(-i\omega)]^{-1}}\,, \tag{5.33}$$

$$\Phi(\tau,\tau') = -UF(\tau,\tau)\delta(\tau-\tau') + t^2 F(\tau,\tau') + (J^2+L^2)F^2(\tau,\tau')F^*(\tau',\tau)\,. \tag{5.34}$$

Note that Eqs. (5.30) and (5.34) generalize the expressions in (5.9) upon the inclusion of the spin exchange and Cooper-pair hopping terms.

5.4 Numerical solutions

We shall now solve the the saddle-point equations (Eqs. (5.29-5.34)) at finite temperature and obtain the normal-state as well as SC solutions. For simplicity and clarity, we will focus on the $\mu = 0$ half-filling case, but the results are qualitatively similar for non-zero μ as we show at the end of this section. Hence, unless otherwise stated $\mu = 0$ throughout this section. We introduce the notation $\widetilde{J} = \sqrt{J^2+L^2}$ since the interactions J and L are on equal footing in the large-M limit, as seen from Eqs. (5.30) and (5.34). Furthermore, we will parameterize the hopping t and interaction $\widetilde{J}$ as

$$t = R\cos\theta\,, \quad \widetilde{J} = R\sin\theta\,, \tag{5.35}$$

where $R = \sqrt{t^2+\widetilde{J}^2}$, and the parameter $\theta \in [0,\pi/2]$ tunes between FL ($\theta = 0$) and SYK-NFL ($\theta = \pi/2$) limits. We will discuss results for different relative strengths with respect to U, i.e., different ratios $R/|U|$.

We solve the saddle-point equations, Eqs. (5.29)-(5.34), on the imaginary (Matsubara) frequency axis at finite temperature. The strategy is as follows. We first start with a free fermion normal Green's function, $G(i\omega_n) = (i\omega_n + \mu)^{-1}$, and a randomly chosen real function $F(i\omega_n)$, and iterate until we find a converged solution for the normal and anomalous Green's functions. The SC order parameter, $\Delta(T) = -U\mathcal{J}_{\alpha\beta}\langle c^\alpha c^\beta\rangle$, is then determined as a function of temperature. It is finite at low temperatures in the superconducting phase, and it vanishes in the normal state at higher temperature. The superconducting critical temperature, T_{sc}, is thus determined numerically using $\Delta(T \to T_{sc}^-) \to 0$. We will use the notation $\Delta_0 \equiv \Delta(T \to 0)$.

In both the normal and SC phases we also compute the spectral function. The spectral function is obtained by numerical analytic continuation of Matsubara Green's functions to the real frequency axis. More details regarding numerical analytic continuation are discussed in Appendix D.1.

5.4.1 Normal State

The normal-state equations with $\Delta = 0$ and $F = 0$ are the same as those in Refs. [69] and [44]. As stated earlier, in our model we tune the parameter θ, defined in (5.35), to go from FL to NFL normal states. At any given temperature T, the normal state is FL like for $\theta \lesssim \theta_{coh}$ and NFL-like for $\theta \gtrsim \theta_{coh}$, where θ_{coh} is defined by $T \sim T_{coh} = t^2/\widetilde{J} = R\cos\theta_{coh}\cot\theta_{coh}$.

In Figure 5.2 (a) we show the spectral function in the normal state. For the FL-like phase (smaller θ) we see the expected semi-circular spectral function, whereas for a NFL-like phase (larger θ) a pronounced peak at $\omega = 0$ is seen. This is consistent with earlier results obtained for a similar random model in Ref. [69].

Also, note that the FL-like normal state ($\theta < \theta_{coh}$) has the usual T^2 dependence of resistivity, while the NFL state ($\theta > \theta_{coh}$) has a linear-in-T resistivity. This is similar to the results obtained in Refs. [44, 69].

The cross-over between the FL and NFL normal states can be further characterized by

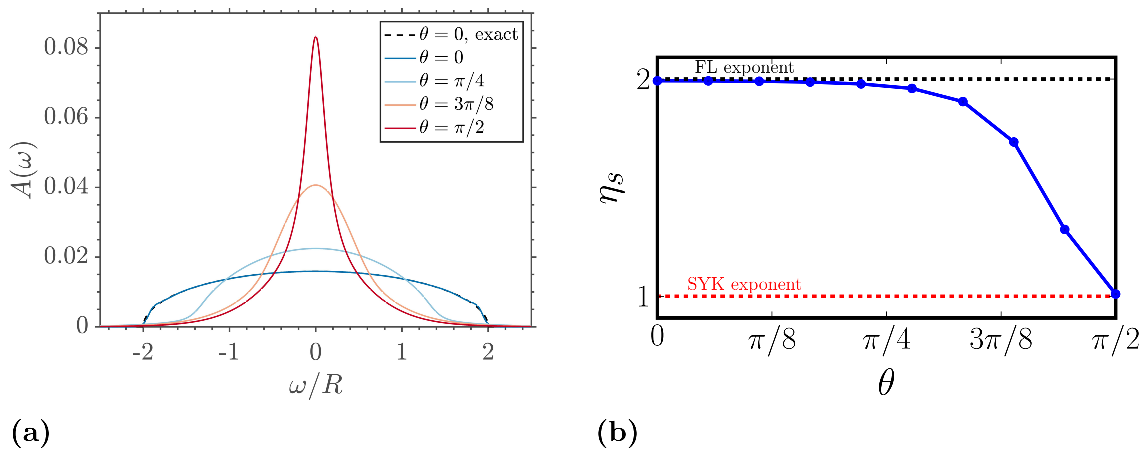

Figure 5.2: (a) The normal-state spectral function $A(\omega)$ for different values of θ at $\mu = 0$, and $R/|U| = 2$. The dashed line is the exact semi-circle solution for $\theta = 0$, as obtained in (5.12). (b) Effective spin exponent as a function of θ in the normal state at $R/|U| = 2$. The spin exponent takes the expected FL value for low θ, while it approaches the SYK value for larger θ.

looking at the effective spin exponent (η_s), which is shown in Figure 5.2 (b). This exponent is extracted from the dynamical susceptibility, $\chi''(\omega)$, which is the imaginary part of the spin correlation. In Appendix D.2 we discuss the details related to the evaluation of the spin exponent η_s. Clearly, for lower values of θ the spin exponent takes the value $\eta_s = 2$ expected for a disordered FL, while in the limit $\theta \to \pi/2$ it takes the value $\eta_s = 1$ corresponding to the marginal NFL. In the intermediate θ region η_s smoothly interpolates between these extreme values. As expected, this crossover is roughly around θ_{coh}.

5.4.2 Superconducting state

Before we discuss the numerical results, we first show analytically that SC phase exists at zero temperature for any infinitesimal attractive on-site interaction. The analysis is similar to that presented in Sec. 5.2. We determine the instability to the superconducting state by expanding the action to second order in $F(i\omega)$. This leads to the same condition for the instability as (5.13). But the important difference is that the Green's function now also contains contribution from the exchange interaction terms and satisfies the equations,

$$
\begin{aligned}
G_0(i\omega) &= \frac{1}{i\omega + \mu - \Sigma_{el}(i\omega) - \Sigma_{in}(i\omega)}\,, \\
\Sigma_{el}(i\omega) &= t^2 G_0(i\omega)\,, \\
\Sigma_{in}(\tau) &= -(J^2 + L^2)[G_0(\tau)]^2 G_0(-\tau)\,.
\end{aligned}
\tag{5.36}
$$

Note that we have separated the self energy into an 'elastic' part Σ_{el}, and an 'inelastic' part Σ_{in}. This is useful because $\mathrm{Im}\,\Sigma_{in}(\omega \to 0) = 0$ at $T = 0$, and that is not true for the elastic part.

From (5.36), we can write a quadratic equation for $G_0(0)$:

$$
t^2[G_0(0)]^2 - (\mu - \Sigma_{in}(0))G_0 + 1 = 0\,. \tag{5.37}
$$

An important point is that $\Sigma_{in}(0)$ is real, and so it can be absorbed into μ. This quadratic equation has two roots, and they correspond to $G_0(i0^+)$ and $G_0(i0^-)$. From the formula for the product of the roots of a quadratic equation we can therefore conclude that at $T = 0$,

$$
\lim_{\omega \to 0} G_0(i\omega)G_0(-i\omega) = \frac{1}{t^2}\,. \tag{5.38}
$$

So this equation holds even when J or L are non-zero, and the denominator in (5.13) vanishes. Thus indicating the presence of SC at $T = 0$.

Let us now discuss the numerical results obtained by solving the saddle-point equations. For low enough temperature we find a SC solution with a non-zero Δ and $F(i\omega)$. In Figure 5.3 we have shown the variation of SC order parameter, Δ, with temperature. It turns out that for small values of θ, i.e., FL-like normal state, the SC-normal state transition is continuous. However, at larger values of θ, the phase transition (SC to NFL) becomes first order for larger values of $R/|U|$ (as seen in Figure 5.3 (a)). Note that although the absolute value of Δ and T_{sc} depends on the value of U, the variation of $\Delta/|U|$ as a function of $T/|U|$ depends only

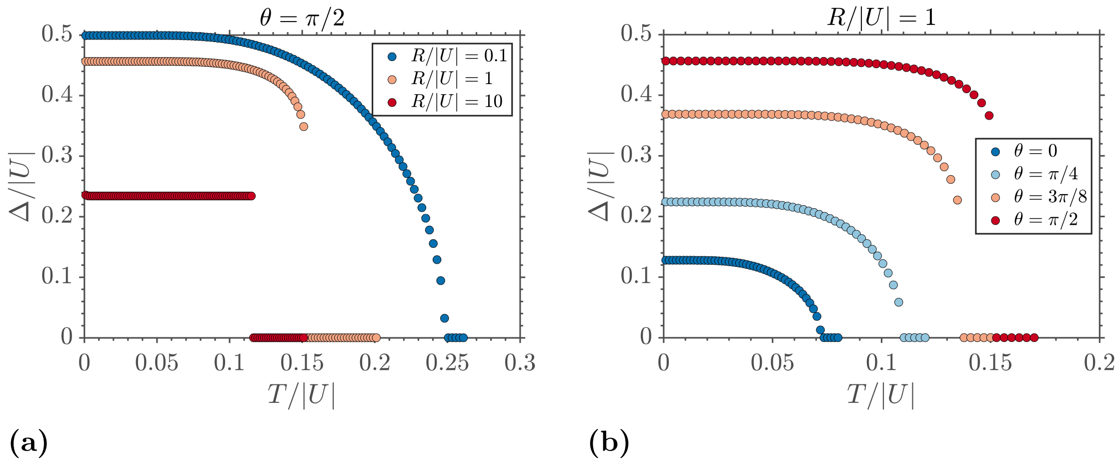

Figure 5.3: SC order parameter, Δ, as a function of temperature, T. (a) SYK-NFL ($\theta = \pi/2$) case with varying $R/|U|$. Note that for larger values of $R/|U|$ the phase transition becomes first order instead of a continuous transition. (b) Here $R = |U|$ is fixed and θ is varied.

on the ratio $R/|U|$.

In Figure 5.4, we show the variation of SC transition temperature (T_{sc}) as a function of θ for different values of $R/|U|$. For very large on-site interaction, i.e., for very small $R/|U|$ there is no difference between SC emerging from FL or NFL. This is because in this case both hopping as well as exchange interaction are sub-dominant. However, at larger values of the ratio $R/|U|$, i.e., weaker on-site interaction the SC transition temperature, T_{sc}, strongly depends on the nature of the normal state or θ. It is larger for NFL-SC transition (larger θ) as compared to the FL-SC transition (smaller θ). The same trend applies to the SC order parameter in the limit of zero temperature, Δ_0, and the SC gap (as obtained from the spectral function) in the $T \to 0$ limit, $\widetilde{\Delta}_0$, as seen in Figure 5.5. Recall that in our model SC phase corresponds to the condensation of doublon, *i.e.*, the Cooper pairs are on the same site. A single-particle hopping tends to break these pairs and destroy SC. The exchange interaction and Cooper-pair hopping have a very weak effect in destruction of SC. Therefore, T_{sc}, Δ_0, and $\widetilde{\Delta}_0$ have very weak dependence on θ for larger on-site interaction (smaller $R/|U|$), as in this case the relative strength of hopping and spin-exchange is unimportant. On the other

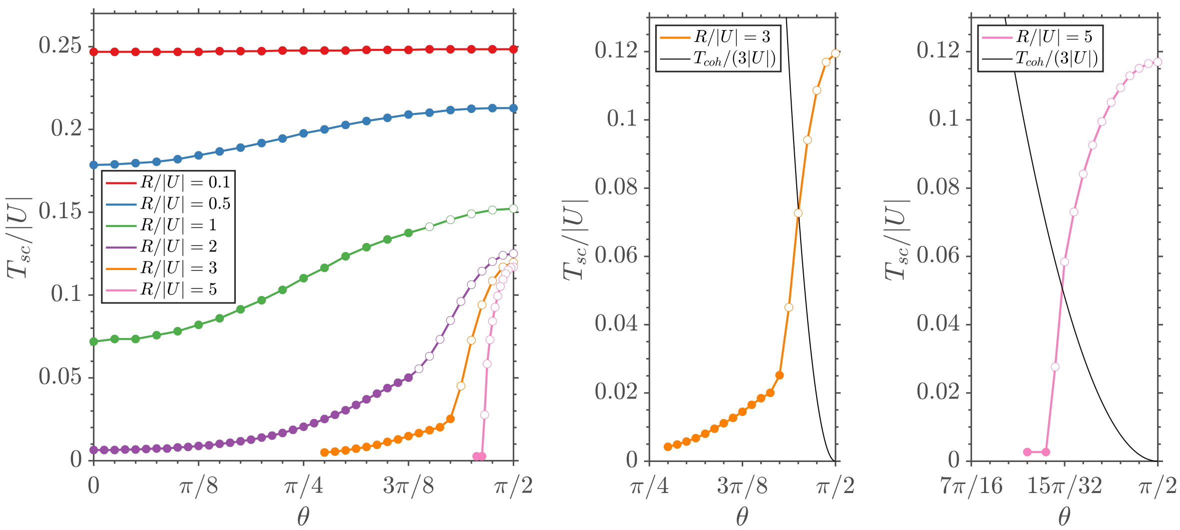

(a) **(b)** **(c)**

Figure 5.4: (a) The SC transition temperature, T_{sc}, as a function of θ for different values of $R/|U|$. Qualitatively, the phase transition becomes first order (indicated by open circles) at larger values of $R/|U|$ and θ instead of a continuous transition (indicated by filled circles). (b) Comparison of T_{sc} and $T_{coh}/3 = t^2/3J = (1/3)R\cos\theta\cot\theta$ at $R/|U| = 3$. For larger values of $R/|U|$ the transition becomes first order for $\theta \gtrsim \theta_{coh}$. (c) Same as (b) but $R/|U| = 5$.

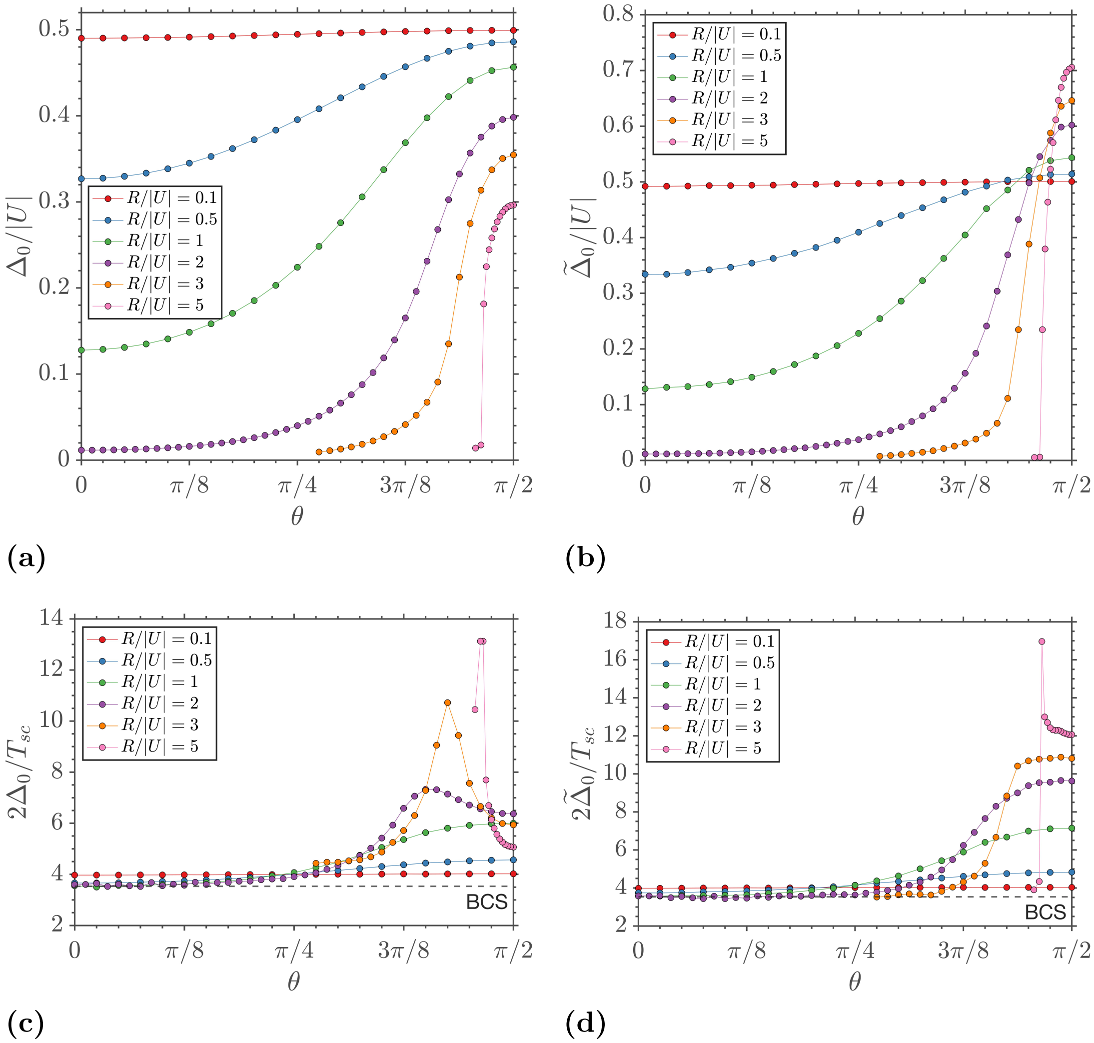

Figure 5.5: (a) The variation of SC order parameter in the zero temperature limit, Δ_0, with θ for different values of the ratio $R/|U|$. (b) The SC gap observed in the spectral function in the zero temperature limit, $\widetilde{\Delta}_0$, as a function of θ. (c) The ratio $2\Delta_0/T_{sc}$. (d) The ratio $2\widetilde{\Delta}_0/T_{sc}$. For larger values of θ, these ratios deviate strongly away from the BCS value of 3.53. As $\theta \to 0$ and $R/|U| \gg 1$, both $2\Delta_0/T_{sc}$ and $2\widetilde{\Delta}_0/T_{sc}$ tend to the BCS result.

hand, for weaker on-site interaction the relative strength of hopping, t, compared to $\widetilde{J}$ is important. Hence for larger θ (weaker t) SC is more stable leading to a higher T_{sc}. This is also the reason why the SC-NFL transition becomes first order in nature for larger $R/|U|$.

We have also calculated the ratio $2\Delta_0/T_{sc}$ and $2\widetilde{\Delta}_0/T_{sc}$, which is 3.53 for the BCS superconductivity (for FL-SC there is no difference between Δ_0 and $\widetilde{\Delta}_0$ as discussed below). This is shown in Figs. 5.5 (c) and (d). We find that in our case, this ratio approaches the BCS value for smaller θ (FL normal state) and weaker on-site interaction. For SC emerging from NFL normal state this ratio deviates strongly from the BCS value. The value of this ratio first increases with θ as long as the transition is continuous, and then tends to decrease as the transition changes its nature to first order. This trend follows from the observation that the transition temperature increases very sharply for large values of θ and $R/|U|$ compared to the much gradual increase in Δ_0. In the FL case (smaller θ), both Δ_0 and T_{sc} are suppressed exponentially as a function of $R/|U|$ such that their ratio is a constant. However, in the NFL case (larger θ) this is not true anymore. Both Δ_0 and T_{sc} appear to decrease with different power-laws with respect to $R/|U|$, and in particular for larger values of θ the transition temperature, T_{sc}, saturates quickly for large θ. This is shown in Figure D.3 in the Appendix.

We have also computed the spectral function for the SC phase. This is shown in Figure 5.6. As expected, we clearly see the SC gap in the spectral function. For $\theta = 0$ (FL normal state) we see the expected square-root divergence near $\omega = \Delta$. The form of this divergence seems to be modified for θ away from zero. In particular, for $\theta = \pi/2$ (SYK-NFL normal state) we see very narrow peaks. We also note that the SC gap ($\widetilde{\Delta}$) observed in the spectral function may not be the same as SC order parameter Δ calculated above, as is shown in Figure 5.5 (a) and (b). The two quantities are same for SC emerging from FL (smaller θ), but may deviate from each other for the SC emerging from a NFL phase (larger θ). In particular, the deviation between Δ and $\widetilde{\Delta}$ is strongest for larger θ and larger values of $R/|U|$ (where the transition is of first order). In Figure 5.8 (a), we show the variation of the ratio of these two quantities in the limit of zero temperature, i.e. $\widetilde{\Delta}_0/\Delta_0$, with respect to θ and $R/|U|$. We do

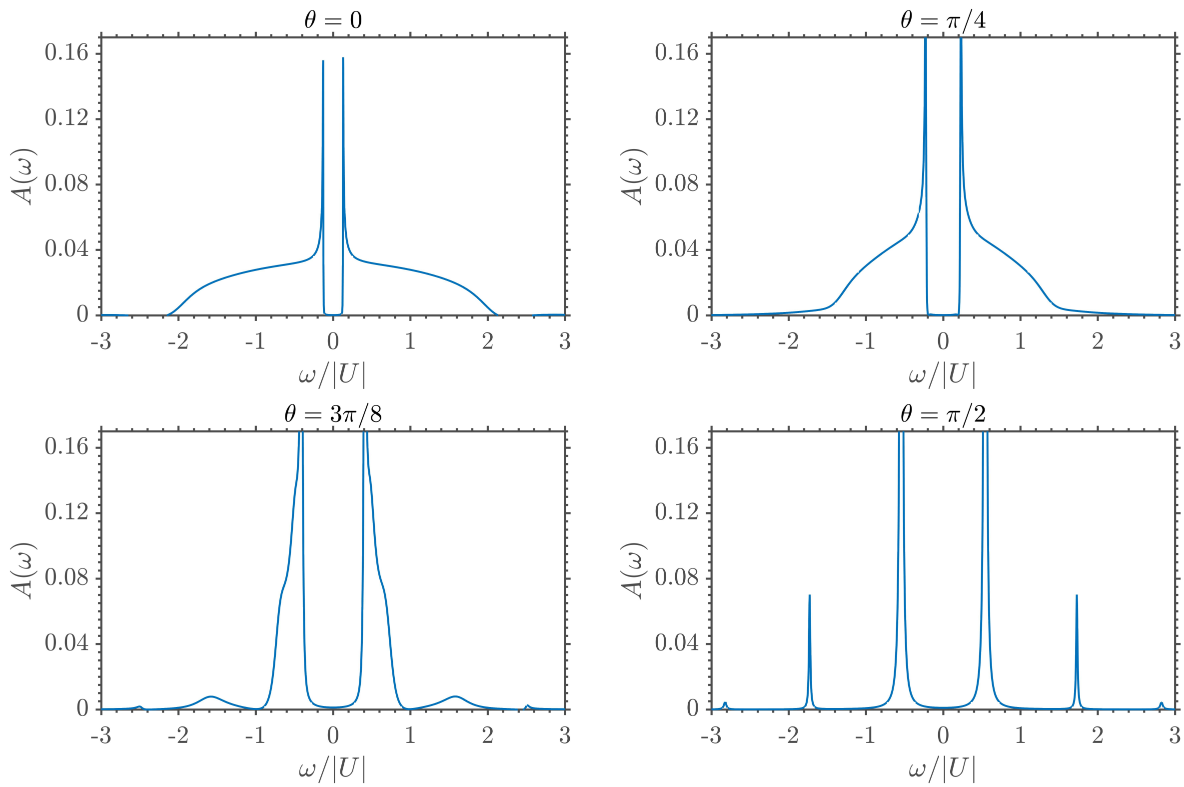

Figure 5.6: The spectral functions in the superconducting phase at $R = |U|$ for different values of θ.

not have an analytic expression for the gap in the spectral function, $\widetilde{\Delta}$. But numerically we find that $\Delta_0 + \widetilde{\Delta}_0 \approx |U|$ at $\theta = \pi/2$, independent of the ratio $R/|U|$. This relation does not hold for other values of θ. This is shown in Figure 5.8 (b).

A noticeable new feature for SC emerging from NFL (larger values of θ) is the presence of peaks at higher energies compared to the SC gap (see Figure 5.6 (c) and (d)). In the limit of $T \to 0$ the first higher-order peak appears at $\sim 3\widetilde{\Delta}$. A dominant all-to-all exchange interaction (large θ) means strongly interacting Cooper pairs, which may be the reason for these additional peaks. For smaller values of θ the Cooper pairs are weakly interacting. Note that such high energy features in the spectral function have also been reported for SYK-like electron-phonon model for SC [160].

We have so far focused on the particle-hole symmetric point, $\mu = 0$, for clarity. However, it is straightforward to also do the same analysis for a non-zero chemical potential. The results are qualitatively the same as discussed above. The main difference seen is the particle-hole asymmetric distribution of the spectral weights at positive and negative frequencies, as shown in Figure 5.7. The gap is however symmetric around $\omega = 0$. In the remainder of the paper we again focus only on $\mu = 0$.

We further also compute the spin correlation in the SC phase. In Figure 5.9 we plot $\chi''(\omega)$ for different values of θ in the SC phase. The features essentially follow from what was discussed for the electron spectral function earlier. The high-energy peak present in the electron spectral function at larger values of θ is also seen in $\chi''(\omega)$.

Using $\chi''(\omega)$ we can also evaluate the temperature dependence of the NMR relaxation rate, $1/T_1$, which we show in Figure 5.10. The NMR relaxation rate is given by the following relation [69]:

$$\frac{1}{T_1} = T \left. \frac{\chi''(\omega)}{\omega} \right|_{\omega=0} . \tag{5.39}$$

Recall that for the standard BCS superconductor one expects a peak (often referred to as the 'Hebel-Slichter' peak) around the critical temperature as a consequence of the square-root divergence in the spectral function [168]. However, one of the signatures of the unconventional

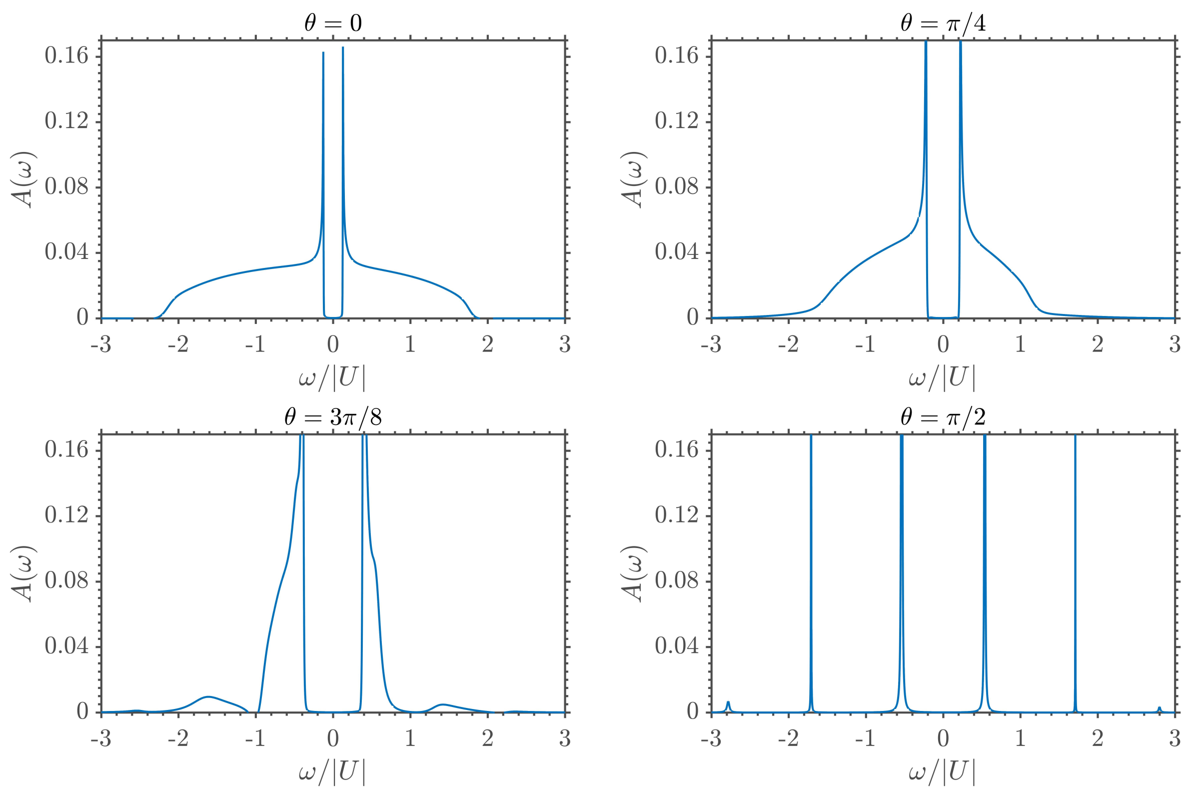

Figure 5.7: The spectral functions in the superconducting phase at $R = |U|$, $\mu/|U| = 0.2$ for different values of θ.

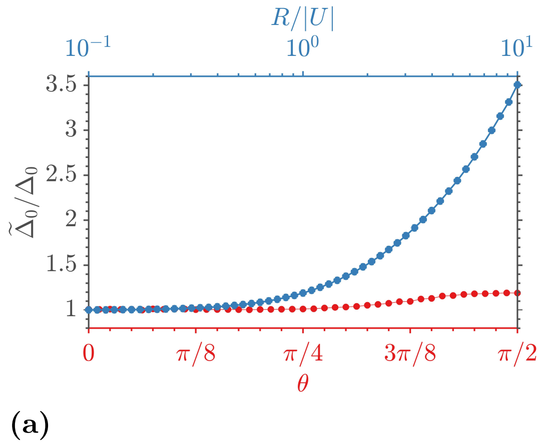

Figure 5.8: (a) In the limit of zero temperature, the ratio of the SC gap, $\widetilde{\Delta}_0$, (as obtained from the spectral function) and the SC order parameter, Δ_0, as a function of $R/|U|$ at $\theta = \pi/2$ (blue) and as a function of θ at $R/|U| = 1$ (red) is shown. The two quantities are in general different away from the FL limit and for small on-site interaction the deviation between the two quantities is strongest. (b) The sum $\widetilde{\Delta}_0$ and Δ_0 as a function of $R/|U|$ at $\theta = \pi/2$ (blue) and as a function of θ at $R/|U| = 1$ (red) is shown. The sum is a constant for $\theta = \pi/2$. However, this is not the case for other values of θ.

superconductivity is the absence of 'Hebel-Slichter' peak, for instance, as observed in cuprates [169] and Fe-based superconductors [170]. We find that for a fixed $R/|U|$ when $\theta \lesssim \theta_{coh}$ there is a well distinguished 'Hebel-Slichter' peak whose strength diminishes with increasing θ (see Figure 5.10 (a) and (b)). After the crossover into the NFL regime for larger θ the peak is absent and there is only a *kink* around the critical temperature (see Figure 5.10 (c) and (d)). This is another distinguishing feature between the FL and NFL case. We also see that the relaxation rate is higher for the NFL case compared to the FL case. In the normal state this trend easily follows from the fact that the critical temperature is much higher in the NFL case. Also note that the height of the 'Hebel-Slichter' peak present for smaller θ is roughly inversely proportional to $R/|U|$, i.e., for smaller Hubbard interaction the peak is smaller.

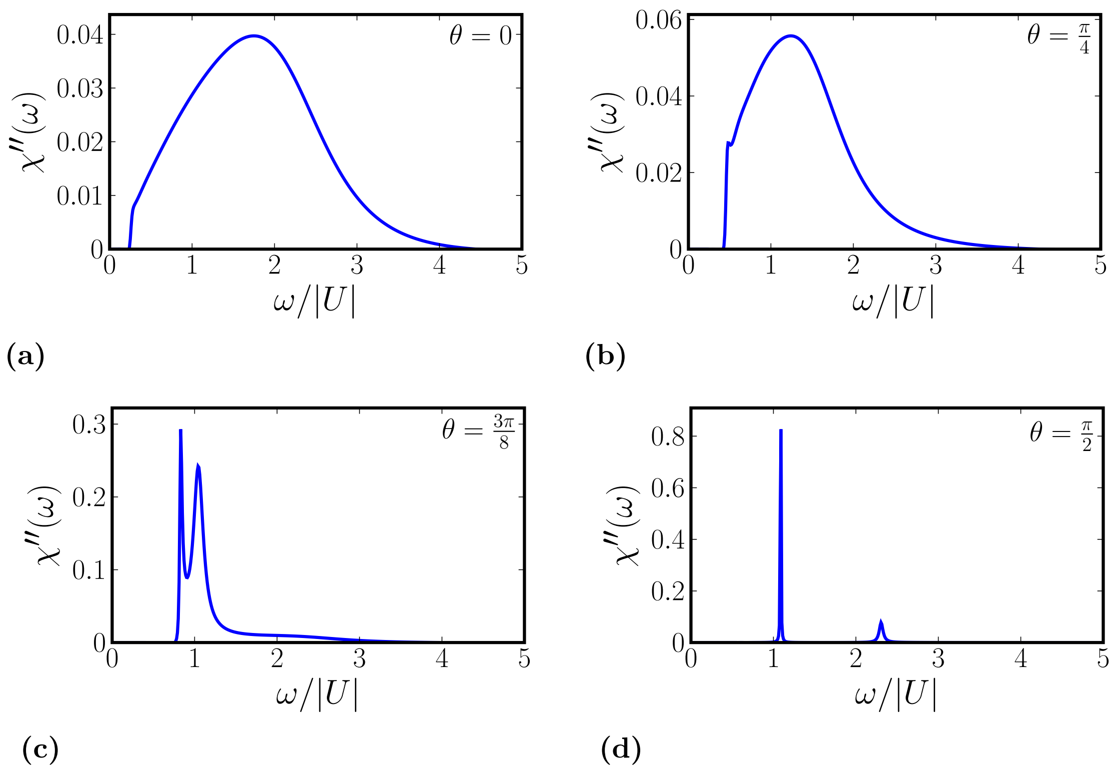

(a) **(b)** **(c)** **(d)**

Figure 5.9: Plot of imaginary part of spin correlation $\chi''(\omega)$ in the SC phase as a function of real frequency for different values of θ at $R = |U|$ and $T = 0.01$.

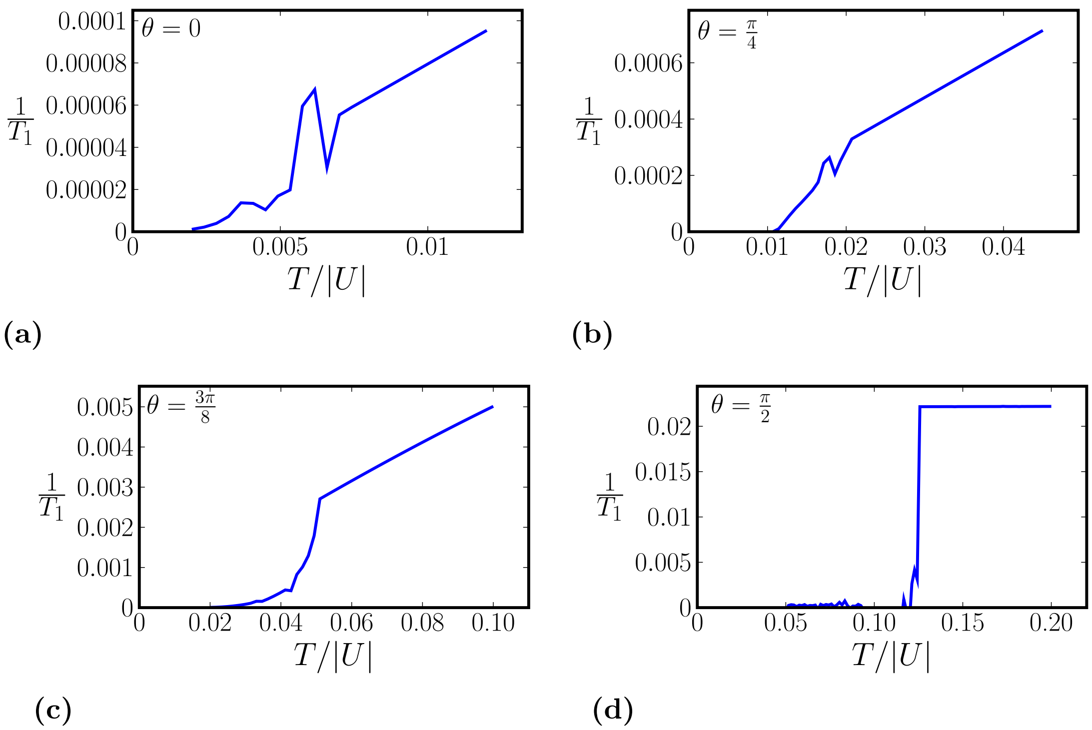

Figure 5.10: Temperature dependence of the NMR relaxation rate, $1/T_1$, for different values of θ at $R = 2|U|$. Note that for smaller values of θ, where the normal state is FL-like, there is a 'Hebel-Slichter' peak around the SC transition temperature. This can be seen in (a) around $T/|U| \sim 0.006$ and in (b) around $T/|U| \sim 0.018$, which have FL normal state. Note that the peak height diminishes as we increase θ and go closer to NFL case. The 'Hebel-Slichter' peak is absent (and replaced by a *kink*) in case of NFL normal state, shown in (c) and (d).

5.5 Discussion

We have investigated the emergence of SC in a SYK-like model of interacting electrons, (5.18). The model is solved in the large-M limit, where we generalize the spin symmetry from SU(2) to SU(M). The solution of the large-M saddle-point equations can be viewed as a dynamical mean-field solution. We have shown the contrast between the emergence of SC from a NFL as opposed to a FL normal state. Several distinguishing features are found for SC emerging from a NFL and we summarize below the salient features of our work.

- Even in the presence of all-to-all and random exchange interaction and Cooper-pair hopping, we show that BCS-type superconducting instability is present, thus ensuring SC ground state at zero temperature for any infinitesimal attractive Hubbard interaction.

- The SC transition temperature, T_{sc}, is shown to be strongly enhanced for NFL normal state as compared to a FL normal state. This is an important highlight of our results. This is understood physically by realizing that the most dominant mechanism to break Cooper pairs is single-particle hopping. However for the NFL case the Cooper pairs are strongly interacting, and single-particle hopping is sub-dominant, thus leading to a higher T_{sc}. This also renders the transition in case of NFL to be first order for weaker Hubbard interaction.

- While for the FL (BCS-like) case both T_{sc} and Δ are exponentially suppressed with respect to $R/|U|$, we show that for NFL case they decay with different power-laws. Consequently, the ratio $2\Delta/T_{sc}$ strongly deviates from the BCS value for SC arising from NFL.

- We have presented a detailed study of the local electron spectral function in the SC as well as the normal states (FL and NFL). This is an observable in photoemission experiments like ARPES. We discuss how the SC gap closes upon approaching T_{sc}.

In the case of a FL normal state the transition is continuous and BCS like, and the spectral function in SC phase features the well-known square-root divergence at $\omega = \Delta$. We show that this is not the case when the normal state is a NFL.

- We show that for SC emerging from a NFL there is a distinct new feature in the local electron spectral function – peaks at higher energy at $\omega \sim 3\Delta$. This is a consequence of strong interactions between Cooper pairs (which is absent in case of FL normal state). We believe that this is a generic feature of SC emerging from a NFL, and could be a relevant observation in many materials. How generic and model independent is this feature is an interesting open question for future.

- In the normal state, as a function of the parameter θ, there is a crossover between FL and NFL phase for a fixed temperature, which we characterize using the effective local spin correlation exponent, η_S. The exponent deviates from FL value for $\theta \gtrsim \theta_{coh}$. We hope that our work motivates the observation of this exponent in neutron scattering experiments.

- We also note that NFL phase, i.e., the normal state for $\theta > \theta_{coh}$ has a linear-in-temperature resistivity. Thus SC emerging from this state may have some relevance to the situation in correlated systems.

- We have evaluated the local dynamic structure factor, $\chi''(\omega)$, an observable in neutron scattering experiments. In the SC phase emerging from NFL $\chi''(\omega)$ shows distinct peaks at high energies akin to that discussed for the spectral function.

- Further we have also calculated the NMR relaxation rate, $1/T_1$, as a function of temperature. Here we show that for FL normal state there is a 'Hebel-Slichter' peak near T_{sc}, which is a hallmark of BCS SC. However for NFL case this peak disappears and the transition temperature is marked by a *kink*. Such observations have been reported in experiments on unconventional SC in cuprates and pnictides. Our work clearly shows the mechanism for the disappearance of the 'Hebel-Slichter' peak in the case of a NFL normal state. This may be of general relevance to the NMR experiments in unconventional SC materials.

We believe that our work will further motivate and provide a pathway to investigate SC emerging from NFL. Our work also motivates numerical investigation of the model in (5.18) at $M = 2$ to further elucidate the SC-NFL phase transition. We hope that our work may also provide a good starting point for constructing more realistic lattice models.

While this work was being completed, we learnt of the study Ref. [163] of essentially the same model, but with a focus on the finite N behavior.

6

Strange metal and superconductor in the two-dimensional Yukawa-SYK model

6.1 Introduction

Higher temperature superconductors of correlated electron materials all display a 'strange metal' phase above the critical temperature for superconductivity [15, 36]. This is a metallic phase of matter where the Landau quasi-particle approach breaks down. It is characterized most famously by a linear in temperature (T) electrical resistivity. We use the term strange metal only for those metals whose resistivity is smaller than the quantum unit (h/e^2 in $d = 2$ spatial dimensions). Metals with a linear-in-T resistivity which is larger than the quantum unit are 'bad metals'.

An often quoted model for a strange or bad metal (*e.g.* [171]) is one in which there is a large density of states of low energy bosonic excitations, usually phonons, and then quasi-elastic scattering of the electrons off the bosons leads to linear-in-T resistivity from the Bose occupation function when T is larger than the typical boson energy. However, studies of the optical conductivity in the strange metal of the cuprates [172] show that the dominant scattering is inelastic, not quasi-elastic, and leads to a non-Drude power-law-in-frequency tail in the optical conductivity. The optical conductivity data has been incisively analyzed recently by Michon *et al.* [39]: they have shown that while transport scattering rate (related to the real part of the inverse optical conductivity) exhibits Planckian scaling behavior [36], there are significant logarithmic deviations from scaling in the frequency and temperature dependent effective transport mass (related to the imaginary part of the inverse optical conductivity). Furthermore, the optical conductivity data connects consistently with d.c. measurements of resistivity and thermodynamics.

In this paper we present a SYK-type self-consistent disorder averaging analysis of the Yukawa-Sachdev-Ye-Kitaev model of quantum phase transitions in a two-dimensional metal in the presence of impurity-induced disorder. We find results that displays all the key characteristics of the optical conductivity and d.c. resistivity described by Michon *et al.*. We also examine the instability of the strange metal to superconductivity, and present the evolution of the electron spectral function and superfluid density at $T < T_c$, the superconducting critical temperature. We show that the Yukawa-SYK exhibits the connection between scattering and pairing discussed by Taillefer [173], with a linear relation between T_c and the slope of the linear-T resistivity.

The Yukawa-SYK Model—Several recent works [25, 47, 48, 174–177] have argued that clean quantum critical metals cannot serve as a universal model for transport in a strange metals, and that impurity-induced spatial disorder is essential. We now present arguments that a SYK-type analysis of the Yukawa-SYK model $\mathcal{L}$ in (6.2) below describes a wide class of quantum critical metals over a significant intermediate temperature range. At very low T, there is a crossover to strong disorder physics with boson localization [178–180], where we cannot use a disorder-averaged analysis.

We consider the Hertz-Millis theory of a quantum phase transition in a metal associated with a Ising-nematic parameter ϕ [181] in the presence of spatial disorder which preserves the Ising symmetry [182, 183] *i.e.* no 'random field' disorder. Other order parameters, including those at non-zero wavevector, and Fermi-volume changing transitions without broken symmetries [184], also map to essentially the same Yukawa-SYK model [25]. We write the Hertz-Millis Lagrangian for ϕ and fermions ψ with dispersion $\varepsilon(\boldsymbol{k})$ and a Fermi surface at wavevectors $\boldsymbol{k}$ where $\varepsilon(\boldsymbol{k}) = 0$ (τ is imaginary time) in spatial dimension $d = 2$:

$$\begin{aligned}\mathcal{L}_{\rm HM} &= \psi_{\boldsymbol{k}}^{\dagger}\left(\frac{\partial}{\partial\tau} + \varepsilon(\boldsymbol{k})\right)\psi_{\boldsymbol{k}} + v(\boldsymbol{r})\psi^{\dagger}(\boldsymbol{r})\psi(\boldsymbol{r}) \\ &+ g\left(\psi^{\dagger}(\boldsymbol{r})[\mathcal{D}_{\boldsymbol{r}}\,\psi(\boldsymbol{r})] + [\mathcal{D}_{\boldsymbol{r}}\,\psi^{\dagger}(\boldsymbol{r})]\psi(\boldsymbol{r})\right)\phi(\boldsymbol{r}) \\ &+ K\left[\nabla_{\boldsymbol{r}}\phi(\boldsymbol{r})\right]^2 + [s + \delta s(\boldsymbol{r})]\left[\phi(\boldsymbol{r})\right]^2 + u\left[\phi(\boldsymbol{r})\right]^4 .\end{aligned} \tag{6.1}$$

The operator $\mathcal{D}_r = \partial_x^2 - \partial_y^2$ is special to the Ising-nematic case, and will be dropped for simplicity in our computations as it unimportant apart from 'cold spots' on the Fermi surface. The transition is tuned by varying the boson 'mass' s. $\mathcal{L}_{HM}$ contains the two sources of disorder most frequently considered. One is the potential $v(\boldsymbol{r})$ acting on the fermions:

- Spatially random potential $v(\boldsymbol{r})$ with $\overline{v(\boldsymbol{r})} = 0$, $\overline{v(\boldsymbol{r})v(\boldsymbol{r}')} = v^2\delta(\boldsymbol{r} - \boldsymbol{r}')$.

Its influence is familiar from the theory of weakly disordered metals [185], leading to marginally relevant localization effects on the fermions [185]. However, much more relevant is the disorder which couples directly to the boson leading to shifts in the local position of the quantum phase transition

- Spatially random mass $\delta s(\boldsymbol{r})$ with $\overline{\delta s(\boldsymbol{r})} = 0$, $\overline{\delta s(\boldsymbol{r})\delta s(\boldsymbol{r}')} = \delta s^2\delta(\boldsymbol{r} - \boldsymbol{r}')$.

This is a consequence of the violation of the Harris criterion $\nu > 2/d$ [186], where ν is the correlation length exponent, and the value $\nu = 1/2$ in $d = 2$. Consequently, it is important that the influence of $\delta s(\boldsymbol{r})$ be treated at the outset. This is also supported by a recent analysis of $v(\boldsymbol{r})$ disorder effects along the lines of Ref.[185] near quantum criticality [187] which found singular corrections to the boson propagator.

Inspired by various works [15] on making the SYK model more realistic, recent work [25] proposed the following approach. We can account for the strongly relevant spatial dependence of $\delta s(\boldsymbol{r})$ by rescaling ϕ to make the mass spatially uniform. But this rescaling induces disorder in the Yukawa coupling g [47, 188–194] (along with disorder in other less-important couplings that we drop) leading to the theory

$$\begin{aligned}\mathcal{L} = &\psi^\dagger_{\boldsymbol{k}} \left(\frac{\partial}{\partial \tau} + \varepsilon(\boldsymbol{k}) \right) \psi_{\boldsymbol{k}} + v(\boldsymbol{r}) \psi^\dagger(\boldsymbol{r}) \psi(\boldsymbol{r}) \\ &+ [g + g'(\boldsymbol{r})] \, \left(\psi^\dagger(\boldsymbol{r}) [\mathcal{D}_{\boldsymbol{r}} \, \psi(\boldsymbol{r})] + [\mathcal{D}_{\boldsymbol{r}} \, \psi^\dagger(\boldsymbol{r})] \psi(\boldsymbol{r}) \right) \, \phi(\boldsymbol{r}) \\ &+ K \, [\nabla_{\boldsymbol{r}} \phi(\boldsymbol{r})]^2 + s \, [\phi(\boldsymbol{r})]^2 + u \, [\phi(\boldsymbol{r})]^4, \end{aligned} \tag{6.2}$$

with the coupling $g'(\boldsymbol{r})$ obeying

- Spatially random Yukawa coupling $g'(\boldsymbol{r})$ with $\overline{g'(\boldsymbol{r})} = 0$, $\overline{g'(\boldsymbol{r}) g'(\boldsymbol{r}')} = g'^2 \delta(\boldsymbol{r} - \boldsymbol{r}')$.

In this form, with a spatially random Yukawa coupling, $\mathcal{L}$ can be analyzed in a SYK-type disorder-averaging theory [25], in contrast to $\mathcal{L}_{HM}$. Within a subsequent expansion in powers of g and g', it was shown that the effects of the spatially uniform Yukawa term with co-efficient g cancelled in the transport response function. In the present paper we will therefore set $g = 0$, and analyze the resulting Yukawa-SYK model in spatial dimension $d = 2$. With $g = 0$, all self-energies become functions of frequency alone, and we will present fully self-consistent frequency-dependent solutions of self energies in the SYK-type disorder average.

A recent work [179] has shown that the mapping from $\mathcal{L}_{\rm HM}$ to $\mathcal{L}$ eventually fails at very low T because of the localization of the eigenmodes of ϕ. The localization is a signal of the flow of the random mass $\delta s(\boldsymbol{r})$ in $\mathcal{L}_{HM}$ to strong disorder. To summarize, it is never appropriate to treat $\delta s(\boldsymbol{r})$ in a disorder average because it is strongly relevant:

(i) When the ϕ eigenmodes are extended, we can transfer the disorder from $\delta s(\boldsymbol{r})$ to the less relevant $g'(\boldsymbol{r})$ in $\mathcal{L}$, and treat the latter in a SYK-like disorder average, as in the present paper. After the mapping to $\mathcal{L}$, we conclude there is also a flow of the random Yukawa coupling $g'(\boldsymbol{r})$ to larger values, and this partially justifies our consideration of the limiting case with $g = 0$.

(ii) When the bosonic ϕ eigenmodes are localized, but the fermionic ψ eigenmodes remain extended [195], we must treat the influence of disorder on the bosonic sector numerically exactly, as in Ref.[179], or map to 'two-level system' models [178, 180].

6.2 Equations for Green's functions

The self-consistent equations for the Green's functions can be obtained by endowing the fields with flavor indices, and making the Yukawa coupling also random in flavor space. We start from the lattice action in imaginary time

$$\begin{aligned} S = &\int \mathrm{d}\tau \mathrm{d}^2 x \sum_{i=1}^{N} \sum_{\sigma=\pm 1} \psi_{i\sigma}^{\dagger}(\tau,x) \left[\partial_\tau + \varepsilon_k\right] \psi_{i\sigma}(\tau,x) \\ &+ \frac{1}{2}\int \mathrm{d}\tau \mathrm{d}^2 x \sum_{i=1}^{N} \phi_i(\tau,x)\left[-\partial_\tau^2 + \omega_q^2\right]\phi_i(\tau,x) \\ &+ \int \mathrm{d}\tau \mathrm{d}^2 x \sum_{i,j,\ell=1}^{N} \sum_{\sigma=\pm 1} \left[\frac{g'_{ij\ell}(x)}{N} \psi_{i\sigma}^{\dagger}(\tau,x)\psi_{j\sigma}(\tau,x)\phi_\ell(\tau,x)\right], \end{aligned} \tag{6.3}$$

with flavor indices $i, j = 1 \cdots N$ and consider the following choice of lattice dispersion

$$\epsilon_k = -2t(\cos k_x + \cos k_y) - \mu\,, \quad \omega_q^2 = m_b^2 + 2J(2 - \cos q_x - \cos q_y)\,. \tag{6.4}$$

Here t is the fermion hopping, μ is the chemical potential, m_b is the bare boson mass and J determines the boson dispersion. The Yukawa couplings g'_{ijl} are complex-valued random variables that obey $g'_{ijl}(x) = g_{1,ij\ell}(x) + i g_{2,ij\ell}(x) = g'_{ji\ell}(x)$. The real part $g_{1,ij\ell}(x)$ and the imaginary part $g_{2,ij\ell}(x)$ have zero mean and variances given by

$$\begin{aligned} \overline{g_{1,ij\ell}(x) g_{1,i'j'\ell'}(x')} &= \left(1 - \frac{\alpha}{2}\right) g'^2 \delta_{\ell,\ell'} \left(\delta_{ii'}\delta_{jj'} + \delta_{ij'}\delta_{ji'}\right) \delta(x - x'), \\ \overline{g_{2,ij\ell}(x) g_{2,i'j'\ell'}(x')} &= \frac{\alpha}{2} g'^2 \delta_{\ell,\ell'} \left(\delta_{ii'}\delta_{jj'} - \delta_{ij'}\delta_{ji'}\right) \delta(x - x'), \\ \overline{g_{1,ij\ell}(x') g_{2,i'j',\ell'}(x')} &= 0. \end{aligned} \tag{6.5}$$

In the $\alpha = 1$ limit, (6.5) reduces to $\left\langle g'_{ij\ell}(x) g'_{i'j'\ell'}(x')^* \right\rangle = g'^2 \delta(x - x') \delta_{ii'} \delta_{jj'} \delta_{kk'}$ and therefore no superconductivity occurs. For $\alpha = 0$, however, the coupling constants are all real valued, which preserves the time-reversal symmetry and gives rise to superconductivity. After a disorder average, we obtain

$$
\begin{aligned}
\frac{S}{N} = &- \operatorname{Tr}\log\Big(\hat{G}_0^{-1} - \hat{\Sigma}\Big) + \frac{1}{2}\operatorname{Tr}\log\big(D_0^{-1} - \Pi\big) \\
&- \int \mathrm{d}\tau \mathrm{d}^2x \int \mathrm{d}\tau' \mathrm{d}^2x' \left(2\Sigma(\tau', x'; \tau, x) G(\tau, x; \tau', x') - \frac{1}{2}\Pi(\tau', x'; \tau, x) D(\tau, x; \tau', x')\right) \\
&- \int \mathrm{d}\tau \mathrm{d}^2x \int \mathrm{d}\tau' \mathrm{d}^2x' \left(\Phi^\dagger(\tau', x'; \tau, x) F(\tau, x; \tau', x') + \Phi(\tau', x'; \tau, x) F^\dagger(\tau, x; \tau', x')\right) \\
&+ g'^2 \int \mathrm{d}\tau \mathrm{d}^2x \int \mathrm{d}\tau' \mathrm{d}^2x' G(\tau, x; \tau', x') G(\tau', x'; \tau, x) D(\tau, x; \tau', x') \delta(x - x') \\
&- g'^2(1 - \alpha) \int \mathrm{d}\tau \mathrm{d}^2x \int \mathrm{d}\tau' \mathrm{d}^2x' F^\dagger(\tau, x; \tau', x') F(\tau', x'; \tau, x) D(\tau, x; \tau', x') \delta(x - x') \\
&- \int \mathrm{d}\tau \mathrm{d}^2x \frac{i\lambda(\tau, x)}{2\gamma}.
\end{aligned}
\tag{6.6}
$$

Here $\hat{G}_0^{-1}$ and $\hat{\Sigma}$ are matrices in Nambu space. We have introduced the time-bilocal fields G, F, D, which are normal and anomalous fermionic Green's functions, as well as bosonic Green's functions. The corresponding self-energies, given by Σ, Φ and Π, are employed as Lagrange multipliers. We also include a fixed length constraint

$$
\sum_q \sum_{i=1}^{N} \phi_{iq}(\tau) \phi_{i,-q}(\tau) = N/\gamma \tag{6.7}
$$

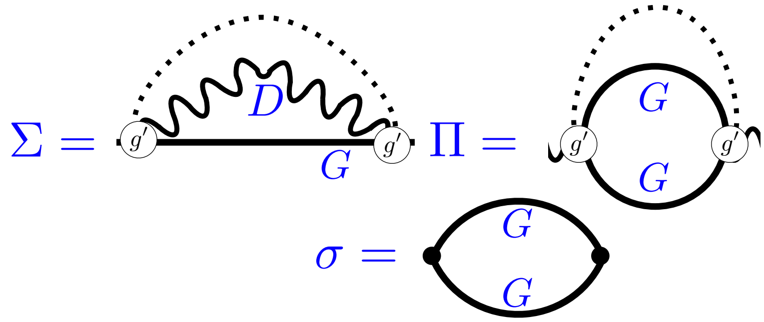

Figure 6.1: Feynman diagrams for the ψ self energy Σ, and the ϕ self energy Π. The wavy line is the ϕ Green's function, and the smooth line is the ψ Green's function. All Green's functions include self energy corrections. The dashed line represents an average over spatial disorder. All Green's functions and self energies become 2×2 matrices in the superconducting phase.

imposed by a Lagrange multiplier λ. Integrating out ψ and ϕ yields this G-Σ action (6.6). In the limit of a large number of flavors, the SYK-type saddle-point equations are given by

$$\hat{G}(i\omega) = \int \frac{\mathrm{d}^2k}{(2\pi)^2}\left(i\omega\sigma_0 + \mu\sigma_3 - \varepsilon_k\sigma_3 - \hat{\Sigma}(i\omega)\right)^{-1}, \tag{6.8a}$$

$$D(i\nu) = \int \frac{\mathrm{d}^2q}{(2\pi)^2}\frac{1}{\nu^2 + \omega_q^2 + m_b^2 - \Pi(i\nu)}, \tag{6.8b}$$

$$\Sigma(\tau) = g'^2 G(\tau)D(\tau), \tag{6.8c}$$

$$\Phi(\tau) = -g'^2(1-\alpha)F(\tau)D(\tau), \tag{6.8d}$$

$$\Pi(\tau) = -2g'^2\left(G(\tau)G(-\tau) - (1-\alpha)F(\tau)F^\dagger(-\tau)\right), \tag{6.8e}$$

$$\frac{1}{\gamma} = T\sum_\nu \int \frac{\mathrm{d}^2q}{(2\pi)^2}\frac{1}{\nu^2 + \omega_q^2 + m_b^2 - \Pi(i\nu)}, \tag{6.8f}$$

which are indicated schematically in Figure 6.1. Different from the translationally invariant model, the self-energies are momentum independent as a result of the extra δ-function in (6.6). Appendix E describes numerical solutions of these equations. We present highlights of the results in normal and superconducting phases below.

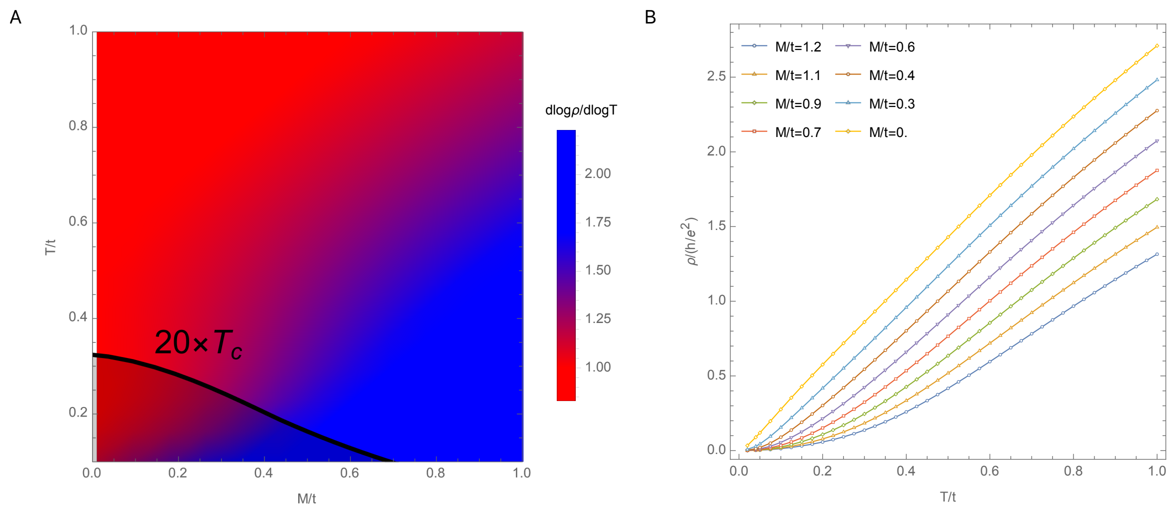

Figure 6.2: A. Resistivity exponent as a function of the $T = 0$ value of the renormalized boson mass M and temperature T, together with the superconducting T_c (T_c has been multipled by a factor of 20 to be on the same scale as the resistivity data.). B. Resistivity for various values of M. The QCP corresponds to $M = 0$; $M > 0$ is on the disordered side of the QCP.

6.3 Results

We have solved the integral equations defined by the diagrams in Figure 6.1 numerically on a 2D square lattice with nearest-neighbor hopping t and with fermion chemical potential $\mu = -0.5t$. These parameters are chosen to represent the generic properties of our model and are not meant to correspond to the detailed microscopic structure of any particular material. Our findings are summarized in the phase diagram in Figure 6.2. The phenomenology we have found is broadly similar to that observed experimentally in a wide variety of strange metals: Above the QCP there is a quantum-critical fan, in which the resistivity has an approximately T-linear temperature dependence. At low temperatures the QCP is ultimately masked by a superconducting phase, with the maximal T_c occurring just above the critical point.

6.3.1 Normal state properties

The d.c. transport properties are shown in more detail in Figure 6.2. At the QCP, the resistivity is essentially T-linear down to the lowest temperature. Logarithmic corrections to the T-linear behavior are expected in the present model [25], but the effects of such corrections are evidently relatively weak for the parameters shown here. On the disordered side of the transition the resistivity is T-linear at elevated temperature inside the quantum critical fan, before going to zero with what is well-approximated by a T^2 power-law below a certain crossover temperature. For temperatures less than the electron hopping t, the resistivity is smaller than the quantum of resistance; the system is thus not in the bad metal regime.

Next, we consider the finite-frequency response. The real and imaginary parts of the optical conductivity $\sigma(\omega)$ at the QCP are presented in Figure 6.3a and 6.3b. At a crude level, the optical conductivity can be seen to obey an approximately Drude-like behavior. To better understand the more detailed structure encoded in $\sigma(\omega)$ we follow Michon *et. al.* [39] and parametrize $\sigma(\omega)$ via a "generalized" Drude formula:

$$\sigma(\omega) = i\frac{K}{\omega m^*(\omega)/m + i/\tau_{\mathrm{tr}}(\omega)}. \tag{6.9}$$

Here the optical weight K is equal to the average electronic kinetic energy via the f-sum rule. With K defined in this way, we may read off a frequency dependent mass-enhancement parameter $m^*(\omega)/m$ and a frequency-dependent transport scattering rate $1/\tau_{\mathrm{tr}}(\omega)$ directly from the real and imaginary parts of the optical conductivity. The optical scattering rate is shown in Figure 6.3c. There is an approximately linear in frequency dependence down to $\omega \sim T$, while for frequencies $\omega \lesssim T$ the scattering rate tends to a T-dependent non-zero value which vanishes in the limit $T \to 0$. The frequency-dependent mass enhancement parameter is shown in Figure 6.3d. For the chosen parameters, the low-frequency mass enhancement does not exceed roughly 20% down to the lowest temperatures we are able to reliably access in the numerical calculations. At sufficiently low temperatures, however, we do anticipate

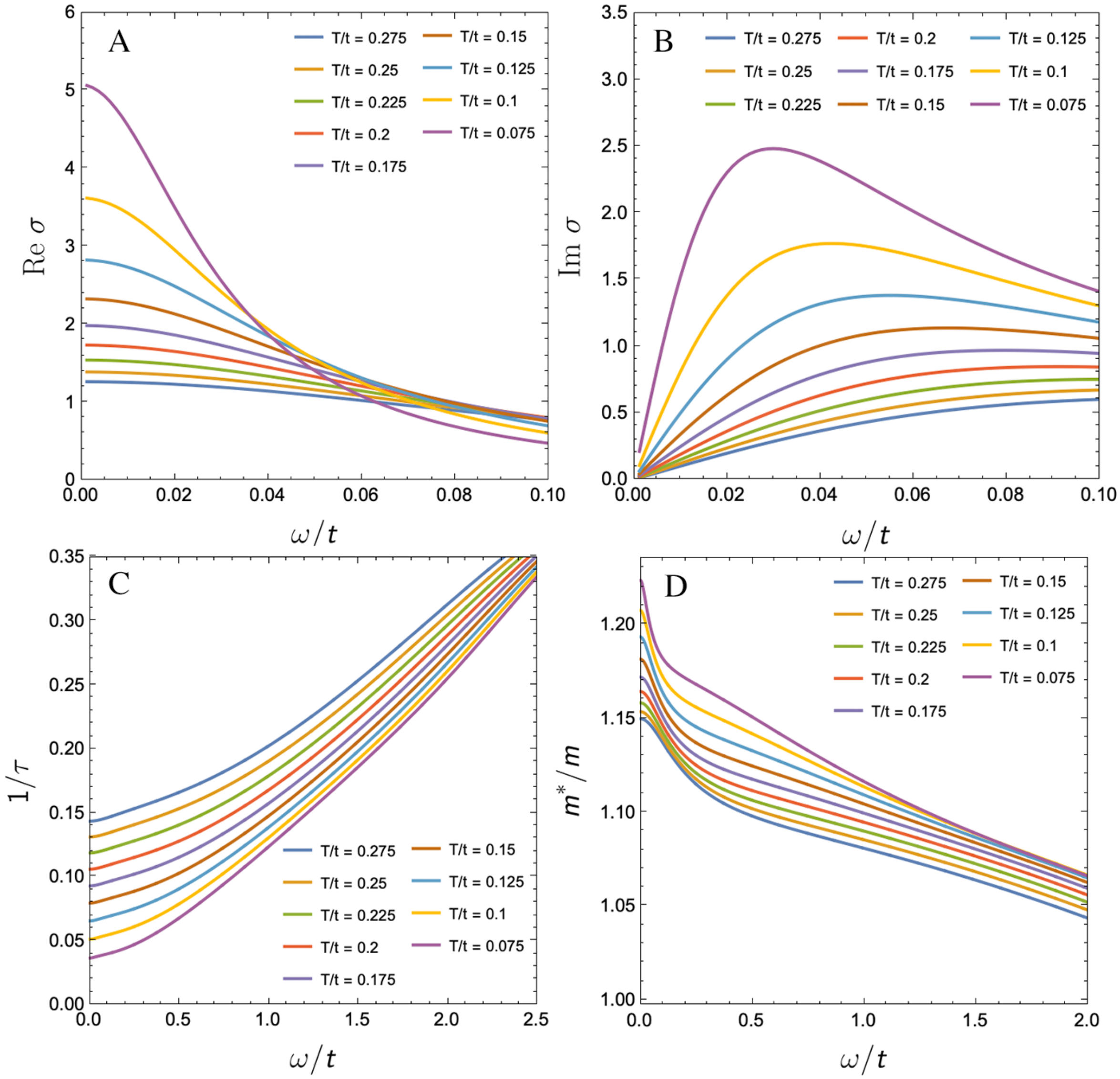

Figure 6.3: Real (A) and imaginary (B) part of the optical conductivity as a function of ω/t for different temperatures. Frequency-dependent optical scattering rate (C) and mass enhancement m^*/m (D) are derived from (6.9).

$m^*(\omega = 0)/m$ diverges logarithmically with T. We note the behavior of the "optical" mass enhancement is consistent with the mass enhancement we have inferred from the fermion self-energy in Appendix E.1. Within the quantum critical fan, frequency-dependent observables are generally expected to obey ω/T scaling. As has been explained in [39], a simple of version of ω/T scaling for the optical conductivity will in fact be spoiled by logarithmic corrections.

6.3.2 Superconducting state

We now investigate the onset of superconducting pairing in our theory. To preserve time-reversal symmetry, we focus on the $\alpha = 0$ limit with real-valued random couplings g'_{ijl}. The superconducting transition temparature T_c, as shown in Figure 6.2, is numerically identified by the linearized gap equation

$$\Phi(i\omega_n) = g'^2(1-\alpha)\frac{1}{\beta}\sum_{\omega_m} D(i\omega_n - i\omega_m)X(i\omega_m)\Phi(i\omega_m)\,. \tag{6.10}$$

Here $D(i\omega_n - i\omega_m)$ and $X(i\omega_m)$ are determined by normal state solutions; see Appendix E.2. For each coupling strength g', we are interested in the superconducting transition at the critical point $\gamma = \gamma_c$, where the renormalized boson mass vanishes approximately as $M^2 \sim T$ and the resistivity exhibits a linear temperature dependence. At low temperatures, we find a linear relation between T_c and A, the slope of the linear-T resistivity $\rho(T) = \rho_0 + AT$. The same correlation between A and T_c is observed in various cuprate superconductors, suggesting pairing and non-Fermi-liquid scattering can stem from the same origin[173].

We have also computed spectral properties as the system goes through the superconducting transition. In Figure 6.5 we show the evolution of the electronic density of states at the quantum critical point: a gap opens as temperatures decreases to $T < T_c$. The fermion self-energy behaves as a marginal Fermi liquid with $-\mathrm{Im}\Sigma \sim |\omega|$, as seen in the inset of Figure 6.5.

We then discuss the superfluid stiffness in the superconducting state. Following approaches discussed by Sacalapino *et al.*[196] and Valentinis *et al.*[176], we express the phase stiffness

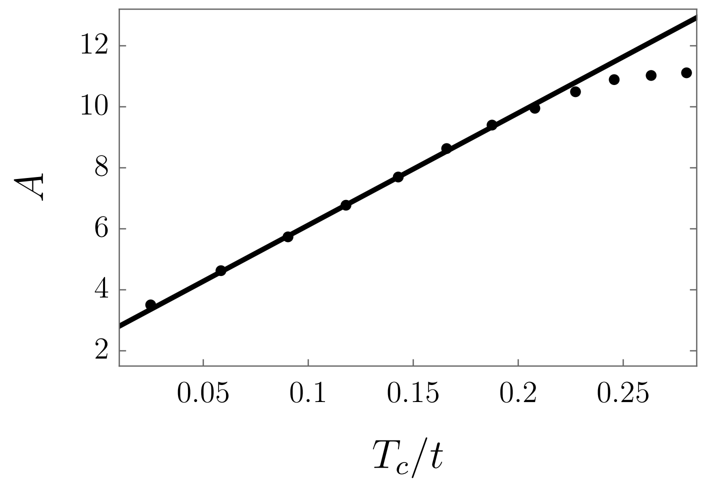

Figure 6.4: Coefficient of the linear term in the resistivity $\rho(T)$ as a function of T_c. All points are calculated at $\gamma = \gamma_c(g')$ for each coupling strength g'. The A coefficient is obtained from a linear fit of $\rho(T)$. The black line is a linear fit to show the correlation between A and T_c.

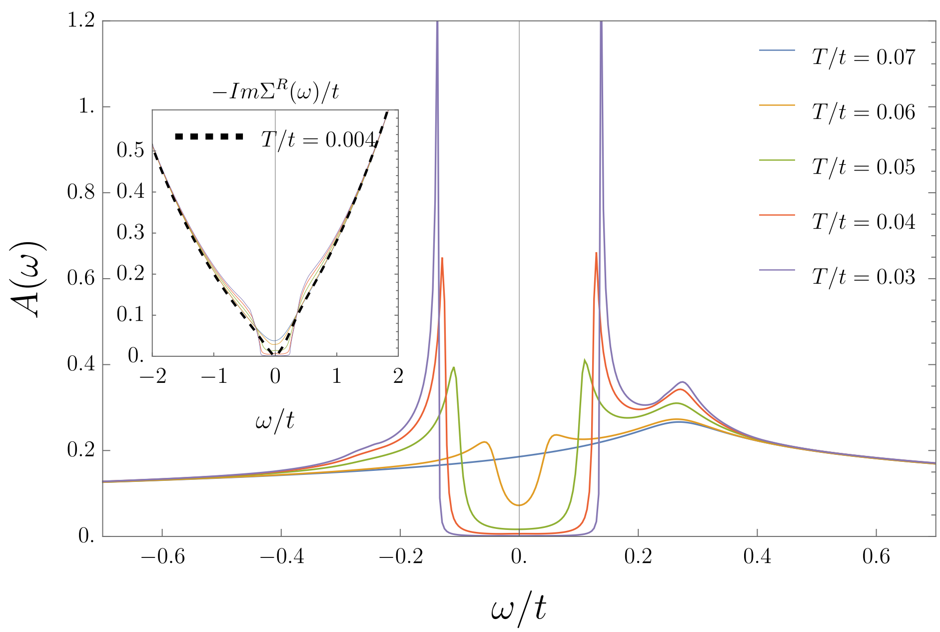

Figure 6.5: Evolution of the local density of states upon cooling through T_c at the QCP. The superconducting transition temperature is $T_c/t = 0.067$. Inset shows the marginal Fermi-liquid form of the fermion self-energy $-\text{Im}\Sigma \sim |\omega|$ at the QCP. Dashed curve is calculated in the $\alpha = 1$ limit at $T/t = 0.004$.

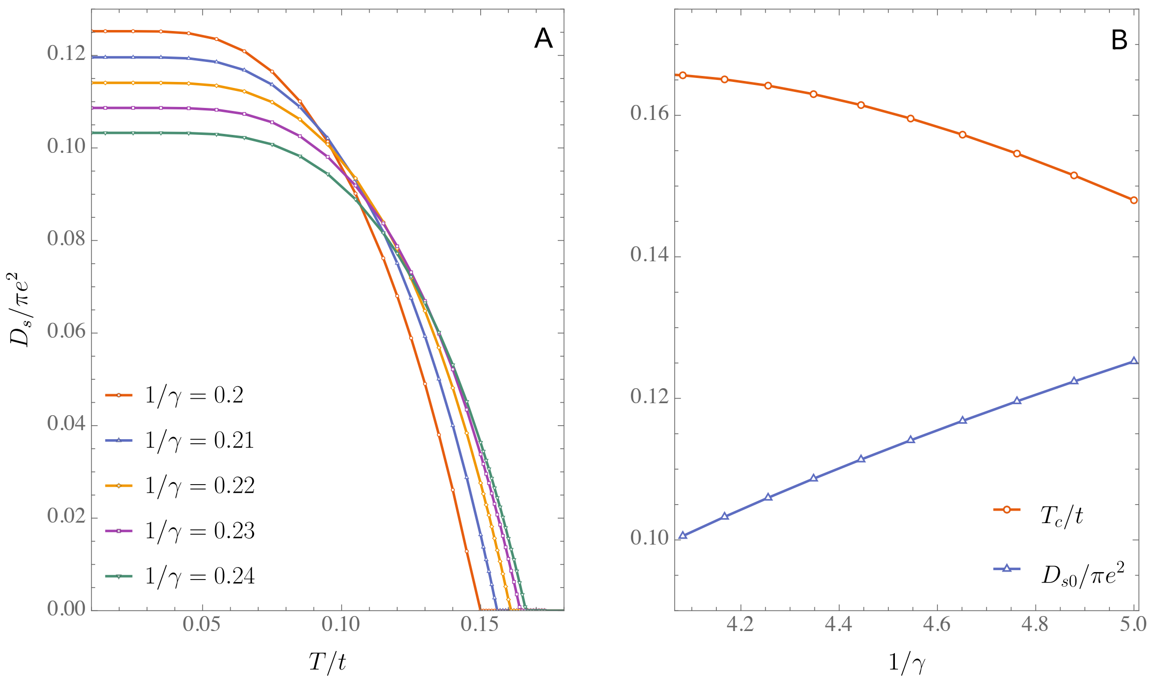

Figure 6.6: A. Temperature dependence of superfluid stiffness D_s at $g = 5$ for various values of $\gamma < \gamma_c = 0.247$. B. Comparison of T_c and superfluid stiffness $D_{s0} = D_s(T \to 0)$.

in terms of the anomalous Green's function on the Matsubara frequencies,

$$\frac{D_s}{\pi e^2} = \frac{2}{\beta} \sum_{\omega_n} \int \mathrm{d}\epsilon \ \rho_{\mathrm{tr}}(\epsilon) F(\epsilon, i\omega_n) F^\dagger(\epsilon, i\omega_n), \tag{6.11}$$

where the density of states $\rho_{\mathrm{tr}}^{\alpha\beta}(\epsilon) \equiv \int_{\boldsymbol{k}} \frac{\partial \varepsilon_{\boldsymbol{k}}}{\partial k_\alpha} \frac{\partial \varepsilon_{\boldsymbol{k}}}{\partial k_\beta} \delta(\epsilon - \varepsilon_{\boldsymbol{k}})$ is analytically computable for the given lattice dispersion (6.4). In figure 6.6A, we show the temperature dependence of superfluid stiffness for a fixed g' and different tuning parameter γ. The stiffness reaches a finite constant value, D_{s0}, for $T \to 0$. As we tune γ towards the critical point γ_c, T_c saturates to its maximal but the D_{s0} decreases, as seen in Figure 6.6B. This result at strong couplings aligns with the superfluid density extracted from muon relaxation experiments in cuprate superconductors [197, 198].

6.4 Conclusions

The two-dimensional Yukawa-SYK model provides a promising framework for the universal theory of strange metals. In our theory, we couple a critical Fermi surface to a scalar field linked to a quantum phase transition. We have shown that a self-consistent disorder averaged analysis of this model describes a variety of disordered quantum critical metals over a wide range temperatures. We provide comprehensive numerical solutions for both the normal and superconducting states in this scenario, calculating superconducting transition temperatures, electronic spectral functions, frequency-dependent conductivity, and superfluid stiffness. A quantum critical fan is observed above the QCP, where the d.c. resistivity is linear-in-T. The optical conductivity in our model aligns closely with the transport properties of cuprates analyzed by Michon *et al.*[39]. Additionally, we investigate the transition of the strange metal to superconductivity, and report a linear relationship between the superconducting critical temperature and the slope of the linear-T resistivity at low temperatures. Our theory would offer new routes to explore the interplay of strange metal and superconductivity in strongly correlated systems like cuprates.

A

Appendix for chapter 2

A.1 Superalgebras

The operators in (2.3) obey the commutation and anti-commutation relations

$$
\begin{aligned}
[S^a, S^b] &= i\epsilon_{abc} S^c \quad , \quad \{c_\alpha, c_\beta\} = 0 \quad , \quad \{c_\alpha, c^\dagger_\beta\} = \delta_{\alpha\beta} V + \sigma^a_{\alpha\beta} S^a \\
[S^a, c_\alpha] &= -\frac{1}{2}\sigma^a_{\alpha\beta} c_\beta \quad , \quad [S^a, c^\dagger_\alpha] = \frac{1}{2}\sigma^a_{\beta\alpha} c^\dagger_\beta \quad , \quad [S^a, V] = 0 \\
[V, c_\alpha] &= \frac{1}{2} c_\alpha \quad , \quad [V, c^\dagger_\alpha] = -\frac{1}{2} c^\dagger_\alpha \,.
\end{aligned}
\tag{A.1}
$$

The constraint (2.4) commutes with all operators of the superalgebra. Imposing this constraint yields the fundamental representation of SU(1|2).

Alternatively, we can use the operators in (2.5). These realize the SU(2|1) algebra, and it can be verified that these operators also obeys the superalgebra in Eq. (A.1). The constraint projecting to the fundamental representation is now (2.6).

A.1.1 Larger symmetries

We consider the model for general M and M', with the electron operator

$$
c_{\ell\alpha} = b^\dagger_\ell f_\alpha \,, \tag{A.2}
$$

acquiring both spin ($\alpha = 1 \dots M$) and 'orbital' ($\ell = 1 \dots M'$) indices. We define the SU(M) spin operator

$$S^a = f^\dagger_\alpha T^a_{\alpha\beta} f_\beta \tag{A.3}$$

where the matrices T^a obey

$$\mathrm{tr}(T^a T^b) = \frac{1}{2}\delta^{ab}, \quad T^a T^a = \frac{M^2-1}{2M} \cdot \mathbf{1}\,, \quad T^a_{\alpha\beta} T^a_{\gamma\delta} = \frac{1}{2}\Big(\delta_{\alpha\delta}\delta_{\beta\gamma} - \frac{1}{M}\delta_{\alpha\beta}\delta_{\gamma\delta}\Big)\,. \tag{A.4}$$

The operators $c_{\ell\alpha}$, S^a, the operator

$$V = \frac{1}{M} f^\dagger_\alpha f_\alpha + \frac{1}{M'} b^\dagger_\ell b_\ell\,, \tag{A.5}$$

and the operators $b^\dagger_\ell T^a_{\ell\ell'} b_{\ell'}$ are the $(M+M')^2 - 1$ generators of the superalgebra SU($M'|M$).

A general constraint fixing the representation is

$$f^\dagger_\alpha f_\alpha + b^\dagger_\ell b_\ell = P\,, \tag{A.6}$$

with P a positive integer, and our interest in the case $P = M/2$ which realizes the representation in which the SU(M) subalgebra is self-conjugate. Note that the fundamental representation of the superalgebra is $P = 1$, but this does not lead to a convenient large M limit.

We can also consider a bosonic spinon and fermionic holon decomposition for general M, M'

$$c_{\ell\alpha} = \mathfrak{f}^\dagger_\ell \mathfrak{b}_\alpha \tag{A.7}$$

The analogous steps will lead to a realization of the SU($M|M'$) superalgebra, which is identical to the SU($M'|M$) superalgebra. However, the constraint

$$\mathfrak{b}^\dagger_\alpha \mathfrak{b}_\alpha + \mathfrak{f}^\dagger_\ell \mathfrak{f}_\ell = P \tag{A.8}$$

now leads to a *different representation* of the superalgebra from (A.6) for $P \neq 1$ [199]. So the models defined by (A.2) and (A.7) are in general different, although they are the same for the $M = 2$, $M' = 1$ case of interest to us. Note also that in all cases the Hamiltonian contains an exchange interaction involving the SU(M) generators only, and not the SU(M') generators.

A.1.2 Operator expectation values

We will compute the only RG equations for the SU($M'|M$) theory in Appendix A.2 following the method in Appendix C of Ref. [89]. After using the identity (A.4), the computations in

Appendix A.2 can be reduced to the following operator traces.

First, let us compute the dimension, $\mathcal{D}(M, M', P)$, of the superspin Hilbert space. To compute this, it is useful to compute the grand-canonical partition function, while ignoring the constraint (A.6).

$$\mathcal{Z}(z) = \mathrm{Tr}\, z^{f_\alpha^\dagger f_\alpha + b_\ell^\dagger b_\ell} = \frac{(1+z)^M}{(1-z)^{M'}} \tag{A.9}$$

where z is the common fugacity. Then we can impose the constraint (A.6), and the dimension of the Hilbert space is given by the coefficient of z^P in the series expansion of $\mathcal{Z}(z)$, or equivalently

$$\mathcal{D}(M, M', P) = \oint_{|z|=c<1} \frac{dz}{2\pi i} \frac{1}{z^{P+1}} \mathcal{Z}(z) \tag{A.10}$$

Some sample values from Mathematica are

$$\mathcal{D}(2,1,1) = 3 \quad , \quad \mathcal{D}(6,6,3) = 292 \quad , \quad \mathcal{D}(20,14,10) = 553844224 \quad , \quad \ldots \tag{A.11}$$

Now we can compute the general expectation value

$$\begin{aligned} \mathcal{I}_{m,m'} &\equiv \left\langle \left(f_\alpha^\dagger f_\alpha\right)^m \left(b_\ell^\dagger b_\ell\right)^{m'} \right\rangle \qquad (A.12) \\ &= \frac{1}{\mathcal{D}(M, M', P)} \oint_{|z|=c<1} \frac{dz}{2\pi i} \frac{1}{z^{P+1}} \left[\left(z \frac{d}{dz} \right)^m (1+z)^M \right] \left[\left(z \frac{d}{dz} \right)^{m'} \frac{1}{(1-z)^{M'}} \right] . \end{aligned}$$

Note $\mathcal{I}_{0,0} = 1$.

The values for $M = 2$, $P = 1$, and $M' = 1$ case of interest to us are simple:

$$\mathcal{I}_{m,0} = \frac{2}{3}, \quad m \geq 1; \quad \mathcal{I}_{0,m'} = \frac{1}{3}, \quad m' \geq 1; \quad \mathcal{I}_{m,m'} = 0, \quad m \geq 1 \text{ and } m' \geq 1 . \tag{A.13}$$

This simplicity is the reason Section 2.3 was able to compute the RG equations using Feynman diagrams and the Abrikosov method.

Some other random values

$$\begin{aligned} \mathcal{I}_{2,3} = \frac{342}{73}, \quad \mathcal{I}_{7,4} = \frac{3384}{73}, & \qquad \text{for } M = 6,\ M' = 6,\ P = 3; \\ \mathcal{I}_{7,4} = \frac{238531161015}{6698}, \quad \mathcal{I}_{3,9} = \frac{3197447102115}{6698}, & \qquad \text{for } M = 20,\ M' = 14,\ P = 10. \end{aligned} \tag{A.14}$$

A.2 RG equations for general M, M'

This appendix generalizes the method of Refs. [88, 89] for SU(2) spins to superspins in SU($M'|M$). This method utilizes only gauge-invariant information contained in the superspin algebra and its representation; thus the Berry phase $\mathcal{S}_B$ (see (2.10) and (2.12)) of the supergroup [74] is exactly accounted for by the commutation and anti-commutation relations. The RG equations obtained here reduce to those of Section 2.3 at $M = 2$, $P = 1$, $M' = 1$.

We consider here the Hamiltonian

$$
\begin{aligned}
H_{\text{imp}} \quad &= g_0 \left(c^\dagger_{\ell\alpha}\, \psi_{\alpha\ell}(0) + \text{H.c.} \right) + \gamma_0 S^a\, \phi_a(0) \\
&\quad + \int |k|^r dk\, k\, \psi^\dagger_{k\alpha\ell} \psi_{k\alpha\ell} + \frac{1}{2} \int d^d x \left[\pi_a^2 + (\partial_x \phi_a)^2 \right] ,
\end{aligned} \tag{A.15}
$$

where $c_{\ell\alpha}$ and S^a are defined in (A.2) and (A.3), and we impose exactly the constraint (A.6). Recall, the indices $\alpha, \beta = 1 \ldots M$, $\ell = 1 \ldots M'$, and $a = 1 \ldots M^2 - 1$.

The setup of the renormalization factors in the present perturbation theory is somewhat different from (2.19). We now write, using the operators defined in (A.2) and (A.3),

$$
S^a = \sqrt{Z_S} S^a_R\,, \quad c_{\ell\alpha} = \sqrt{Z_c} c_{R,\ell\alpha}\,, \quad \gamma_0 = \frac{\mu^{\epsilon/2} \widetilde{Z}_\gamma}{\sqrt{Z_S \widetilde{S}_{d+1}}} \gamma\,, \quad g_0 = \frac{\mu^{\bar{r}} \widetilde{Z}_g}{\sqrt{Z_c \Gamma(r+1)}} g\,. \tag{A.16}
$$

The renormalization constants Z_S and Z_c are the same as those defined in (2.47), but we will now compute them in a different manner. The notation of our renormalization constants also differs from that in Ref. [90], and we provide a translation in Table A.1. Unlike Ref. [90],

Ref. [90]	Present paper
Z_h	Z_f
$\widetilde{Z}_\gamma$	Z_γ
Z	$Z_\phi = 1$
Z'	Z_S
Z_γ	$\widetilde{Z}_\gamma = 1$

Table A.1: Correspondence between the notations of Ref. [90] and the present paper.

we do not have bulk interactions of the bosonic bath field ϕ, and hence we have $Z_\phi = 1$, as we noted in Section 2.3.3. For the same reasons, it was argued in Refs. [88–90] that (in our notation) $\widetilde{Z}_\gamma = 1$ in the absence of bulk interactions. The reasoning extends also to the fermionic bath, and so we have $\widetilde{Z}_\gamma = 1$ and $\widetilde{Z}_g = 1$ exactly. These identities can also be understood from the statement below (2.47) that the vertex corrections $\Lambda_{S,c}$ arise from the same diagrams as $Z_{\gamma,g}$. We compute Z_S and Z_c by renormalizing the two-point correlators of S^a and $c_{\ell\alpha}$

$$\frac{\epsilon}{2}\gamma Z_S + \left[Z_S - \frac{\gamma}{2}\frac{\partial Z_S}{\partial\gamma}\right]\beta(\gamma) - \frac{\gamma}{2}\frac{\partial Z_S}{\partial g}\beta(g) = 0\,, \tag{A.17}$$

$$\bar{r} g Z_c + \left[Z_c - \frac{g}{2}\frac{\partial Z_c}{\partial g}\right]\beta(g) - \frac{g}{2}\frac{\partial Z_c}{\partial\gamma}\beta(\gamma) = 0\,. \tag{A.18}$$

We have used the exact relations $\widetilde{Z}_g = \widetilde{Z}_\gamma = 1$ in obtaining these equations. Solving these two equations and using the expressions for the renormalization factors found above we obtain the following one-loop beta functions,

$$\beta(g) = -\bar{r}g + \frac{P_g}{2}g^3 + \frac{P_\gamma}{2}g\gamma^2\,, \tag{A.19}$$

$$\beta(\gamma) = -\frac{\epsilon}{2}\gamma + \frac{L_\gamma}{2}\gamma^3 + \frac{L_g}{2}\gamma g^2\,. \tag{A.20}$$

Recall that at $M = 2, M' = 1$, we have $P_g = 3$, $P_\gamma = 3/4$, $L_g = 2$, and $L_\gamma = 2$. With this the above expressions match the one-loop beta functions derived earlier in Sec. 2.3.

We can also calculate the anomalous dimension for the spin and electron operators, defined in (2.49). From (A.17) and (A.18) we obtain exactly the same equations derived before, *i.e.*, (2.52) and (2.54). Thus at the non-trivial fixed point where $\gamma * \neq 0, g* \neq 0$ we obtain $\eta_S = \epsilon$ and $\eta_c = 2\bar{r}$ to all orders in ϵ and $\bar{r}$.

A.3 Large M limit

In this appendix we consider the large M limit examined originally in the insulating spin model in Ref. [1]. To extend the large M limit to the t-J model, we also need to endow the electron with an additional orbital index $\ell = 1 \ldots M'$ as in (A.2), and take the large M limit at fixed

$$k \equiv \frac{M'}{M} \tag{A.21}$$

using SU($M'|M$) superspin formulation of Appendix A.1.1 while imposing the constraint (A.6) at $P = M/2$. Similar large M limits were taken in particle-hole symmetric models in Refs. [84–87] and for a non-random t-J model in Refs. [82, 83].

A sketch of our proposed large M phase diagram is shown in Fig. A.1. This applies to the theory obtained by taking the large M limit of the path integral $\mathcal{Z}$ in (2.10) by inserting the SU($M'|M$) superspin operators in (A.2) and (A.3), and rescaling $t^2 \to t^2/M$ and $J^2 \to J^2/M$. See Ref. [87] for details of a similar computation with particle-hole symmetry. In our case, both the boson and fermion Green's functions will have to be particle-hole asymmetric, as in Refs. [1, 70, 71, 135].

We will perform an analytic low energy analysis of the large M equations, and find a

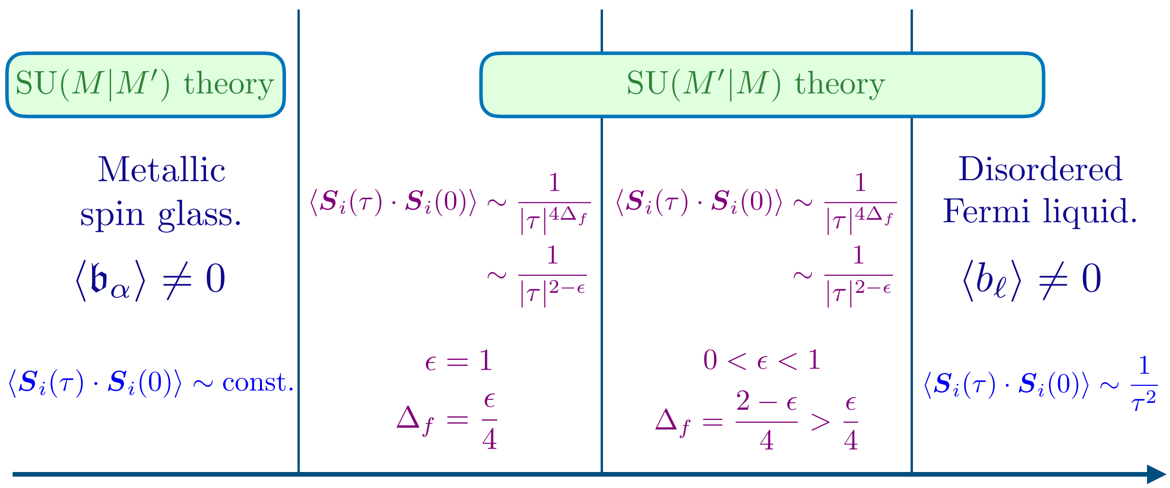

Figure A.1: Schematic phase diagram in the large M limit, with the phases displaying more rapidly decaying spin correlations as we move to the right. This appendix describes only the two intermediate critical phases in the SU($M'|M$) theory with bosonic holons and fermionic spinons. We propose in the present paper that for the case $M = 2$, $M' = 1$, these two critical phases reduce to a critical point with the characteristics of the $\epsilon = 1$ phase, as shown in Fig. 2.1 . A description of the spin glass phase in the large M limit requires fermionic holons and bosonic spinons in the SU($M|M'$) theory, which we do not examine here. We also note that for $M' > 1$, the disordered Fermi liquid phase also has glassy correlations associated with the 'orbital' index $\ell = 1 \ldots M'$.

critical solution which is in close correspondence with the RG fixed point FP_4 in Section 2.3. However, the large M solution appears to be present for a range of dopings, and not at a critical doping as in the RG analysis. We expect that either constraints from the higher energy structure of the large M theory, or corrections higher order in $1/M$, will convert the critical phase to a critical point. It appears that the numerical studies of Haule *et al.* [82, 83] examined the finite temperature behavior about the critical phase described here as their model of the pseudogap. This contrasts with our model of the pseudogap in Fig. 2.1 as a metallic spin glass flanking a critical point. We also note that the present large M limit, with fermionic spinons, cannot obtain a metallic spin glass; instead we have to use the bosonic spinon approach outlined in Section 2.4.2.

A.3.1 Green's functions

We follow the condensed matter notation for Green's functions in which

$$G_f(\tau) = -\langle T_\tau (f(\tau) f^\dagger(0))\rangle, \tag{A.22}$$

$$G_b(\tau) = -\langle T_\tau (b(\tau) b^\dagger(0))\rangle. \tag{A.23}$$

We drop indices α, ℓ, and all Green's functions are diagonal in these indices. It is useful to make ansatzes for the retarded Green's functions in the complex frequency plane, because then the constraints from the positivity of the spectral weight are clear. At the Matsubara frequencies, the Green's function is defined by

$$G(i\omega_n) = \int_0^{1/T} d\tau e^{i\omega_n \tau} G(\tau). \tag{A.24}$$

So the bare Green's functions are

$$G_{f0}(i\omega_n) = \frac{1}{i\omega_n - \mu_f} \tag{A.25}$$

$$G_{b0}(i\omega_n) = \frac{1}{i\omega_n - \mu_b}. \tag{A.26}$$

The Green's functions are continued to all complex frequencies z via the spectral representation

$$G(z) = \int_{-\infty}^{\infty} \frac{d\Omega}{\pi} \frac{\rho(\Omega)}{z - \Omega}. \tag{A.27}$$

For fermions, the spectral density obeys

$$\rho_f(\Omega) > 0, \tag{A.28}$$

for all real Ω and T, and for bosons the constraint is

$$\Omega\, \rho_b(\Omega) > 0. \tag{A.29}$$

The retarded Green's function is $G^R(\omega) = G(\omega + i\eta)$ with η a positive infinitesimal, while the advanced Green's function is $G^A(\omega) = G(\omega - i\eta)$. It is also useful to tabulate the inverse Fourier transforms at $T = 0$

$$G(\tau) = \begin{cases} -\displaystyle\int_0^\infty \frac{d\Omega}{\pi} \rho(\Omega) e^{-\Omega\tau} & , \quad \text{for } \tau > 0 \text{ and } T = 0 \\ \displaystyle\int_0^\infty \frac{d\Omega}{\pi} \rho(-\Omega) e^{\Omega\tau} & , \quad \text{for } \tau < 0 \text{ and } T = 0 \end{cases} . \tag{A.30}$$

A.3.2 Saddle point and self-consistency equations

The saddle-point equations of the SU($M'|M$) form of (2.10), after rescaling $t^2 \to t^2/M$ and $J^2 \to J^2/M$, for the boson and fermion Green's functions are

$$G_b(i\omega_n) = \frac{1}{i\omega_n + \mu_b - \Sigma_b(i\omega_n)}, \quad \Sigma_b(\tau) = t^2 G_f(\tau) R(-\tau) \tag{A.31}$$

$$G_f(i\omega_n) = \frac{1}{i\omega_n + \mu_f - \Sigma_f(i\omega_n)}, \quad \Sigma_f(\tau) = J^2 G_f(\tau) Q(\tau) - k\, t^2 R(\tau) G_b(\tau)\,, \tag{A.32}$$

while the self-consistency equations in (2.9) are

$$R(\tau) = -G_f(\tau) G_b(-\tau) \quad , \quad Q(\tau) = -G_f(\tau) G_f(-\tau) \tag{A.33}$$

Here μ_f and μ_b are chemical potentials, determined by ϵ_0 and the saddle point value of λ, and chosen to satisfy

$$\left\langle f^\dagger f \right\rangle = \frac{1}{2} - kp \quad , \quad \left\langle b^\dagger b \right\rangle = p\,. \tag{A.34}$$

Eqs. (A.32,A.33,A.34) are identical to the ones considered in Refs [82, 83] as an EDMFT approximation to the non-random t-J model. We will look for gapless critical solutions of the above equations. We expect that such solutions exist only for $p < p_c$, and that for $p > p_c$ the boson condenses, leading to a Fermi liquid solution.

A.3.3 Low frequency ansatzes

For the fermion Green's function, we write at a complex frequency $|z| \ll J$

$$G_f(z) = C_f \frac{e^{-i(\pi\Delta_f + \theta_f)}}{z^{1-2\Delta_f}} \quad , \quad \text{Im}(z) > 0, \tag{A.35}$$

which is expressed in terms of three real parameters, C_f, Δ_f and θ_f. Then the constraint (A.28) becomes

$$\sin(\pi\Delta_f + \theta_f) > 0 \quad , \quad \sin(\pi\Delta_f - \theta_f) > 0. \tag{A.36}$$

The particle-hole symmetric value is $\theta_f = 0$. Using (A.30) we obtain in τ space for $|\tau| \gg 1/J$

$$G_f(\tau) = \begin{cases} -\dfrac{C_f \Gamma(2\Delta_f)\sin(\pi\Delta_f + \theta_f)}{\pi|\tau|^{2\Delta_f}} & , \quad \text{for } \tau > 0 \text{ and } T = 0 \\ \dfrac{C_f \Gamma(2\Delta_f)\sin(\pi\Delta_f - \theta_f)}{\pi|\tau|^{2\Delta_f}} & , \quad \text{for } \tau < 0 \text{ and } T = 0 \end{cases} . \tag{A.37}$$

We can also write corresponding ansatz for the fermionic correlator $R(\tau)$, which we will only need as a function of τ for $|\tau| \gg 1/J$

$$R(\tau) = \begin{cases} -\dfrac{C_{+R}}{|\tau|^{2(1-\bar{r})}} & , \quad \text{for } \tau > 0 \text{ and } T = 0 \\ \dfrac{C_{-R}}{|\tau|^{2(1-\bar{r})}} & , \quad \text{for } \tau < 0 \text{ and } T = 0 \end{cases} . \tag{A.38}$$

where $C_{+R} > 0$ and $C_{-R} > 0$, but they need not be equal. This corresponds to the ansatz in (2.14) which has $C_{+R} = C_{-R}$. We can allow these amplitudes to be distinct in the large M limit. We also examined generalization of the RG analysis in Section 2.3 to the case $C_{+R} \neq C_{-R}$; we found that the perturbative RG then gave inconsistent renormalizations of the coupling g, and so $C_{+R} = C_{-R}$ in the context of the ϵ and $\bar{r}$ expansion.

For the boson Green's function, we write at a complex frequency $|z| \ll J$

$$G_b(z) = C_b \frac{e^{-i(\pi\Delta_b + \theta_b)}}{z^{1-2\Delta_b}} \quad , \quad \text{Im}(z) > 0, \tag{A.39}$$

expressed in terms of the three real parameters, C_b, Δ_b and θ_b. The constraint (A.29) becomes

$$\sin(\pi\Delta_b + \theta_b) > 0 \quad , \quad \sin(\pi\Delta_b - \theta_b) < 0. \tag{A.40}$$

Using (A.30) we obtain in τ space for $|\tau| \gg 1/J$

$$G_b(\tau) = \begin{cases} -\dfrac{C_b \Gamma(2\Delta_b) \sin(\pi\Delta_b + \theta_b)}{\pi |\tau|^{2\Delta_b}} & , \quad \text{for } \tau > 0 \text{ and } T = 0 \\ \dfrac{C_b \Gamma(2\Delta_b) \sin(\pi\Delta_b - \theta_b)}{\pi |\tau|^{2\Delta_b}} & , \quad \text{for } \tau < 0 \text{ and } T = 0 \end{cases} . \tag{A.41}$$

Finally, we can write expressions similar to (A.38) for $Q(\tau)$ for $|\tau| \gg 1/J$

$$Q(\tau) = \begin{cases} \dfrac{C_Q}{|\tau|^{2-\epsilon}} & , \quad \text{for } \tau > 0 \text{ and } T = 0 \\ \dfrac{C_Q}{|\tau|^{2-\epsilon}} & , \quad \text{for } \tau < 0 \text{ and } T = 0 \end{cases} . \tag{A.42}$$

where $C_Q > 0$. This corresponds to the ansatz for $Q(\tau)$ in (2.14)

We can relate the parameters in the ansatzes for the bosonic bath $Q(\tau)$ and the fermionic bath $R(\tau)$ to the parameters in the ansatzes for the Green's functions G_f and G_b, by using the self-consistency conditions (A.33). This yields expressions for $\bar{r}$, ϵ, $C_{\pm R}$, and C_Q in terms of $\Delta_{f,b}$, $\theta_{f,b}$, and $C_{f,b}$:

$$\begin{aligned} \bar{r} &= 1 - \Delta_f - \Delta_b \\ \epsilon &= 2(1 - 2\Delta_f) \\ C_{+R} &= -\frac{C_f C_b \Gamma(2\Delta_f)\Gamma(2\Delta_b) \sin(\pi\Delta_f + \theta_f) \sin(\pi\Delta_b - \theta_b)}{\pi^2} \\ C_{-R} &= \frac{C_f C_b \Gamma(2\Delta_f)\Gamma(2\Delta_b) \sin(\pi\Delta_f - \theta_f) \sin(\pi\Delta_b + \theta_b)}{\pi^2} \\ C_Q &= \frac{\left[C_f \Gamma(2\Delta_f)\right]^2 \sin(\pi\Delta_f + \theta_f) \sin(\pi\Delta_f - \theta_f)}{\pi^2} . \end{aligned} \tag{A.43}$$

However, in keeping with RG computation, we will defer application of the relations in (A.43).

A.3.4 Luttinger constraints

The Luttinger constraints on the spectral asymmetries of the Green's functions are very similar to those in Refs. [71, 200], and can be obtained by the method of Ref. [201]:

$$\begin{aligned} \frac{\theta_f}{\pi} + \left(\frac{1}{2} - \Delta_f\right) \frac{\sin(2\theta_f)}{\sin(2\pi\Delta_f)} &= kp \\ \frac{\theta_b}{\pi} + \left(\frac{1}{2} - \Delta_b\right) \frac{\sin(2\theta_b)}{\sin(2\pi\Delta_b)} &= \frac{1}{2} + p . \end{aligned}$$

These constraints imply $-\pi\Delta_f < \theta_f < \pi\Delta_f$ and $\pi\Delta_b < \theta_b < \pi/2$. The determine the spectral asymmetry angles $\theta_{f,b}$ in terms of the density p and the scaling dimensions $\Delta_{f,b}$.

A.3.5 Self-energies

We can now collect the corresponding expressions for the fermionic and bosonic self energies at $|\tau| \gg 1/J$ and $T = 0$:

$$\begin{aligned}\Sigma_f(\tau) &= -kt^2 \left[\frac{C_b C_{+R} \Gamma(2\Delta_b)}{\pi}\right] \frac{\sin(\pi\Delta_b + \theta_b)}{|\tau|^{2\Delta_b + 2(1-\bar{r})}} \\ &\quad - J^2 \left[\frac{C_f C_Q \Gamma(2\Delta_f)}{\pi}\right] \frac{\sin(\pi\Delta_f + \theta_f)}{|\tau|^{2\Delta_f + 2 - \epsilon}}, \quad \tau > 0\end{aligned} \tag{A.44}$$

$$\begin{aligned}\Sigma_f(\tau) &= -kt^2 \left[\frac{C_b C_{-R} \Gamma(2\Delta_b))}{\pi}\right] \frac{\sin(\pi\Delta_b - \theta_b)}{|\tau|^{2\Delta_b + 2(1-\bar{r})}} \\ &\quad + J^2 \left[\frac{C_f C_Q \Gamma(2\Delta_f)}{\pi}\right] \frac{\sin(\pi\Delta_f - \theta_f)}{|\tau|^{2\Delta_f + 2 - \epsilon}}, \quad \tau < 0\end{aligned} \tag{A.45}$$

$$\Sigma_b(\tau) = -t^2 \left[\frac{C_f C_{-R} \Gamma(2\Delta_f)}{\pi}\right] \frac{\sin(\pi\Delta_f + \theta_f)}{|\tau|^{2\Delta_f + 2(1-\bar{r})}}, \quad \tau > 0 \tag{A.46}$$

$$\Sigma_b(\tau) = -t^2 \left[\frac{(C_f C_{+R} \Gamma(2\Delta_f)}{\pi}\right] \frac{\sin(\pi\Delta_f - \theta_f)}{|\tau|^{2\Delta_f + 2(1-\bar{r})}}, \quad \tau < 0 \tag{A.47}$$

We also use the spectral representations for the self energies

$$\Sigma(z) = \int_{-\infty}^{\infty} \frac{d\Omega}{\pi} \frac{\sigma(\Omega)}{z - \Omega}. \tag{A.48}$$

Performing the inverse of the Laplace transforms in (A.30) we obtain at $T = 0$ and $|\Omega| \ll J$

$$\begin{aligned}\sigma_f(\Omega) &= \frac{\pi k t^2}{\Gamma(2\Delta_b + 2(1-\bar{r}))} \left[\frac{C_b C_{+R} \Gamma(2\Delta_b)}{\pi}\right] \frac{\sin(\pi\Delta_b + \theta_b)}{|\Omega|^{1 - 2\Delta_b - 2(1-\bar{r})}} \\ &\quad + \frac{\pi J^2}{\Gamma(2\Delta_f + 2 - \epsilon)} \left[\frac{C_f C_Q \Gamma(2\Delta_f)}{\pi}\right] \frac{\sin(\pi\Delta_f + \theta_f)}{|\Omega|^{-1 - 2\Delta_f + \epsilon}}, \quad \Omega > 0\end{aligned} \tag{A.49}$$

$$\begin{aligned}\sigma_f(\Omega) &= -\frac{\pi k t^2}{\Gamma(2\Delta_b + 2(1-\bar{r}))} \left[\frac{C_b C_{-R} \Gamma(2\Delta_b)}{\pi}\right] \frac{\sin(\pi\Delta_b - \theta_b)}{|\Omega|^{1 - 2\Delta_b - 2(1-\bar{r})}} \\ &\quad + \frac{\pi J^2}{\Gamma(2\Delta_f + 2 - \epsilon)} \left[\frac{C_f C_Q \Gamma(2\Delta_f)}{\pi}\right] \frac{\sin(\pi\Delta_f - \theta_f)}{|\Omega|^{-1 - 2\Delta_f + \epsilon}}, \quad \Omega < 0\end{aligned} \tag{A.50}$$

$$\sigma_b(\Omega) = \frac{\pi t^2}{\Gamma(2\Delta_f + 2(1-\bar{r}))}\left[\frac{C_f C_{-R}\Gamma(2\Delta_f)}{\pi}\right]\frac{\sin(\pi\Delta_f + \theta_f)}{|\Omega|^{1-2\Delta_f-2(1-\bar{r})}}, \quad \Omega > 0 \tag{A.51}$$

$$\sigma_b(\Omega) = -\frac{\pi t^2}{\Gamma(2\Delta_f + 2(1-\bar{r}))}\left[\frac{C_f C_{+R}\Gamma(2\Delta_f)C_b}{\pi}\right]\frac{\sin(\pi\Delta_f - \theta_f)}{|\Omega|^{1-2\Delta_f-2(1-\bar{r})}}, \quad \Omega < 0 \tag{A.52}$$

A.3.6 Solution of the saddle point equations

We will now determine the constraints placed by the saddle point equations (A.31) and (A.32) on the parameters of the low frequency ansatzes presented in Section A.3.3. As in the body of the text, we will defer application of the self-consistency conditions (A.33), which led to the relations (A.43). This will allow us to make a more complete comparison of the results of the large M theory with that in Section 2.3.

From (A.39) we have

$$\Sigma_b(z) = -\frac{1}{C_b}e^{i(\pi\Delta_b + \theta_b)}z^{(1-2\Delta_b)}. \tag{A.53}$$

Comparing (A.51), (A.52) and (A.53) we have the exponent identity

$$\Delta_f + \Delta_b = \bar{r}\,. \tag{A.54}$$

In the present large M limit, the electron Green's function is given by

$$G_c(\tau) = -G_f(\tau)G_b(-\tau)\,, \tag{A.55}$$

and so the anomalous dimension of the electron operator is

$$\eta_c = 2(\Delta_f + \Delta_b)\,. \tag{A.56}$$

Now we see that the large M result (A.54) is precisely the result (2.55) for the electron anomalous dimension obtained to all orders in the ϵ and $\bar{r}$ expansions.

Comparing the amplitudes of (A.51), (A.52) and (A.53) we obtain

$$\frac{\pi t^2}{\Gamma(2\Delta_f + 2(1-\bar{r}))}\left[\frac{C_f C_{-R}\Gamma(2\Delta_f)}{\pi}\right]\sin(\pi\Delta_f + \theta_f) = \frac{\sin(\pi\Delta_b + \theta_b)}{C_b} \tag{A.57}$$

$$\frac{\pi t^2}{\Gamma(2\Delta_f + 2(1-\bar{r}))}\left[\frac{C_f C_{+R}\Gamma(2\Delta_f)}{\pi}\right]\sin(\pi\Delta_f - \theta_f) = -\frac{\sin(\pi\Delta_b - \theta_b)}{C_b} \tag{A.58}$$

From (A.35) we have

$$\Sigma_f(z) = -\frac{1}{C_f} e^{i(\pi\Delta_f + \theta_f)} z^{(1-2\Delta_f)}. \tag{A.59}$$

The comparison of this with (A.49), (A.50) leads to two possible solutions, appearing as the two intermediate critical phases in Fig. A.1.

A.3.6.1 $\Delta_f > \epsilon/4$

The second J^2 terms in (A.49) and (A.50) are much smaller than the t^2 terms when $\Delta_f - \epsilon/2 > \Delta_b - \bar{r}$; using (A.54), we obtain the condition $\Delta_f > \epsilon/4$. So the J^2 terms can be neglected. Indeed, the low energy solution is then entirely independent of the strength of the exchange interaction, which is rather different from the structure of the FP_4 fixed point in Section 2.3 with both $g*$ and $\gamma*$ non-zero. Instead, it is the FP_3 fixed point, with $\gamma* = 0$, which matches the structure of the present large M solution, and this fixed point was found to be unstable in the RG analysis for $M = 2$, $M' = 1$. We will therefore only write down the saddle point equations here, and not consider this case further.

From (A.59), (A.49) and (A.50) we have

$$\frac{\pi k t^2}{\Gamma(2\Delta_b + 2(1-\bar{r}))} \left[\frac{C_b C_{+R} \Gamma(2\Delta_b)}{\pi}\right] \sin(\pi\Delta_b + \theta_b) = \frac{\sin(\pi\Delta_f + \theta_f)}{C_f} \tag{A.60}$$

$$\frac{\pi k t^2}{\Gamma(2\Delta_b + 2(1-\bar{r}))} \left[\frac{C_b C_{-R} \Gamma(2\Delta_b)}{\pi}\right] \sin(\pi\Delta_b - \theta_b) = -\frac{\sin(\pi\Delta_f - \theta_f)}{C_f} \tag{A.61}$$

The combination of (A.57), (A.61) or (A.58), (A.60) yields

$$\frac{\Gamma(2\Delta_f) \sin(\pi\Delta_f + \theta_f) \sin(\pi\Delta_f - \theta_f)}{\Gamma(2\Delta_b) \sin(\pi\Delta_b + \theta_b) \sin(\pi\Delta_b - \theta_b)} = -k \tag{A.62}$$

We also have from (A.57), (A.58) or (A.60), (A.61)

$$\frac{C_{+R}}{C_{-R}} = -\frac{\sin(\pi\Delta_f + \theta_f) \sin(\pi\Delta_b - \theta_b)}{\sin(\pi\Delta_f - \theta_f) \sin(\pi\Delta_b + \theta_b)} \tag{A.63}$$

which is consistent with the relations in (A.43).

We can also apply the self-consistency relations in (A.43) to the exponents, and obtain $\bar{r} = 1/2$ and $\Delta_f = (2-\epsilon)/4$.

A.3.6.2 $\Delta_f = \epsilon/4$

Now the t^2 and J^2 terms in (A.49) and (A.50) are equally important, and we will see that the structure of this large M solution is very similar to that of the critical point found in the RG analysis in Section 2.3.

Solving (A.54) and $\Delta_f - \epsilon/2 = \Delta_b - \bar{r}$ we obtain the scaling dimensions.

$$\Delta_f = \frac{\epsilon}{4} \tag{A.64}$$

$$\Delta_b = \bar{r} - \frac{\epsilon}{4} \tag{A.65}$$

In the large M limit, the spin correlator is given by

$$\langle \boldsymbol{S}(\tau) \cdot \boldsymbol{S}(0) \rangle \sim -G_f(\tau) G_f(-\tau) \tag{A.66}$$

and so the anomalous dimension of the spin operator is

$$\eta_S = 4\Delta_f \tag{A.67}$$

We now see that the spin anomalous dimension implied by the large M equations (A.64) and (A.67) is consistent with the result (2.53) obtained to all orders in the ϵ and $\bar{r}$ expansion.

Comparison of the amplitude of (A.49) with (A.59) yields

$$\begin{aligned} kt^2 \frac{C_b C_{+R} \Gamma(2\bar{r} - \epsilon/2)}{\Gamma(2 - \epsilon/2)} & \sin(\pi \Delta_b + \theta_b) \\ + J^2 \frac{C_f C_Q \Gamma(\epsilon/2)}{\Gamma(2 - \epsilon/2)} & \sin(\pi \Delta_f + \theta_f) = \frac{\sin(\pi \Delta_f + \theta_f)}{C_f} \end{aligned} \tag{A.68}$$

while the comparison of (A.50) with (A.59) yields

$$\begin{aligned} -kt^2 \frac{C_b C_{-R} \Gamma(2\bar{r} - \epsilon/2)}{\Gamma(2 - \epsilon/2)} & \sin(\pi \Delta_b - \theta_b) \\ + J^2 \frac{C_f C_Q \Gamma(\epsilon/2)}{\Gamma(2 - \epsilon/2)} & \sin(\pi \Delta_f - \theta_f) = \frac{\sin(\pi \Delta_f - \theta_f)}{C_f} \end{aligned} \tag{A.69}$$

Comparison of (A.68) and (A.69) again yields (A.63), which is consistent with (A.43).

Let us combine the saddle point equations (A.57), (A.58), (A.64), (A.65), (A.68), and (A.69) with self-consistency equations (A.43), and collect all the equations which determine the parameters $\Delta_{f,b}$, $\theta_{f,b}$, and $C_{f,b}$ in the low frequency ansatzes for G_f and G_b in (A.35) and (A.39). All these equations reduce to $\epsilon = 1$, $\bar{r} = 1/2$, and the following independent equations

$$\begin{aligned} \Delta_f &= \frac{1}{4} \\ \Delta_b &= \frac{1}{4} \\ t^2 C_f^2 C_b^2 \cos(2\theta_f) &= \pi \\ J^2 C_f^4 \cos(2\theta_f) - kt^2 C_f^2 C_b^2 \cos(2\theta_b) &= \pi \,. \end{aligned} \tag{A.70}$$

Note that the values of Δ_f and Δ_b above, combined with (A.56) and (A.67) yield the self-consistent values in (2.56). For the last two equations in (A.70), notice the bounds $|\theta_f| < \pi/4$ and $\pi/4 < \theta_b < \pi/2$ below (A.44); so all the co-efficients on the left hand sides of (A.70) are positive, and the last two equations determine the values of C_f and C_b. The values of θ_f and θ_b are then determined by the particle density p from (A.44). So this low energy solution can exist at a variable particle density, and the present low energy $M = \infty$ theory describes a potential critical phase, rather than a critical point.

Finally, let us note the form of the electron Green's function from (A.55)

$$G_c(\tau) = \begin{cases} \dfrac{C_f C_b \sin(\pi/4 + \theta_f)\sin(\pi/4 - \theta_b)}{\pi|\tau|} & , \quad \text{for } \tau > 0 \text{ and } T = 0 \\ \dfrac{C_f C_b \sin(\pi/4 - \theta_f)\sin(\pi/4 + \theta_b)}{\pi|\tau|} & , \quad \text{for } \tau < 0 \text{ and } T = 0 \end{cases} . \tag{A.71}$$

The exponent and signs of (A.71) agree with the self-consistent electron Green's function obtained in (2.57) (recall (A.36) and (A.40)), but it appears that the magnitudes of the amplitudes in (A.71) can be different between $\tau > 0$ and $\tau < 0$. This is a subtle feature of the large M theory which is not reproduced by the ϵ and $\bar{r}$ expansion in the body of the paper. This is related to the discussion below (A.38).

Also note that the $1/\tau$ decay of (A.71) is similar to that of a Fermi liquid. Nevertheless, this state is not a Fermi liquid because the spin correlator in (A.66) decays as $1/|\tau|$, in contrast to the $1/\tau^2$ decay expected in a Fermi liquid. The exponents in (A.66) and (A.71) can be understood together in a picture of fractionalization of the electron into spinons and holons, where the spinon and holon correlators both decay as $1/\sqrt{\tau}$.

A.4 RG details

This appendix contains further details on the RG computation of Section 2.3.

The beta functions are defined as follows:

$$\beta(g) = \mu \frac{dg}{d\mu}|_{g_0}\,; \qquad \beta(\gamma) = \mu \frac{d\gamma}{d\mu}|_{\gamma_0} \tag{A.72}$$

To begin,

$$\mu \frac{dg_0}{d\mu} = 0 = \bar{r}\frac{\mu^{\bar{r}} Z_g g}{\sqrt{Z_f Z_b}} + \mu \frac{\mu^{\bar{r}} g}{\sqrt{Z_f Z_b}}\frac{dZ_g}{d\mu} + \mu \frac{\mu^{\bar{r}} Z_g}{\sqrt{Z_f Z_b}}\frac{dg}{d\mu} - \frac{\mu}{2}\frac{\mu^{\bar{r}} Z_g g}{\sqrt{Z_f Z_b}}\left[\frac{1}{Z_f}\frac{dZ_f}{d\mu} + \frac{1}{Z_b}\frac{dZ_b}{d\mu}\right], \tag{A.73}$$

which gives us,

$$\bar{r}gZ_gZ_fZ_b + \beta(g)\left[Z_gZ_fZ_b + gZ_fZ_b\frac{\partial Z_g}{\partial g} - \frac{g}{2}\left(Z_gZ_b\frac{\partial Z_f}{\partial g} + Z_gZ_f\frac{\partial Z_b}{\partial g}\right)\right] \\ + \beta(\gamma)\left[gZ_fZ_b\frac{\partial Z_g}{\partial \gamma} - \frac{g}{2}\left(Z_gZ_b\frac{\partial Z_f}{\partial \gamma} + Z_gZ_f\frac{\partial Z_b}{\partial \gamma}\right)\right] = 0\,. \tag{A.74}$$

Similarly, we have

$$\frac{\epsilon}{2}\gamma Z_\gamma Z_f + \beta(g)\gamma\left[Z_f\frac{\partial Z_\gamma}{\partial g} - Z_\gamma\frac{\partial Z_f}{\partial g}\right] + \beta(\gamma)\left[\gamma Z_f\frac{\partial Z_\gamma}{\partial \gamma} + Z_fZ_\gamma - \gamma Z_\gamma\frac{\partial Z_f}{\partial \gamma}\right] = 0\,. \tag{A.75}$$

A.4.1 Flow away from criticality

For the flow equation of s at one-loop, we will follow the momentum-shell RG procedure, where the cut-off D is kept explicitly. In this case, we introduce masses for bosons and fermions, but keeping in mind that only their difference is physically relevant. To this end we consider the Fourier-transformed action,

$$S(D-\delta D) = S_\psi(D-\delta D) + S_g(D-\delta D) + S_\gamma(D-\delta D) + S_\phi(D-\delta D) \\ + \frac{1}{\beta}\sum_{i\omega_n,\alpha} f_\alpha^\dagger\left[-i\omega_n + \lambda + m_f + \Sigma_F\right]f_\alpha + \frac{1}{\beta}\sum_{i\omega_n} b^\dagger\left[-i\omega_n + \lambda + m_b + \Sigma_B\right]b\,, \tag{A.76}$$

where the self energies are evaluated as follows:

$$\Sigma_a = g_0^2\int_{D-\delta D}^{D} dk\frac{k^r}{i\omega_n - \lambda - k - mb} = -g_0^2 D^{r-1}\left(\delta D + (i\omega_n - \lambda - m_b)\frac{\delta D}{D}\right) \\ = -g^2\left(\delta D + (i\omega_n - \lambda - m_b)\frac{\delta D}{D}\right) \qquad (\text{with } \; g^2 \equiv g_0^2 D^{r-1})\,, \tag{A.77}$$

$$\Sigma_b = \gamma_0^2\frac{3}{4}\frac{S_d}{2}\int_{D-\delta D}^{D} dk\frac{k^{d-2}}{i\omega_n - \lambda - k - m_f} = -\frac{3}{4}\gamma_0^2\frac{S_d}{2}D^{d-3}\left(\delta D + (i\omega_n - \lambda - m_f)\frac{\delta D}{D}\right) \\ = -\frac{3}{4}\gamma^2\frac{S_d}{2\widetilde{S}_{d+1}}\left(\delta D + (i\omega_n - \lambda - m_f)\frac{\delta D}{D}\right) \qquad (\text{with } \; \gamma^2 \equiv \gamma_0^2 D^{d-3}\widetilde{S}_{d+1})\,, \tag{A.78}$$

$$\Sigma_c = 2g_0^2\int_{D-\delta D}^{D} dk\frac{k^r}{i\omega_n - \lambda - k - mb} = -2g_0^2 D^{r-1}\left(\delta D + (i\omega_n - \lambda - m_b)\frac{\delta D}{D}\right) \\ = -2g^2\left(\delta D + (i\omega_n - \lambda - m_b)\frac{\delta D}{D}\right) \qquad (\text{with } \; g^2 \equiv g_0^2 D^{r-1})\,, \tag{A.79}$$

with $\Sigma_F = \Sigma_a + \Sigma_b$ and $\Sigma_B = \Sigma_c$. The scaling factor is $l = 1 + \delta D/D$ such that under the scaling $k' = lk$ and $i\omega' = li\omega$. Thus we have,

$$
\begin{aligned}
S'(D) &= l^{-3-r}(S'_c(D) + S'_g(D)) + l^{-1}S'_\gamma(D) + l^{-d+1}S'_\phi(D) \\
&\quad + \frac{l^{-2}}{\beta}\sum_{i\omega'_n} f^\dagger[(-i\omega'_n + \lambda)(1 + g^2\frac{\delta D}{D} + \frac{3}{4}\gamma^2\frac{\delta D}{D}) + lm_f(1 + \frac{3}{4}\gamma^2\frac{\delta D}{D}) \\
&\qquad\qquad - lg^2\delta D + lg^2 m_b\frac{\delta D}{D} - l\frac{3}{4}\gamma^2\delta D]f \\
&\quad + \frac{l^{-2}}{\beta}\sum_{i\omega'_n} b^\dagger\left[(-i\omega'_n + \lambda)(1 + 2g^2\frac{\delta D}{D}) + lm_b - l2g^2\delta D + l2g^2 m_f\frac{\delta D}{D}\right]b\,.
\end{aligned}
\tag{A.80}
$$

Thus we have the following expressions for the renormalized masses:

$$
m'_f = \left(1 + \frac{\delta D}{D} - g^2\frac{\delta D}{D}\right)m_f - \left(g^2 + \frac{3}{4}\gamma^2\right)\frac{\delta D}{D} + g^2 m_b\frac{\delta D}{D}\,, \tag{A.81}
$$

$$
m'_b = \left(1 + \frac{\delta D}{D} - 2g^2\frac{\delta D}{D}\right)m_b - 2g^2\frac{\delta D}{D} + 2g^2 m_f\frac{\delta D}{D}\,. \tag{A.82}
$$

Note that along with this the fermionic and bosonic operators, bosonic field and the coupling constants are also renormalized. For instance, $f' = l^{-1+g^2/2+3\gamma^2/8}f$ and $b' = l^{-1+g^2}b$. In addition to the self-energy corrections there is also a vertex correction to γ at this order. However, this does not influence the mass renormalization and thus we can already proceed to calculate the flow equation for the mass. In our notation introduced earlier, $s \equiv m_f - m_b$. Now,

$$
\beta(s) \equiv -D\frac{\delta s}{\delta D} = -s + 3g^2 s - g^2 + \frac{3}{4}\gamma^2\,. \tag{A.83}
$$

We can compute the relevant eigenvalue associated with the flow of s at the fixed points of the beta functions, and find

$$
\lambda_s = 1 + \frac{3\epsilon - 16\bar{r}}{6}\,, \tag{A.84}
$$

at the non-trivial fixed point FP_4. At the self-consistent values, *i.e.*, $\epsilon = 1$ and $\bar{r} = 1/2$ we have $\lambda_s = 1/6$, although we cannot trust the result at such large values of ϵ and $\bar{r}$. Similarly, at FP_1, FP_2, and FP_3 we find λ_s to be 1, 1, and $1 - 2\bar{r}$ respectively.

Within the momentum-shell RG, we get the same beta functions for g and γ, after considering the vertex correction as well.

A.4.2 Particle density

We can also calculate the particle densities ($n_{f/b}$). This can be done at any s. We will first make the following identification: $s = \tilde{s}/\beta$, such that $\tilde{s}$ is small. This will facilitate us to do

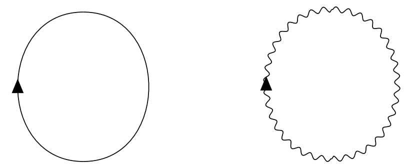

(a) (b)

Figure A.2: Lowest order diagrams for particle densities. There are corrections, which are expected to vanish at $T = 0$.

a small $\tilde{s}$ expansion. From the diagrams we find,

$$q_f(\lambda) = 2e^{-\beta(\lambda+s)} \sim 2e^{-\beta\lambda}(1-\tilde{s})\,, \tag{A.85}$$

$$q_b(\lambda) = e^{-\beta\lambda}\,. \tag{A.86}$$

$q(\lambda) = q_f(\lambda) + q_b(\lambda)$, such that,

$$n_{f/b} = \lim_{\lambda\to\infty} \frac{q_{f/b}}{q}\,. \tag{A.87}$$

So, we have,

$$n_f = \frac{2-2\tilde{s}}{3-2\tilde{s}} \sim \frac{2}{3}(1-\tilde{s})(1+\frac{2}{3}\tilde{s}) \sim \frac{2}{3} - \frac{2}{9}\tilde{s}\,, \tag{A.88}$$

$$n_b = \frac{1}{3-2\tilde{s}} \sim \frac{1}{3}(1+\frac{2}{3}\tilde{s}) \sim \frac{1}{3} + \frac{2}{9}\tilde{s}\,. \tag{A.89}$$

Note that we still satisfy the particle density constraint $n_f + n_b = 1$ exactly.

B

Appendix for chapter 3

B.1 Stability of fixed points

In this subsection we discuss the stability of fixed points found above and listed in Eqs. (3.39) - (3.42). First we construct the stability matrix,

$$J \equiv \begin{bmatrix} J_1 & J_2 & J_3 \\ J_4 & J_5 & J_6 \\ J_7 & J_8 & J_9 \end{bmatrix} , \tag{B.1}$$

where,

$$\begin{aligned} &J_1 \equiv \frac{\partial \beta_\gamma}{\partial \gamma} = \frac{\epsilon - \epsilon'}{2} - \frac{U}{\pi A_0^2} + \frac{\zeta}{2\pi} , \quad J_2 \equiv \frac{\partial \beta_\gamma}{\partial U} = -\frac{\gamma}{\pi A_0^2} , \quad J_3 \equiv \frac{\partial \beta_\gamma}{\partial \zeta} = \frac{\gamma}{2\pi} , \\ &J_4 \equiv \frac{\partial \beta_U}{\partial \gamma} = -\frac{3\gamma}{4\pi} , \quad J_5 \equiv \frac{\partial \beta_U}{\partial U} = \epsilon , \quad J_6 \equiv \frac{\partial \beta_U}{\partial \zeta} = 0 , \\ &J_7 \equiv \frac{\partial \beta_\zeta}{\partial \gamma} = \frac{\gamma}{\pi A_0^2} , \quad J_8 \equiv \frac{\partial \beta_\zeta}{\partial U} = 0 , \quad J_9 \equiv \frac{\partial \beta_\zeta}{\partial \zeta} = -\epsilon' + \frac{\zeta}{\pi} . \end{aligned} \tag{B.2}$$

The eigenvalues of matrix J at the trivial fixed points (3.39) and (3.40) are $(\epsilon, (\epsilon - \epsilon')/2, -\epsilon')$ and $(\epsilon, (\epsilon + \epsilon')/2, \epsilon')$ respectively. Thus, for any positive values of ϵ and ϵ' all the eigenvalues corresponding to FP_2 are positive, and thus it is a stable fixed point. The eigenvalues at the non-trivial fixed points (3.41) and (3.42) are given by the roots of their respective characteristic polynomials,

$$p_3(\lambda) = \lambda^3 + a_3\lambda^2 + b_3\lambda + c_3 , \quad p_4(\lambda) = \lambda^3 + a_4\lambda^2 + b_4\lambda + c_4 , \tag{B.3}$$

where,

$$a_{3,4} = -\frac{\epsilon \pm \xi}{3}\,, \quad b_{3,4} = \frac{\epsilon}{9}(-11\epsilon \mp 2\xi)\,, \quad c_{3,4} = \pm\frac{2}{9}\epsilon\xi(\epsilon \pm \xi)\,. \tag{B.4}$$

Recall that for non-trivial fixed points to be real we need ξ to be real as well as $\epsilon > \xi$. Now examining the coefficients of the characteristic polynomials we see that the fixed point (3.41) has one negative eigenvalue and two positive eigenvalues, while (3.42) has two negative eigenvalues and one positive eigenvalue.

B.2 Onset of spin glass order in a metal

This Appendix will address the transition from the disordered Fermi liquid phase to the metallic spin glass. There are 3 possible theories of this transition:
(i) At large U, and for $p > 0$, eliminate the doubly-occupied site, and address the transition in the t-J model. This yields a deconfined critical point, described in Ref. [2].
(ii) At small U, and at $p = 0$, perform the RG analysis presented in Section 3.4. This yields fixed point FP_3, which could describe the onset of spin glass order in a metal.
(iii) Use a weak-coupling Landau functional approach to quantum spin glasses [63, 202], which we review in this section.

We begin with the disordered-averaged imaginary time path integral of the Hamiltonian in (3.1), keeping track of replica indices, $a, b = 1 \ldots n$; at the end we need to take the $n \to 0$ limit. The path integral has the form

$$\begin{aligned}
\mathcal{Z} &= \int \mathcal{D}Q^{ab}(\tau_1,\tau_2) \exp\left(-N\mathcal{S}[Q]\right) \\
\mathcal{S}[Q] &= \frac{3J^2}{4}\int d\tau_1 d\tau_2 \sum_{ab} \Big[Q^{ab}(\tau_1,\tau_2)\Big]^2 + \mathcal{S}_1[Q]
\end{aligned} \tag{B.5}$$

where the functional $\mathcal{S}_1[Q]$ is to obtained by a path integral over the electrons. Near the transition, it turns out to be sufficient to evaluate $\mathcal{S}_1[Q]$ in powers of J^2 and U to understand the basic structure of the critical point, as in other theories of the onset of broken symmetry in metals [203]. Explicitly the expression is

$$\begin{aligned}
\exp\left(-N\mathcal{S}_1[Q]\right) &= \int \mathcal{D}R^{ab}(\tau_1,\tau_2) \exp\left(-\frac{Nt^2}{2}\left|R^{ab}(\tau_1,\tau_2)\right|^2 - N\mathcal{S}_2[Q,R]\right) \\
\exp\left(-\mathcal{S}_2[Q,R]\right) &= \int \mathcal{D}c_\alpha^a(\tau) \exp\bigg\{-\int d\tau \left[c_\alpha^{a\dagger}(\tau)\left(\frac{\partial}{\partial\tau} - \mu\right)c_\alpha^a(\tau) + \frac{U}{2}c_\alpha^{a\dagger}(\tau)c_\beta^{a\dagger}(\tau)c_\beta^a(\tau)c_\alpha^a(\tau)\right] \\
&+ t^2\int d\tau d\tau' R^{ab}(\tau,\tau')c_\alpha^{a\dagger}(\tau)c_\alpha^b(\tau') + \frac{J^2}{2}\int d\tau d\tau' Q^{ab}(\tau,\tau')\boldsymbol{S}^a(\tau)\cdot\boldsymbol{S}^b(\tau')\bigg\}
\end{aligned} \tag{B.6}$$

where the second expression generalizes (2.10). Analyzing the saddle-point equations of (B.5) and (B.6) in the large N limit, it can be verified that we obtain the replica generalizations of the self-consistency conditions in (3.5) and (2.9).

First, we explicitly solve the saddle-point equations for R at $J^2 = U = 0$. The solution is replica diagonal and depends only on time differences

$$R^{ab}(\tau, \tau') = \delta^{ab} R(\tau - \tau')\,. \tag{B.7}$$

The equation for $R(\tau)$ is easily expressed in frequency space

$$R(i\omega) = \frac{1}{i\omega + \mu - t^2 R(i\omega)}\,, \tag{B.8}$$

and yields the Green's function of a disordered Fermi liquid with the expected semi-circular density of the states

$$R(i\omega) = \frac{1}{2t^2}\left(i\omega + \mu - \sqrt{(i\omega+\mu)^2 - 4t^2}\right)\,. \tag{B.9}$$

For $|\mu| < 2t$, we have a non-zero density of states at the Fermi level, and the low frequency behavior

$$R(i\omega) = \frac{\mu}{2t^2} - \mathrm{sgn}(\omega)\frac{\sqrt{4t^2 - \mu^2}}{2t^2}\,. \tag{B.10}$$

This is just the Fourier transform of the electron Green's function in (3.25) with $\Delta_f + \Delta_b = 1/2$.

Next we expand (B.6) in powers of J^2 and U, and evaluate the path integral over the c^a_α. This results in an expression for $\mathcal{S}[Q]$ as a polynomial in the $Q^{ab}(\tau_1, \tau_2)$ which has the form described in Ref. [63]; see also Chapter 22 in Ref. [26]. A crucial term in this expansion is a term linear in Q of the form

$$\begin{aligned} -\frac{J^2}{2}\int d\tau d\tau' Q^{ab}(\tau,\tau')\left\langle \boldsymbol{S}^a(\tau)\cdot\boldsymbol{S}^b(\tau')\right\rangle \;&\sim\; -\frac{J^2}{2}\int d\tau d\tau' \frac{Q^{aa}(\tau,\tau')}{(\tau-\tau')^2} \\ &\sim\; TJ^2 \sum_{\omega_n} Q^{aa}(i\omega_n, -i\omega_n)\left[r + |\omega_n|\right]\,, \end{aligned} \tag{B.11}$$

where $\omega_n = 2\pi n T$ is a Matsubara frequency. The $1/\tau^2$ term is characteristic of the decay of spin correlations in a disordered Fermi liquid, a direct consequence of the constant density of states at the Fermi level in (B.10). The frequency dependence in (B.11) is primarily responsible for the low frequency dynamics of the spin glass order parameter, and the frequency depends of all the other terms in the action for Q can be safely neglected. Near the critical point, it turns out to be sufficient to keep only the following terms in the effective action [63]

$$\begin{aligned}\mathcal{S}[Q] &= \frac{r}{\kappa}\int d\tau\, Q^{aa}(\tau,\tau) - \frac{1}{\pi\kappa}\int d\tau d\tau'\,\frac{Q^{aa}(\tau,\tau')}{(\tau-\tau')^2} \\ &- \frac{\kappa}{3}\int d\tau_1 d\tau_2 d\tau_3 \sum_{abc} Q^{ab}(\tau_1,\tau_2)Q^{bc}(\tau_2,\tau_3)Q^{ca}(\tau_3,\tau_1) + \frac{u}{2}\int d\tau\,[Q^{aa}(\tau,\tau)]^2\end{aligned} \tag{B.12}$$

Here we have performed a shift by an unimportant short-time correlator, $Q^{ab}(\tau,\tau') \to Q^{ab}(\tau,\tau') - C\delta^{ab}\delta(\tau-\tau')$, to eliminate quadratic terms in the action similar to that in (B.5).

It is now a straightforward matter to solve the saddle point equations of (B.12). The saddle-point value Q has the following structure in Matsubara frequency space

$$Q^{ab}(i\omega_n, i\epsilon_n) = \frac{\delta_{\omega_n,0}\delta_{\epsilon_n,0}}{T^2}\, q^{ab} + \frac{\delta_{\omega_n+\epsilon_n,0}}{T}\,\delta^{ab}\, Q(i\omega_n)\,. \tag{B.13}$$

Here q^{ab} is the spin-glass order parameter, which is non-zero only for the parameter r (appearing in (B.11)) smaller than a critical value, $r < r_c$. Focusing first on the Fermi liquid state found for $r > r_c$, it was shown that the second term in (B.13) has the form

$$Q(i\omega_n) \sim -\sqrt{r - r_c + |\omega_n|} \quad , \quad r \geq r_c\,. \tag{B.14}$$

This quantity is just the Fourier transform of $Q(\tau)$ appearing in (3.5) and (2.9), and so at the critical point $r = r_c$, the spin correlations decay as

$$Q(\tau) \sim \frac{1}{|\tau|^{3/2}} \quad , \quad r = r_c\,. \tag{B.15}$$

Comparing with (3.35), we see that $\epsilon' = -1/2$. So the present critical point appears distinct from the fixed point FP_3 found in Section 3.4, which can satisfy the self-consistency conditions only for $\epsilon' > 0$.

Finally, let us also recall [63, 202] the nature of the solution for $r < r_c$. Here the spin glass order parameter q^{ab} is non-zero. In the simplest replica-symmetric ansatz, $q^{ab} = q_{EA}$, the Edwards-Anderson order parameter for all a and b, and

$$q_{EA} \sim r_c - r \quad , \quad r < r_c \tag{B.16}$$

At $T > 0$, the stable solution has replica symmetry breaking, but the structure of this is very similar to that of the classical spin glass. The replica diagonal term $Q(\tau)$ in (B.13) is the only one with non-trivial time dependence, and this remains pinned at the $r = r_c$ form in (B.15) for $r < r_c$.

C

Appendix for chapter 4

C.1 Stability of fixed points

Here we discuss the stability of the fixed points (Eqs. (4.24)-(4.31)) by looking at the eigenvalues of the following stability matrix:

$$J \equiv \begin{bmatrix} J_1 & J_2 & J_3 \\ J_4 & J_5 & J_6 \\ J_7 & J_8 & J_9 \end{bmatrix} , \tag{C.1}$$

where,

$$\begin{aligned}
&J_1 \equiv \frac{\partial \beta(g)}{\partial g} = -\bar{r} + 3g^2 + \frac{3}{8}\gamma^2 + \frac{v^2}{2} , \quad J_2 \equiv \frac{\partial \beta(g)}{\partial \gamma} = \frac{3}{4} g\gamma , \quad J_3 \equiv \frac{\partial \beta(g)}{\partial v} = gv , \\
&J_4 \equiv \frac{\partial \beta(\gamma)}{\partial g} = 4\gamma g , \quad J_5 \equiv \frac{\partial \beta(\gamma)}{\partial \gamma} = -\frac{\epsilon}{2} + 3\gamma^2 + 2g^2 , \quad J_6 \equiv \frac{\partial \beta(\gamma)}{\partial v} = 0 , \\
&J_7 \equiv \frac{\partial \beta(v)}{\partial g} = 4vg , \quad J_8 \equiv \frac{\partial \beta(v)}{\partial \gamma} = 0 , \quad J_9 \equiv \frac{\partial \beta(v)}{\partial v} = -\frac{\epsilon'}{2} + 3v^2 + 2g^2 .
\end{aligned} \tag{C.2}$$

We shall consider $\bar{r} > 0$, $\epsilon > 0$ and $\epsilon' > 0$. From the eigenvalues,

$$E_1^{(1)} = -\bar{r} , \quad E_2^{(1)} = -\frac{\epsilon}{2} , \quad E_3^{(2)} = -\frac{\epsilon'}{2} , \tag{C.3}$$

it is immediately clear that the Gaussian fixed point FP_1 is unstable. The fixed point FP_2 has the following eigenvalues:

$$E_1^{(2)} = 2\bar{r}\,, \quad E_2^{(2)} = \frac{4\bar{r} - \epsilon}{2}\,, \quad E_3^{(2)} = \frac{4\bar{r} - \epsilon'}{2}\,. \tag{C.4}$$

So FP_2 is stable for any $\epsilon < 4\bar{r}$ and $\epsilon' < 4\bar{r}$. The fixed point FP_3 is unstable and has one relevant direction as seen from the eigenvalues,

$$E_1^{(3)} = \epsilon\,, \quad E_2^{(3)} = \frac{3\epsilon - 16\bar{r}}{2}\,, \quad E_3^{(3)} = -\frac{\epsilon'}{2}\,. \tag{C.5}$$

FP_4 is stable if $4\bar{r} < \epsilon < 16\bar{r}/3$ and $\epsilon' < 16\bar{r} - 3\epsilon$, which follows from its eigenvalues,

$$E_1^{(4)} = 5\epsilon - 16\bar{r} - \Psi\,, \quad E_2^{(4)} = 5\epsilon - 16\bar{r} + \Psi\,, \quad E_3^{(4)} = \frac{16\bar{r} - 3\epsilon - \epsilon'}{2}\,, \tag{C.6}$$

where $\Psi = \sqrt{768\bar{r}^2 - 384\bar{r}\epsilon + 49\epsilon^2} > 0$. The fixed point FP_5 is unstable and has one relevant direction as is evident from the eigenvalues,

$$E_1^{(5)} = -\frac{\epsilon}{2}\,, \quad E_2^{(5)} = \epsilon'\,, \quad E_3^{(5)} = \frac{\epsilon' - 4\bar{r}}{4}\,. \tag{C.7}$$

The fixed point FP_6 has the eigenvalues,

$$E_1^{(6)} = \epsilon\,, \quad E_2^{(6)} = \epsilon'\,, \quad E_3^{(6)} = \frac{-16\bar{r} + 3\epsilon + 4\epsilon'}{16}\,. \tag{C.8}$$

Thus it is stable if $-16\bar{r} + 3\epsilon + 4\epsilon' > 0$. We will discuss the eigenvalues at FP_7,

$$E_1^{(7)} = \frac{4\bar{g}^2 - \epsilon}{2}\,, \quad E_2^{(7)} = 0\,, \quad E_3^{(7)} = 16\bar{r} - 8\bar{g}^2\,. \tag{C.9}$$

It is then clear that FP_7 is marginally stable if $2\bar{r} > \bar{g}^2 > \epsilon/4$. The first inequality is trivially satisfied by the points on the ellipse describing FP_7. The second inequality is satisfied if $\epsilon < 4\bar{r}$ (since $\bar{g}^2 < \bar{r}$), which leads to atleast one stable fixed points. For lower values of ϵ there is a fixed line on the ellipse describing FP_7.

The stability of FP_8 can be best studied by looking at the characteristic equation,

$$E^3 + AE^2 + BE + C = 0\,, \tag{C.10}$$

where $A = -J_1 - J_5 - J_9 = -2(g^{*2} + \gamma^{*2} + v^{*2}) < 0$, $B = J_1J_5 + J_1J_9 + J_5J_9 - J_2J_4 - J_3J_7 = g^{*2}\gamma^{*2} + 4\gamma^{*2}v^{*2} > 0$, and $C = J_3J_7J_5 + J_2J_4J_9 - J_1J_5J_9 = 6g^{*2}\gamma^{*2}v^{*2} > 0$, with g^*, γ^*, v^* being the values at FP_8. It is clear that $C = -E_1^{(8)}E_2^{(8)}E_3^{(8)}$, $B = E_1^{(8)}E_2^{(8)} + E_1^{(8)}E_3^{(8)} + E_2^{(8)}E_3^{(8)}$, and $A = -(E_1^{(8)} + E_2^{(8)} + E_3^{(8)})$, where $E_i^{(8)}$ are the eigenvalues. So, if FP_8 is real, one of its eigenvalue is negative and so it is an unstable fixed point.

C.2 Solving the saddle point equations in large-M analysis

We proceed by introducing a low-frequency ansatz for the Green's functions defined earlier. In terms of the imaginary time, τ, such that $|\tau| \gg 1/J$ we write at $T = 0$,

$$G_a(\tau) = -\text{sgn}(\tau)\frac{C_a\Gamma(2\Delta_a)\sin(\pi\Delta_a + \text{sgn}(\tau)\theta_a)}{\pi|\tau|^{2\Delta_a}}\,, \tag{C.11}$$

where parameters C_a, Δ_a and θ_a are real. To simplify the expression, we define

$$C_a^{\pm} = \frac{C_a\Gamma(2\Delta_a)\sin(\pi\Delta_a \pm \text{sgn}(\tau)\theta_a)}{\pi}\,. \tag{C.12}$$

Positivity constraints on the spectral densities impose restrictions on asymmetry angles:

$$-\pi\Delta_f < \theta_f < \pi\Delta_f\,, \quad \pi\Delta_b < \theta_b < \pi/2\,, \quad \pi\Delta_d < \theta_d < \pi/2\,. \tag{C.13}$$

We can now collect the corresponding expressions for self energies at $|\tau| \gg 1/J$ and $T = 0$ by plugging (C.11) into (4.61)-(4.63) and obtain,

$$\Sigma_b(\tau) = -\text{sgn}(\tau)t^2\left(\frac{C_b^+C_f^+C_f^-}{|\tau|^{4\Delta_f+2\Delta_b}} - \frac{C_d^-{C_f^+}^2}{|\tau|^{4\Delta_f+2\Delta_d}}\right) + \text{sgn}(\tau)k^2L^2\frac{C_b^+C_d^+C_d^-}{|\tau|^{2\Delta_b+4\Delta_d}}\,, \tag{C.14}$$

$$\Sigma_d(\tau) = -\text{sgn}(\tau)t^2\left(\frac{C_d^+C_f^+C_f^-}{|\tau|^{4\Delta_f+2\Delta_d}} - \frac{C_b^-{C_f^+}^2}{|\tau|^{4\Delta_f+2\Delta_b}}\right) + \text{sgn}(\tau)k^2L^2\frac{C_b^+C_b^-C_d^+}{|\tau|^{2\Delta_d+4\Delta_b}}\,, \tag{C.15}$$

$$\Sigma_f(\tau) = \text{sgn}(\tau)kt^2\left(\frac{C_f^+C_b^+C_b^-}{|\tau|^{2\Delta_f+4\Delta_b}} - \frac{2C_f^-C_b^+C_d^+}{|\tau|^{2\Delta_f+2\Delta_b+2\Delta_d}} + \frac{C_f^+C_d^+C_d^-}{|\tau|^{2\Delta_f+4\Delta_d}}\right) - \text{sgn}(\tau)J^2\frac{{C_f^+}^2C_f^-}{|\tau|^{6\Delta_f}}. \tag{C.16}$$

Using the spectral representation of the self energies,

$$\Sigma(z) = \int_{-\infty}^{\infty}\frac{d\Omega}{\pi}\frac{\sigma(\Omega)}{z - \Omega}\,. \tag{C.17}$$

we perform the Laplace transforms at $T=0$, $|\Omega| \ll J$ and obtain

$$\begin{aligned}
\sigma_b(\Omega) = &\quad \frac{\pi t^2}{\Gamma(2\Delta_b+4\Delta_f)} \frac{C_b^+ C_f^+ C_f^-}{|\Omega|^{1-2\Delta_b-4\Delta_f}} - \frac{\pi t^2}{\Gamma(2\Delta_d+4\Delta_f)} \frac{C_d^- {C_f^+}^2}{|\Omega|^{1-2\Delta_d-4\Delta_f}} - \frac{\pi k^2 L^2}{\Gamma(2\Delta_b+4\Delta_d)} \frac{C_b^+ C_d^+ C_d^-}{|\Omega|^{1-2\Delta_b-4\Delta_d}}\,, \\
\sigma_d(\Omega) = &\quad \frac{\pi t^2}{\Gamma(2\Delta_d+4\Delta_f)} \frac{C_d^+ C_f^+ C_f^-}{|\Omega|^{1-2\Delta_d-4\Delta_f}} - \frac{\pi t^2}{\Gamma(2\Delta_b+4\Delta_f)} \frac{C_b^- {C_f^+}^2}{|\Omega|^{1-2\Delta_b-4\Delta_f}} - \frac{\pi k^2 L^2}{\Gamma(2\Delta_d+4\Delta_b)} \frac{C_b^+ C_b^- C_d^+}{|\Omega|^{1-2\Delta_d-4\Delta_b}}\,, \\
\sigma_f(\Omega) = &\quad -\frac{\pi k t^2}{\Gamma(2\Delta_f+4\Delta_b)} \frac{C_f^+ C_b^+ C_b^-}{|\Omega|^{1-2\Delta_f-4\Delta_b}} - \frac{\pi k t^2}{\Gamma(2\Delta_f+4\Delta_d)} \frac{C_f^+ C_d^+ C_d^-}{|\Omega|^{1-2\Delta_f-4\Delta_d}} \\
&\quad + \frac{\pi k t^2}{\Gamma(2\Delta_f+2\Delta_b+2\Delta_d)} \frac{2C_f^- C_b^+ C_d^+}{|\Omega|^{1-2\Delta_f-2\Delta_b-2\Delta_d}} + \frac{\pi J^2}{\Gamma(6\Delta_f)} \frac{{C_f^+}^2 C_f^-}{|\Omega|^{1-6\Delta_f}}\,,
\end{aligned} \tag{C.18}$$

where

$$C_a^{\pm} = \frac{C_a \Gamma(2\Delta_a) \sin(\pi\Delta_a \pm \mathrm{sgn}(\Omega)\theta_a)}{\pi}\,. \tag{C.19}$$

On the other hand, we can rewrite the saddle point equations (4.64) at $|\omega| \ll J$ and perform the analytic continuation to obtain

$$\sigma_a(\Omega) = \quad \frac{1}{C_a} \frac{\sin(\pi\Delta_a + \mathrm{sgn}(\Omega)\theta_a)}{|\Omega|^{2\Delta_a-1}}\,, \quad a = f,\, b,\, d\,. \tag{C.20}$$

Comparison of (C.20) with (C.18) for both positive and negative Ω leads to the solutions to the saddle point equations in Sec. 4.4.3.

C.3 Large M analysis with bosonic spinon + fermionic holon and doublon

We now discuss the other fractionalization scheme, consisting of bosonic spinons $\mathfrak{b}_\alpha$ and fermionic holons $\mathfrak{f}_\ell$ and doublons $\mathfrak{d}_\ell$,

$$c_{\ell\alpha} = \mathfrak{b}_\alpha \mathfrak{f}_\ell^\dagger + \mathcal{J}_{\alpha\beta} \mathfrak{b}_\beta^\dagger \mathfrak{d}_\ell\,, \tag{C.21}$$

where $\mathcal{J}$ is the USp(M) invariant tensor (see Section 2.2 of Ref. [146]), while the spin index $\alpha = 1 \ldots M$ (M even) and the orbital index $\ell = 1 \ldots M'$. This representation has a U(1) gauge invariance,

$$\mathfrak{f}_{i\alpha} \to \mathfrak{f}_{i\alpha} e^{i\phi_i(\tau)}, \quad \mathfrak{b}_{i\ell} \to \mathfrak{b}_{i\ell} e^{i\phi_i(\tau)}, \quad \mathfrak{d}_{i\ell} \to \mathfrak{d}_{i\ell} e^{i\phi_i(\tau)}\,. \tag{C.22}$$

We also have the constraint fixing the U(1) gauge charge on each site,

$$\sum_{\alpha=1}^{M} \mathfrak{b}_{i\alpha}^\dagger \mathfrak{b}_{i\alpha} + \sum_{\ell=1}^{M'} \left(\mathfrak{f}_{i\ell}^\dagger \mathfrak{f}_{i\ell} + \mathfrak{d}_{i\ell}^\dagger \mathfrak{d}_{i\ell}\right) = \frac{M}{2}\,. \tag{C.23}$$

The large M analysis will proceed as Sec. 3.3, Refs. [87] and [2]. We first take the $N \to \infty$ limit and perform disorder average, as discussed in Sec. 2.2 to obtain the single-site action in the large-M limit,

$$\begin{aligned}
\mathcal{Z} &= \int \mathcal{D}\mathfrak{b}_\alpha \mathcal{D}\mathfrak{f}_\ell \mathcal{D}\mathfrak{d}_\ell \mathcal{D}\lambda e^{-\mathcal{S}} \\
\mathcal{S} &= \int_0^{1/T} d\tau \Bigg[\sum_\ell \mathfrak{f}_\ell^\dagger \left(\frac{\partial}{\partial\tau} + \mu + \frac{U}{2} + i\lambda\right) \mathfrak{f}_\ell + \sum_\ell \mathfrak{d}_\ell^\dagger \left(\frac{\partial}{\partial\tau} - \mu + \frac{U}{2} + i\lambda\right) \mathfrak{d}_\ell \\
&\qquad\qquad + \sum_\alpha \mathfrak{b}_\alpha^\dagger \left(\frac{\partial}{\partial\tau} + i\lambda\right) \mathfrak{b}_\alpha - i\lambda\frac{M}{2}\Bigg] \\
&+ \frac{t^2}{M} \sum_{\ell,\alpha} \int_0^{1/T} d\tau d\tau' R(\tau-\tau') c_{\ell\alpha}^\dagger(\tau) c_{\ell\alpha}(\tau') \\
&- \frac{J^2}{2M} \sum_{\alpha,\beta} \int_0^{1/T} d\tau d\tau' Q(\tau-\tau') \mathfrak{b}_\alpha^\dagger(\tau)\mathfrak{b}_\beta(\tau)\mathfrak{b}_\beta^\dagger(\tau')\mathfrak{b}_\alpha(\tau') \\
&- \frac{L^2}{M'} \sum_{\ell\ell'} \int_0^{1/T} d\tau d\tau' P(\tau-\tau') \mathfrak{f}_\ell^\dagger(\tau)\mathfrak{d}_{\ell'}(\tau)\mathfrak{d}_{\ell'}^\dagger(\tau')\mathfrak{f}_\ell(\tau')\,,
\end{aligned} \tag{C.24}$$

where T is the temperature. In the large-M limit the Lagrange multiplier, $\lambda(\tau)$ imposes the constraint in Eq. (C.23) and the self-consistency condition reads as follows:

$$\begin{aligned}
R(\tau-\tau') &= -\frac{1}{MM'} \sum_{\ell,\alpha} \left\langle c_{\ell\alpha}(\tau) c_{\ell\alpha}^\dagger(\tau')\right\rangle_{\mathcal{Z}}\,, \\
Q(\tau-\tau') &= \frac{1}{M^2} \sum_{\alpha,\beta} \left\langle \mathfrak{b}_\alpha^\dagger(\tau)\mathfrak{b}_\beta(\tau)\mathfrak{b}_\beta^\dagger(\tau')\mathfrak{b}_\alpha(\tau')\right\rangle_{\mathcal{Z}} \\
P(\tau-\tau') &= \frac{1}{M'^2} \sum_{\ell,\ell'} \left\langle \mathfrak{f}_\ell(\tau)\mathfrak{d}_{\ell'}^\dagger(\tau)\mathfrak{d}_{\ell'}(\tau')\mathfrak{f}_\ell^\dagger(\tau')\right\rangle_{\mathcal{Z}}\,.
\end{aligned} \tag{C.25}$$

C.3.1 Saddle point equations

Introducing bilocal fields

$$G_\mathfrak{b}(\tau,\tau') = -\frac{1}{M}\sum_\alpha \mathfrak{b}_\alpha(\tau)\mathfrak{b}_\alpha^\dagger(\tau')\,,\quad G_\mathfrak{f}(\tau,\tau') = -\frac{1}{M'}\sum_\ell \mathfrak{f}_\ell(\tau)\mathfrak{f}_\ell^\dagger(\tau')\,,\quad G_\mathfrak{d}(\tau,\tau') = -\frac{1}{M'}\sum_\ell \mathfrak{d}_\ell(\tau)\mathfrak{d}_\ell^\dagger(\tau') \tag{C.26}$$

and the corresponding self-energies, we can obtain the saddle point equations:

$$G_{\mathfrak{a}}(i\omega) = \frac{1}{i\omega - \mu_{\mathfrak{a}} - \Sigma_{\mathfrak{a}}(i\omega)}\,, \quad \mathfrak{a} = \mathfrak{f}, \mathfrak{b}, \mathfrak{d} \tag{C.27}$$

$$\Sigma_{\mathfrak{b}}(\tau) = kt^2 R(-\tau) G_{\mathfrak{d}}(\tau) - kt^2 R(\tau) G_{\mathfrak{f}}(\tau) + J^2 Q(\tau) G_{\mathfrak{b}}(\tau)\,, \tag{C.28}$$

$$\Sigma_{\mathfrak{f}}(\tau) = t^2 G_{\mathfrak{b}}(\tau) R(-\tau) + k^2 L^2 G_{\mathfrak{d}}(\tau) P(\tau)\,, \tag{C.29}$$

$$\Sigma_{\mathfrak{d}}(\tau) = -t^2 R(\tau) G_{\mathfrak{b}}(\tau) + k^2 L^2 G_{\mathfrak{f}}(\tau) P(-\tau)\,. \tag{C.30}$$

Here $\mu_{\mathfrak{a}}$ are chemical potentials, determined by U and the saddle point value of λ to satisfy

$$\left\langle \mathfrak{f}^\dagger \mathfrak{f} \right\rangle = \delta_{\mathfrak{f}}\,, \tag{C.31}$$

$$\left\langle \mathfrak{b}^\dagger \mathfrak{b} \right\rangle = \delta_{\mathfrak{b}}\,, \tag{C.32}$$

$$\left\langle \mathfrak{d}^\dagger \mathfrak{d} \right\rangle = \delta_{\mathfrak{d}}\,, \tag{C.33}$$

$$\frac{2}{MM'} \sum_{\ell,\alpha} \left\langle c^\dagger_{\ell\alpha} c_{\ell\alpha} \right\rangle = n = 1 - \delta = 1 + \delta_{\mathfrak{d}} - \delta_{\mathfrak{f}}\,, \tag{C.34}$$

with the gauge-charge constraint (C.23) implying

$$\delta_{\mathfrak{b}} + k(\delta_{\mathfrak{f}} + \delta_{\mathfrak{d}}) = \frac{1}{2}\,. \tag{C.35}$$

The self-consistency equations are

$$R(\tau) = G_{\mathfrak{b}}(\tau) G_{\mathfrak{f}}(-\tau) - G_{\mathfrak{b}}(-\tau) G_{\mathfrak{d}}(\tau)\,, \tag{C.36}$$

$$Q(\tau) = G_{\mathfrak{b}}(\tau) G_{\mathfrak{b}}(-\tau)\,, \tag{C.37}$$

$$P(\tau) = -G_{\mathfrak{f}}(\tau) G_{\mathfrak{d}}(-\tau)\,. \tag{C.38}$$

We solve Eqs. (C.27)-(C.30) in a similar procedure as in Sec. 3.3 and Appendix C.2. We introduce a low-frequency ansatz for the Green's functions in terms of the imaginary time $|\tau| \gg 1/J$ at $T = 0$,

$$G_a(\tau) = -\mathrm{sgn}(\tau) \frac{C_a \Gamma(2\Delta_a) \sin(\pi\Delta_a + \mathrm{sgn}(\tau)\theta_a)}{\pi |\tau|^{2\Delta_a}}\,, \quad a = \mathfrak{f},\, \mathfrak{b},\, \mathfrak{d} \tag{C.39}$$

where parameters C_a, Δ_a and θ_a are real and positivity constraints on the spectral densities yields

$$-\pi\Delta_{\mathfrak{f}} < \theta_{\mathfrak{f}} < \pi\Delta_{\mathfrak{f}}\,, \quad \pi\Delta_{\mathfrak{b}} < \theta_{\mathfrak{b}} < \pi/2\,, \quad -\pi\Delta_{\mathfrak{d}} < \theta_{\mathfrak{d}} < \pi\Delta_{\mathfrak{d}}\,. \tag{C.40}$$

Assuming $\Delta_f = \Delta_b = \Delta_d = 1/4$, the exponents in t^2, J^2 and L^2 terms in Eqs. (C.28)-(C.30) are equal, and so all terms are important in our low-frequency analysis. Combination of Eqs.

(C.27)-(C.30) yields

$$-t^2C_{\mathfrak{b}}^2\left[C_{\mathfrak{f}}^2\cos(2\theta_{\mathfrak{b}}) - 2C_{\mathfrak{f}}C_{\mathfrak{d}}\frac{\sin(\pi/4-\theta_{\mathfrak{d}})\sin^2(\pi/4+\theta_{\mathfrak{b}})}{\sin(\pi/4+\theta_{\mathfrak{f}})}\right] + k^2L^2C_{\mathfrak{f}}^2C_{\mathfrak{d}}^2\cos(2\theta_{\mathfrak{d}}) = \pi , \tag{C.41}$$

$$-t^2C_{\mathfrak{b}}^2\left[C_{\mathfrak{d}}^2\cos(2\theta_{\mathfrak{b}}) - 2C_{\mathfrak{f}}C_{\mathfrak{d}}\frac{\sin(\pi/4-\theta_{\mathfrak{f}})\sin^2(\pi/4+\theta_{\mathfrak{b}})}{\sin(\pi/4+\theta_{\mathfrak{d}})}\right] + k^2L^2C_{\mathfrak{f}}^2C_{\mathfrak{d}}^2\cos(2\theta_{\mathfrak{f}}) = \pi , \tag{C.42}$$

$$\begin{aligned}-J^2C_{\mathfrak{b}}^4\cos(2\theta_{\mathfrak{b}}) + kt^2C_{\mathfrak{b}}^2\Bigg[&C_{\mathfrak{f}}^2\cos(2\theta_{\mathfrak{f}}) + C_{\mathfrak{d}}^2\cos(2\theta_{\mathfrak{d}}) \\ &- 4C_{\mathfrak{f}}C_{\mathfrak{d}}\frac{\sin(\pi/4-\theta_{\mathfrak{b}})\sin(\pi/4+\theta_{\mathfrak{f}})\sin(\pi/4+\theta_{\mathfrak{d}})}{\sin(\pi/4+\theta_{\mathfrak{b}})}\Bigg] = \pi ,\end{aligned} \tag{C.43}$$

and a restriction on asymmetry angles

$$\frac{\sin(\pi\Delta+\theta_{\mathfrak{f}})}{\sin(\pi\Delta-\theta_{\mathfrak{f}})}\frac{\sin(\pi\Delta-\theta_{\mathfrak{b}})}{\sin(\pi\Delta+\theta_{\mathfrak{b}})} = \frac{\sin(\pi\Delta+\theta_{\mathfrak{b}})}{\sin(\pi\Delta-\theta_{\mathfrak{b}})}\frac{\sin(\pi\Delta-\theta_{\mathfrak{d}})}{\sin(\pi\Delta+\theta_{\mathfrak{d}})} . \tag{C.44}$$

Notice the bounds $|\theta_{\mathfrak{f}}| < \pi/4$, $\pi/4 < \theta_{\mathfrak{b}} < \pi/2$ and $|\theta_{\mathfrak{d}}| < \pi/4$, which leads to all the coefficients on the left-hand sides of Eqs. (C.41) - (C.43) being positive. Since $C_{\mathfrak{f}}$, $C_{\mathfrak{b}}$, $C_{\mathfrak{d}}$ are defined to be real positive numbers, we find another constraint for $\theta_{\mathfrak{f}}$, $\theta_{\mathfrak{b}}$ and $\theta_{\mathfrak{d}}$ at nonzero t, J, L:

$$\cos(2\theta_{\mathfrak{b}}) \leq -k\big[\cos(2\theta_{\mathfrak{f}}) - \cos(2\theta_{\mathfrak{d}})\big] \leq -\cos(2\theta_{\mathfrak{b}}) \tag{C.45}$$

and at $L = 0$:

$$\cos(2\theta_{\mathfrak{b}}) \leq -k\big[\cos(2\theta_{\mathfrak{f}}) + \cos(2\theta_{\mathfrak{d}})\big] \leq -\cos(2\theta_{\mathfrak{b}}) \tag{C.46}$$

Therefore the parameters of the solution ($\theta_{\mathfrak{d}}$, $C_{\mathfrak{f}}$, $C_{\mathfrak{b}}$ and $C_{\mathfrak{d}}$) are fully determined by the two asymmetry angles $\theta_{\mathfrak{f}}$ and $\theta_{\mathfrak{b}}$. Note that the values of $\theta_{\mathfrak{f}}$ and $\theta_{\mathfrak{b}}$ are now related to the particle densities $\delta_{\mathfrak{f}}$, $\delta_{\mathfrak{d}}$ via the Luttinger constraints in analogy with Eqs. (4.83)-(4.85) of the other represention:

$$\frac{\theta_{\mathfrak{f}}}{\pi} + \left(\frac{1}{2} - \Delta_{\mathfrak{f}}\right)\frac{\sin(2\theta_{\mathfrak{f}})}{\sin(2\pi\Delta_{\mathfrak{f}})} = \frac{1}{2} - \delta_{\mathfrak{f}} , \tag{C.47}$$

$$\frac{\theta_{\mathfrak{b}}}{\pi} + \left(\frac{1}{2} - \Delta_{\mathfrak{b}}\right)\frac{\sin(2\theta_{\mathfrak{b}})}{\sin(2\pi\Delta_{\mathfrak{b}})} = \frac{1}{2} + \delta_{\mathfrak{b}} , \tag{C.48}$$

$$\frac{\theta_{\mathfrak{d}}}{\pi} + \left(\frac{1}{2} - \Delta_{\mathfrak{d}}\right)\frac{\sin(2\theta_{\mathfrak{d}})}{\sin(2\pi\Delta_{\mathfrak{d}})} = \frac{1}{2} - \delta_{\mathfrak{d}} . \tag{C.49}$$

At half-filling with particle-hole symmetry, we have $n = 1$ and $\delta_{\mathfrak{f}} = \delta_{\mathfrak{d}}$. Consequently, all parameters of the solution are fully determined at fixed doping density. So this large-M theory also describes a critical point.

C.3.2 Conductivity

The calculation follows the steps in Ref. [143]. We first generalize the Greens function to finite temperature similar to Eq. (4.101) in Sec. 4.4.5 with $\zeta_{\mathfrak{b}} = 1$, $\zeta_{\mathfrak{f}} = \zeta_{\mathfrak{d}} = -1$. Here the subscript $a = \mathfrak{b}, \mathfrak{f}, \mathfrak{d}$ is used for spinon, holon and doublon respectively.

We assume the system living on a Bethe lattice and consider both electron's and cooper pair's contribution to the residual resistivity:

$$\sigma_0^A = \frac{M' e^2 t^2 a^{2-d}}{2\pi z} \int d\omega A_c(\omega)^2 \beta n_F(\omega) n_F(-\omega) + \frac{M'(2e)^2 k L^2 a^{2-d}}{2\pi z} \int d\omega A_\Delta(\omega)^2 \beta n_B(\omega) n_B(-\omega)\,, \tag{C.50}$$

where a is lattice constant, z is coordination number, $A_c(\omega)$ is electron spectral density and $A_\Delta(\omega)$ is Cooper pair spectral density,

$$A_c(\omega) = 2\pi C e^{-\pi\mathcal{E}} \frac{\cosh(\beta\omega/2)}{\cosh(\beta\omega/2 - \pi\mathcal{E})} + 2\pi C' e^{-\pi\mathcal{E}'} \frac{\cosh(\beta\omega/2)}{\cosh(\beta\omega/2 - \pi\mathcal{E}')}\,, \tag{C.51}$$

$$A_\Delta(\omega) = -2\pi C_\Delta e^{-\pi\mathcal{E}_\Delta} \frac{\sinh(\beta\omega/2)}{\cosh(\beta\omega/2 - \pi\mathcal{E}_\Delta)}\,. \tag{C.52}$$

Here the parameters are defined as $\mathcal{E} = \mathcal{E}_{\mathfrak{b}} - \mathcal{E}_{\mathfrak{f}}$, $\mathcal{E}' = \mathcal{E}_d - \mathcal{E}_{\mathfrak{b}}$, $\mathcal{E}_\Delta = \mathcal{E}_{\mathfrak{f}} - \mathcal{E}_{\mathfrak{d}}$, $C = C_f C_b \sin(\theta_{\mathfrak{f}} - \pi/4)\sin(\theta_{\mathfrak{b}} + \pi/4)/\pi$, $C' = -C_{\mathfrak{b}} C_{\mathfrak{d}} \sin(\theta_{\mathfrak{b}} - \pi/4)\sin(\theta_{\mathfrak{d}} + \pi/4)/\pi$, $C_\Delta = -C_{\mathfrak{f}} C_{\mathfrak{d}} \sin(\theta_{\mathfrak{d}} - \pi/4)\sin(\theta$ The ratio in this fermionic holon representation then becomes

$$\mathcal{R} = \frac{\sigma_0^A}{\sigma_0^N} = \pi^2 \left[t^2 \left(C^2 e^{-2\pi\mathcal{E}} + C'^2 e^{-2\pi\mathcal{E}'} + 2CC' e^{-\pi(\mathcal{E}+\mathcal{E}')} \frac{\pi(\mathcal{E}-\mathcal{E}')}{\sinh\left[\pi(\mathcal{E}-\mathcal{E}')\right]} \right) + 4kL^2 C_\Delta^2 e^{-2\pi\mathcal{E}_\Delta} \right]. \tag{C.53}$$

We could transfer the bosonic holon scheme in Sec. 3.3 into the fermionic holon scheme by

$$\theta_{\mathfrak{f}} = \frac{\pi}{2} - \theta_b\,, \quad \theta_{\mathfrak{b}} = \frac{\pi}{2} - \theta_f\,. \tag{C.54}$$

Therefore both schemes give the same ratio $\mathcal{R}$ at the particle-hole symmetric solution $\theta_f = 0$, $\theta_b = \pi/2$.

D

Appendix for chapter 5

D.1 Numerical analytic continuation

We also perform numerical analytic continuation to real frequency. In general, performing analytic continuation is an ill-posed problem if the function on the imaginary axis is known only at a finite number of points. There are several techniques to do analytic continuation. But for simplicity we use the Pade approximation method. This technique parametrizes the function on imaginary axis as a ratio of two polynomials or by terminating a continued fraction. There are several ways for implementing Pade approximation. We adopt the simple strategy outlined in Ref. [204] of evaluating the coefficients of the two polynomials recursively, which is based on Thiele's reciprocal difference method. Details of the algorithm can be found in the Appendix of Ref. [204]. Briefly, we first solve the saddle-point equations on the imaginary-frequency axis to obtain the required Green's function, say $G(i\omega)$, at non-negative Matsubara frequencies. The number of Matsubara frequencies used in our calculation is 10^5. Then we evaluate the required polynomials, $A_n(z)$ and $B_n(z)$, to approximate the imaginary-frequency function, $G(z) = A_n(z)/B_n(z)$. The accuracy of these polynomials depends on the number of Pade points, n, and in our calculation we find that $n = 200$ points are sufficient to obtain accurate results. We have checked our results by increasing or decreasing n and it does not result in any significant improvement. The resulting ratio of polynomials then corresponds to the retarded Green's function on real-frequency axis, once we identify $z = \omega + i0^+$. Imaginary part of this function then gives the spectral function.

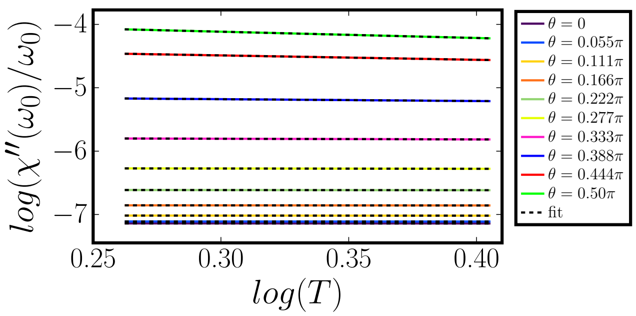

Figure D.1: Plot of $\log(\chi''(\omega_0)/\omega_0)$ versus $\log(T)$ at $\omega_0 = 0.2$, $R/|U| = 2$, and in the temperature range between $T/|U| = 0.13$ and $T/|U| = 0.15$, for different values of θ. The slope of the linear fit (black dashed lines) gives $\eta_s - 2$, from Eq. (D.3). This is used to plot the curve of η_s as a function of θ in Fig. 5.2 (b).

D.2 Effective spin exponent

In this appendix we discuss the evaluation of the effective spin exponent (η_s) in the normal state. To start with, we first evaluate the spin correlation, $\chi(\tau) = \langle \boldsymbol{S}(\tau) \cdot \boldsymbol{S}(0) \rangle \sim -G(\tau)G(-\tau)$, which is straightforward to obtain from the imaginary frequency numerics. We then Fourier transform to obtain $\chi(i\omega)$, and then perform numerical analytic continuation to obtain $\chi(\omega)$ whose imaginary part is the dynamical susceptibility, $\chi''(\omega)$. This is shown in Fig. D.2 for the normal state and in Fig. 5.9 in the SC phase.

At temperature above the SC transition temperature, the normal state solution is one of the SYK-type conformal solutions at low energy ($\omega \ll \tilde{J}$). For such a solution the spin susceptibility follows the scaling relation [69, 205, 206],

$$\chi''(\omega) \sim T^{\eta_s - 1} \Phi_{\eta_s}\left(\frac{\hbar\omega}{k_B T}\right), \tag{D.1}$$

where

$$\Phi_{\eta_s}(y) = \sinh\left(\frac{y}{2}\right) \left|\Gamma\left(\frac{\eta_s}{2} + i\frac{y}{2\pi}\right)\right|^2 . \tag{D.2}$$

For $\hbar\omega \ll k_B T$ we have,

$$\chi''(\omega) \sim \omega\, T^{\eta_s - 2}, \tag{D.3}$$

while in the limit of $\hbar\omega \gg k_B T$, the result is similar to the zero temperature form, $\chi''(\omega) \sim \mathrm{sgn}(\omega)|\omega|^{\eta_s - 1}$.

We can thus use Eq. (D.3) to extract the effective spin exponent (η_s) from the slope of plot of $\log(\chi''(\omega_0)/\omega_0)$ versus $\log(T)$, where ω_0 is a fixed small frequency. In Fig. D.1 we present the data for such a procedure for $R/|U| = 2$ in the temperature range of $T/|U| = 0.13$ and $T/|U| = 0.15$, with $\omega_0 = 0.2$. We have also checked our results for two other small frequency

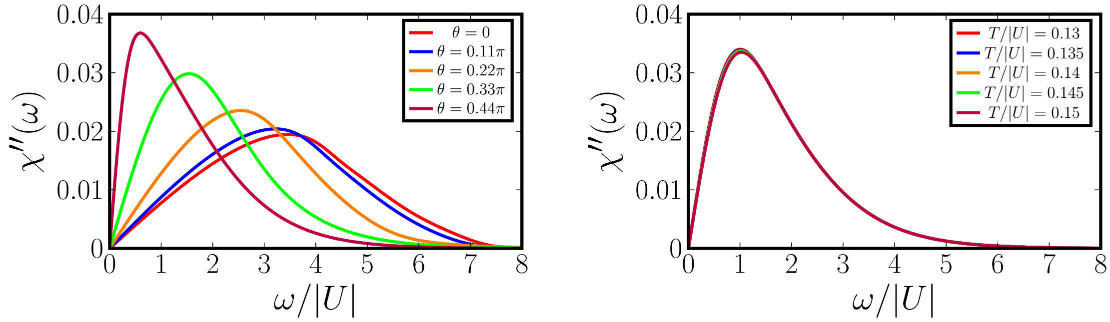

(a) **(b)**

Figure D.2: (a) Plot of $\chi''(\omega)$ for different values of θ at a fixed temperature $T/|U| = 0.13$ in the normal state. (b) Plot of $\chi''(\omega)$ for different values of temperature at a fixed value of $\theta = 0.388\pi$. In both the plots, $R/|U| = 2$.

points, and the results are unchanged. The resulting η_s as a function of θ is plotted in Fig. 5.2 (b). Similar procedure can be done at other values of $R/|U|$. This works well for larger values of $R/|u|$. At smaller values of $R/|U|$ the transition temperature is relatively high, where our numerical analytic continuation is not very reliable, and so extracting η_s there is difficult.

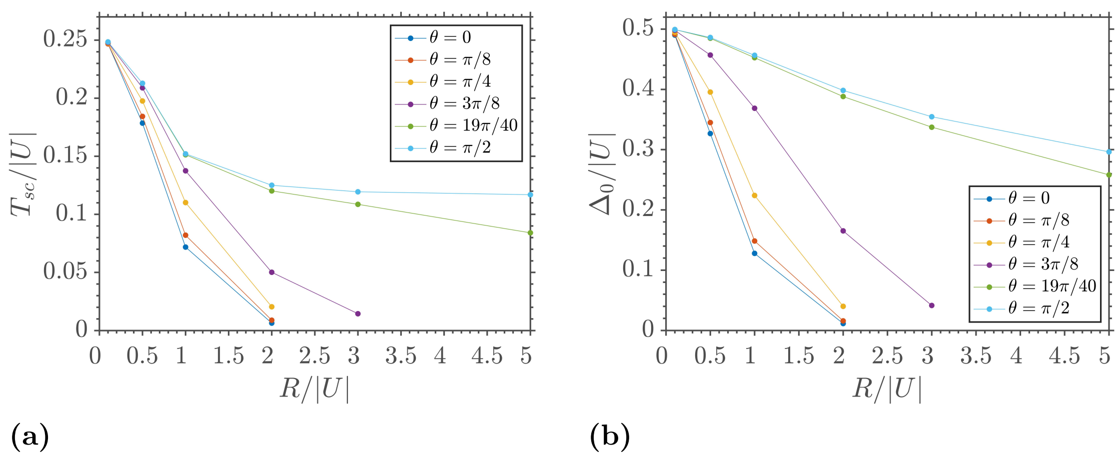

Figure D.3: Plots of transition temperature T_{sc}, the SC order parameter Δ_0 and the SC gap $\widetilde{\Delta}_0$ versus R for different values of θ. Note that for smaller values of θ when the normal state is FL-like, there is an exponential decay with respect to $R/|U|$. In contrast, in the case of NFL normal state these are replaced by different power-laws.

E

Appendix for chapter 6

The plan of this supplement is as follows. We present a full numerical solution of the large N equations for the complete Fermi surface in Section E.1 for complex couplings and E.2 for real couplings. We then discuss transport properties in Section E.3.

E.1 Numerical solutions to the Complex Yukawa-SYK model

We first solve the saddle-point equations in the normal state and consider complex-valued $g'_{ij\ell}$ extracted from the Gaussian unitary ensemble[160, 207]. In this limit, the anomalous terms disappear and saddle point equations (6.8a)-(6.8e) are simplified as

$$\Sigma(i\omega_n) = g'^2 T \sum_m G(i\omega_n - i\nu_m) D(i\nu_m), \tag{E.1a}$$

$$\Pi(i\nu_n) = -2g'^2 T \sum_m G(i\nu_n + i\omega_m) G(i\omega_m), \tag{E.1b}$$

$$G(i\omega_n) = \int \frac{\mathrm{d}^2 k}{(2\pi)^2} \frac{1}{i\omega_n - \varepsilon_k + \mu - \Sigma(i\omega_n)}, \tag{E.1c}$$

$$D(i\nu_n) = \int \frac{\mathrm{d}^2 q}{(2\pi)^2} \frac{1}{\nu_n^2 + \omega_q^2 + m_b^2 - \Pi(i\nu_n)}. \tag{E.1d}$$

For the lattice dispersion (6.4), the momentum integrations for the local Green's functions can be worked out analytically, giving rise to the local Green's function

$$G_{\rm loc}(z) = \frac{1}{4t}\mathcal{G}\left(\frac{z+\mu-\Sigma(z)}{4t}\right). \tag{E.2}$$

Here we define

$$\mathcal{G}(z) \equiv \frac{2}{\pi z}K(1/z^2), \tag{E.3}$$

with K the complete elliptic integral of the first kind. Similarly, for the bosons we obtain

$$D_{\rm loc}(z) = \frac{1}{4J}\mathcal{G}\left(\frac{z^2-m_b^2-4J-\Pi(z)}{4J}\right), \tag{E.4}$$

where m_b^2 is obtained by solving the above equations with the constraint (6.8f)

$$D_{\rm loc}(\tau=0) = -\frac{1}{\gamma}, \tag{E.5}$$

and will be plugged in the equations of the real-axis. Because we have taken care of the momentum integrations analytically, we work directly in the thermodynamic limit. For fast Fourier transform (FFT) of physical quantities between imaginary time-frequency domains, see Ref [208].

The real version of (E.1) originates from the analytic continuation $i\omega_n \to \omega + i0^+$ of imaginary propagators. To proceed, we introduce the following spectral functions

$$A(\omega) = -\frac{1}{\pi}{\rm Im}G^R(\omega), \tag{E.6a}$$

$$B(\omega) = -\frac{1}{\pi}{\rm Im}D^R(\omega), \tag{E.6b}$$

where $G^R(\omega) = G(i\omega_n)|_{i\omega_n\to\omega+i0^+}$ and $D^R(\omega) = D(i\nu_n)|_{i\nu_n\to\omega+i0^+}$ are the retarded Green's functions. From the spectral representation, we derive the following retarded self energies

$$\Sigma_R(\omega) = g'^2\int_{\omega'}\widetilde{A}(\omega')D_R(\omega-\omega') - \widetilde{B}(\omega')G_R(\omega+\omega'), \tag{E.7a}$$

$$\Pi_R(\omega) = g'^2\int_{\omega'}\widetilde{A}(\omega')([G_R(\omega'-\omega)]^* + G_R(\omega+\omega')),. \tag{E.7b}$$

Here we define $\widetilde{A}(\omega) \equiv A(\omega)n_F(\omega)$ and $\widetilde{B}(\omega) \equiv B(\omega)n_B(\omega)$. After the usual Fourier transform, we obtain self energies in real time domain

$$\Sigma_R(t) = ig'^2(2\pi)^2\theta(t)[\widetilde{A}(t)B(t) - \widetilde{B}(-t)A(t)], \tag{E.8a}$$

$$\Pi_R(t) = ig'^2(2\pi)^2\theta(t)[\widetilde{A}(t)A(-t) - \widetilde{A}(-t)A(t)]. \tag{E.8b}$$

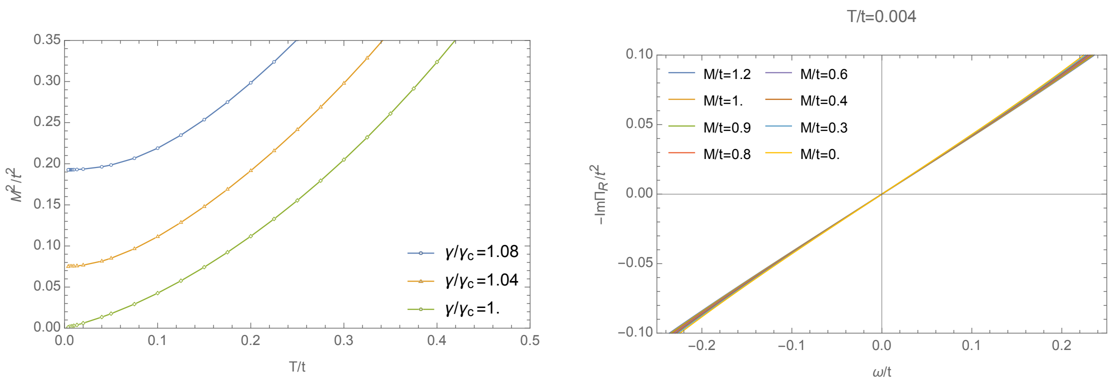

Figure E.1: Left: Renormalized boson mass as a function of T for $\gamma \geq \gamma_c$. Right: Imaginary part of the bosonic self-energy as a function of ω/t at $T/t = 0.004$ for different values of boson mass.

For numerical results in this section, we will use the following choice of parameters:

$$\mu = -0.5t, \quad J = t^2, \quad \lambda = \frac{g'^2}{JW} = 0.5, \quad (W = 8t = \text{bandwidth}) \tag{E.9}$$

E.1.1 Boson properties

We define the renormalized thermal boson mass following Esterlis *et al.* [47]. At the QCP, the boson mass decays as $M^2(T) \sim T$ at low temperatures up to logs, as is seen in the left panel of Figure E.1. The retarded boson self-energy shown in Figure E.1 obeys $-\mathrm{Im}\Pi_R \sim \omega$, also the expected Landau damping form. The low-frequency behavior is essentially independent of the distance to the QCP.

E.1.2 Fermion properties

Figure E.2 shows maginary part of the fermionic self-energy $-\mathrm{Im}\Sigma_R \sim |\omega|$ at the QCP and $-\mathrm{Im}\Sigma_R \sim \omega^2$ in the FL regime. There is also an appreciable mass enhancement, as seen in Figure E.3, although it is not clear if the growth is indeed $m^*/m \sim \log(1/T)$ at low temperatures.

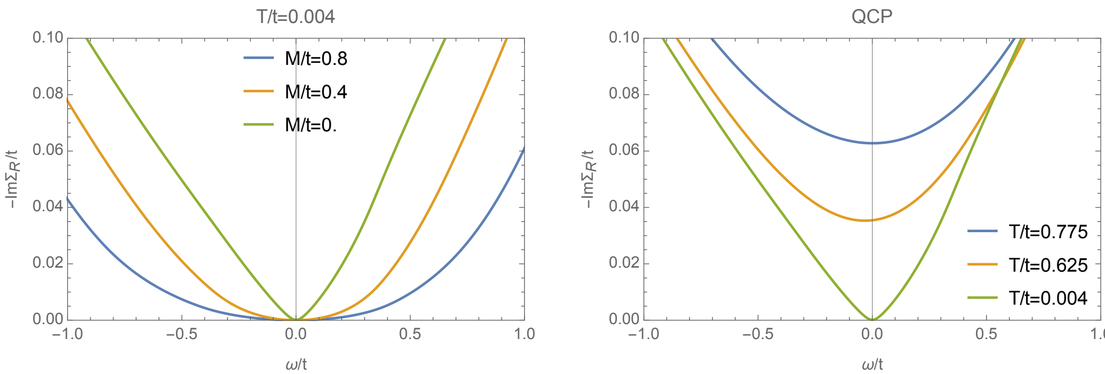

Figure E.2: Left: Imaginary part of the fermionic self-energy as a function of ω/t at $T/t = 0.004$ for different values of the boson mass. Right: Same as Left but at the QCP for different temperatures.

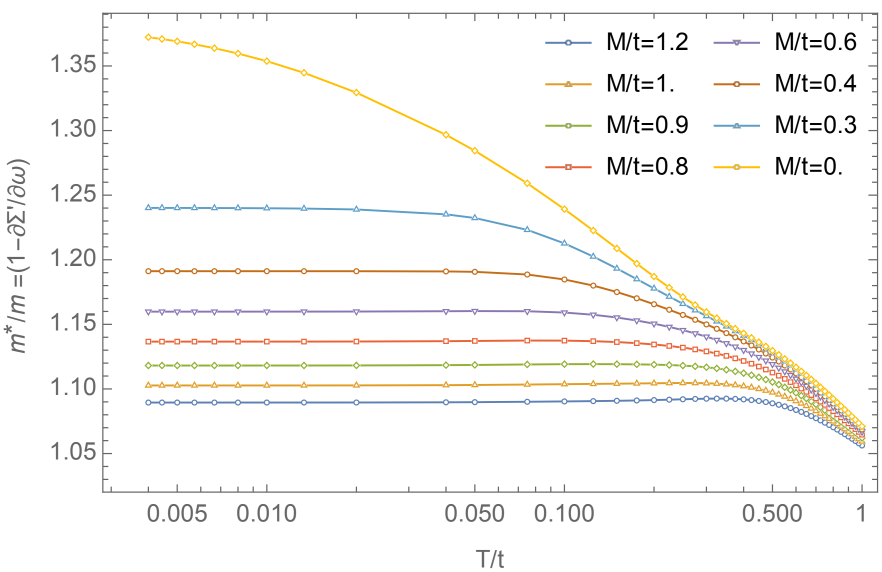

Figure E.3: Enhancement of the effective mass

E.2 Numerical solutions to the Real Yukawa-SYK model

E.2.1 Linearized gap equations and T_c

Now we turn to real-valued $g'_{ij\ell}$ extracted from the Gaussian orthogonal ensemble[160, 207], and start from the linearized gap equations

$$\Phi(i\omega_n) = g'^2(1-\alpha)T\sum_m D(i\omega_n - i\omega_m)X(i\omega_m)\Phi(i\omega_m)\,. \tag{E.10}$$

Here $X(i\omega_m)$ is determined by normal state solutions

$$X(i\omega_m) = \frac{G^N(i\omega_m) - G^N(-i\omega_m)}{2i\omega_m - \Sigma(i\omega_m) + \Sigma(-i\omega_m)}, \quad G^N(i\omega_m) = \frac{1}{4t}\mathcal{G}\left(\frac{i\omega_m + \mu - \Sigma(i\omega_m)}{4t}\right). \tag{E.11}$$

The superconducting transition temperature T_c can be determined by imposing that the matrix

$$g'^2(1-\alpha)T\sum_m D(i\omega_n - i\omega_m)X(i\omega_m)\,, \tag{E.12}$$

has eigenvalue 1.

E.2.2 Full solutions to the coupled saddle point equations

The momentum integrations can also be worked out analytically for the local Green's functions (6.8a). Under the given lattice dispersion (6.4), we have a generalized version of (E.2):

$$\begin{aligned} G_{\rm loc}(z) = &\frac{1}{2}\left(1 + \frac{zZ(z)}{\sqrt{(zZ(z))^2 - \Phi(z)^2}}\right)\frac{1}{4t}\mathcal{G}\left(\frac{-\chi(z) + \mu + \sqrt{(zZ(z))^2 - \Phi(z)^2}}{4t}\right) \\ &+ \frac{1}{2}\left(1 - \frac{zZ(z)}{\sqrt{(zZ(z))^2 - \Phi(z)^2}}\right)\frac{1}{4t}\mathcal{G}\left(\frac{-\chi(z) + \mu - \sqrt{(zZ(z))^2 - \Phi(z)^2}}{4t}\right), \end{aligned} \tag{E.13a}$$

$$\begin{aligned} F_{\rm loc}(z) = &\frac{\Phi(z)}{2\sqrt{(zZ(z))^2 - \Phi(z)^2}}\frac{1}{4t}\mathcal{G}\left(\frac{-\chi(z) + \mu + \sqrt{(zZ(z))^2 - \Phi(z)^2}}{4t}\right) \\ &- \frac{\Phi(z)}{2\sqrt{(zZ(z))^2 - \Phi(z)^2}}\frac{1}{4t}\mathcal{G}\left(\frac{-\chi(z) + \mu - \sqrt{(zZ(z))^2 - \Phi(z)^2}}{4t}\right). \end{aligned} \tag{E.13b}$$

Here we define

$$\Sigma(z) + \Sigma(-z) \equiv 2\chi(z), \tag{E.14}$$

$$\Sigma(z) - \Sigma(-z) \equiv 2z(1 - Z(z)). \tag{E.15}$$

The Green's functions (E.13) reduces to (E.2) when $\Phi(z) = 0$. The analytic continuation $i\omega_n \to \omega + i0^+$ of (E.13) will lead to the Green's function on real axis. Following a similar procedure shown in E.1, we obtain the self energies in real time domain

$$\Sigma_R(t) = ig'^2(2\pi)^2\theta(t)[\widetilde{A}(t)B(t) - \widetilde{B}(-t)A(t)], \tag{E.16a}$$

$$\Phi_R(t) = -i(1-\alpha)g'^2(2\pi)^2\theta(t)[\widetilde{A}_F(t)B(t) - \widetilde{B}(-t)A_F(t)], \tag{E.16b}$$

$$\begin{aligned}\Pi_R(t) = i2g'^2(2\pi)^2\theta(t)[&\widetilde{A}(t)A(-t) - \widetilde{A}(-t)A(t),\\ &- (1-\alpha)(\widetilde{A}_F(t)A_F(-t) - \widetilde{A}_F(-t)A_F(t))].\end{aligned} \tag{E.16c}$$

The self-consistent equations can also be readily solved directly on the real-axis for the retarded functions.

E.3 Conductivity and superfluid stiffness

E.3.1 Current-current correlator

The current-current response is just the dressed bubble as seen in Figure 6.1

$$\begin{aligned}\Lambda_{\alpha\beta}(i\omega_n) &= -T\sum_{n'}\int_{\boldsymbol{k}} v_{\boldsymbol{k}\alpha}v_{\boldsymbol{k}\beta}\Big(G_{\boldsymbol{k}}(i\omega_{n'})\,G_{\boldsymbol{k}}(i\omega_n + i\omega_{n'}) + F^\dagger_{\boldsymbol{k}}(i\omega_{n'})\,F_{\boldsymbol{k}}(i\omega_n + i\omega_{n'})\Big)\\ &= -T\sum_{n'}\int d\epsilon\rho^{\alpha\beta}_{\mathrm{tr}}(\epsilon)\Big(G(\epsilon, i\omega_{n'})\,G(\epsilon, i\omega_n + i\omega_{n'}) + F^\dagger(\epsilon, i\omega_{n'})\,F(\epsilon, i\omega_n + i\omega_{n'})\Big).\end{aligned} \tag{E.17}$$

In the last step we introduced the "transport" DOS

$$\rho^{\alpha\beta}_{\mathrm{tr}}(\epsilon) = \int_{\boldsymbol{k}} \frac{\partial\varepsilon_{\boldsymbol{k}}}{\partial k_\alpha}\frac{\partial\varepsilon_{\boldsymbol{k}}}{\partial k_\beta}\delta(\epsilon - \varepsilon_{\boldsymbol{k}}) \tag{E.18}$$

and assumed that the normal and anomalous self energies are momentum independent. For the given dispersion (6.4), this quantity is analytically computable

$$\rho_{\mathrm{tr}}(\epsilon) = \frac{2t}{\pi^2}\left[E(1-\epsilon^2/16t^2) - \frac{\epsilon^2}{16t^2}K(1-\epsilon^2/16t^2)\right], \tag{E.19}$$

where E is the complete elliptic integral of the second kind. In the normal state, the analytic continuation for the retarded (R) function is

$$\Lambda_R(\omega) = \int \mathrm{d}\epsilon \; \rho_{\mathrm{tr}}(\epsilon) \int \mathrm{d}\omega' \; n_F(\omega') A(\epsilon, \omega') \{G_R(\epsilon, \omega + \omega') + [G_R(\epsilon, \omega' - \omega)]^*\}, \tag{E.20}$$

where n_F is the Fermi function. The final expression is efficiently evaluated via FFTs by rewriting the convolution in real-time:

$$\Lambda_R(t) = \int \mathrm{d}\epsilon \; \rho_{\mathrm{tr}}(\epsilon) \times 2\pi \{[\widetilde{A}(\epsilon, t)]^* G_R(\epsilon, t) + \widetilde{A}(\epsilon, t)[G_R(\epsilon, t)]^*\}\,. \tag{E.21}$$

E.3.2 conductivity

The conductivity is related to Λ_R according to [196]

$$\sigma(\omega) = -e^2 \frac{\langle -K \rangle / d - \Lambda_R(\omega)}{i(\omega + i0^+)}, \tag{E.22}$$

where $\langle -K \rangle$ is the (negative of) the average kinetic energy per site and d is the spatial dimension (for us $d = 2$). Explicitly

$$K = -t \sum_{\langle ij \rangle} (c_i^\dagger c_j + \mathrm{h.c.}). \tag{E.23}$$

We may write

$$\sigma(\omega) = D\delta(\omega) + \sigma_{\mathrm{reg}}(\omega), \tag{E.24}$$

where the Drude weight is

$$D = \pi e^2 [\langle -K/2 \rangle - \Lambda_R'(\omega \to 0)] \tag{E.25}$$

specialized to $d = 2$ and

$$\sigma_{\mathrm{reg}}(\omega)/e^2 = \frac{\Lambda_R''(\omega)}{\omega} - i \frac{\Lambda_R'(\omega) - \langle -K/2 \rangle}{\omega}. \tag{E.26}$$

In a disordered system, the δ-function contribution vanishes in the normal state (there is a finite dc resistance), from which we find

$$D = 0 \;\Rightarrow\; \langle -K/2 \rangle = \Lambda_R'(\omega \to 0), \tag{E.27}$$

and we may also write

$$\sigma(\omega)/e^2 = \frac{\Lambda''_R(\omega)}{\omega} - i\frac{\Lambda'_R(\omega) - \Lambda'_R(\omega \to 0)}{\omega} \quad \text{(disordered)}. \tag{E.28}$$

This form is useful since it does not require computing independently $\langle K \rangle$ (although explicitly comparing the left-and right-hand sides of Eq. (E.27) is a useful consistency check). Another useful result that follows from Kramers-Kronig is the sum rule

$$\int_{-\infty}^{\infty} \mathrm{d}\omega \; \sigma(\omega) = \pi e^2 \langle -K/2 \rangle. \tag{E.29}$$

Finally, note the dc limit for the conductivity can also be taken explicitly:

$$\sigma_{\mathrm{dc}}/e^2 = \lim_{\omega \to 0} \frac{\Lambda''_R(\omega)}{\omega} = \pi \int \mathrm{d}\epsilon \; \rho_{\mathrm{tr}}(\epsilon) \int \mathrm{d}\omega' \; \left(-\frac{\partial n_F}{\partial \omega'} \right) [A(\epsilon, \omega')]^2. \tag{E.30}$$

E.3.3 Superfluid stiffness

The coefficient D of the delta function, the Drude weight, can be obtained by extrapolating $i\omega_n \to 0$[196]. If there is a gap, $D = D_s$, the superfluid stiffness is

$$\frac{D_s}{\pi e^2} = \langle -K \rangle / d - \Lambda(i\omega_n = 0) \,, \qquad d = 2 \tag{E.31}$$

The two weighted densities of states $\rho_{\mathrm{tr}}(\epsilon) \equiv \frac{1}{N} \sum_k v_k^2 \delta(\epsilon - \epsilon_k)$ and $\rho_0(\epsilon) \equiv \frac{1}{N} \sum_k \delta(\epsilon - \epsilon_k)$ are closely related with each other

$$\frac{\mathrm{d}\rho_{\mathrm{tr}}(\epsilon)}{\mathrm{d}\epsilon} = -\frac{\epsilon}{2} \rho_0(\epsilon) \,. \tag{E.32}$$

Therefore, we can rewrite the average kinetic energy per site as

$$\begin{aligned} \langle K \rangle &= \frac{1}{\beta} \sum_{\omega_n} \frac{1}{N} \sum_k \epsilon_k G(k, i\omega_n) e^{i\omega_n 0^+} = \frac{1}{\beta} \sum_{\omega_n} \int \mathrm{d}\epsilon \rho_0(\epsilon) \epsilon G(\epsilon, i\omega_n) e^{i\omega_n 0^+} \\ &= -\frac{2}{\beta} \sum_{\omega_n} \int \mathrm{d}\epsilon \frac{d\rho_{tr}(\epsilon)}{d\epsilon} G(\epsilon, i\omega_n) e^{i\omega_n 0^+} = \frac{2}{\beta} \sum_{\omega_n} \int \mathrm{d}\epsilon \rho_{\mathrm{tr}}(\epsilon) \frac{dG(\epsilon, i\omega_n)}{d\epsilon} e^{i\omega_n 0^+} \end{aligned} \tag{E.33}$$

From Dyson equation,

$$\frac{\partial G\left(\epsilon, i\omega_n\right)}{\partial \epsilon} = G\left(\epsilon, i\omega_n\right)^2 - F^{\dagger}\left(\epsilon, i\omega_n\right) F\left(\epsilon, i\omega_n\right), \tag{E.34}$$

and we get for the superfluid stiffness

$$\begin{aligned}
\frac{D_s}{\pi e^2} &= \langle -K/2 \rangle - \Lambda(0) \\
&= -T \sum_n \int d\epsilon \rho_{\mathrm{tr}}(\epsilon) \Big(G(\epsilon, i\omega_n)^2 - F^\dagger(\epsilon, i\omega_n) F(\epsilon, i\omega_n) \Big) \\
&+ T \sum_n \int d\epsilon \rho_{\mathrm{tr}}(\epsilon) \Big(G(\epsilon, i\omega_n)^2 + F^\dagger(\epsilon, i\omega_n) F(\epsilon, i\omega_n) \Big) \\
&= 2T \sum_n \int d\epsilon \rho_{\mathrm{tr}}(\epsilon) F^\dagger(\epsilon, i\omega_n) F(\epsilon, i\omega_n) . \qquad \text{(E.35)}
\end{aligned}$$

References

[1] S. Sachdev and J. Ye. Gapless spin-fluid ground state in a random quantum Heisenberg magnet. *Phys. Rev. Lett.*, 70:3339, 1993.

[2] Darshan G. Joshi, Chenyuan Li, Grigory Tarnopolsky, Antoine Georges, and Subir Sachdev. Deconfined critical point in a doped random quantum Heisenberg magnet. *Phys. Rev. X to appear*, 2019.

[3] L. Arrachea and M. J. Rozenberg. Infinite-range quantum random Heisenberg magnet. *Phys. Rev. B*, 65(22):224430, June 2002.

[4] A. Camjayi and M. J. Rozenberg. Quantum and Thermal Fluctuations in the SU(N) Heisenberg Spin-Glass Model near the Quantum Critical Point. *Phys. Rev. Lett.*, 90(21):217202, May 2003.

[5] L. D. Landau. The Theory of a Fermi Liquid. *Zh. Eksp. Teor. Fiz.*, 30(6):1058, 1956.

[6] Lev Davidovich Landau. On the Theory of the Fermi Liquid. *J. Exp. Theor. Phys.*, 35, 1958.

[7] X.G. Wen. *Quantum Field Theory of Many-Body Systems:From the Origin of Sound to an Origin of Light and Electrons: From the Origin of Sound to an Origin of Light and Electrons*. Oxford Graduate Texts. OUP Oxford, 2004.

[8] P. Nozieres and D. Pines. *Theory Of Quantum Liquids*. Advanced Books Classics. Avalon Publishing, 1999.

[9] E.M. Lifshitz and L.P. Pitaevskii. *Statistical Physics: Theory of the Condensed State*. Number v. 9 in Course of Theoretical Physics. Elsevier Science, 2013.

[10] E. Pavarini, E. Koch, A.I. Lichtenstein, D. Vollhardt, Institute for Advanced Simulation, and Forschungszentrum Jülich. *Dynamical Mean-field Theory of Correlated Electrons*. Schriften des Forschungszentrums Jülich / Reihe Modeling and Simulation. Forschungszentrum Jülich, Zentralbibliothek, Verlag, 2022.

[11] J. Bardeen, L. N. Cooper, and J. R. Schrieffer. Theory of superconductivity. *Phys. Rev.*, 108:1175–1204, Dec 1957.

[12] N. N. Bogoljubov, V. V. Tolmachov, and D. V. Širkov. A new method in the theory of superconductivity. *Fortschritte der Physik*, 6(11-12):605–682, 1958.

[13] Ivar Giaever and Karl Megerle. Study of superconductors by electron tunneling. *Phys. Rev.*, 122:1101–1111, May 1961.

[14] Subir Sachdev. *Quantum Phases of Matter*. Cambridge University Press, 2023.

[15] Debanjan Chowdhury, Antoine Georges, Olivier Parcollet, and Subir Sachdev. Sachdev-ye-kitaev models and beyond: Window into non-fermi liquids. *Rev. Mod. Phys.*, 94:035004, Sep 2022.

[16] H. Takagi, B. Batlogg, H. L. Kao, J. Kwo, R. J. Cava, J. J. Krajewski, and W. F. Peck. Systematic evolution of temperature-dependent resistivity in $\mathrm{la}_{2-x}\mathrm{sr}_x\mathrm{cuo}_4$. *Phys. Rev. Lett.*, 69:2975–2978, Nov 1992.

[17] B. Keimer, S. A. Kivelson, M. R. Norman, S. Uchida, and J. Zaanen. From quantum matter to high-temperature superconductivity in copper oxides. *Nature*, 518(7538):179–186, 2015.

[18] S. Kasahara, T. Shibauchi, K. Hashimoto, K. Ikada, S. Tonegawa, R. Okazaki, H. Shishido, H. Ikeda, H. Takeya, K. Hirata, T. Terashima, and Y. Matsuda. Evolution from non-fermi- to fermi-liquid transport via isovalent doping in $\mathrm{bafe}_2(\mathrm{As}_{1-x}\mathrm{P}_x)_2$ superconductors. *Phys. Rev. B*, 81:184519, May 2010.

[19] James G. Analytis, H-H. Kuo, Ross D. McDonald, Mark Wartenbe, P. M. C. Rourke, N. E. Hussey, and I. R. Fisher. Transport near a quantum critical point in bafe2(as1xpx)2. *Nature Physics*, 10(3):194–197, 2014.

[20] T. Shibauchi, A. Carrington, and Y. Matsuda. A quantum critical point lying beneath the superconducting dome in iron pnictides. *Annual Review of Condensed Matter Physics*, 5(Volume 5, 2014):113–135, 2014.

[21] G. R. Stewart. Non-fermi-liquid behavior in d- and f-electron metals. *Rev. Mod. Phys.*, 73:797–855, Oct 2001.

[22] Yuan Cao, Debanjan Chowdhury, Daniel Rodan-Legrain, Oriol Rubies-Bigorda, Kenji Watanabe, Takashi Taniguchi, T. Senthil, and Pablo Jarillo-Herrero. Strange metal in magic-angle graphene with near planckian dissipation. *Phys. Rev. Lett.*, 124:076801, Feb 2020.

[23] Debanjan Chowdhury, Yochai Werman, Erez Berg, and T. Senthil. Translationally invariant non-fermi-liquid metals with critical fermi surfaces: Solvable models. *Phys. Rev. X*, 8:031024, Jul 2018.

[24] C. M. Varma, P. B. Littlewood, S. Schmitt-Rink, E. Abrahams, and A. E. Ruckenstein. Phenomenology of the normal state of cu-o high-temperature superconductors. *Phys. Rev. Lett.*, 63:1996–1999, Oct 1989.

[25] Aavishkar A. Patel, Haoyu Guo, Ilya Esterlis, and Subir Sachdev. Universal theory of strange metals from spatially random interactions. *Science*, 381(6659):790–793, 2023.

[26] Subir Sachdev. *Quantum Phase Transitions*. Cambridge University Press, 2 edition, 2011.

[27] Tôru Moriya and Kazuo Ueda. Spin fluctuations and high temperature superconductivity. *Advances in Physics*, 49(5):555–606, 2000.

[28] Subir Sachdev and Bernhard Keimer. Quantum criticality. *Physics Today*, 64(2):29–35, 02 2011.

[29] Chandra Varma. Mind the pseudogap. *Nature*, 468(7321):184–185, 2010.

[30] J. G. Bednorz and K. A. Müller. Possible hightc superconductivity in the balacuo system. *Zeitschrift für Physik B Condensed Matter*, 64(2):189–193, 1986.

[31] N. P. Armitage, P. Fournier, and R. L. Greene. Progress and perspectives on electron-doped cuprates. *Rev. Mod. Phys.*, 82:2421–2487, Sep 2010.

[32] Cyril Proust and Louis Taillefer. The remarkable underlying ground states of cuprate superconductors. *Annual Review of Condensed Matter Physics*, 10(1):409–429, March 2019.

[33] P. Giraldo-Gallo, J. A. Galvis, Z. Stegen, K. A. Modic, F. F. Balakirev, J. B. Betts, X. Lian, C. Moir, S. C. Riggs, J. Wu, A. T. Bollinger, X. He, I. Božović, B. J. Ramshaw, R. D. McDonald, G. S. Boebinger, and A. Shekhter. Scale-invariant magnetoresistance in a cuprate superconductor. *Science*, 361(6401):479–481, August 2018.

[34] J. A. N. Bruin, H. Sakai, R. S. Perry, and A. P. Mackenzie. Similarity of scattering rates in metals showing ¡i¿t¡/i¿-linear resistivity. *Science*, 339(6121):804–807, 2013.

[35] Gaël Grissonnanche, Yawen Fang, Anaëlle Legros, Simon Verret, Francis Laliberté, Clément Collignon, Jianshi Zhou, David Graf, Paul A. Goddard, Louis Taillefer, and B. J. Ramshaw. Linear-in temperature resistivity from an isotropic planckian scattering rate. *Nature*, 595(7869):667–672, 2021.

[36] Sean A. Hartnoll and Andrew P. Mackenzie. Colloquium : Planckian dissipation in metals. *Reviews of Modern Physics*, 94(4), November 2022.

[37] Subir Sachdev. Strange metals and black holes: Insights from the sachdev-ye-kitaev model, December 2023.

[38] A. Legros, S. Benhabib, W. Tabis, F. Laliberté, M. Dion, M. Lizaire, B. Vignolle, D. Vignolles, H. Raffy, Z. Z. Li, P. Auban-Senzier, N. Doiron-Leyraud, P. Fournier, D. Colson, L. Taillefer, and C. Proust. Universal t-linear resistivity and planckian dissipation in overdoped cuprates. *Nature Physics*, 15(2):142–147, 2019.

[39] Bastien Michon, Christophe Berthod, Carl Willem Rischau, Amirreza Ataei, Lu Chen, Seiki Komiya, Shimpei Ono, Louis Taillefer, Dirk van der Marel, and Antoine Georges. Reconciling scaling of the optical conductivity of cuprate superconductors with planckian resistivity and specific heat. *Nature Communications*, 14(1), May 2023.

[40] T. J. Reber, X. Zhou, N. C. Plumb, S. Parham, J. A. Waugh, Y. Cao, Z. Sun, H. Li, Q. Wang, J. S. Wen, Z. J. Xu, G. Gu, Y. Yoshida, H. Eisaki, G. B. Arnold, and D. S. Dessau. A unified form of low-energy nodal electronic interactions in hole-doped cuprate superconductors. *Nature Communications*, 10(1):5737, 2019.

[41] B. Michon, C. Girod, S. Badoux, J. Kačmarčík, Q. Ma, M. Dragomir, H. A. Dabkowska, B. D. Gaulin, J. S. Zhou, S. Pyon, T. Takayama, H. Takagi, S. Verret, N. Doiron-Leyraud, C. Marcenat, L. Taillefer, and T. Klein. Thermodynamic signatures of quantum criticality in cuprate superconductors. *Nature*, 567(7747):218–222, 2019.

[42] A. Y. Kitaev. Talks at KITP, University of California, Santa Barbara. *Entanglement in Strongly-Correlated Quantum Matter*, 2015.

[43] Juan Maldacena and Douglas Stanford. Remarks on the Sachdev-Ye-Kitaev model. *Phys. Rev. D*, 94(10):106002, 2016.

[44] X.-Y. Song, C.-M. Jian, and L. Balents. Strongly Correlated Metal Built from Sachdev-Ye-Kitaev Models. *Phys. Rev. Lett.*, 119(21):216601, November 2017.

[45] Aavishkar A. Patel, Michael J. Lawler, and Eun-Ah Kim. Coherent superconductivity with a large gap ratio from incoherent metals. *Physical Review Letters*, 121(18), October 2018.

[46] Peter Cha, Nils Wentzell, Olivier Parcollet, Antoine Georges, and Eun-Ah Kim. Linear resistivity and sachdev-ye-kitaev (syk) spin liquid behavior in a quantum critical metal with spin-1/2 fermions. *Proceedings of the National Academy of Sciences*, 117(31):18341–18346, July 2020.

[47] Ilya Esterlis, Haoyu Guo, Aavishkar A. Patel, and Subir Sachdev. Large- ¡mml:math xmlns:mml=”http://www.w3.org/1998/math/mathml”¿¡mml:mi¿n¡/mml:mi¿¡/mml:math¿ theory of critical fermi surfaces. *Physical Review B*, 103(23), June 2021.

[48] Haoyu Guo, Aavishkar A. Patel, Ilya Esterlis, and Subir Sachdev. Large-n theory of critical fermi surfaces. ii. conductivity. *Phys. Rev. B*, 106:115151, Sep 2022.

[49] Cyril Proust and Louis Taillefer. The Remarkable Underlying Ground States of Cuprate Superconductors. *Annual Review of Condensed Matter Physics*, 10:409–429, Mar 2019.

[50] I. M. Vishik, M. Hashimoto, Rui-Hua He, Wei-Sheng Lee, Felix Schmitt, Donghui Lu, R. G. Moore, C. Zhang, W. Meevasana, T. Sasagawa, S. Uchida, Kazuhiro Fujita, S. Ishida, M. Ishikado, Yoshiyuki Yoshida, Hiroshi Eisaki, Zahid Hussain, Thomas P. Devereaux, and Zhi-Xun Shen. Phase competition in trisected superconducting dome. *Proceedings of the National Academy of Science*, 109(45):18332–18337, Nov 2012.

[51] Y. He, Y. Yin, M. Zech, A. Soumyanarayanan, M. M. Yee, T. Williams, M. C. Boyer, K. Chatterjee, W. D. Wise, I. Zeljkovic, T. Kondo, T. Takeuchi, H. Ikuta, P. Mistark, R. S. Markiewicz, A. Bansil, S. Sachdev, E. W. Hudson, and J. E. Hoffman. Fermi Surface and Pseudogap Evolution in a Cuprate Superconductor. *Science*, 344:608–611, May 2014.

[52] K. Fujita, C. K. Kim, I. Lee, J. Lee, M. H. Hamidian, I. A. Firmo, S. Mukhopadhyay, H. Eisaki, S. Uchida, M. J. Lawler, E.-A. Kim, and J. C. Davis. Simultaneous Transitions in Cuprate Momentum-Space Topology and Electronic Symmetry Breaking. *Science*, 344:612–616, May 2014.

[53] S. Badoux, W. Tabis, F. Laliberté, G. Grissonnanche, B. Vignolle, D. Vignolles, J. Béard, D. A. Bonn, W. N. Hardy, R. Liang, N. Doiron-Leyraud, Louis Taillefer, and Cyril Proust. Change of carrier density at the pseudogap critical point of a cuprate superconductor. *Nature*, 531(7593):210–214, Mar 2016.

[54] J.W. Loram, J. Luo, J.R. Cooper, W.Y. Liang, and J.L. Tallon. Evidence on the pseudogap and condensate from the electronic specific heat. *Journal of Physics and Chemistry of Solids*, 62(1):59 – 64, 2001.

[55] Jeffery L. Tallon, James G. Storey, John R. Cooper, and John W. Loram. Locating the pseudogap closing point in cuprate superconductors: Absence of entrant or reentrant behavior. *Physical Review B*, 101(17), May 2020.

[56] B. Michon, C. Girod, S. Badoux, J. Kačmarčík, Q. Ma, M. Dragomir, H. A. Dabkowska, B. D. Gaulin, J. S. Zhou, S. Pyon, T. Takayama, H. Takagi, S. Verret, N. Doiron-Leyraud, C. Marcenat, L. Taillefer, and T. Klein. Thermodynamic signatures of quantum criticality in cuprate superconductors. *Nature*, 567(7747):218–222, Feb 2019.

[57] Yang Tang, Lucile Mangin-Thro, Andrew Wildes, Mun K. Chan, Chelsey J. Dorow, Jaehong Jeong, Yvan Sidis, Martin Greven, and Philippe Bourges. Orientation of the intra-unit-cell magnetic moment in the high-T_c superconductor $HgBa_2CuO_{4+\delta}$. *Phys. Rev. B*, 98(21):214418, Dec 2018.

[58] Su-Di Chen, Makoto Hashimoto, Yu He, Dongjoon Song, Ke-Jun Xu, Jun-Feng He, Thomas P. Devereaux, Hiroshi Eisaki, Dong-Hui Lu, Jan Zaanen, and Zhi-Xun Shen. Incoherent strange metal sharply bounded by a critical doping in Bi2212. *Science*, 366(6469):1099–1102, 2019.

[59] C. Panagopoulos, J. L. Tallon, B. D. Rainford, T. Xiang, J. R. Cooper, and C. A. Scott. Evidence for a generic quantum transition in high-T_c cuprates. *Phys. Rev. B*, 66(6):064501, Aug 2002.

[60] C. Panagopoulos, A. P. Petrovic, A. D. Hillier, J. L. Tallon, C. A. Scott, and B. D. Rainford. Exposing the spin-glass ground state of the nonsuperconducting $La_{2-x}Sr_xCu_{1-y}Zn_yO_4$ high-T_c oxide. *Phys. Rev. B*, 69(14):144510, Apr 2004.

[61] Mehdi Frachet, Igor Vinograd, Rui Zhou, Siham Benhabib, Shangfei Wu, Hadrien Mayaffre, Steffen Krämer, Sanath K. Ramakrishna, Arneil Reyes, Jérôme Debray, Tohru Kurosawa, Naoki Momono, Migaku Oda, Seiki Komiya, Shimpei Ono, Masafumi Horio, Johan Chang, Cyril Proust, David LeBoeuf, and Marc-Henri Julien. Hidden magnetism at the pseudogap critical point of a high temperature superconductor. *arXiv e-prints*, Sep 2019.

[62] T. Senthil, A. Vishwanath, L. Balents, S. Sachdev, and M. P. A. Fisher. Deconfined Quantum Critical Points. *Science*, 303:1490–1494, March 2004.

[63] Subir Sachdev, N. Read, and R. Oppermann. Quantum field theory of metallic spin glasses. *Phys. Rev. B*, 52(14):10286–10294, Oct 1995.

[64] Anirvan M. Sengupta and Antoine Georges. Non-Fermi-liquid behavior near a $T = 0$ spin-glass transition. *Phys. Rev. B*, 52(14):10295–10302, Oct 1995.

[65] Dan Mao, Debanjan Chowdhury, and T. Senthil. Slow scrambling and hidden integrability in a random rotor model. *Physical Review B*, 102(9), September 2020.

[66] T. Senthil, Subir Sachdev, and Matthias Vojta. Quantum phase transitions out of the heavy Fermi liquid. *Physica B Condensed Matter*, 359:9–16, Apr 2005.

[67] P. Coleman, C. Pépin, Qimiao Si, and R. Ramazashvili. Topical Review: How do Fermi liquids get heavy and die? *Journal of Physics Condensed Matter*, 13(35):R723–R738, Sep 2001.

[68] Kristjan Haule and Gabriel Kotliar. Strongly correlated superconductivity: A plaquette dynamical mean-field theory study. *Phys. Rev. B*, 76(10):104509, Sep 2007.

[69] O. Parcollet and A. Georges. Non-Fermi-liquid regime of a doped Mott insulator. *Phys. Rev. B*, 59:5341, 1999.

[70] Antoine Georges, Olivier Parcollet, and Subir Sachdev. Mean Field Theory of a Quantum Heisenberg Spin Glass. *Phys. Rev. Lett.*, 85(4):840–843, Jul 2000.

[71] A. Georges, O. Parcollet, and S. Sachdev. Quantum fluctuations of a nearly critical Heisenberg spin glass. *Phys. Rev. B*, 63(13):134406, Apr 2001.

[72] Philipp Werner, Aaram J. Kim, and Shintaro Hoshino. Spin-freezing and the Sachdev-Ye model. *Europhys. Lett.*, 124(5):57002, Dec 2018.

[73] Naoto Tsuji and Philipp Werner. Out-of-time-ordered correlators of the Hubbard model: Sachdev-Ye-Kitaev strange metal in the spin-freezing crossover region. *Phys. Rev. B*, 99(11):115132, 2019.

[74] P. B. Wiegmann. Superconductivity in strongly correlated electronic systems and confinement versus deconfinement phenomenon. *Phys. Rev. Lett.*, 60:821–824, Feb 1988.

[75] Chong Wang, Adam Nahum, Max A. Metlitski, Cenke Xu, and T. Senthil. Deconfined quantum critical points: symmetries and dualities. *Phys. Rev. X*, 7(3):031051, 2017.

[76] Andreas Karch and David Tong. Particle-Vortex Duality from 3d Bosonization. *Phys. Rev. X*, 6(3):031043, 2016.

[77] E. Witten. Global aspects of current algebra. *Nucl. Phys. B*, 223:422–432, 1983.

[78] Akihiro Tanaka and Xiao Hu. Many-Body Spin Berry Phases Emerging from the π-Flux State: Competition between Antiferromagnetism and the Valence-Bond-Solid State. *Phys. Rev. Lett.*, 95(3):036402, Jul 2005.

[79] T. Senthil and Matthew P. A. Fisher. Competing orders, nonlinear sigma models, and topological terms in quantum magnets. *Phys. Rev. B*, 74(6):064405, Aug 2006.

[80] Junhyun Lee and Subir Sachdev. Wess-Zumino-Witten Terms in Graphene Landau Levels. *Phys. Rev. Lett.*, 114(22):226801, Jun 2015.

[81] J. Lleweilun Smith and Qimiao Si. Spatial correlations in dynamical mean-field theory. *Phys. Rev. B*, 61(8):5184–5193, Feb 2000.

[82] K. Haule, A. Rosch, J. Kroha, and P. Wölfle. Pseudogaps in an Incoherent Metal. *Phys. Rev. Lett.*, 89(23):236402, Nov 2002.

[83] K. Haule, A. Rosch, J. Kroha, and P. Wölfle. Pseudogaps in the t-J model: An extended dynamical mean-field theory study. *Phys. Rev. B*, 68(15):155119, Oct 2003.

[84] Serge Florens and Antoine Georges. Quantum impurity solvers using a slave rotor representation. *Phys. Rev. B*, 66(16):165111, Oct 2002.

[85] Serge Florens and Antoine Georges. Slave-rotor mean-field theories of strongly correlated systems and the Mott transition in finite dimensions. *Phys. Rev. B*, 70(3):035114, Jul 2004.

[86] Serge Florens, Priyanka Mohan, C. Janani, T. Gupta, and R. Narayanan. Magnetic fluctuations near the Mott transition towards a spin liquid state. *EPL*, 103:17002, Jun 2013.

[87] Wenbo Fu, Yingfei Gu, Subir Sachdev, and Grigory Tarnopolsky. $\mathbb{Z}_2$ fractionalized phases of a solvable, disordered, t-J model. *Phys. Rev. B*, 98(7):075150, 2018.

[88] Subir Sachdev, Chiranjeeb Buragohain, and Matthias Vojta. Quantum Impurity in a Nearly Critical Two Dimensional Antiferromagnet. *Science*, 286(5449):2479–2482, 1999.

[89] Matthias Vojta, Chiranjeeb Buragohain, and Subir Sachdev. Quantum impurity dynamics in two-dimensional antiferromagnets and superconductors. *Phys. Rev. B*, 61(22):15152–15184, Jun 2000.

[90] Subir Sachdev. Static hole in a critical antiferromagnet: field-theoretic renormalization group. *Physica C Superconductivity*, 357:78–81, Sep 2001.

[91] Matthias Vojta and Lars Fritz. Upper critical dimension in a quantum impurity model:Critical theory of the asymmetric pseudogap Kondo problem. *Phys. Rev. B*, 70(9):094502, Sep 2004.

[92] Lars Fritz and Matthias Vojta. Phase transitions in the pseudogap Anderson and Kondo models: Critical dimensions, renormalization group, and local-moment criticality. *Phys. Rev. B*, 70(21):214427, Dec 2004.

[93] L. Fritz. Quantum Phase Transitions in Models of Magnetic Impurities. *Ph. D. Dissertation, Universität Karlsruhe*, 2006.

[94] Qimiao Si and G. Kotliar. Fermi-liquid and non-Fermi-liquid phases of an extended Hubbard model in infinite dimensions. *Phys. Rev. Lett.*, 70:3143–3146, May 1993.

[95] Qimiao Si and Gabriel Kotliar. Metallic non-Fermi-liquid phases of an extended Hubbard model in infinite dimensions. *Phys. Rev. B*, 48(18):13881–13903, Nov 1993.

[96] Carlos Gonzalez-Buxton and Kevin Ingersent. Renormalization-group study of Anderson and Kondo impurities in gapless Fermi systems. *Phys. Rev. B*, 57(22):14254–14293, Jun 1998.

[97] Anirvan M. Sengupta. Spin in a fluctuating field: The Bose(+Fermi) Kondo models. *Phys. Rev. B*, 61:4041–4043, Feb 2000.

[98] Qimiao Si, Silvio Rabello, Kevin Ingersent, and J. Lleweilun Smith. Locally critical quantum phase transitions in strongly correlated metals. *Nature*, 413(6858):804–808, Oct 2001.

[99] Lijun Zhu and Qimiao Si. Critical local-moment fluctuations in the Bose-Fermi Kondo model. *Phys. Rev. B*, 66(2):024426, Jul 2002.

[100] J. H. Pixley, Stefan Kirchner, Kevin Ingersent, and Qimiao Si. Quantum criticality in the pseudogap Bose-Fermi Anderson and Kondo models: Interplay between fermion- and boson-induced Kondo destruction. *Phys. Rev. B*, 88(24):245111, Dec 2013.

[101] Yuan Huang, Kun Chen, Youjin Deng, and Boris Svistunov. Trapping centers at the superfluid-Mott-insulator criticality: Transition between charge-quantized states. *Phys. Rev. B*, 94(22):220502(R), Dec 2016.

[102] Seth Whitsitt and Subir Sachdev. Critical behavior of an impurity at the boson superfluid–Mott-insulator transition. *Phys. Rev. A*, 96(5):053620, 2017.

[103] Kun Chen, Yuan Huang, Youjin Deng, and Boris Svistunov. Halon: A quasiparticle featuring critical charge fractionalization. *Phys. Rev. B*, 98(21):214516, 2018.

[104] Pengfei Zhang. Dispersive Sachdev-Ye-Kitaev model: Band structure and quantum chaos. *Phys. Rev. B*, 96(20):205138, November 2017.

[105] Debanjan Chowdhury, Yochai Werman, Erez Berg, and T. Senthil. Translationally invariant non-Fermi liquid metals with critical Fermi-surfaces: Solvable models. *Phys. Rev. X*, 8(3):031024, 2018.

[106] Aavishkar A. Patel, John McGreevy, Daniel P. Arovas, and Subir Sachdev. Magnetotransport in a model of a disordered strange metal. *Phys. Rev. X*, 8(2):021049, 2018.

[107] Aavishkar A. Patel and Subir Sachdev. Theory of a Planckian metal. *Phys. Rev. Lett.*, 123(6):066601, 2019.

[108] M. Mitrano, A. A. Husain, S. Vig, A. Kogar, M. S. Rak, S. I. Rubeck, J. Schmalian, B. Uchoa, J. Schneeloch, R. Zhong, G. D. Gu, and P. Abbamonte. Anomalous density fluctuations in a strange metal. *Proceedings of the National Academy of Science*, 115(21):5392–5396, May 2018.

[109] A. A. Husain, M. Mitrano, M. S. Rak, S. I. Rubeck, B. Uchoa, J. Schneeloch, R. Zhong, G. D. Gu, and P. Abbamonte. Crossover of Charge Fluctuations across the Strange Metal Phase Diagram. *Phys. Rev. X*, 9:041062, Mar 2019.

[110] Bill Sutherland. Model for a multicomponent quantum system. *Phys. Rev. B*, 12:3795–3805, Nov 1975.

[111] P. A. Bares and G. Blatter. Supersymmetric t-J model in one dimension: Separation of spin and charge. *Phys. Rev. Lett.*, 64:2567–2570, May 1990.

[112] S Sarkar. The supersymmetric t-J model in one dimension. *J. Phys. A: Math. Gen.*, 24(5):1137–1151, mar 1991.

[113] Fabian H. L. Essler and Vladimir E. Korepin. Higher conservation laws and algebraic Bethe Ansätze for the supersymmetric t-J model. *Phys. Rev. B*, 46:9147–9162, Oct 1992.

[114] Frank Göhmann and Alexander Seel. A Note on the Bethe Ansatz Solution of the Supersymmetric t-J Model. *Czechoslovak Journal of Physics*, 53(11):1041–1046, Nov 2003.

[115] Subir Sachdev, Harley D. Scammell, Mathias S. Scheurer, and Grigory Tarnopolsky. Gauge theory for the cuprates near optimal doping. *Phys. Rev. B*, B99(5):054516, 2019.

[116] Masatoshi Imada, Atsushi Fujimori, and Yoshinori Tokura. Metal-insulator transitions. *Rev. Mod. Phys.*, 70:1039–1263, Oct 1998.

[117] Michael Hermele. SU(2) gauge theory of the Hubbard model and application to the honeycomb lattice. *Phys. Rev. B*, 76(3):035125, July 2007.

[118] T. Senthil. Theory of a continuous Mott transition in two dimensions. *Phys. Rev. B*, 78(4):045109, Jul 2008.

[119] Daniel Podolsky, Arun Paramekanti, Yong Baek Kim, and T. Senthil. Mott Transition between a Spin-Liquid Insulator and a Metal in Three Dimensions. *Phys. Rev. Lett.*, 102(18):186401, May 2009.

[120] William Witczak-Krempa, Pouyan Ghaemi, T. Senthil, and Yong Baek Kim. Universal transport near a quantum critical Mott transition in two dimensions. *Phys. Rev. B*, 86:245102, 2012.

[121] Juan Maldacena, Stephen H. Shenker, and Douglas Stanford. A bound on chaos. *JHEP*, 08:106, 2016.

[122] Juan Maldacena and Douglas Stanford. Remarks on the Sachdev-Ye-Kitaev model. *Phys. Rev. D*, 94(10):106002, 2016.

[123] Alexei Kitaev and S. Josephine Suh. The soft mode in the Sachdev-Ye-Kitaev model and its gravity dual. *JHEP*, 05:183, 2018.

[124] Aharon Kapitulnik, Steven A. Kivelson, and Boris Spivak. Anomalous metals – failed superconductors. *Rev. Mod. Phys.*, 91:011002, 2019.

[125] Xinyang Zhang, Bar Hen, Alexander Palevski, and Aharon Kapitulnik. Robust anomalous metallic states and vestiges of self-duality in two-dimensional granular in-inox composites. *npj Quantum Materials*, 6(1):30, 2021.

[126] Paul Malinowski, Qianni Jiang, Joshua J. Sanchez, Joshua Mutch, Zhaoyu Liu, Preston Went, Jian Liu, Philip J. Ryan, Jong-Woo Kim, and Jiun-Haw Chu. Suppression of superconductivity by anisotropic strain near a nematic quantum critical point. *Nature Physics*, 16(12):1189–1193, January 2020.

[127] C. G. L. Bøttcher, F. Nichele, M. Kjaergaard, H. J. Suominen, J. Shabani, C. J. Palmstrøm, and C. M. Marcus. Superconducting, insulating and anomalous metallic regimes in a gated two-dimensional semiconductor-superconductor array. *Nature Physics*, 14(11):1138–1144, August 2018.

[128] Thomas Dubouchet, Benjamin Sacépé, Johanna Seidemann, Dan Shahar, Marc Sanquer, and Claude Chapelier. Collective energy gap of preformed Cooper pairs in disordered superconductors. *Nature Physics*, 15(3):233–236, December 2018.

[129] Vladimir Dobrosavljevic, Nandini Trivedi, and James M. Valles, editors. *Conductor-Insulator Quantum Phase Transitions.* Oxford University Press, Oxford, 2012.

[130] A. M. Goldman. Superconductor-Insulator Transitions. *International Journal of Modern Physics B*, 24:4081–4101, August 2010.

[131] M. V. Feigel'man, L. B. Ioffe, V. E. Kravtsov, and E. Cuevas. Fractal superconductivity near localization threshold. *Annals of Physics*, 325(7):1390–1478, July 2010.

[132] Victor M. Galitski, G. Refael, Matthew P. Fisher, and T. Senthil. Vortices and Quasiparticles near the Superconductor-Insulator Transition in Thin Films. *Phys. Rev. Lett.*, 95(7):077002, August 2005.

[133] S. L. Sondhi, S. M. Girvin, J. P. Carini, and D. Shahar. Continuous quantum phase transitions. *Reviews of Modern Physics*, 69(1):315–333, January 1997.

[134] A. M. Finkel'stein. *JETP Lett.*, 45:46, 1987.

[135] Subir Sachdev. Bekenstein-Hawking Entropy and Strange Metals. *Phys. Rev. X*, 5(4):041025, 2015.

[136] Yingfei Gu, Alexei Kitaev, Subir Sachdev, and Grigory Tarnopolsky. Notes on the complex Sachdev-Ye-Kitaev model. *JHEP*, 02:157, 2020.

[137] I. L. Kurland, I. L. Aleiner, and B. L. Altshuler. Mesoscopic magnetization fluctuations for metallic grains close to the Stoner instability. *Phys. Rev. B*, 62:14886–14897, Dec 2000.

[138] Y. Alhassid. The Statistical theory of quantum dots. *Rev. Mod. Phys.*, 72:895–968, 2000.

[139] I. L. Aleiner, P. W. Brouwer, and L. I. Glazman. Quantum effects in Coulomb blockade. *Physics Reports*, 358(5-6):309–440, March 2002.

[140] Grigory Tarnopolsky, Chenyuan Li, Darshan G. Joshi, and Subir Sachdev. Metal-insulator transition in a random Hubbard model. *Phys. Rev. B*, 101(20):205106, 2020.

[141] Darshan G. Joshi and Subir Sachdev. Anomalous density fluctuations in a random t -J model. *Phys. Rev. B*, 102(16):165146, October 2020.

[142] Henry Shackleton, Alexander Wietek, Antoine Georges, and Subir Sachdev. Quantum phase transition at nonzero doping in a random t–j model. *Phys. Rev. Lett.*, 126:136602, Mar 2021.

[143] Haoyu Guo, Yingfei Gu, and Subir Sachdev. Linear in temperature resistivity in the limit of zero temperature from the time reparameterization soft mode. *Annals of Physics*, 418:168202, 2020.

[144] Antoine Georges, Gabriel Kotliar, Werner Krauth, and Marcelo J. Rozenberg. Dynamical mean-field theory of strongly correlated fermion systems and the limit of infinite dimensions. *Rev. Mod. Phys.*, 68:13–125, Jan 1996.

[145] Gabriel Kotliar and Andrei E. Ruckenstein. New Functional Integral Approach to Strongly Correlated Fermi Systems: The Gutzwiller Approximation as a Saddle Point. *Phys. Rev. Lett.*, 57:1362–1365, Sep 1986.

[146] S. Sachdev. Quantum phase transitions of antiferromagnets and the cuprate superconductors. *Lect. Notes Phys.*, 843:1, 2012.

[147] Maria Tikhanovskaya, Haoyu Guo, Subir Sachdev, and Grigory Tarnopolsky. Excitation spectra of quantum matter without quasiparticles. i. sachdev-ye-kitaev models. *Physical Review B*, 103(7), February 2021.

[148] Maria Tikhanovskaya, Haoyu Guo, Subir Sachdev, and Grigory Tarnopolsky. Excitation spectra of quantum matter without quasiparticles. ii. random $t - j$ models. *Phys. Rev. B*, 103:075142, Feb 2021.

[149] Shang-Shun Zhang, Yi-Ming Wu, Artem Abanov, and Andrey V. Chubukov. Interplay between superconductivity and non-Fermi liquid at a quantum critical point in a metal. VI. The γ model and its phase diagram at $2 < \gamma < 3$. *Phys. Rev. B*, 104(14):144509, October 2021.

[150] Dimitri Pimenov and Andrey V. Chubukov. Twists and turns of superconductivity from a repulsive dynamical interaction. *Annals of Physics*, 447:169049, December 2022.

[151] Carsten Bauer, Yoni Schattner, Simon Trebst, and Erez Berg. Hierarchy of energy scales in an O(3) symmetric antiferromagnetic quantum critical metal: A Monte Carlo study. *Physical Review Research*, 2(2):023008, April 2020.

[152] Max A. Metlitski, David F. Mross, Subir Sachdev, and T. Senthil. Cooper pairing in non-Fermi liquids. *Phys. Rev. B*, 91:115111, Mar 2015.

[153] Ipsita Mandal. Superconducting instability in non-Fermi liquids. *Phys. Rev. B*, 94(11):115138, September 2016.

[154] Ilya Esterlis, Haoyu Guo, Aavishkar A. Patel, and Subir Sachdev. Large N theory of critical Fermi surfaces. *Phys. Rev. B*, 103(23):235129, 2021.

[155] Chenyuan Li, Darshan G. Joshi, and Subir Sachdev. Critical anomalous metals near superconductivity in models with random interactions. *Phys. Rev. B*, 103(11):115147, March 2021.

[156] Igor R. Klebanov, Alexey Milekhin, Grigory Tarnopolsky, and Wenli Zhao. Spontaneous breaking of U(1) symmetry in coupled complex SYK models. *Journal of High Energy Physics*, 2020(11):162, November 2020.

[157] Étienne Lantagne-Hurtubise, Vedangi Pathak, Sharmistha Sahoo, and Marcel Franz. Superconducting instabilities in a spinful Sachdev-Ye-Kitaev model. *Phys. Rev. B*, 104(2):L020509, July 2021.

[158] Yuxuan Wang. Solvable Strong-Coupling Quantum-Dot Model with a Non-Fermi-Liquid Pairing Transition. *Phys. Rev. Lett.*, 124(1):017002, January 2020.

[159] Hanteng Wang, A. L. Chudnovskiy, Alexander Gorsky, and Alex Kamenev. Sachdev-Ye-Kitaev superconductivity: Quantum Kuramoto and generalized Richardson models. *Phys. Rev. Res.*, 2(3):033025, 2020.

[160] Ilya Esterlis and Jörg Schmalian. Cooper pairing of incoherent electrons: An electron-phonon version of the sachdev-ye-kitaev model. *Physical Review B*, 100(11), September 2019.

[161] Aavishkar A. Patel, Michael J. Lawler, and Eun-Ah Kim. Coherent Superconductivity with a Large Gap Ratio from Incoherent Metals. *Phys. Rev. Lett.*, 121(18):187001, November 2018.

[162] Debanjan Chowdhury and Erez Berg. Intrinsic superconducting instabilities of a solvable model for an incoherent metal. *Physical Review Research*, 2(1):013301, March 2020.

[163] A.L. Chudnovskiy and Alex Kamenev. Superconductor-insulator transition in a non-fermi liquid. *Physical Review Letters*, 129(26), December 2022.

[164] Sharmistha Sahoo, Étienne Lantagne-Hurtubise, Stephan Plugge, and Marcel Franz. Traversable wormhole and Hawking-Page transition in coupled complex SYK models. *Physical Review Research*, 2(4):043049, October 2020.

[165] Emil A. Yuzbashyan, Alexander A. Baytin, and Boris L. Altshuler. Strong-coupling expansion for the pairing Hamiltonian for small superconducting metallic grains. *Phys. Rev. B*, 68(21):214509, December 2003.

[166] Emil A. Yuzbashyan, Alexander A. Baytin, and Boris L. Altshuler. Finite-size corrections for the pairing Hamiltonian. *Phys. Rev. B*, 71(9):094505, March 2005.

[167] Maine Christos, Felix M. Haehl, and Subir Sachdev. Spin liquid to spin glass crossover in the random quantum Heisenberg magnet. *Phys. Rev. B*, 105(8):085120, 2022.

[168] L. C. Hebel and C. P. Slichter. Nuclear spin relaxation in normal and superconducting aluminum. *Phys. Rev.*, 113:1504–1519, Mar 1959.

[169] M. Takigawa, A. P. Reyes, P. C. Hammel, J. D. Thompson, R. H. Heffner, Z. Fisk, and K. C. Ott. Cu and o nmr studies of the magnetic properties of $\mathrm{yba_2cu_3o_{6.63}}$ (t_c=62 k). *Phys. Rev. B*, 43:247–257, Jan 1991.

[170] Hideto Fukazawa, Yuji Yamada, Kenji Kondo, Taku Saito, Yoh Kohori, Kentarou Kuga, Yosuke Matsumoto, Satoru Nakatsuji, Hijiri Kito, Parasharam M. Shirage, Kunihiro Kihou, Nao Takeshita, Chul-Ho Lee, Akira Iyo, and Hiroshi Eisaki. Possible multiple gap superconductivity with line nodes in heavily hole-doped superconductor kfe2as2 studied by 75as nuclear quadrupole resonance and specific heat. *Journal of the Physical Society of Japan*, 78(8):083712, 2009.

[171] Seongjin Ahn and Sankar Das Sarma. Planckian properties of two-dimensional semiconductor systems. *Phys. Rev. B*, 106(15):155427, October 2022.

[172] D. van der Marel, H. J. A. Molegraaf, J. Zaanen, Z. Nussinov, F. Carbone, A. Damascelli, H. Eisaki, M. Greven, P. H. Kes, and M. Li. Quantum critical behaviour in a high-T_c superconductor. *Nature*, 425(6955):271–274, September 2003.

[173] Louis Taillefer. Scattering and Pairing in Cuprate Superconductors. *Annual Review of Condensed Matter Physics*, 1:51–70, April 2010.

[174] Erik E. Aldape, Tessa Cookmeyer, Aavishkar A. Patel, and Ehud Altman. Solvable theory of a strange metal at the breakdown of a heavy Fermi liquid. *Phys. Rev. B*, 105(23):235111, June 2022.

[175] Haoyu Guo, Davide Valentinis, Jörg Schmalian, Subir Sachdev, and Aavishkar A. Patel. Cyclotron resonance and quantum oscillations of critical Fermi surfaces. *Phys. Rev. B*, 109:075162, Feb 2024.

[176] Davide Valentinis, Gian Andrea Inkof, and Jörg Schmalian. BCS to incoherent superconductivity crossovers in the Yukawa-SYK model on a lattice. *arXiv e-prints*, February 2023.

[177] Hossein Hosseinabadi, Shane P. Kelly, Jörg Schmalian, and Jamir Marino. Thermalization of non-Fermi-liquid electron-phonon systems: Hydrodynamic relaxation of the Yukawa-Sachdev-Ye-Kitaev model. *Phys. Rev. B*, 108(10):104319, September 2023.

[178] Noga Bashan, Evyatar Tulipman, Jörg Schmalian, and Erez Berg. Tunable non-Fermi liquid phase from coupling to two-level systems. October 2023.

[179] Aavishkar A. Patel, Peter Lunts, and Subir Sachdev. Localization of overdamped bosonic modes and transport in strange metals. *Proc. Nat. Acad. Sci.*, 121:e2402052121, 2024.

[180] Evyatar Tulipman, Noga Bashan, Jörg Schmalian, and Erez Berg. Solvable models of two-level systems coupled to itinerant electrons: Robust non-Fermi liquid and quantum critical pairing. April 2024.

[181] Hilbert V. Löhneysen, Achim Rosch, Matthias Vojta, and Peter Wölfle. Fermi-liquid instabilities at magnetic quantum phase transitions. *Rev. Mod. Phys.*, 79(3):1015–1075, July 2007.

[182] Sean A. Hartnoll, Raghu Mahajan, Matthias Punk, and Subir Sachdev. Transport near the Ising-nematic quantum critical point of metals in two dimensions. *Phys. Rev. B*, 89(15):155130, April 2014.

[183] Aavishkar A. Patel and Subir Sachdev. dc resistivity at the onset of spin density wave order in two-dimensional metals. *Phys. Rev. B*, 90(16):165146, October 2014.

[184] Subir Sachdev. Strange metals and black holes: insights from the Sachdev-Ye-Kitaev model. *Oxford Research Encyclopedia in Physics*, 5 2023.

[185] Patrick A. Lee and T. V. Ramakrishnan. Disordered electronic systems. *Rev. Mod. Phys.*, 57:287–337, Apr 1985.

[186] J. T. Chayes, L. Chayes, Daniel S. Fisher, and T. Spencer. Finite-Size Scaling and Correlation Lengths for Disordered Systems. *Phys. Rev. Lett.*, 57:2999–3002, Dec 1986.

[187] Tsz Chun Wu, Yunxiang Liao, and Matthew S. Foster. Quantum interference of hydrodynamic modes in a dirty marginal Fermi liquid. *Phys. Rev. B*, 106(15):155108, October 2022.

[188] Wenbo Fu, Davide Gaiotto, Juan Maldacena, and Subir Sachdev. Supersymmetric Sachdev-Ye-Kitaev models. *Phys. Rev. D*, 95(2):026009, 2017. [Addendum: Phys.Rev.D 95, 069904 (2017)].

[189] Jeff Murugan, Douglas Stanford, and Edward Witten. More on Supersymmetric and 2d Analogs of the SYK Model. *JHEP*, 08:146, 2017.

[190] Aavishkar A. Patel and Subir Sachdev. Critical strange metal from fluctuating gauge fields in a solvable random model. *Phys. Rev. B*, 98(12):125134, 2018.

[191] Eric Marcus and Stefan Vandoren. A new class of SYK-like models with maximal chaos. *JHEP*, 01:166, 2019.

[192] Yuxuan Wang. Solvable Strong-coupling Quantum Dot Model with a Non-Fermi-liquid Pairing Transition. *Phys. Rev. Lett.*, 124(1):017002, 2020.

[193] Yuxuan Wang and Andrey V. Chubukov. Quantum Phase Transition in the Yukawa-SYK Model. *Phys. Rev. Res.*, 2(3):033084, 2020.

[194] Wei Wang, Andrew Davis, Gaopei Pan, Yuxuan Wang, and Zi Yang Meng. Phase diagram of the spin-1/2 Yukawa-Sachdev-Ye-Kitaev model: Non-Fermi liquid, insulator, and superconductor. *Phys. Rev. B*, 103(19):195108, May 2021.

[195] Milica Milovanović, Subir Sachdev, and R. N. Bhatt. Effective-field theory of local-moment formation in disordered metals. *Phys. Rev. Lett.*, 63:82–85, Jul 1989.

[196] Douglas J. Scalapino, Steven R. White, and Shoucheng Zhang. Insulator, metal, or superconductor: The criteria. *Phys. Rev. B*, 47:7995–8007, Apr 1993.

[197] Z.-X. Shen and J. R. Schrieffer. Momentum, temperature, and doping dependence of photoemission lineshape and implications for the nature of the pairing potential in high- T_c superconducting materials. *Phys. Rev. Lett.*, 78:1771–1774, Mar 1997.

[198] D. L. Feng, D. H. Lu, K. M. Shen, C. Kim, H. Eisaki, A. Damascelli, R. Yoshizaki, J. i. Shimoyama, K. Kishio, G. D. Gu, S. Oh, A. Andrus, J. O'Donnell, J. N. Eckstein, and Z. X. Shen. Signature of superfluid density in the single-particle excitation spectrum of bi2sr2cacu2o8+. *Science*, 289(5477):277–281, 2024/04/24 2000.

[199] N. Read and Subir Sachdev. Some features of the phase diagram of the square lattice SU(N) antiferromagnet. *Nucl. Phys. B*, 316(3):609 – 640, 1989.

[200] R. A. Davison, W. Fu, A. Georges, Y. Gu, K. Jensen, and S. Sachdev. Thermoelectric transport in disordered metals without quasiparticles: The Sachdev-Ye-Kitaev models and holography. *Phys. Rev. B*, 95(15):155131, April 2017.

[201] Yingfei Gu, Alexei Kitaev, Subir Sachdev, and Grigory Tarnopolsky. Notes on the complex sachdev-ye-kitaev model. *Journal of High Energy Physics*, 2020(2), February 2020.

[202] N. Read, Subir Sachdev, and J. Ye. Landau theory of quantum spin glasses of rotors and Ising spins. *Phys. Rev. B*, 52(1):384–410, July 1995.

[203] John A. Hertz. Quantum critical phenomena. *Phys. Rev. B*, 14:1165–1184, Aug 1976.

[204] H. J. Vidberg and J. W. Serene. Solving the eliashberg equations by means ofn-point padé approximants. *Journal of Low Temperature Physics*, 29:179–192, 1977.

[205] Subir Sachdev, T. Senthil, and R. Shankar. Finite-temperature properties of quantum antiferromagnets in a uniform magnetic field in one and two dimensions. *Phys. Rev. B*, 50(1):258–272, July 1994.

[206] Olivier Parcollet, Antoine Georges, Gabriel Kotliar, and Anirvan Sengupta. Overscreened multichannel SU(N) Kondo model: Large-N solution and conformal field theory. *Phys. Rev. B*, 58(7):3794–3813, August 1998.

[207] Daniel Hauck, Markus J. Klug, Ilya Esterlis, and Jörg Schmalian. Eliashberg equations for an electron–phonon version of the sachdev–ye–kitaev model: Pair breaking in non-fermi liquid superconductors. *Annals of Physics*, 417:168120, 2020. Eliashberg theory at 60: Strong-coupling superconductivity and beyond.

[208] P. M. Dee, K. Nakatsukasa, Y. Wang, and S. Johnston. Temperature-filling phase diagram of the two-dimensional Holstein model in the thermodynamic limit by self-consistent Migdal approximation. *Phys. Rev. B*, 99:024514, Jan 2019.